



**HAL**  
open science

# Développement et validation d'un modèle global de houle basé sur les observations de Radar à Ouverture Synthétique en mode vague

Romain Husson

► **To cite this version:**

Romain Husson. Développement et validation d'un modèle global de houle basé sur les observations de Radar à Ouverture Synthétique en mode vague. Sciences de la Terre. Université de Bretagne occidentale - Brest, 2012. Français. NNT : 2012BRES0050 . tel-00863728

**HAL Id: tel-00863728**

**<https://theses.hal.science/tel-00863728>**

Submitted on 19 Sep 2013

**HAL** is a multi-disciplinary open access archive for the deposit and dissemination of scientific research documents, whether they are published or not. The documents may come from teaching and research institutions in France or abroad, or from public or private research centers.

L'archive ouverte pluridisciplinaire **HAL**, est destinée au dépôt et à la diffusion de documents scientifiques de niveau recherche, publiés ou non, émanant des établissements d'enseignement et de recherche français ou étrangers, des laboratoires publics ou privés.



université de bretagne  
occidentale



**THÈSE / UNIVERSITÉ DE BRETAGNE  
OCCIDENTALE**

*sous le sceau de l'Université européenne de Bretagne*

pour obtenir le titre de

**DOCTEUR DE L'UNIVERSITÉ DE BRETAGNE OCCIDENTALE**

*Mention : Océanographie Physique*

**École Doctorale des Sciences de la Mer**

présentée par

**Romain Husson**

Préparée à CLS

(Collecte Localisation Satellite),

Direction des Applications Radar

Développement et validation  
d'un modèle global de houle  
basé sur les observations de  
Radar à Ouverture Synthétique  
en mode vague

Development and validation of a global  
observation-based swell model  
using wave mode operating  
Synthetic Aperture Radar

**Thèse soutenue le 26 Octobre 2012**

devant le jury composé de :

**Fabrice ARDHUIN**

Chercheur, IFREMER / *qualité*

**Xavier CARTON**

Professeur, UBO / *président du jury*

**Bertrand CHAPRON**

Chercheur, IFREMER / *examineur*

**Fabrice COLLARD**

Chercheur, CLS / *examineur*

**Ben HOLT**

Chercheur, Jet Propulsion Laboratory / *rapporteur*

**Hendrik TOLMAN**

Directeur du service NOAA/NCEP/MMAB, NOAA / *rapporteur*

**Jean TOURNADRE**

Chercheur, IFREMER / *directeur de thèse*

THIS PAGE INTENTIONALLY LEFT BLANK

## Résumé

L'océan tient une place centrale dans notre environnement, d'un point de vue climatologique tant qu'économique. Nos besoins pour une meilleure compréhension des dynamiques océaniques, une sécurité accrue du transport de marchandises, une exploitation croissante des énergies marines renouvelables, des ressources offshore et halieutiques requièrent sans cesse l'amélioration de nos moyens d'observations et nos capacités de prédiction.

L'intérêt des observations satellites fournies par l'observation par satellite pour l'étude et la compréhension de la machine océan est largement démontré avec le premier lancement du satellite SEASAR en 1978. Plus spécifiquement, les observations d'*Alpers et al. (1981)* et *Vesecky and Stewart (1982)* indiquent que les images issues de l'instrument SAR (de l'anglais Synthetic Aperture Radar) peuvent être utilisées pour obtenir une information spectrale de l'état de mer. Cependant, la transformation entre le spectre de l'image SAR et celui des vagues est complexe et peut présenter des non-linéarités importantes à cause du processus imageur de l'instrument (*Hasselmann and Hasselmann, 1991*). Le principal phénomène limitant, la coupure azimutale, agit comme un filtre passe-bas qui empêche l'observation des vagues courtes comme la mer du vent. Dans le cas d'observation de vagues longues comme la houle, la transformation devient quasi-linéaire et le spectre de vagues associé peut-être estimé (*Krogstad, 1992; Engen and Johnsen, 1995*). Rappelons que la houle est une onde de gravité qui se propage à la surface de la mer, parfois sur plusieurs milliers de kilomètres et qui a été générée par des vents violents loin de la zone d'observation. L'ensemble des vagues générées par une tempête forme un champ (ou système).

Le développement d'un nouveau mode d'acquisition, le mode vague, qui a équipé les SAR embarqués sur les missions ERS-1/2 et ENVISAT a non seulement prouvé sa capacité à mesurer le spectre de la houle avec une précision croissante (*Engen and Johnsen, 1995; Johnsen and Collard, 2004; Johnsen et al., 2006; Collard et al., 2009*) mais également à observer la propagation de champs de houle à l'échelle d'un bassin océanique (*Holt et al., 1998; Heimbach and Hasselmann, 2000; Collard et al., 2009; Ardhuin et al., 2009*). En particulier, le SAR est le seul instrument de mesure qui permette d'avoir la vision spatio-temporelle globale nécessaire à l'étude de tels phénomènes (*Delpy et al., 2010*). Ainsi, l'utilisation de ces données a d'ores et déjà permis une meilleure compréhension des processus dissipatifs, qui a ensuite entraîné une meilleure paramétrisation des modèles d'états de mer comme WAVEWATCH III<sup>®</sup>, noté WW3 (*Ardhuin et al., 2010*). Ces avancées et les pistes de développement dégagées dans ces dernières publications laissent un large espace pour de nouveaux développements. Ceux-ci sont par ailleurs motivés par les prochaines missions Sentinel-1 A/B et CFOSAT qui

assureront, à partir de 2013, une pérennité de la donnée pour les 10 années à venir.

Malgré tout, l'utilisation des données SAR pour l'observation et la prédiction de la houle reste restreinte. Les principales causes sont l'échantillonnage spatio-temporel parfois très irrégulier des champs de houle, la complexité de la mesure et l'absence de méthodes permettant de fournir une information filtrée dont la précision est connue. Le but de cette thèse est donc de développer et de valider une méthodologie pour l'exploitation des données SAR du mode vague à leur plein potentiel pour l'étude, la compréhension et la prédiction de la propagation des champs de houle.

Tout d'abord, les principes de la mesure de spectre de houle à l'aide du SAR et les propriétés de la houle sont rappelés dans les chapitres 1 et 2.

Dans le chapitre suivant, en utilisant le réseau de bouées NDBC (de l'anglais National Data Buoy Center), les performances de l'estimation des mesures de spectres de houle<sup>1</sup> sont quantifiées en utilisant une méthodologie de co-localisation et de comparaison des données inspirée de *Portilla et al.* (2009). Les erreurs statistiques sont ainsi estimées pour les trois paramètres intégraux. La hauteur significative, la période pic et la direction pic de propagation donnent respectivement des erreurs standards de 30 cm, 0.7 s et 16°. Toutefois, il apparaît que les mesures de hauteur significative et de période pic comportent des biais importants qui tendent à sous-estimer les valeurs les plus importantes et surestimer les valeurs les plus faibles. Par exemple, les hauteurs significatives sont largement sous-estimées pour la houle de plus de 2 m (biais de -26 cm en moyenne). Le biais moyen sur la période pic des houles de plus de 15.5 s est lui d'environ 1 s.

De nombreux paramètres influencent la qualité de la mesure : la variance normalisée de l'image SAR à partir de laquelle le spectre de houle est calculé, la vitesse du vent de surface, le contraste entre les différentes partitions de houle dans le spectre observé<sup>2</sup>, la coupure azimutale et l'indicateur de confiance dans la direction de propagation. L'effet de ces paramètres sur la précision et le biais de mesure est également estimé.

Une méthode de reconstruction de champs de houle est ensuite proposée dans le chapitre 5. Elle permet de rassembler entre elles les observations SAR relatives à un même champ de houle. Elle est basée sur l'hypothèse selon

---

1. Dernière génération des produits vagues de niveau 2 issus du capteur ASAR à bord d'ENVISAT et processés avec les algorithmes développés dans le cadre du projet européen Globwave.

2. A la surface de la mer, plusieurs champs de houle peuvent être présents simultanément. Il convient alors de découper le spectre de houle en partitions, qui correspondent aux domaines fréquentiel et directionnel relatifs aux différents champs en présence.

laquelle les positions estimées dans le passé des observations appartenant au même système convergent vers la même zone de tempête (*Barber and Ursell, 1948; Munk and Snodgrass, 1957; Munk et al., 1963; Snodgrass et al., 1966*). Une des principales innovation de la méthode proposée est qu'elle ne suppose pas une source ponctuelle en temps et en espace. Une analyse de l'année 2008 a permis de démontrer qu'en moyenne au sein d'un même champ de houle, les vagues les plus longues quittent la zone de génération avant les vagues les plus courtes. Dans ces cas-ci, l'intervalle de temps moyen et la déviation standard associée sont respectivement égales à 14 et 12 h. Dans certains exemples de champs de houle, cette différence peut être supérieure à 48h. Ces observations semblent indiquer que la génération des vagues reste un processus important durant la phase d'affaiblissement des tempêtes.

Une fois la reconstruction effectuée, les observations SAR associées décrivent les propriétés spatio-temporelles du nouveau champ de houle qu'elles définissent. Cette approche, valable en océan profond, en l'absence de courant et en dehors des zones d'ombres des îles, est un outil indépendant aussi bien pour la prévision des conditions de houle à quelques jours que pour leur étude climatologique et celle des tempêtes associées. En particulier, les principaux foyers de générations identifiés sur l'année 2008 sont en accord avec ceux déjà identifiés grâce aux altimètres et aux diffusiomètres. Dans le futur, l'utilisation des archives issues du satellite ERS-2, lancé en 1995, devrait permettre d'établir une climatologie de la distribution de l'énergie des tempêtes sur les 17 dernières années.

Un champ de houle reconstruit grâce à la méthode précédemment décrite est constitué d'un ensemble de mesures SAR propagées dont la distribution spatio-temporelle et la qualité sont très inhomogènes. Ces constatations viennent alimenter deux travaux sciemment différents : comprendre les raisons de cette hétérogénéité d'une part (chapitre 4), et proposer une méthodologie pour remédier à cette donnée du problème d'autre part (chapitre 6). Ainsi, après avoir discuté des limitations de la mesure inhérentes à l'instrument, les limitations de l'observation de champs de houle liées à son échantillonnage par le SAR sont traitées dans le chapitre 4. Celles-ci sont liées aux déplacements d'un champ de houle relativement à l'orbite du satellite. En effet, il existe des configurations particulières pour lesquelles la houle se propage précisément à la même vitesse que la trace de l'instrument entraînant, selon le phasage, un échantillonnage systématique ou au contraire l'absence de mesure. Pour ces raisons, on parle d'*échantillonnage stroboscopique* de la houle. Ces conditions n'étant jamais réalisées sur l'intégralité d'un champ de houle, son échantillonnage par le SAR présente souvent d'importantes inhomogénéités spatiales. Les conditions et les probabilités d'occurrence de ce phénomène sont d'abord estimées dans le cas du satellite ENVISAT puis de la future mission Sentinel-1. Il apparaît que la répétitivité de l'orbite de ce dernier et le nouveau mode d'acquisition, dit en "leap frog" (de

l'anglais "saut de grenouille" pour désigner le mode correspondant à l'alternance des angles d'incidence entre chaque acquisition), des mesures du mode vague amélioreront considérablement l'homogénéité de l'échantillonnage des champs de houle. Cette étude apparaît particulièrement intéressante pour le choix des orbites des futures missions telles que CFOSAT.

Dans le chapitre 6, une méthode de construction d'un champ synthétique est développée à partir des champs de houle reconstruits afin de filtrer les données de mauvaise qualité et de combiner les autres pour produire une information sur les paramètres intégraux sur une grille régulière. Les performances sont estimées en comparant ces champs synthétiques à des observations *in situ*. Un facteur de qualité est également identifié : la précision des estimations dépend en effet linéairement de la densité d'observations SAR propagées à l'intérieur du champ de houle.

Cette nouvelle approche permet de considérablement accroître le nombre de co-localisations avec des données *in-situ* comparativement aux observations seules, ce qui a pour effet de mieux caractériser la donnée.

Les perspectives ouvertes par ce nouveau produit sont multiples. Premièrement, il permettra de mieux quantifier les biais de mesures sur la hauteur significative et la période pic constatés sur les observations SAR et clairement, reproduits par les champs synthétiques.

Par ailleurs, l'inspection des données aberrantes permet de mettre en évidence pour la première fois un biais de mesure des hauteurs significatives lié à la direction de la houle relativement à l'instrument. Autour de la direction azimutale, la hauteur significative apparaît sous-estimée de 15 cm en moyenne et ce biais est supérieur à 70 cm dans certains cas. Ces biais de mesure feront l'objet d'une attention particulière dans les tâches de calibration/validation des futures missions SAR Sentinel-1 A/B. Une nouvelle piste de recherche liée à un modèle de dissipation d'énergie inadapté aux cas de tempêtes spatialement étendues est également dégagée. Grâce à l'importante base de données constituée, les champs synthétiques devraient permettre d'affiner les modèles déjà établis par le passé grâce à la donnée SAR. Enfin, une inter-comparaison avec le modèle WW3 montre que les données issues du champ synthétique fournissent une information plus précise dans des cas bien caractérisés.

Pour faciliter l'accès à la donnée SAR, l'ensemble des chaînes de traitement nécessaires au reprocessing des archives, à la prévision journalière et à la dissémination des résultats sont déjà disponibles et seront déployées de façon opérationnelle. Par le passé, elles ont été utilisées pour la fourniture à EDF d'un service de prévision de houle à la Réunion pour l'installation d'un prototype d'houlomotrice.

Dans le futur, les champs synthétiques SAR pourraient être avantageusement utilisés dans les schémas d'assimilation pour corriger les erreurs du modèle liées par exemple à un forçage atmosphérique ou un paramétrage erronés. Déjà, l'utilisation des simples observations SAR a montré une amélioration des performances modèles (*Aouf and Lefèvre, 2012*). Les lancements de la constellation Sentinel-1A/B et du satellite CFOSAT devraient encore considérablement améliorer notre capacité d'observation, de compréhension et de prévision de la houle.

## Bibliographie

- Alpers, W. R., D. B. Ross, et C. L. Rufenach (1981), On the detectability of ocean surface waves by real and synthetic aperture radar, *J. Geophys. Res.*, *86*(C7), 6481–6498. ii, 1, 24
- Aouf, L., et J.-M. Lefèvre (2012), On the impact of ASAR wave spectra in the operational wave model MFWAM, in *Proceedings of SEASAR 2012*, ESA, Tromsø. vi, 2
- Ardhuin, F., B. Chapron, et F. Collard (2009), Observation of swell dissipation across oceans, *Geophys. Res. Lett.*, *36*, L06,607, doi :10.1029/2008GL037030. ii, 2, 70, 71, 152, 181, 237
- Ardhuin, F., E. Rogers, A. Babanin, J.-F. c. Filipot, R. Magne, A. Roland, A. v. d. Westhuysen, P. Queffelec, J.-M. Lefevre, L. Aouf, et F. Collard (2010), Semi-empirical dissipation source functions for wind-wave models : part i, definition, calibration and validation, *J. Phys. Oceanogr.*, *40*(9), 1917–1941. ii, 237, 238, 239
- Barber, N. F., et F. Ursell (1948), The generation and propagation of ocean waves and swell. i wave periods and velocities, *Phil. Trans. Roy. Soc. London A*, *240*, 527–560. iv, 56, 67
- Collard, F., F. Ardhuin, et B. Chapron (2009), Monitoring and analysis of ocean swell fields from space : New methods for routine observations, *Journal of Geophysical Research-Oceans*, *114*(C7), C07,023. ii, 2, 68, 69, 70, 71, 80, 85, 111, 152, 153, 155, 219, 239
- Delpey, M., F. Ardhuin, F. Collard, et B. Chapron (2009), Space-time structure of long ocean swell fields.
- Engen, G., et H. Johnsen (1995), SAR-ocean wave inversion using image cross spectra, *IEEE transactions on geoscience and remote sensing*, *33*(4), 1047–1056. ii, 2, 34, 37, 44
- Hasselmann, K., et S. Hasselmann (1991), On the nonlinear mapping of an ocean wave spectrum into a synthetic aperture radar image spectrum and

- its inversion, *Journal of Geophysical Research*, 96(C6), 10,713–10. ii, 2, 31, 34, 38, 45
- Heimbach, P., et K. Hasselmann (2000), Development and application of satellite retrievals of ocean wave spectra, *Elsevier Oceanography Series*, 63, 5–33. ii, 2, 239
- Holt, B., A. K. Liu, D. W. Wang, A. Gnanadesikan, et H. S. Chen (1998), Tracking storm-generated waves in the northeast pacific ocean with ERS-1 synthetic aperture radar imagery and buoys, *Journal of Geophysical Research*, 103(C4). ii, 2, 239
- Johnsen, H., et F. Collard (2004), ASAR wave mode processing-validation of reprocessing upgrade, *Tech. rep.*, technical report for ESA-ESRIN under contract 17376/03/I-OL, Tech. Rep. 168, NORUT. ii, 80, 83, 91, 111
- Johnsen, H., G. Engen, F. Collard, V. Kerbaol, et B. Chapron (2006), ENVISAT ASAR wave mode products-quality assessment and algorithm upgrade, *Proceedings of SEASAR*. ii, 2, 111
- Krogstad, H. E. (1992), A simple derivation of Hasselmann's nonlinear ocean-synthetic aperture radar transform, *J. Geophys. Res.*, 97(C2), 2421–2425. ii, 2, 34, 36, 37, 38, 45, 242
- Munk, W., et F. Snodgrass (1957), Measurements of southern swell at guadalupe island, *Deep Sea Research (1953)*, 4, 272, IN1–IN2, 273–286, doi:10.1016/0146-6313(56)90061-2. iv, 56, 67
- Munk, W. H., G. R. Miller, F. E. Snodgrass, et N. F. Barber (1963), Directional recording of swell from distant storms, *Philosophical Transactions of the Royal Society of London. Series A, Mathematical and Physical Sciences*, 255(1062), 505–584. iv, 2, 56, 67, 237
- Portilla, J., F. Ocampo-Torres, et J. Monbaliu (2009), Spectral partitioning and identification of wind sea and swell, *Journal of Atmospheric and Oceanic Technology*, 26(1), 107–122. iii, 86, 87
- Snodgrass, F. E., G. W. Groves, K. F. Hasselmann, G. R. Miller, W. H. Munk, and W. H. Powers (1966), Propagation of ocean swell across the pacific, *Philosophical Transactions of the Royal Society of London. Series A, Mathematical and Physical Sciences*, 259(1103), 431. iv, 2, 56, 69, 70, 152, 168, 192
- Vesecky, J., et R. Stewart (1982), The observation of ocean surface phenomena using images from the SEASAT synthetic aperture radar, *J. Geophys. Res.*, 87(C5), 3397–3430. ii, 1

## Abstract

The capability to observe ocean swell using spaceborne Synthetic Aperture Radar (SAR) has been demonstrated starting with ERS-1 mission in 1992. This dissertation shows how ocean swell properties can be used to combine swell observations of heterogeneous quality and acquired at various times and locations for the observation and forecast of ocean swell fields using ASAR instrument on-board ENVISAT. The first section is a review of how ocean swell spectra can be derived from the SAR complex images of the ocean surface using a quasi-linear transformation. Then, significant swell heights, peak periods and peak directions from *in situ* measurements are used to assess the accuracy of the SAR observed swell spectra. Using linear propagation in deep ocean, a new swell field reconstruction methodology is developed in order to gather SAR swell observations related to the same swell field. Propagated from their generation region, these observations render the spatio-temporal properties of the emanating ocean swell fields. Afterwards, a methodology is developed for the exclusion of outliers taking advantage of the swell field consistency. Also, using the irregularly sampled SAR observations, quality controlled estimations of swell field integral parameters are produced on a regular space-time grid. Validation against *in situ* measurements reveals the dramatic impact of the density of propagated observations on the integral parameters estimated accuracy. Specifically, this parameter is shown to be very dependent on the satellite orbit. Finally, comparisons with the numerical wave model WAVEWATCH-III<sup>®</sup> prove it could potentially benefit from the SAR swell field estimates for assimilation purposes.

Keywords: Synthetic Aperture Radar (SAR), swell, Earth observation, remote sensing, seismic noise, wave model.

## Acknowledgments

I thank all those who have passionately shared and passed on to me their love for Earth observation. I am particularly grateful to Fabrice Colard, Alexis Mouche and Bertrand Chapron for the many and very exciting hours we have spent interpreting ocean SAR images, debating study results, brainstorming on future developments and much more...

Also, I deeply thank Fabrice Ardhuin for sharing his scientific experience and for his guidance along these three years.

I truly enjoyed working at CLS and IFREMER during these three years. Thanks to all those who have warmly contributed to the very friendly and welcoming atmosphere.

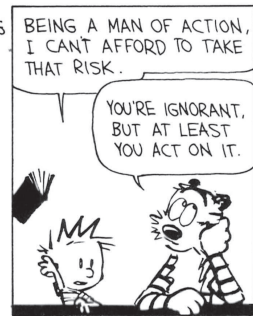
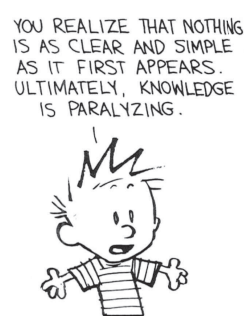
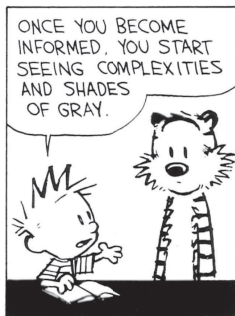
Being a student from the EDSM, a special thought goes to Elisabeth Bondu at the EDSM for her great kindness and availability.

I owe my first and ever lasting interest in Earth sciences and observation to Ben Holt who accepted me for a one year internship at JPL. This corresponds to the period when I started to find *my* way through my engineering school.

I am grateful to Yves-Louis Desnos for helping me find the right persons to work with in and outside ESRIN and to Vincent Kerbaol for accepting me as a PhD student at CLS.

Special thank goes to my housemates and family: Lolette, Fanfan, Romain, Boots, Momo, Lise, Mika and all our friends for accompanying me all along this period, sometimes fun, sometimes not; to Lily for her endless smiles; to my parents for supporting me the best they could.

I also thank the ANRT (Agence National pour la Recherche et la Technologie) for funding my research during these three years.





# Contents

<b>Résumé</b>	<b>ii</b>
<b>Abstract</b>	<b>viii</b>
<b>Acknowledgments</b>	<b>ix</b>
<b>Introduction</b>	<b>1</b>
Bibliography . . . . .	6
<b>Chapter1 Ocean imaging using Synthetic Aperture Radar</b>	<b>9</b>
1.1 SAR fundamental principles . . . . .	10
1.1.1 Spaceborne SAR History . . . . .	10
1.1.2 SAR geometry and resolution . . . . .	11
1.1.3 SAR wave mode . . . . .	16
1.2 Sea surface backscattering . . . . .	16
1.2.1 Mechanisms . . . . .	17
1.2.2 Modulation processes and transfer functions . . . . .	24
1.3 SAR-ocean wave inversion . . . . .	34
1.3.1 Non-linear transformation . . . . .	35
1.3.2 Quasi-linear transformation . . . . .	38
1.3.3 Azimuth cut-off . . . . .	40
1.3.4 Wave feature filtering . . . . .	42
1.3.5 Cross-spectra . . . . .	44
1.4 Conclusion . . . . .	47
Bibliography . . . . .	49
<b>Chapter2 Ocean swell: theory and observations</b>	<b>55</b>
2.1 Airy theory . . . . .	56
2.1.1 Solutions . . . . .	56
2.1.2 Phase and group velocity . . . . .	58
2.1.3 Energy and significant wave height . . . . .	59
2.1.4 Deep ocean propagation properties . . . . .	60
2.2 Generation of waves by wind . . . . .	61
2.2.1 Wind-wave growth observations . . . . .	61
2.2.2 Wave age and wave growth laws . . . . .	65

---

2.2.3	Non-linear wave-wave interactions . . . . .	66
2.3	Swell propagation in deep ocean . . . . .	67
2.3.1	Storm sources . . . . .	67
2.3.2	Swell energy decay . . . . .	68
2.3.3	Energy dissipation . . . . .	69
2.4	Conclusion . . . . .	72
	Bibliography . . . . .	74
<b>Chapter3 Validation of SAR swell measurements</b>		<b>79</b>
3.1	Buoy dataset . . . . .	80
3.1.1	Wave measurements . . . . .	80
3.1.2	Buoy networks . . . . .	82
3.2	SAR dataset . . . . .	83
3.2.1	Data quality . . . . .	83
3.2.2	Data Correction . . . . .	85
3.3	Methodology . . . . .	86
3.3.1	Spectral partitioning . . . . .	86
3.3.2	Integral parameter estimation . . . . .	89
3.3.3	Peak-to-peak association . . . . .	90
3.3.4	Graphical summary . . . . .	91
3.4	Statistical results . . . . .	91
3.4.1	Matchup criteria . . . . .	91
3.4.2	Matchup dataset . . . . .	93
3.4.3	Main statistics . . . . .	95
3.4.4	Dependences . . . . .	96
3.5	Conclusion . . . . .	111
	Bibliography . . . . .	116
<b>Chapter4 Swell stroboscopic imaging</b>		<b>119</b>
4.1	Stroboscopic imaging principle . . . . .	120
4.1.1	The phenomenon . . . . .	120
4.1.2	Classification . . . . .	121
4.1.3	Stroboscopic swell configurations . . . . .	127
4.1.4	Case examples of SI . . . . .	127
4.2	Probability of missing a swell system . . . . .	132
4.2.1	Considering ascending and descending passes alone . . . . .	132
4.2.2	Considering a full orbit . . . . .	137
4.3	Case of Sentinel-1 . . . . .	138
4.3.1	Stroboscopic swell configurations . . . . .	141
4.3.2	Probability of missing a swell system considering a full orbit	145
4.4	Conclusion . . . . .	148
	Bibliography . . . . .	150
<b>Chapter5 Swell field reconstruction</b>		<b>151</b>

5.1	Dataset Description . . . . .	153
5.1.1	Wind field data . . . . .	153
5.1.2	StormWatch database . . . . .	154
5.1.3	Wave data . . . . .	154
5.2	Methodology . . . . .	155
5.2.1	Retro-propagation . . . . .	156
5.2.2	Refocusing . . . . .	157
5.2.3	Swell observations' association . . . . .	161
5.2.4	Swell observations' filter . . . . .	162
5.2.5	Swell field analysis . . . . .	163
5.2.6	Virtual buoy and swell field association . . . . .	163
5.3	Results . . . . .	168
5.3.1	StormWatch co-location . . . . .	169
5.3.2	Single cases . . . . .	169
5.3.3	Yearly analysis . . . . .	173
5.4	Discussion . . . . .	178
5.5	Conclusion . . . . .	180
	Bibliography . . . . .	182
	<b>Chapter6 Synthetic swell field</b>	<b>185</b>
6.1	Synthetic swell field estimation . . . . .	187
6.1.1	Surface fitting . . . . .	187
6.1.2	Iterative filtering . . . . .	202
6.2	Validation . . . . .	210
6.2.1	Methodology . . . . .	213
6.2.2	Tested configurations . . . . .	213
6.2.3	Statistical results . . . . .	214
6.2.4	Single cases . . . . .	216
6.2.5	Dependences . . . . .	219
6.2.6	Rejected Data . . . . .	227
6.3	Comparison with the numerical wave model . . . . .	229
6.3.1	Methodology . . . . .	229
6.3.2	Statistical results . . . . .	230
6.4	Conclusion . . . . .	231
	Bibliography . . . . .	235
	Appendix	
6.A	GRL publication: Revealing forerunners on ASAR . . . . .	237
	<b>Conclusion</b>	<b>253</b>
	<b>Acronyms</b>	<b>257</b>

# Introduction

The global ocean plays a central role in our environment from a climatological perspective as well as from an economic perspective. Our increasing need for a better understanding of ocean dynamics, for safer shipping, increased exploitation of marine energies, offshore and fishery resources pushes for improved observation and prediction capabilities. Spaceborne radar instruments are of particular interest as they provide weather independent night and day Earth observations. Already, by the end of the 20<sup>th</sup> century, satellite missions like QuikSCAT for wind field measurements and Topex/Poseidon for ocean surface topography had shown their great potential for environmental monitoring.

The history of high resolution ocean imaging with radar started in 1951 with the discovery of the Synthetic Aperture Radar (SAR) principles by Carl Wiley. This technological breakthrough opened the way for high-resolution imaging. Ever since the first SAR spaceborne mission, SEASAT, flown in 1978, a dozen SAR civil missions have been launched and contributed to the understanding of both ocean surface and SAR imaging processes. Today, mature developments have led to ocean applications for the estimations of wind, sea-state and currents, monitoring of marine traffic, sea-ice and oil-spill. The various applications have different requirements on ocean surface sampling, ground coverage, image resolution, etc., that can be met by different SAR operating modes. More specifically, SAR instruments on-board ERS-1/2 and ENVISAT have been equipped with wave modes dedicated to the observation of ocean waves, thereby enabling the accumulation of an amazing 20-year long wave mode dataset with global coverage.

SAR is the only instrument able to provide directional wave spectra information on a global scale. This capability to image long gravity waves was first proven using early SEASAT measurements (e.g. *Alpers et al.*, 1981; *Vesecky and Stewart*, 1982). However, because of the complex SAR imaging process, SAR image spectra may be very different from the ocean wave spectra. Thanks to the efforts brought by the Marine and Remote Sensing (MARSSEN) experiment in 1985 in merging existing theories and experimental results (*Hasselmann et al.*, 1985), a full mathematical description of the

ocean-to-SAR spectrum transformation was established by *Hasselmann and Hasselmann* (1991), further enriched by the work of *Krogstad* (1992) and *Engen and Johnsen* (1995). Altogether, these studies led to a much better understanding of the main limitation to measurement of ocean waves with SAR such as the so-called azimuth cut-off, which prevents the detection of small and steep waves propagating close to the satellite azimuth direction. At present, cross-correlation methods have been developed for the calculation of this parameter (*Kerbaol*, 1997) and, away from this limitation, long waves can be measured on a daily basis with satisfactory accuracies (*Johnsen et al.*, 2006).

Swell is a series of long gravity waves that have propagated away from the storm region from which they originate and we call swell systems the ensemble of waves generated by the same storm event. Swell often propagates in moderate to low wind, that is ideal conditions for wave imaging with SAR. Besides, early observations indicate that swell systems are very coherent and can propagate for thousands of kilometers with trajectories and propagation speeds following Airy theory (*Gain*, 1918; *Darbyshire*, 1952; *Munk et al.*, 1963). This is based on swell propagation in deep ocean, away from island shadows and in the absence of currents. Using these properties, observations of the same swell system at different times and locations have been shown possible using pressure recorders (*Snodgrass et al.*, 1966), SAR imagery (*Holt et al.*, 1998; *Heimbach and Hasselmann*, 2000) and buoy measurements (*Hanson and Phillips*, 2001). Later, *Collard et al.* (2009) have shown the SAR wave mode space and time sampling could advantageously be used for the automatic monitoring of ocean swell fields on a near-real time basis, making observation-based predictions of swell states possible several days ahead.

These latest studies are very promising and the work presented here represents a continuation of these efforts. Already, studies have provided rough yet original information on the spatial distribution of the swell field energy (*Delpy et al.*, 2010) and have led to a better estimation of the swell energy dissipation (*Ardhuin et al.*, 2009) which has greatly benefited numerical wave models (*Ardhuin et al.*, 2008). Still, many questions remain open: to what extent can SAR wave mode data be used to deliver accurate information on swell state for hindcasting as well as for forecasting? How does it compare with current numerical wave models and what are the main limitations? Already, *Aouf and Lefèvre* (2012) have shown the positive effects of assimilating isolated SAR wave mode observations in the MFWAM numerical wave model<sup>3</sup> and it is expected that the use of higher level SAR swell information will have a greater impact on the model's performances. Also, SAR data can

---

3. MFWAM stands for Wave Action Model of Météo-France.

be used in numerical wave models to correct for erroneous swell predictions that can be caused by under-estimated input wind forcing (*Bidlot, 2009*).

To investigate these issues, I will use the SAR wave mode products acquired by ASAR instrument on-board ENVISAT and distributed by the European Space Agency (ESA) as Level-2 products containing directional ocean swell spectrum measurements. Even if not directly involved in the estimation of these products, I will show in the last chapter how their accuracy and limitations directly impact the performances of higher level SAR products, thereby pointing out the need to better understand the input data. Therefore, Chapter 1 is dedicated to the presentation of the processes involved in the estimation of the Level-2 SAR products. It was a personal choice to provide a rather detailed presentation, motivated by the idea that, in the future, the improvement of SAR-based forecasts will require the improvement of the SAR observations themselves.

One of the main limitations of SAR observations is that these measurements are intermittent and constrained by the satellite orbit. The initial observation-based information is therefore sparse in time and space. To increase the density of information, I will show how linear theory of wave propagation can be used to estimate the future and past positions and characteristics of a swell observation identifying the main properties of ocean swell in Chapter 2. This chapter is particularly important since many limitations to the further developed methodologies are directly related to the swell propagation model under use.

In the following four chapters, I will develop the four research subjects investigated during these three years. In Chapter 3, the detailed validation and error estimation of the Level-2 SAR products is proposed. This step is necessary to better understand the error estimations of the higher level SAR products presented in Chapter 6. Chapter 4 describes the limitation to swell observation due to the satellite orbit. It is rather independent from the other chapters and is not a requirement for the understanding of the following ones. Yet, it provides an original work for possible optimization of satellite orbit for swell monitoring, particularly relevant for future mission design. After observing many different swell events imaged by the SAR wave mode, it became clear that the spatio-temporal sampling of ocean swells by spaceborne SAR could lead to very heterogeneous propagated-observation distributions depending on the swell event. As I will further show in Chapter 6, the accuracy of the SAR-based swell estimates increases with the density of propagated SAR observations and therefore increasing ocean swell sampling by SAR is an additional source of improvements for the SAR-based swell estimates.

In Chapters 5 and 6, I will develop the methodology through which swell persistency while propagating and the consistency of the many SAR observations of the same swell can be exploited to deliver information on the

spatio-temporal swell field evolution in terms of peak period, peak direction and energy.

After a brief presentation of the SAR fundamental principles, I will describe in the first chapter the mechanisms explaining the signal backscatter from the ocean surface and the processes at work in SAR image formation. A description of the ocean-to-SAR spectrum transformation will follow with specific focus on wave detection limitation caused by azimuth cut-off. I will also discuss the advantages of using SAR cross spectra for suppression of speckle noise and determination of the wave propagation direction.

In the second chapter, I will present the governing laws for the propagation of ocean swell in the simplified case of a deep ocean, away from island shadows and in the absence of currents. Swell main properties will be exposed, followed by wave growth empirical laws explaining their generation in storm regions. Afterwards, I will describe the energy exchanges induced by non-linear wave-wave interactions and the swell energy decay and dissipation model further used in following chapters.

Third, I will estimate the accuracy of the SAR swell spectra measurements using co-located SAR/buoy dataset. I will then describe the validation methodology further used in Chapter 6. It will be followed by the statistical results with error estimates given for each integral parameter, namely significant swell height, peak period and peak direction. I will conclude this chapter with an impact study of the different parameters influencing the accuracy of each of these integral parameters.

In the fourth chapter, I will show how the swell trajectories and the space-borne instrument ground sampling can lead to what I call *swell stroboscopic imaging*: occurring for certain swell configurations, the SAR instrument can always or never image a propagating swell system. These configurations depend on the satellite orbit. The occurrence conditions this phenomenon will be exhaustively described and probabilities that a swell system can be totally missed by the instrument will be estimated in the case of ENVISAT. The same approach will be applied for the future Sentinel-1 mission and comparisons will be drawn between these two satellite missions.

In the fifth chapter, I will describe a new and automated method for the merging of isolated SAR swell observations into coherent swell fields. This swell field reconstruction method specifically tackles the issue raised by swell systems generated by long-lived and/or extended storms. The data used as ancillary information and for validation will first be presented, followed by the detailed full methodology. Then, I will present the results of a yearly analysis, focusing on the capacity of our method to render the effects of

moving storms by detecting the slightly different times and region of swell generation within a given swell system.

In the last chapter, I will show how these reconstructed swell fields can be used to provide a filtered, quality-controlled and regularly sampled information: the so-called *synthetic swell field*. I will start with the estimation of the data confidence attributed to each propagated SAR swell observation and will continue with the methodology and its different tested configurations. I will then present the validation with the overall statistical results obtained for each configuration and the effects of the different parameters impacting the accuracy of our estimations. I will show how the input data density can be a good quality flag. I will conclude this chapter comparing accuracy of synthetic swell field estimations against the numerical wave model WAVEWATCH-III<sup>®</sup>. Most importantly, I will show how our SAR-based estimates can correct strong biases in the wave model.

Regarding the manuscript organization, each chapter contains its own introduction and conclusion where main results are summarized, together with the new opportunities and perspectives this work has opened. It also comes with its own bibliography and appendix. At the end of the manuscript, a list of acronyms is provided.

I will conclude this manuscript recalling the main results of this work and presenting newly raised research topics.

## Bibliography

- Alpers, W. R., D. B. Ross, and C. L. Rufenach (1981), On the detectability of ocean surface waves by real and synthetic aperture radar, *J. Geophys. Res.*, *86*(C7), 6481–6498. ii, 1, 24
- Aouf, L., and J.-M. Lefèvre (2012), On the impact of ASAR wave spectra in the operational wave model MFWAM, in *Proceedings of SEASAR 2012*, ESA, Tromsø. vi, 2
- Ardhuin, F., F. Collard, B. Chapron, P. Queffelec, J.-F. c. Filipot, and M. Hamon (2008), Spectral wave dissipation based on observations: a global validation, in *Proceedings of Chinese-German Joint Symposium on Hydraulics and Ocean Engineering, Darmstadt, Germany*, p. 391–400, ISBN: 3-936146-23-3. 2, 152
- Ardhuin, F., B. Chapron, and F. Collard (2009), Observation of swell dissipation across oceans, *Geophys. Res. Lett.*, *36*, L06,607, doi:10.1029/2008GL037030. ii, 2, 70, 71, 152, 181, 237
- Bidlot, J.-R. (2009), Intercomparison of operational wave forecasting systems against buoys: data from ECMWF, MetOffice, FNMO, NCEP, DWD, BoM, SHOM and JMA, september 2008 to november 2009, *Tech. rep.*, Joint WMO-IOC Technical Commission for Oceanography and Marine Meteorology, available from <http://tinyurl.com/3vpr7jd>. 3
- Collard, F., F. Ardhuin, and B. Chapron (2009), Monitoring and analysis of ocean swell fields from space: New methods for routine observations, *Journal of Geophysical Research-Oceans*, *114*(C7), C07,023. ii, 2, 68, 69, 70, 71, 80, 85, 111, 152, 153, 155, 219, 239
- Darbyshire, J. (1952), The generation of waves by wind, *Proceedings of the Royal Society of London. Series A, Mathematical and Physical Sciences*, p. 299–328. 2, 61, 237
- Delpey, M., F. Ardhuin, F. Collard, and B. Chapron (2010), Space-time structure of long swell systems, *J. Geophys. Res.*, *115*, C12,037, doi:10.1029/2009JC005885. ii, 2, 90, 152, 180, 186, 189, 192, 241
- Engen, G., and H. Johnsen (1995), SAR-ocean wave inversion using image cross spectra, *IEEE transactions on geoscience and remote sensing*, *33*(4), 1047–1056. ii, 2, 34, 37, 44
- Gain, L. (1918), La prédiction des houles au maroc, *Annales Hydrographiques*, pp. 65–75. 2, 56, 61, 237

- Hanson, J. L., and O. M. Phillips (2001), Automated analysis of ocean surface directional wave spectra, *J. Atmos. Ocean Technol.*, 18, 277–293. 2, 86, 91, 152, 192
- Hasselmann, K., and S. Hasselmann (1991), On the nonlinear mapping of an ocean wave spectrum into a synthetic aperture radar image spectrum and its inversion, *Journal of Geophysical Research*, 96(C6), 10,713–10. ii, 2, 31, 34, 38, 45
- Hasselmann, K., R. K. Raney, W. J. Plant, W. R. Alpers, R. A. Shuchman, D. R. Lyzenga, C. L. Rufenach, and M. J. Tucker (1985), Theory of synthetic aperture radar ocean imaging: A MARSSEN view, *Journal of Geophysical Research*, 90(C3), PP. 4659–4686, doi:198510.1029/JC090iC03p04659. 1, 24, 28, 34
- Heimbach, P., and K. Hasselmann (2000), Development and application of satellite retrievals of ocean wave spectra, *Elsevier Oceanography Series*, 63, 5–33. ii, 2, 239
- Holt, B., A. K. Liu, D. W. Wang, A. Gnanadesikan, and H. S. Chen (1998), Tracking storm-generated waves in the northeast pacific ocean with ERS-1 synthetic aperture radar imagery and buoys, *Journal of Geophysical Research*, 103(C4). ii, 2, 239
- Johnsen, H., G. Engen, F. Collard, V. Kerbaol, and B. Chapron (2006), ENVISAT ASAR wave mode products-quality assessment and algorithm upgrade, *Proceedings of SEASAR*. ii, 2, 111
- Kerbaol, V. (1997), Analyse spectrale et statistique vent-vague des images radar à ouverture synthétique (ROS)–application aux données des satellites ERS1/2, Ph.D. thesis, Thèse de doctorat, Rennes I, France. 2, 12, 15, 23, 27, 33, 34, 41, 42, 45
- Krogstad, H. E. (1992), A simple derivation of Hasselmann’s nonlinear ocean-synthetic aperture radar transform, *J. Geophys. Res.*, 97(C2), 2421–2425. ii, 2, 34, 36, 37, 38, 45, 242
- Munk, W. H., G. R. Miller, F. E. Snodgrass, and N. F. Barber (1963), Directional recording of swell from distant storms, *Philosophical Transactions of the Royal Society of London. Series A, Mathematical and Physical Sciences*, 255(1062), 505–584. iv, 2, 56, 67, 237
- Snodgrass, F. E., G. W. Groves, K. F. Hasselmann, G. R. Miller, W. H. Munk, and W. H. Powers (1966), Propagation of ocean swell across the pacific, *Philosophical Transactions of the Royal Society of London. Series A, Mathematical and Physical Sciences*, 259(1103), 431. iv, 2, 56, 69, 70, 152, 168, 192

Vesecky, J., and R. Stewart (1982), The observation of ocean surface phenomena using images from the SEASAT synthetic aperture radar, *J. Geophys. Res.*, 87(C5), 3397–3430. ii, 1

# Chapter 1

## Ocean imaging using Synthetic Aperture Radar

### Contents

---

1.1	SAR fundamental principles . . . . .	<b>10</b>
1.1.1	Spaceborne SAR History . . . . .	10
1.1.2	SAR geometry and resolution . . . . .	11
1.1.3	SAR wave mode . . . . .	16
1.2	Sea surface backscattering . . . . .	<b>16</b>
1.2.1	Mechanisms . . . . .	17
1.2.2	Modulation processes and transfer functions . . . . .	24
1.3	SAR-ocean wave inversion . . . . .	<b>34</b>
1.3.1	Non-linear transformation . . . . .	35
1.3.2	Quasi-linear transformation . . . . .	38
1.3.3	Azimuth cut-off . . . . .	40
1.3.4	Wave feature filtering . . . . .	42
1.3.5	Cross-spectra . . . . .	44
1.4	Conclusion . . . . .	<b>47</b>
	Bibliography . . . . .	<b>49</b>

---

This chapter introduces the SAR instrument and provides an overview of the mechanisms enabling ocean wave spectra measurement. First, the basic principles governing the behavior of the SAR instrument are discussed together with the SAR imaging geometry and resolution performances. Second, the processes governing the sea surface backscattering mechanism and the processes modulating this phenomenon are reviewed together with the associated modulation transfer functions. Finally, the different steps and models permitting ocean wave spectrum retrieval are presented with special focus on using the image cross spectrum.

## 1.1 SAR fundamental principles

Retrieval of geophysical parameters from SAR instrument data involves substantial signal processing. This was an obstacle in the early days of SAR remote sensing but, with increased processing capacities, the SAR instrument has now won its legitimacy among present spaceborne instruments thanks to its great imaging advantages:

- it is an active instrument. Thus, the instrument does not require any sunlight, the radiation source is known and corrections of measurements for spurious sources of radiation are unnecessary;
- it operates in microwave frequency. Unlike optical observation, the SAR signal interaction with the Earth atmosphere is very limited, especially when considering X and C bands. The instrument can thus provide information about the Earth surface even in presence of clouds and precipitation;
- it provides unique high-resolution and wide swath images of the Earth surface. For instance, the SAR sensor on-board COSMO-SkyMed satellite can provide images of the Earth surface that are 200 km-wide with a  $100 \times 100 \text{ m}^2$  resolution or 10 km-wide with a  $1 \times 1 \text{ m}^2$  resolution depending on the acquisition mode (*COSMO-SkyMed*, 2007).

In the following subsections, a brief reminder of spaceborne SAR history is proposed. It is followed by the presentation of the SAR instrument geometry and achievable resolutions. At the end of this section, the characteristics of a specific SAR mode dedicated to wave observation, referred to as the SAR wave mode, are exposed. More information about the SAR fundamental principles may be found in *Curlander and McDonough* (1991); *Jackson et al.* (2004); *Massonnet and Souyris* (2008).

### 1.1.1 Spaceborne SAR History

The SAR principles were first described by Carl Wiley in 1951 and opened the way for new high-resolution imaging perspective (*Lasswell*, 2005). First experiments of this technique started in 1962 with the Jet Propulsion

Laboratory (JPL) for the preparation of the Apollo Lunar Sounder Experiment (ALSE). Its purpose was to map the lunar surface at radar wavelengths with an L-band sounding radar. At first, the radar was placed on rockets launched at the White Sands, New Mexico, and in 1966, it was eventually upgraded to the JPL airborne SAR system. This system was operated for 10 years during which flights over the ocean, in hurricanes, land and sea ice proved the SAR system to be capable of collecting data useful for the study of oceanic phenomena (*Elachi et al., 1977*). These tests, together with the success of the lunar sounder experiment on Apollo 17 in 1972 eventually led to the approval of SAR as part of the Seasat mission. Launched in July 1978, the Seasat SAR could provide ocean images 100 km-wide with a 25 m resolution. It observed a number of unique ocean features that significantly contributed to our understanding of the global oceans (*Fu and Holt, 1982*). The success of Seasat, however, was limited in terms of the duration of the data collection since a complete power failure prematurely ended the mission just one hundred days after its launch. Nevertheless, since the Seasat launch, hundreds of papers using its data have been published and have significantly contributed to remote sensing science. Ever since, the SAR missions succeeded one after the other with the SIR-A, SIR-B and SIR-C series embarked on the American Space Shuttle in 1981, 1984 and 1994, respectively; the European satellites ERS-1, ERS-2 and ENVISAT launched 1991, 1995 and 2002; the Japanese JERS-1 and ALOS launched in 1992 and 2002; the Canadian Radarsat-1 and Radarsat-2 launched in 1995 and 2007; the Italian COSMO-SkyMed launched in 2007 and the German TerraSAR-X launched in 2007. In 2013 and 2014, the European SAR missions Sentinel-1A and Sentinel-1B shall be appended to this long yet not exhaustive list.

## 1.1.2 SAR geometry and resolution

### 1.1.2.1 Geometry

Here we consider monostatic sensors only and let aside bistatic sensors. This means that the same SAR instrument is used to both transmit and receive the electromagnetic waves using a single antenna whereas, for a bistatic SAR, the signal is transmitted and received by two different instruments.

The SAR instrument geometry is presented on Figure 1.1. As a reference, the azimuth and the range direction are defined by the directions parallel and perpendicular to the platform trajectory, respectively. In particular, the slant range direction is given by the straight line joining the instrument to the illuminated target and the ground range direction corresponds to its projection on the ground.

While the satellite orbits the Earth at speed  $v$ , the radar illuminates an

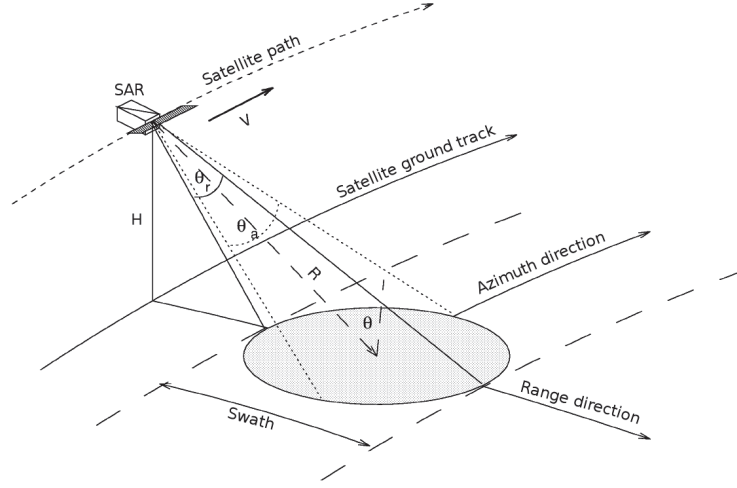


Figure 1.1: SAR geometry. The ground region illuminated by the instrument while orbiting is represented in gray. Adapted from *Kerbaol (1997)*.

area situated off-nadir with microwave radiation at frequency  $f_r$ , which is the frequency of the instrument's oscillator. The corresponding radar wavelength  $\lambda_r$  is defined by  $\lambda_r = c/f_r$  where  $c$  is the speed of light. A portion of the transmitted radar energy is then scattered back towards the radar. The size of the illuminated target is determined by the aperture range beamwidth  $\theta_r$  and the aperture azimuth beamwidth  $\theta_a$ . The latter parameter also impacts the time during which a target is illuminated by the radar beam, called the integration time. Within the radar beam, the position of a target in the range direction is estimated measuring the time difference between the transmission and reception of a given pulse whereas its position in the azimuth direction is estimated measuring the Doppler shift between the transmission and reception of a given pulse.

### 1.1.2.2 Range resolution

The range resolution of a radar system is the minimum distance between objects that may be resolved by the radar. As the target range is obtained by sorting the echo of each pulse as a function of its time of return, the range resolution is therefore linked to the sampling frequency  $f_s$ , of the received echoes.

The elapsed time between two radar pulses is  $T$ . This defines the Pulse Repetition Frequency (PRF) which is the frequency at which these pulses are transmitted, equal to  $1/T$ . The time period during which the pulses

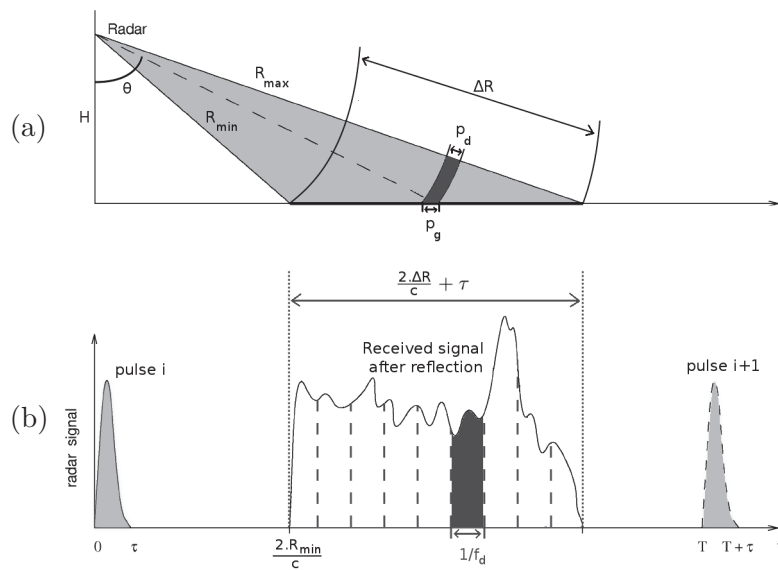


Figure 1.2: (a) SAR geometry of the illuminated scene. The vertical axis represents the altitude and the horizontal axis, the ground distance. The Radar beam, represented in light gray, illuminated a region whose slant range distance ranges from  $R_{min}$  to  $R_{max}$ . Unlike the resolution in slant range direction  $p_d$ , the resolution in the ground range direction  $p_g$  depends on the incidence angle. (b) Intensity of the SAR emitted and received signal versus time.

are emitted equals  $\tau$ . Each pulse first reaches the near range part of the illuminated target, at a slant range distance  $R_{min}$  and then the far range part of the illuminated target, at a slant range distance  $R_{max} = R_{min} + \Delta R$  from the satellite, as illustrated by Figure 1.2. Variables  $p_g$  and  $p_d$  refer to the resolutions achieved by the instrument in the ground range and slant range direction, respectively. To dissociate two successive echoes of the radar pulse,  $T$  has to satisfy the following condition:

$$T > 2 \frac{R_{min} + \Delta R}{c} + \tau \quad (1.1)$$

where the factor 2 accounts for the round trip time.

For the echo to be sampled correctly,  $f_s$  must be larger than the pulse modulation bandwidth,  $B_d$ , in order to satisfy Shannon's sampling conditions. In the end, the resolution in slant range direction is given by equation 1.2. To obtain the resolution in the ground range direction,  $p_g$ , the slant range resolution,  $p_d$ , is projected onto the ground:

$$p_d = \frac{c}{2f_s} \quad (1.2a)$$

$$p_g = \frac{p_d}{\sin \theta} = \frac{c}{2f_s \sin \theta} \quad (1.2b)$$

where  $\theta$  is the incidence angle of the illuminated target.

Thus, it should be pointed out that the ground range resolution increases when the target range distance increases and decreases when the pulse duration decreases. For technical reasons however, it is difficult to create a very short pulse carrying enough energy. It is therefore preferable to create a much longer pulse using a pulse compression technique. This long pulse, known as a *chirp*, is linearly modulated in frequency. With appropriate signal processing, the long pulse provides a fine range resolution.

### 1.1.2.3 Azimuthal resolution

In the azimuth direction, also called cross-range or along-track, the SAR is distinctive from a Real Aperture Radar (RAR) as it records not only the signal amplitude but also its phase. As a comparison, optical sensors and RAR are diffraction-limited systems and their azimuth resolution is therefore proportional to  $\lambda R/D$ , where  $\lambda$  is the instrument wavelength,  $D$ , the antenna diameter and  $R$ , the target range. Achieving azimuthal resolution of the order of a few meters would therefore imply using several kilometer-long antennas, which is unrealistic.

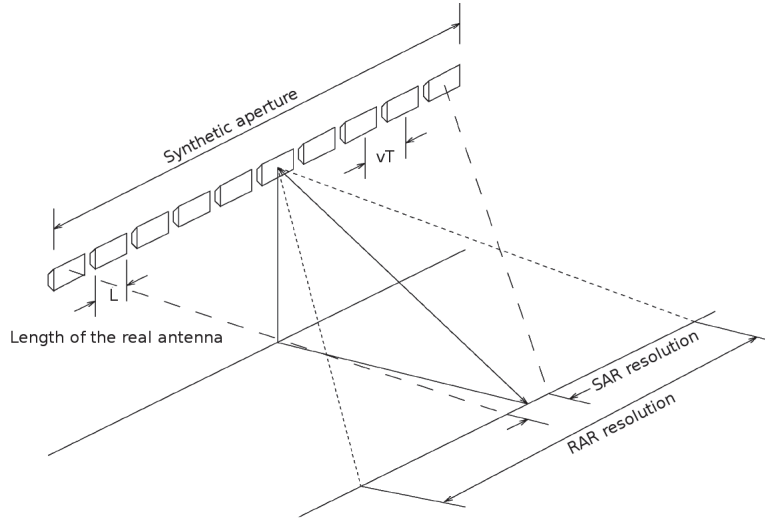


Figure 1.3: SAR azimuthal fine resolution achieved by a virtual network of antennas. Adapted from *Kerbaol* (1997).

On the contrary, the SAR records the phase of the signal backscattered from a target point during the entire integration time for which it is illuminated by the SAR beam. This can also be seen as a virtual network of antennas, separated from one another by a distance  $vT$ , as illustrated by Figure 1.3. After correcting the phase shift for the path length between the virtual antennas and the target for each pulse record, phases can be coherently summed in such a way that the final azimuth resolution,  $p_{az}$ , equals half the length of the SAR antenna,  $L$ :

$$p_{az} = \frac{L}{2} \quad (1.3)$$

Using all the pulses reflected during the integration time for coherent summation will result in a so-called *single-look image*. Alternatively, these pulses can be split into several sets with respect to their time of acquisition and thereby producing independent *looks* of the same scene. The technique consisting in proceeding to a coherent summation of them is called *multi-look*. It can be very useful for the removal of unwanted noise like the speckle<sup>1</sup>.

In the end, the coherent processing achieved by SAR synthesizes an antenna much longer than the real one and the azimuth resolution is independent of the SAR wavelength and target range. In this case, one can wonder

1. Its description and main characteristics are further detailed in paragraph 1.3.5.1, page 44.

how far we can take this for spaceborne SAR. In fact, there are serious application constraints that limit taking along-track spatial performance too far. These constraints manifest themselves by placing unacceptable limits on important application goals such as area coverage or integration time (coherence vs. moving targets). Also, there are associated technology limitations that set application limits, such as data collection rate and volume, and limiting antenna design factors, such as pulse power.

### 1.1.3 SAR wave mode

In the past, only SAR sensors on-board ERS-1, ERS-2 and ENVISAT have been equipped with a specific mode dedicated to wave observation, the so-called *wave mode*, operating in C-band ( $\lambda_r \simeq 5.6$  cm) with VV polarization. Even though it is a low priority mode as compared to the other wider swath modes, the SAR sensor usually switches to it over open ocean regions. The characteristics of the actual and future European SAR missions are given in Table 1.1.

SAR on-board	ENVISAT	Sentinel-1
Ground coverage [range $\times$ azimuth km <sup>2</sup> ]	10 $\times$ 7	20 $\times$ 20
Nominal resolution [range $\times$ azimuth m <sup>2</sup> ]	9 $\times$ 6	5 $\times$ 5
Incidence angle [deg]	23.5	23.5 and 36.5
Along track sampling [km]	100	100
Polarization	VV or HH	VV or HH

Table 1.1: Characteristics of the SAR wave mode sensor on-board ENVISAT and Sentinel-1. The nominal resolutions concern land mapping as it will be shown that for ocean mapping other processes cause a degradation of the image resolution.

## 1.2 Sea surface backscattering

The SAR imaging process is sensitive to numerous geophysical parameters such as the geometry, the physical properties and the motion of sea surface in the illuminated scene. On top of this, properties of the SAR instrument itself such as the incidence angle, polarization and frequency greatly influence the response from the ocean surface. Here, we focus on the mechanisms allowing the SAR to image ocean waves and do not address other phenomena modifying the SAR imaging processes like eddies, oil slicks or ship detection.

First, the main processes responsible for the signal backscatter are presented, namely Bragg scattering, quasi-specular reflection and wave breaking. Then, the processes responsible for the modulation of this backscatter and the associated modulation transfer functions (MTF) are detailed.

### 1.2.1 Mechanisms

Theories for the interaction of electromagnetic and ocean waves have known major improvements during the second half of the last century thanks to experimental investigations of the electromagnetic scatter from the ocean (*Crombie, 1955; Ward, 1969; Long and Trizna, 1973*) and in controlled wave tanks (*Duncan et al., 1974; Keller and Wright, 1975*). They established that the most important mechanism contributing to the electromagnetic wave ocean-surface interaction at intermediate incident angles is *Bragg scattering*, also known as *resonant scattering*, effective for surface ocean waves whose wavelengths are of the order of the incident electromagnetic wave. Also, quasi-specular reflection and scattering from breaking waves plays an important role in the same range of incidence angle but to a lesser extent. The backscattered intensity with respect to the incidence angle is illustrated on Figure 1.4 together with the ranges of incidence angle for which the aforementioned scattering phenomena occur.

At low incidence angles ( $\theta < 20^\circ$ ), Bragg scattering becomes less important. In our case, the SAR wave mode on-board ENVISAT and Sentinel-1 operates at incidence angles between  $23.5$  and  $36.5^\circ$ . Therefore, we limit our study to incidence angles smaller than  $40^\circ$  and avoid the complex mechanisms that arise near grazing, like shadow effects and multiple scattering.

#### 1.2.1.1 Normalized Radar Cross Section

To quantify the radar signal intensity measured by the SAR, the Normalized Radar Cross Section (NRCS) or  $\sigma_0$  is introduced: it is a dimensionless quantity measured in decibels and defined as the average incident signal intensity scattered back to the SAR antenna by a ground surface unit. This surface normalization corrects for the increasing illuminated surface with the increasing incidence angle.

The three main mechanisms governing the NRCS in the range of incidence angles we consider are randomly distributed on the sea surface and are statistically independent. Hence, the total NRCS of the sea surface can be decomposed as the linear contribution of each of these processes:

$$\sigma_0 = \sigma_0^B + \sigma_0^{gs} + \sigma_0^{wb} \quad (1.4)$$

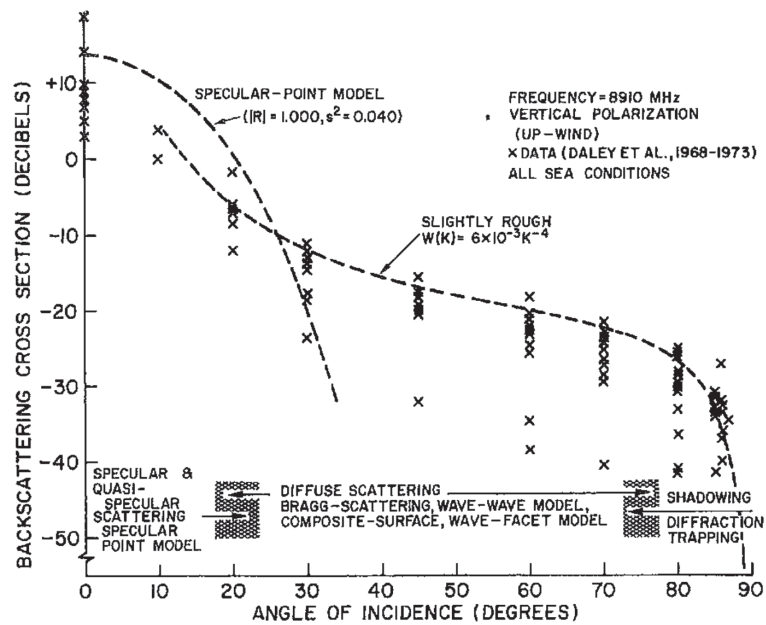


Figure 1.4: Contribution from various scattering mechanisms to the ocean radar backscatter, with respect to the incidence angle. The Backscattered intensity decreases with increasing incidence angle. At low incidence angles, backscattering is dominated by specular scattering while at intermediate incidence angles, it is dominated by Bragg scattering. After *Valenzuela (1978)*.

where,  $\sigma_0^B$  is the NRCS due to Bragg scattering;  
 $\sigma_0^{qs}$ , the NRCS due to quasi-specular reflection;  
 $\sigma_0^{wb}$ , the NRCS due to non-Bragg scattering from breaking waves.

### 1.2.1.2 Bragg scattering

Under Bragg scattering, the incident radar signal of frequency  $\lambda_r$  is backscattered by the short wave components of the ocean surface whose wavelengths  $\lambda_B$  satisfies to the condition illustrated in Figure 1.5 and given below:

$$\lambda_B = \frac{\lambda_r}{2 \sin \theta} \quad (1.5)$$

where  $\theta$  is the local angle of incidence.

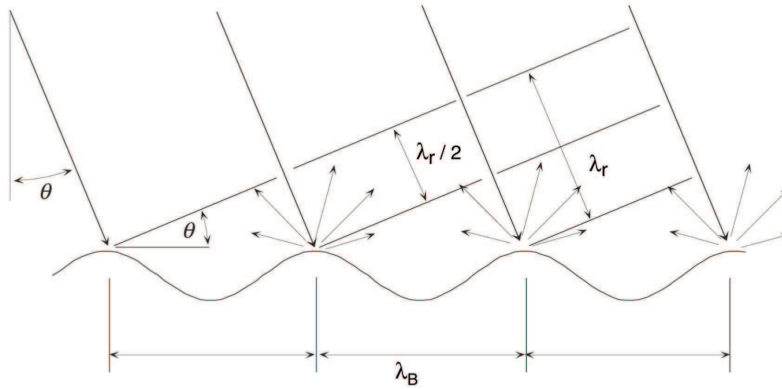


Figure 1.5: Illustration of Bragg scattering, where  $\lambda_r$  is the radar wavelength;  $\lambda_B$ , the sea surface wavelength, and  $\theta$ , the local angle of incidence. Taken from *Holt (2004)*.

This results in a coherent addition (resonance) of returns from adjacent waves that are in phase. Their coherent interference is stronger when they are traveling towards or away from the radar and in directions very close to the range (*Plant and Keller, 1990*). These waves are generated by the wind and propagate freely. As wind-waves are usually continuously distributed in wavelength (cf. Chapter 2, Section 2.2), resonant waves are commonly present. Besides, wind-wave spectra show a rather wide angular distribution centered around the wind blowing direction which also ensures the presence of resonant waves in the range direction, even when the wind blows in perpendicular direction. In the end, the conditions for Bragg scattering are generally met. In this case, the intensity of the backscattered signal is proportional to the density of elements with wavelength close to  $\lambda_B$ . This

implies that only waves with wavelengths of 5-10 cm contribute to this imaging mechanism for C-band SAR systems. Thus, imaging the ocean surface with SAR relies on the existence of a minimum wind speed. Its minimum acceptable value lies around  $3 \text{ m.s}^{-1}$ .

Using the small perturbation method (*Ulabiy et al., 1982*), the normalized backscatter from the sea surface for a pure Bragg scattering,  $\sigma_0^B$ , as given by *Kudryavtsev et al. (2003a)*, is proportional to the surface elevation spectrum at Bragg wavelength and in the azimuth direction  $F_r(k_B, \varphi)$ , which is directly related to the directional wavenumber spectrum  $F$ :

$$\sigma_{0pp}^B = 16\pi k_r^4 |\alpha_{pp}(\theta)|^2 F_r(k_B, \varphi) \quad (1.6a)$$

with,

$$F_r(k_B, \varphi) = 0.5 [F(k_B, \varphi) + F(k_B, \varphi + \pi)] \quad (1.6b)$$

and,

$$k_r = 2\pi/\lambda_r \quad (1.6c)$$

where,  $\varphi$  is azimuth of the antenna look direction;  
 $\alpha_{pp}(\theta)$ , the Bragg scattering geometric coefficient;  
 $pp$ , the polarization of the emitted and received signal where  $p$  refers to:

- H for horizontal;
- V for vertical.

$F_r$ , the 2D-wavenumber variance (folded) spectrum of the sea surface displacement;

$F$ , the directional wavenumber spectrum.

These coefficients  $\alpha_{pp}$ , as estimated by *Plant (1986)* considering a dielectric constant of the sea water equal to 81, are given by:

$$\alpha_{HH}(\theta) = \frac{\cos^4 \theta}{(0.111 \cos \theta + 1)^4} \quad (1.7a)$$

$$\alpha_{VV}(\theta) = \frac{\cos^4(\theta)(1 + \sin^2 \theta)^2}{(\cos \theta + 0.111)^4} \quad (1.7b)$$

In reality, the concerned centimetric waves evolve on longer surface waves that modify the local incidence angle and the previous formulation is to be combined with the local-tilting effects that these longer waves induce (*Plant, 1986; Romeiser et al., 1994; Romeiser and Alpers, 1997; Janssen et al., 1998*). Considering long waves of small slopes and whose scale exceed several times that of the Bragg waves,  $\sigma_0^B$  is determined at moderate incidence angle ( $\theta > 20^\circ$ ) by:

$$\sigma_{0pp}^B = 16\pi k_r^4 \left\langle |\alpha_{pp}(\theta - s_x, s_y)|^2 F_r(k'_B, \varphi) \right\rangle \quad (1.8a)$$

with,

$$k'_B = 2k_B \sin(\theta - s_x) \quad (1.8b)$$

where,  $\langle \dots \rangle$  denotes an averaging over scales of long waves;  
 $s_x$ , the slope of the tilting along the incidence plane;  
 $s_y$ , the slope of the tilting across the incidence plane.

Using this formulation, the coefficients  $\alpha_{pp}$  are now given by:

$$\alpha_{HH}(\theta - s_x, s_y) = \alpha_{HH}(\theta - s_x) + \left( \frac{s_y}{\sin \theta} \right)^2 \alpha_{VV}(\theta) \quad (1.9a)$$

$$\alpha_{VV}(\theta - s_x, s_y) = \alpha_{VV}(\theta - s_x) \quad (1.9b)$$

The combination of the Bragg theory with the modulation induced by long waves is referred to as the standard composite Bragg theory.

### 1.2.1.3 Quasi-specular reflection

**Specular reflection** An example of specular reflection from a smooth flat surface is given on Figure 1.6: part of the incident energy is reflected into the specular direction and the rest is refracted into the medium. To first

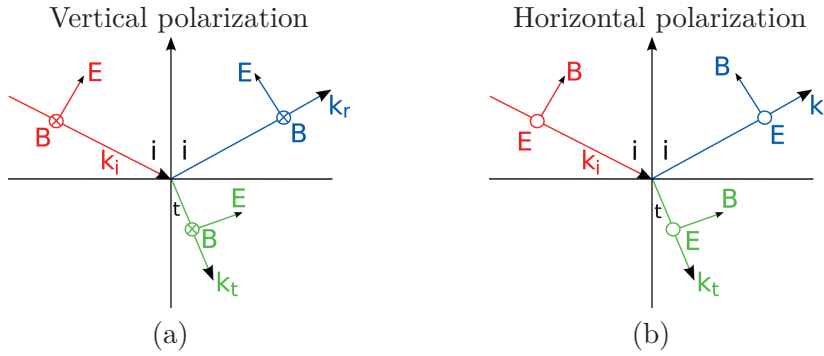


Figure 1.6: Geometry of specular reflection and refraction from a plane interface where the lower medium has different relative dielectric constant. Subplots (a) and (b) show the fields orientation when the incident electric field is parallel (Vertical polarization) and perpendicular (Horizontal polarization), respectively, to the plane of incidence (*Thompson, 2004*).

order, the penetration of the radar signal into a medium depends on its dielectric constant (*Ulaby et al., 1982; Apel, 1987*). This constant characterizes the medium's response to the presence of an electric field. For instance, for a perfect conductor there is no penetration into the medium, and all the

incident energy is reflected. Sea ice, because of its high salinity, is a low dielectric medium whereas ocean water exhibits an opposite behavior and the radar signal penetration into ocean water does not exceed a few millimeters. Therefore, the penetration depth in ocean water is called *skin depth*. However, features that occur below the ocean surface like internal waves can still be seen by the SAR as they interfere with the surface short wave field.

As we only consider monostatic radar systems<sup>2</sup> in our case, it would receive no backscattered signal from a flat and smooth surface. Actually, the specular contribution in the backscattered signal is associated with sea surface roughness which causes a small amount of the incident radiation to be scattered back toward the radar antenna. Indeed, the sea surface roughness spectrum can span over various scales, from several hundred-meter swell waves, through wind-generated waves with wavelengths ranging from several tens of meters to a centimeter or so, to short capillary waves with wavelengths of only a few millimeters (*Thompson, 2004*). An accurate description of microwave scattering from the sea is therefore considerably more complicated than for the case of the smooth flat interface discussed above. Consequently, a statistical approach is preferred which assumes the sea surface to be rough relatively to the incident electromagnetic wave. This condition can be expressed using the Rayleigh criterion:

$$k_z \sigma_\eta = k_r \sigma_\eta \cos \theta \gg 1 \quad (1.10)$$

where,  $k_z$  is radar signal vertically projected wavenumber;  
 $\sigma_\eta$ , the standard deviation of the scatterers' elevation;  
 $\theta$ , the incidence angle.

Whenever the radius of curvature associated with the sea surface elevation variations is large compared to the incident wavelength of radiation, the sea surface can be decomposed into an ensemble of plane facets (tangent planes approximation) and the NRCS is related to the probability that wave facets are oriented perpendicularly to the incident signal. Within the frame of the Kirchhoff approximation method (*Beckmann and Spizzichino, 1963*), the resulting NRCS, for an isotropic rough surface of Gaussian statistics,

$$\sigma_0^{qs} = \frac{|C_R|^2}{2 \langle s_\perp \rangle \langle s_i \rangle} \sec^4(\theta) \exp\left(-\frac{\tan^2 \theta}{2 \langle s_i^2 \rangle}\right) \quad (1.11)$$

---

2. The same SAR sensor is used to transmit and receive the electromagnetic waves using a single antenna.

where,  $C_R$  is the Fresnel reflection coefficient at normal incidence;  
 $\langle s_{\perp} \rangle$ , the standard deviation of slopes of waves in the direction perpendicular to the incidence plane;  
 $\langle s_i \rangle$ , the standard deviation of slopes of waves in the direction of the incidence plane;  
 $\langle s_i^2 \rangle$ , the corresponding mean square slope.

This formulation can be seen as the product of the nominal value at nadir ( $\theta = 0$ ), which is inversely proportional to the mean square slope with the probability of observation of these facets at the given incidence angle. Assuming that relation 1.10 is fulfilled, the formulation is independent of the incident wavelength and polarization. This particular case of specular reflection is denoted *quasi-specular reflection*.

At low incidence angle, this mechanism dominates the NRCS. Then, above 15-20° and with increasing incidence, it becomes negligible compared to the Bragg scattering component. In the following, we will not consider this specular component since we are interested in observations at incidence angles larger than 20°.

#### 1.2.1.4 Wave breaking

Several studies have shown that the composite Bragg theory alone is not fully appropriate to explain and represent the radar signature at moderate incidence angles, when  $\theta > 20^\circ$  (*Tran, 1999; Quilfen et al., 1999*). Specifically, while it may be consistent for VV polarization, this theory does not agree with observations for HH polarization (*Plant, 1990; Janssen et al., 1998*), most probably because the effect of wave breaking on signal scattering is not taken into account. Laboratory observations of radar backscattering from stationary breaking waves by *Ericson et al. (1999)*, performed at  $\theta = 45^\circ$ , have revealed a strong increase of incoherent backscatter near the breaking crest, resulting from an enhanced surface roughness. This may explain the evanescent scattering observed on the wave mode products acquired by the SAR instrument on-board ERS-1/2 by *Kerbaol (1997)*.

Based on the work undertaken by *Phillips (1988)*, *Kudryavtsev et al. (2003a)* proposes that the NRCS resulting from wave breaking is a particular case of quasi-specular reflection. This implies that the radar return is mostly due to breaking waves much larger than the radar wavelength. The semi-empirical formulation of the NRCS attributed to wave breaking is given by:

$$\sigma_0^{wb} = q \left[ \frac{\sec^4 \theta}{\langle s_{wb}^2 \rangle} \exp \left( -\frac{\tan^2 \theta}{\langle s_{wb}^2 \rangle} \right) + \frac{\varepsilon_{wb}}{\langle s_{wb}^2 \rangle} \right] \quad (1.12)$$

where,  $\langle s_{wb}^2 \rangle$ , is the mean square slope of the enhanced roughness of the breaking zone. It is assumed isotropic and wind independent;  
 $\varepsilon_{wb}$ , a constant proportional to the ratio of breaker thickness to its length;  
 $q$ , the fraction of the sea surface covered by breaking zones.

These variables were determined based on observations:  $\langle s_{wb}^2 \rangle = 0.19$ ,  $\varepsilon_{wb} = 0.05$  and  $q = 3\%$  at  $U_{10} = 10 \text{ m.s}^{-1}$  and  $q = 18\%$  at  $U_{10} = 20 \text{ m.s}^{-1}$  (*Kudryavtsev et al., 2003b*). This formulation separates the contribution to the NRCS by the cap of the breaking zone, taken into account by the first term and very similar to the formulation proposed for the quasi-specular reflection, from that of the side of the breaking zone, taken into account by the second term ( $\varepsilon_{wb}q / \langle s_{wb}^2 \rangle$ ).

In this approach,  $\sigma_0^{wb}$  is independent of the radar polarization, as confirmed by observations.

### 1.2.2 Modulation processes and transfer functions

For a detailed formulation of the modulation processes, a 3D axes is defined choosing **Oxy** in the illuminated scene plane, with **Oy** parallel to the azimuth direction and oriented in the satellite traveling direction, and **Ox** perpendicular to it and oriented toward the observed target.

Bragg scattering, quasi-specular reflection and scattering from wave breaking allow the SAR emitted signal to be reflected back to the SAR antenna. The present subsection focuses on the main processes modulating this backscatter. They are responsible for the SAR imaging of ocean waves and have been studied by *Elachi et al. (1977)*; *Alpers et al. (1981)*; *Alpers (1983a,b)*; *Hasselmann et al. (1985)*. They are briefly presented hereafter before entering into details at a latter time:

- the tilt modulation: backscattered signal modulation caused by the change in the local incidence angle (tilt) of the scattering facets through the long wave slope;
- the hydrodynamic modulation: interaction between short and long waves, which modulates the energy and wave number of the short Bragg scattering waves along the long wave profile;
- the velocity bunching: the advection of the backscattering facets by the long wave orbital velocity, which produces a Doppler shift in the return signal and induces an azimuthal displacement of the scattering elements in the image plane.

Range elevation bunching, due to the sea surface elevation variations in the range direction is also briefly described. It is a process of lower importance in the SAR imaging mechanism. Scanning distortion mechanisms are not discussed here as they do not concern spaceborne SAR instruments be-

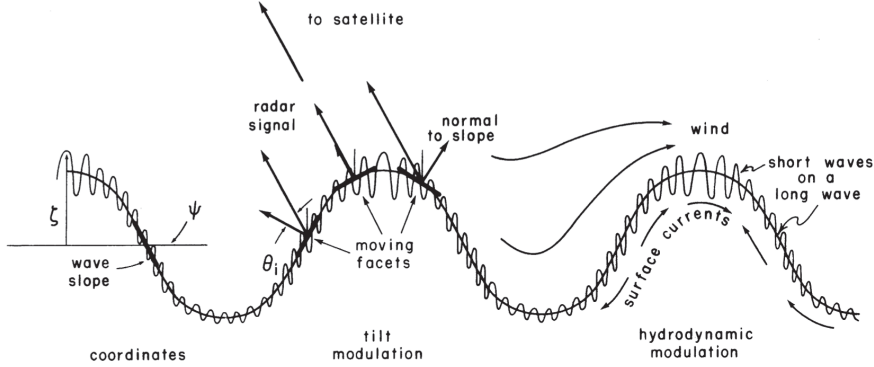


Figure 1.7: Illustration of tilt and hydrodynamic modulation. The longer waves change the local orientation or slope (tilt modulation) and distribution (hydrodynamic modulation) of the shorter wave fields. Symbols include local incident angle,  $\theta$ ; wavenumber spectrum,  $\Psi$  and sea surface elevation,  $\zeta$  (*Holt, 2004*).

cause the satellite velocity is much larger than that of the observed target, as opposed to airborne instruments. Among all these processes, those that do not require the use of the phase information in the backscattered signal, and thus both apply for RAR and SAR, are the tilt and hydrodynamic modulations. They are illustrated in Figure 1.7 and range elevation bunching.

For each of the aforementioned processes, the MTF is the function linking the modulation of the sea surface elevation to that of the NRCS. The total surface elevation  $\zeta(\mathbf{r}, t)$ , at location  $\mathbf{r}$  and time  $t$  is represented by the linear superposition of the contributions from all waves. Given their wave vector  $\mathbf{k}$ , and their pulsation  $\omega$ , the backscattered cross section  $\sigma(\mathbf{r}, t)$  is introduced together with the cross-section modulation factor  $m_j$ :

$$\zeta(\mathbf{r}, t) = \sum_j \zeta_j e^{i(\mathbf{k}\cdot\mathbf{r}-\omega t)} + c.c. \quad (1.13a)$$

$$\sigma(\mathbf{r}, t) = \langle \sigma \rangle \left\{ 1 + \left[ \sum_j m_j e^{i(\mathbf{k}\cdot\mathbf{r}-\omega t)} + c.c. \right] \right\} \quad (1.13b)$$

with,

$$\omega = \sqrt{gk}$$

where, c.c. designates the complex conjugate in the preceding expression;  
 $\langle \sigma \rangle$ , the spatially averaged specific cross section.

The MTF of the SAR instrument is then defined by:

$$m_j = \zeta_j (T_t + T_h + ik_y T_{vb} + ik_x T_{rb}) \quad (1.14a)$$

where,  $T_t$  is the tilt MTF;  
 $T_h$ , the hydrodynamic MTF;  
 $T_{vb}$ , the velocity bunching MTF;  
 $T_{rb}$ , the range bunching MTF;  
 $k_y$ , the wavenumber in the azimuth direction;  
 $k_x$ , the wavenumber in the range direction.

### 1.2.2.1 Velocity bunching

Sea surface displacements introduce Doppler shifts in the returned radar signal. As this information determines the position of the scatterers in the azimuth direction, echoes will be misplaced at a position  $r + \xi^{vb}(y)$  instead of their true position  $r$ . Here, we only consider the modulation of the sea surface displacements caused by the presence of ocean waves regardless of any other potential source of sea surface motions due to ocean currents for instance. The sea surface displacements induced by ocean waves are called orbital motions (cf. Chapter 2, Section 2.1). Their effect on SAR-ocean wave imaging were studied by *Alpers and Rufenach (1979)*; *Swift and Wilson (1979)*; *Tucker (1985)*. First, it affects the frequency of the return signal  $f$  as follows:

$$f = f_0 + 2f_0 \frac{V_r(y)}{c} + 2f_0 \frac{u_r(y)}{c} \quad (1.15)$$

where,  $f_0$  is the frequency of the SAR emitted signal;  
 $V_r$ , the satellite velocity projected in the radar look direction;  
 $u_r$ , the velocity of a surface scattering elements projected in the radar look direction (Figure 1.8).

Thus, after the SAR image formation, the scattering elements are mispositioned with an error in the azimuth direction  $\xi^{vb}$  given by:

$$\xi^{vb}(y) = \frac{R}{V} u_r(y) \quad (1.16)$$

where,  $R$  is the radar to scattering element distance;  
 $V$ , the SAR platform velocity.

The ratio  $R/V$  is much larger for spaceborne than for a airborne sensor. Besides, for space-borne instruments, the integration time is small compared to the wave period and therefore, to the first order, the instantaneous orbital velocity is a good approximation of the average orbital velocity over the integration time.

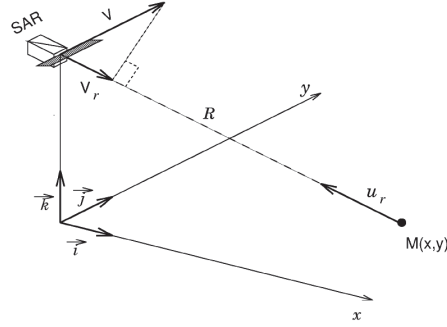


Figure 1.8: Observation of a scattering elements  $M(x,y)$ , with an approaching speed  $V_r$ , relatively to the SAR platform. Taken from *Kerbaol (1997)*.

This reorganization of the backscattered energy in the final image depends on the considered wave scales. Indeed, this mechanism can be *constructive* for waves with a strong space and time coherence (e.g. swell) because of their small slope and regular organization (*Swift and Wilson, 1979*). For long range-traveling waves, there is no apparent offset in the wave position while for waves traveling in different directions, the radial velocity component will have an apparent shift in the azimuth direction. The periodic orbital motion of long waves will produce an apparent increase (bunching) and decrease in the density of scatterers, thereby making long azimuth-traveling waves detectable on the SAR image plane but shifted from their true position.

On the contrary, as the coherence decreases with the decreasing wavelength or increasing slope, the energy reorganization becomes random and the velocity bunching *destructive*, which leads to an apparent image blurring. This effect is analogous to a camera picture when shooting a moving scene, in the azimuth direction referred to as *azimuth cut-off* (*Tucker, 1985; Alpers and Brüning, 1986*). It is further discussed in Subsection 1.3.3, page 40.

With these assumptions, the velocity bunching MTF is given by:

$$T_{vb}(\mathbf{k}) = -\frac{R}{V} \omega \left( \frac{k_r}{|k|} \sin \theta + i \cos \theta \right) \quad (1.17)$$

This principle is illustrated on Figure 1.9. At the top, the black solid line represents an ocean wave propagating in the azimuth direction. The rays leaving the wave surface are drawn with a slope relatively to the vertical



Figure 1.9: Graphic representation of the velocity bunching mechanism with respect to the wave steepness. The black solid line on top represents an ocean wave propagating in the azimuth direction. The rays leaving the wave surface are drawn with a slope relatively to the vertical which is proportional to the wave velocity component in the radar look direction, therefore having maximum slopes for rays starting near wave crests and minimum slopes for rays starting near wave troughs. The scatter points displacement induced by velocity bunching is proportional this slope. For the given wavelength, The impact of different wave heights on this displacement is represented by the greater distance between the transect and the wave profile. The black dashed lines plotted above each transect are the reconstructed wave profiles resulting from the velocity bunching effect. Transect (a) lies in the linear imaging region, while the images at transects (b) and (c) are strongly nonlinear. Taken from *Hasselmann et al.* (1985).

which is proportional to  $u_r$ , the wave velocity component in the radar look direction. Therefore, slopes are maximum for rays starting near wave crests and minimum for rays starting near wave troughs. As indicated by equation 1.16, the scatter points displacement induced by velocity bunching is also proportional this slope. For a given wavelength, the orbital velocity increases with wave height (cf. Chapter 2, equation 2.5) and the resulting increase of  $u_r$  can be represented by the greater distance between the transect and the wave profile. The black dashed lines plotted above each transect are the reconstructed wave profiles resulting from the velocity bunching effect. Transect (a) lies in the linear imaging region, while the images at transects (b) and (c) are strongly nonlinear.

**Correlation function in azimuth** In strong wind conditions, the ocean spectrum is dominated by the wind-sea, whose energy is distributed over broad range of directions and wavelength (cf. Chapter 2, Section 2.2). In this case, the energy reorganization is random and *Collard et al. (2005)* have shown that the SAR signal intensity is equivalent to a stochastic redistribution of the RAR signal intensity and its mean value is conserved<sup>3</sup>. Now, given two scatter points distant from one another by  $\varepsilon$ , their new distance  $\varepsilon_{\text{SAR}}$ , after rearrangement of the sea surface scatterers becomes, on average:

$$\varepsilon_{\text{SAR}} = \varepsilon \left( 1 + \left\langle \left[ \xi^{vb}(\varepsilon) - \xi^{vb}(0) \right]^2 \right\rangle / \varepsilon^2 \right)^{1/2} \quad (1.18)$$

At small distances, this value approaches  $\varepsilon(1+m)^{1/2}$ , where  $m$  is the variance of the displacements' derivative. Hence, the SAR image covariance function measured at distance  $\varepsilon$  corresponds to a RAR covariance function evaluated at a smaller distance. This factor can be of the order of 50, which means that the backscattered signal registered in the SAR image for two scatter points at an actual distance of 1 m can be spaced 50 m apart. The SAR covariance function exhibits very slow decays in the along-track direction, corresponding to the very fast decay in the spectral domain, a direct consequence of the cut-off.

On the opposite, when  $\varepsilon$  increases, this value tends to one and the RAR and the SAR covariance almost coincide.

**Impact on NRCS** Reminded that the NRCS has been defined as the average signal intensity scattered back to the SAR antenna from a ground surface unit, it is now understood that this intensity does not result from the contribution of the scatter points located in the considered resolution cell only. Thus, even if the SAR image resolution of the SAR wave mode reaches about ten meters, under the influence of wind-sea, random contribution of

---

3. Therefore, a high-resolution SAR image can still be used as a scatterometer to assess wind information from the intensity averaged over a large enough area.

scatterers from farther locations interfere, resulting in signal averaging in the azimuth direction (azimuth cut-off phenomenon) and a loss of contrast. This observation is crucial since it is supposed to be one of the main reasons impacting the error estimates of the significant swell height measured latter presented in Chapter 3.

### 1.2.2.2 Hydrodynamic modulation

Long waves are known to govern part of the dynamics of the shorter wave spectrum. As commonly observed, the roughness distribution is not homogeneous along the long waves' profile. Current parameterizations are still subject of on-going active research efforts.

Derived from a two-scale model, the hydrodynamic MTF models the hydrodynamic short wave-long wave interactions with a simple relaxation type source term, characterized by a damping factor  $\mu$ . It describes the response of the short waves to the orbital velocity advection from long waves (*Keller and Wright, 1975*). Hence, assuming an ocean wave spectrum following a Phillips  $k^{-4}$  distribution (cf. Chapter 2, Section 2.2), the hydrodynamic MTF is given by:

$$T_h(\mathbf{k}) = \frac{\omega - i\mu}{\omega^2 + \mu^2} 4.5|k|\omega \frac{k_x^2}{k^2} \quad (1.19)$$

The factor 4.5 comes from the shape of the wave spectrum. It can be questioned/modified depending on the range of wave frequency. It is important to notice the impact of the damping factor  $\mu$  on the hydrodynamic MTF,  $T_h$ :

- close to zero, the relaxation time becomes important and the imaginary part of  $T_h$  is null. This represents the fact that the short waves are located on the crest of longer waves;
- if  $\mu$  increases, the relaxation time becomes smaller which is the case for short waves. Then, the real part  $T_h$  is null and its imaginary part negative which means that the short waves are mostly located ahead of the crest, on the front side of the long waves. Hence, the NRCS should be higher for long waves propagating toward the SAR than away from it which explains the downwind/upwind differences in the NRCS.

Although *in situ* measurements have proven that this modulation effectively applies for decimetric waves (L and P-band), they showed that centimetric waves (X and C-band) are essentially modulated by the wind (*Feindt et al., 1986; Hara and Plant, 1994*). Indeed, the short wave growth along the long wave profile leads to an increased roughness which in return, modifies the wind friction and thus, the wave growth. To account for this effect, a feedback term  $Y_r + iY_i$ , was introduced in the hydrodynamic MTF.

It is then formulated as follows (*Hasselmann and Hasselmann, 1991*):

$$T_h(\mathbf{k}) = \frac{\omega - i\mu}{\omega^2 + \mu^2} 4.5|k|\omega \left( \frac{k_x^2}{k^2} + Y_r + iY_i \right) \quad (1.20)$$

This description has the advantage of taking into account the hydrodynamic modulation for azimuth propagating waves. Indeed, *Askari and Keller (1994)* noticed this effect was observable for strong sea conditions.

**Impact of moderate winds** For large wave slopes, wave breaking starts to become important. In the presence of a significant wind component in the wave direction, wind stress is maximum near the wave crest and wave breaking is modulated by the long wave profile. This modulation is particularly important at moderate winds. However, if the wind direction is near the azimuth, this effect is minimized by azimuthal blurring and the total NRCS modulation is under-estimated. Again, it impacts our capability to estimate significant swell heights using the SAR (cf. Chapter 3, Section 3.4).

### 1.2.2.3 Tilt modulation

Besides modifying the short wave dynamics, long waves also modify the local incidence angle as pictured in Figure 1.7, producing a local change in cross section. This so-called tilt modulation is thus linearly related to the slope of long waves. As a comparison, this modulation is about two to four times larger than hydrodynamic modulation for incidence angles of  $23.5^\circ$ . The exact formulation of the associated MTF is given by:

$$T_t(\mathbf{k}) = \frac{1}{\sigma(\theta)} \frac{\partial \sigma}{\partial \theta_i} \Big|_{\theta_i=0} i\mathbf{k} \cdot \mathbf{r} \quad (1.21)$$

From this expression, it can be noted that there is no modulation for waves oriented in the azimuth direction.

Some theoretical models giving an explicit formulation of this modulation have been developed (cf. *Monaldo and Lyzenga, 1986*). However, they were not satisfying, primarily because they did not render the dependence on the local sea state. In the following paragraphs, two different approaches for the estimation of  $T_t(\mathbf{k})$  are described: a semi-empirical and an empirical model.

**Semi-empirical model** Using the NRCS formulation given by equation 1.4 and neglecting quasi-specular reflection for moderate incident angles, the expression in equation 1.21 is further developed by *Kudryavtsev et al. (2003b)*. The resulting MTFs and their incidence angle dependence is illustrated in Figure 1.10. This graphs highlights the important role that wave breaking processes plays in the signal backscatter for HH polarization.

theoretical

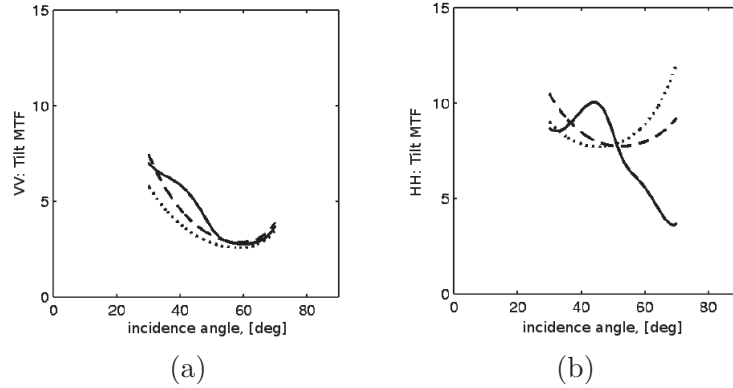


Figure 1.10: Tilt MTF for VV (a) and HH (b) polarization, versus incidence angle as given by a pure Bragg scattering model (dotted lines), the composite Bragg model (dashed lines) and the total scattering model including scattering from wave breaking (solid lines). This is for a wind speed of  $10 \text{ m}\cdot\text{s}^{-1}$ , at C-band, for an upwind radar look-direction. Taken from *Kudryavtsev et al.* (2003b).

**Empirical model** As an alternative to semi-empirical or theoretical models, other MTFs based on the empirical CMOD<sup>4</sup> backscattering models were developed (cf. *Stoffelen and Anderson, 1993*; *Kerbaol and Chapron, 1997*). They use the empirical relation between the incidence angle, the wind vector and the NRCS measured by scatterometers. It also depends on the signal polarization and radar frequency. To obtain an empirical MTF, the idea is to associate the description given by equation 1.21 to this empirical behavior. An example of this MTF is given by Figure 1.11. It was estimated using the empirical backscattering model CMOD-IFR2 (*IFREMER, 1996*), for ERS-1 wave mode products whose incidence angle equals  $23.5^\circ$ .

The empirical model highlights a significant wind speed dependence. More precisely, low wind conditions exhibit a difference of factor 2 as compared to strong winds which is confirmed by other observations (*Romeiser et al., 1994*). This wind speed dependence is important as an under-estimation of the MTF would induce a wave height over-estimation (*Kerbaol and Chapron, 1997*). As regards the wind direction dependence, its effect on the MTF is reproduced, even though variations are minor compared to that resulting from the wind speed.

**Impact of CMOD on NRCS** It is difficult, if not impossible, to distinguish the respective contribution of the tilt and hydrodynamic modulations

4. Refers to MTF for C-band radars.

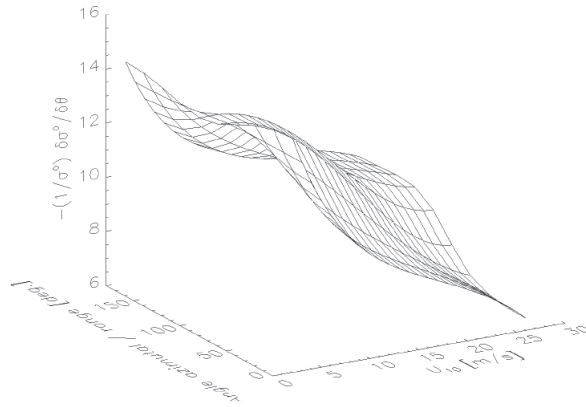


Figure 1.11: MTF associated with tilt modulation, estimated using the empirical backscattering model CMOD-IFR2, for an incidence angle of  $23.5^\circ$  with respect to wind speed (horizontal axis on the right-hand side) and direction relatively to the range direction (horizontal axis on the left-hand side, equal to zero when the instrument is looking contrary to the wind blowing direction). Taken from *Kerbaol (1997)*.

to the measured NRCS and the effects of both phenomena are actually mixed. On the contrary, CMOD models are based on scatterometer data whose resolution cell is of the order of 10 km. The hydrodynamic modulation, whose characteristic length does not exceed a few hundred kilometers, is smoothed over such distances so that it has no effect on the CMOD. Hence, for a given incidence angle variation, the CMOD indicates NRCS modulations smaller than that effectively noticed within the SAR image and this effect increases with the importance of the hydrodynamic modulation, proportional to the wavenumber. In the end, this is expected to lead to an over-estimation of the significant wave height.

Still, at moderate and strong winds, the NRCS blurring in the azimuth direction diminishes the NRCS modulations modeled by MTFs using CMOD, which is then closer to reality.

#### 1.2.2.4 Range elevation bunching

This is a purely geometrical effect due the sea surface elevation variations caused by the waves with important slopes (*Gower, 1983*). It is a consequence of the flat ocean assumption. The surface elevation  $\zeta$ , thus causes a mis-positioning  $\xi^{rb}(\mathbf{r}, t)$ , of the scattering element in the radar look direction as illustrated in Figure 1.12 and satisfying:

$$\xi^{rb}(\mathbf{r}, t) = \zeta(\mathbf{r}, t) \tan^{-1}(\theta) \quad (1.22)$$

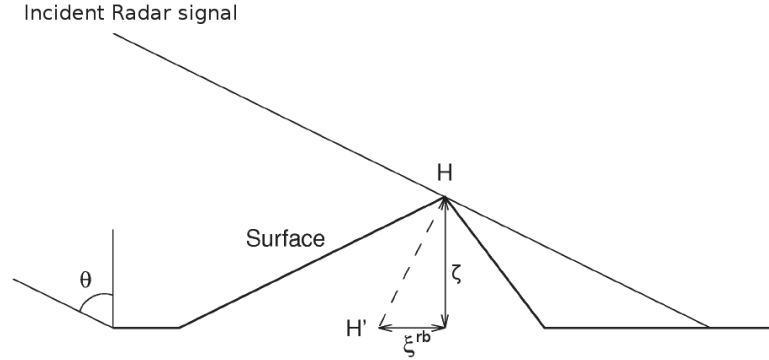


Figure 1.12: Mis-positioning of a scattering element in the radar look direction due to local surface elevation variations. Adapted from *Kerbaol (1997)*.

The range elevation bunching MTF  $T_{rb}$ , is given by:

$$T_{rb}(\mathbf{k}) = \frac{1}{\tan(\theta)} \quad (1.23)$$

Given the fact that SAR observation is best suited for long waves, with relatively small steepness, the effect of the range elevation bunching can be considered much smaller relatively to the tilt and hydrodynamic modulations.

### 1.3 SAR-ocean wave inversion

The first mathematical description of the SAR-ocean imaging process was initiated by *Alpers and Rufenach (1979)* using a deterministic approach. After, through the Marine Remote Sensing (MARSEN) experiment conducted by *Hasselmann et al. (1985)*, a considerable effort was spent to gather the already existing SAR ocean imaging models including *Larson et al. (1976)*; *Alpers and Rufenach (1979)*; *Swift and Wilson (1979)*; *Tucker (1983)*; *Plant and Keller (1983)*. A new generalized imaging model was then proposed and further detailed in *Hasselmann and Hasselmann (1991)*. It gives an analytical and general description of the mapping of the ocean wave spectrum using SAR. One year after, a simplified version of this formulation was given by *Krogstad (1992)*. These two methods require an *a priori* estimation of the ocean wave spectrum in order to remove the  $180^\circ$  ambiguity of the wave direction of propagation. Also, they do not take into account the range bunching process. It was introduced in the SAR-ocean wave inversion by *Engen and Johnsen (1995)*, who additionally uses the image cross-spectra to assess the wave direction of propagation, thereby avoiding using an *a priori* wave spectrum information.

First, the full non-linear transformation is detailed. Then, we explain how it can be simplified in a quasi-linear transformation and present the azimuth cut-off. Next, the practical retrieval of swell spectra is detailed addressing wave feature filtering and cross-spectra methods.

### 1.3.1 Non-linear transformation

#### 1.3.1.1 SAR image intensity

The signal intensity  $I_\sigma(\mathbf{r}, t)$  backscattered toward the SAR is first formulated neglecting the effects of sea surface displacements on scatterers' re-arrangement. Under this temporary assumption, the associated MTF only contains the hydrodynamic and the tilt modulation components expressed in equation 1.14a. since it is equivalent to the intensity measured by a RAR plus an additional speckle noise. Its description and main characteristics are further detailed in paragraph 1.3.5.1, page 44. For the moment, we only need to consider that it is a multiplicative noise. Hence, the backscattered intensity  $I_\sigma(\mathbf{r}, t)$ , at point  $\mathbf{r}$  and time  $t$  can be written as the noise-free intensity of the backscattered signal  $I_R(\mathbf{r}, t)$ , multiplied by the speckle noise  $n(\mathbf{r}, t)$ :

$$I_\sigma(\mathbf{r}, t) = I_R(\mathbf{r}, t)n(\mathbf{r}, t) \quad (1.24)$$

where,  $n(\mathbf{r}, t)$  is the speckle noise intensity. Its standard deviation is equal to its mean divided by the square root number of looks. Also,  $\langle n \rangle = 1$ ;  
 $I_R(\mathbf{r}, t)$ , the noise-free intensity of the backscattered signal for RARs.

Following linear modulation theory, if the backscattered intensity modulation  $I$  remains small compared to the average intensity  $I_0$ , which can also be expressed by the condition  $T_j^R \xi_j \ll 1$ , the backscattered signal can be written:

$$I_\sigma(\mathbf{r}, t) = I_0(1 + I(\mathbf{r}, t))n(\mathbf{r}, t) \quad (1.25)$$

Now, taking into account the range and velocity bunching effects, the position of the sea surface scatterers are shifted by a displacement  $\xi$ , which decomposes in the  $\mathbf{Oxy}$  reference system as:

$$\xi = (\xi_{rb}, \xi_{vb}) = (\xi_x, \xi_y) \quad (1.26)$$

The intensity measured by the SAR can then be obtained by modifying the position of each facet by  $\mathbf{r} = \mathbf{r}' + \xi(\mathbf{r}')$  in equation 1.25. and introducing the instrument impulse response  $h(\mathbf{r})$ . The SAR image intensity  $I_S(\mathbf{r}, t)$ , is written as the superposition of the statistically independent intensities of all

backscattering facets multiplied by the instrument impulse response:

$$\begin{aligned}
I_S(\mathbf{r}, t) &= \int_{\mathbf{r}'} I_\sigma(\mathbf{r}', t) h(\mathbf{r} - \mathbf{r}' - \xi(\mathbf{r}')) d\mathbf{r}' \\
&= h(\mathbf{r}) \left[ \int_{\mathbf{r}'} I_\sigma(\mathbf{r}', t) \delta(\mathbf{r} - \mathbf{r}' - \xi(\mathbf{r}')) d\mathbf{r}' \right] \\
&= h(\mathbf{r}) \left[ \sum_{\mathbf{r}'} I_\sigma(\mathbf{r}', t) \left| \frac{d\mathbf{r}'}{d\mathbf{r}} \right| \right]_{\mathbf{r}' = \mathbf{r} - \xi(\mathbf{r}')} \quad (1.27a)
\end{aligned}$$

with,

$$h(\mathbf{r}) = \frac{\pi}{2\sigma_x\sigma_y} e^{-\pi^2 x^2 / (2\sigma_x^2) - \pi^2 y^2 / (2\sigma_y^2)} \quad (1.27b)$$

where,  $\sigma_x$  and  $\sigma_y$  are the spatial resolution of the SAR for stationary targets in range and azimuth, respectively;  $|d\mathbf{r}'/d\mathbf{r}|$ , the Jacobian representing the local variation of scatter density which can also be written  $|1 + d\xi(\mathbf{r}')/d\mathbf{r}'|^{-1}$ .

### 1.3.1.2 SAR cross image spectrum

The SAR cross image spectrum  $P^S$ , between two independent looks acquired at times  $t$  and  $t + \tau$ , is defined by:

$$P^S(\mathbf{k}, t, \tau) = \langle \widehat{I}_S(\mathbf{k}, t) \widehat{I}_S^*(\mathbf{k}, t + \tau) \rangle - I_0^2 \delta(\mathbf{k}) \quad (1.28)$$

where,  $\widehat{I}_S$  is the Fourier transform of  $I$ ;  
 $\widehat{I}_S^*$ , its complex conjugate.

Assuming  $I_\sigma$  and  $\xi$  are stationary fields, the SAR cross image spectrum is given by *Krogstad* (1992):

$$P^S(\mathbf{k}, \tau) = \int e^{-i\mathbf{k}\cdot\mathbf{r}} G(\mathbf{r}, \tau, \mathbf{k}) d\mathbf{r} - I_0^2 \delta(\mathbf{k}) \quad (1.29a)$$

with,

$$G(\mathbf{r}, \tau, \mathbf{k}) = \widehat{h}(\mathbf{k}) \langle I_R(\mathbf{r}, \tau) n(\mathbf{r}, \tau) I_R(\mathbf{0}, 0) n(\mathbf{0}, 0) e^{-i\mathbf{k}\xi(\mathbf{r}, \tau)} e^{-\xi(\mathbf{0}, 0)} \rangle \quad (1.29b)$$

Since  $I_0$  and  $n$  are independent variables and assuming the speckle to be white uncorrelated noise, we have:

$$\langle n(\mathbf{r}, \tau) n(\mathbf{0}, 0) \rangle = \langle 1 \rangle^2 + \sigma_n^2 \delta(\mathbf{r}) \delta(\tau) \quad (1.30)$$

where  $\sigma_n$  is the variance of the speckle intensity.

Then, the  $G$ -function can be written as:

$$\begin{aligned} G(\mathbf{r}, \tau, \mathbf{k}) &= \hat{h}(\mathbf{k})G_1(\mathbf{r}, \tau, \mathbf{k}) \left(1 + \sigma_n^2 \delta(\mathbf{r})\delta(\tau)\right) \\ &= \hat{h}(\mathbf{k})G_1(\mathbf{r}, \tau, \mathbf{k}) + \hat{h}(\mathbf{k})\sigma_n^2 G_1(\mathbf{0}, 0, \mathbf{k})\delta(\mathbf{r})\delta(\tau) \end{aligned} \quad (1.31a)$$

with,

$$G_1(\mathbf{r}, \tau, \mathbf{k}) = \left\langle I_0(\mathbf{r}, \tau)I_0(\mathbf{0}, 0)e^{i\mathbf{k}(\xi(\mathbf{r}, \tau) - \xi(\mathbf{0}, 0))} \right\rangle \quad (1.31b)$$

Let  $\mathbf{X}$ , be the vector  $\mathbf{X} = (I_0(\mathbf{r}, \tau), I_0(\mathbf{0}, 0), \xi(\mathbf{r}, \tau), \xi(\mathbf{0}, 0))$ , assumed Gaussian. Then, the  $G_1$ -function may now be written as:

$$G_1 = \frac{-\partial^2}{\partial K_1 \partial K_2} \left\langle e^{i\mathbf{K} \cdot \mathbf{X}} \right\rangle \Big|_{\mathbf{K}=(0,0,k_x,k_y)} \quad (1.32)$$

where  $K_1$  and  $K_2$  refer to the two first coordinates.

After some algebra, the  $G_1$ -function is found to be (*Krogstad, 1992; Engen and Johnsen, 1995*):

$$\begin{aligned} G_1(\mathbf{r}, \tau, \mathbf{k}) &= I_0^2 e^{k_x^2 \mu_{\xi_x \xi_x}(\mathbf{r}, \tau) + k_y^2 \mu_{\xi_y \xi_y}(\mathbf{r}, \tau)} \\ &\quad e^{k_x k_y [\mu_{\xi_x \xi_y}(\mathbf{r}, \tau) + \mu_{\xi_y \xi_x}(\mathbf{r}, \tau)]} \\ &\quad \times \left[ 1 + \rho_{II}(\mathbf{r}, \tau) + ik_x [\rho_{I\xi_x}(\mathbf{r}, \tau) - \rho_{\xi_x I}(\mathbf{r}, \tau)] \right. \\ &\quad \quad + ik_y [\rho_{I\xi_y}(\mathbf{r}, \tau) - \rho_{\xi_y I}(\mathbf{r}, \tau)] \\ &\quad \quad + k_x^2 [\mu_{I\xi_x}(\mathbf{r}, \tau)\mu_{\xi_x I}(\mathbf{r}, \tau)] \\ &\quad \quad + k_y^2 [\mu_{I\xi_y}(\mathbf{r}, \tau)\mu_{\xi_y I}(\mathbf{r}, \tau)] \\ &\quad \quad \left. + k_y k_x [\mu_{I\xi_x}(\mathbf{r}, \tau)\mu_{\xi_y I}(\mathbf{r}, \tau) \right. \\ &\quad \quad \left. + \mu_{I\xi_y}(\mathbf{r}, \tau)\mu_{\xi_x I}(\mathbf{r}, \tau)] \right] \end{aligned} \quad (1.33a)$$

with,

$$\rho_{ab}(\mathbf{r}, \tau) = \langle [a(\mathbf{0}, 0) - \langle a \rangle] [b(\mathbf{r}, \tau) - \langle b \rangle] \rangle \quad (1.33b)$$

$$\mu_{ab}(\mathbf{r}, \tau) = \rho_{ab}(\mathbf{r}, \tau) - \rho_{ab}(\mathbf{0}, 0) \quad (1.33c)$$

where  $a$  and  $b$  are indexes referring to  $I$ ,  $\xi_x$  or  $\xi_y$ .

The cross-correlation function,  $\rho_{ab}$ , is related to the wave spectrum  $S$ , by the MTF  $T_a$  and  $T_b$  by the relation:

$$\begin{aligned} \rho_{ab}(\mathbf{r}, t) &= \frac{1}{(2\pi)^2} \int \frac{1}{2} e^{i\mathbf{k} \cdot \mathbf{r}} [T_a(\mathbf{k})T_b^*(\mathbf{k})e^{-i\omega t} S(\mathbf{k}) + \\ &\quad T_a^*(-\mathbf{k})T_b(-\mathbf{k})e^{i\omega t} S(-\mathbf{k})] d\mathbf{k} \end{aligned} \quad (1.34)$$

where,  $T_{\xi_x}$  refers to the range bunching MTF:  $T_{rb}$ ;  
 $T_{\xi_y}$ , to the velocity bunching MTF:  $T_{vb}$ ;  
 $T_I$ , to the tilt and hydrodynamic MTFs:  $T_t + T_h$ .

For instance:

$$\rho_{\xi_y \xi_y} = (R/V)^2 \sigma_{u_r} \quad (1.35a)$$

$$\rho_{\xi_x \xi_x} = \sigma_\eta^2 / \tan^2 \theta \quad (1.35b)$$

In the end, the non-linearity of this transformation comes from the exponential terms in the expression of the  $G_1$ -function. The respective contributions of the range and velocity bunching in this exponential was compared for a wind-sea with a JONSWAP (cf. Chapter 2, Section 2.2) spectrum (*Elfouhaily, 1997*) and the wave mode products of ENVISAT. Applied to equations 1.35, for  $R/V = 115$  s, the ratio  $\rho_{\xi_y \xi_y} / \rho_{\xi_x \xi_x}$  is greater than 500 for winds up to  $25 \text{ m.s}^{-1}$ .

Therefore, the range bunching effect is usually neglected compared to the velocity bunching effect. Finally, the SAR cross image spectrum can be written as:

$$P^S(\mathbf{k}, \tau) = \hat{h}(\mathbf{k}) \left[ \int e^{-i\mathbf{k}\cdot\mathbf{r}} G_1(\mathbf{r}, \tau, \mathbf{k}) d\mathbf{r} - I_0^2 \delta(\mathbf{k}) \right] + \hat{h}(\mathbf{k}) \sigma_n^2 \left( 1 + \rho_{II}(\mathbf{0}, 0) \right) \delta(\tau) \quad (1.36)$$

The first term of the expression corresponds to the spectral contribution from the modulation induced by the detected ocean waves while the second term corresponds to the spectral noise induced by the speckle, once filtered by the impulse response of the instrument.

### 1.3.2 Quasi-linear transformation

The  $G_1$ -function expression given in equation 1.33a is rather complex. It can be simplified, as proposed by *Hasselmann and Hasselmann (1991)* and *Krogstad (1992)* by linearizing the exponential term. Using the fact that  $\rho_{ab}(\mathbf{r}, \tau)$  is an even function and replacing  $\mu$  by its expression given by

equation 1.33c in 1.33a, we obtain:

$$\begin{aligned}
G_1(\mathbf{r}, \tau, \mathbf{k}) &= I_0^2 e^{-k_x^2 \rho_{\xi_x \xi_x}(\mathbf{0}, 0) - k_y^2 \rho_{\xi_y \xi_y}(\mathbf{0}, 0)} \\
&\quad e^{-2k_x k_y \rho_{\xi_x \xi_y}(\mathbf{0}, 0)} \\
&\quad \times \left[ 1 + \rho_{II}(\mathbf{r}, \tau) + ik_x [\rho_{I\xi_x}(\mathbf{r}, \tau) - \rho_{I\xi_x}(-\mathbf{r}, -\tau)] \right. \\
&\quad \quad + ik_y [\rho_{I\xi_y}(\mathbf{r}, \tau) - \rho_{I\xi_y}(-\mathbf{r}, -\tau)] \\
&\quad \quad + k_x^2 \rho_{\xi_x \xi_x}(\mathbf{r}, \tau) + k_y^2 \rho_{\xi_y \xi_y}(\mathbf{r}, \tau) \\
&\quad \quad + k_x k_y [\rho_{\xi_x \xi_y}(\mathbf{r}, \tau) - \rho_{\xi_x \xi_y}(-\mathbf{r}, -\tau)] \\
&\quad \quad + O\left((k_x \rho_{I\xi_x})^2\right) + O\left((k_y \rho_{I\xi_y})^2\right) + O\left((k_x k_y \rho_{I\xi_x} \rho_{I\xi_y})\right) \\
&\quad \quad + O\left((k_x \rho_{\xi_x \xi_x})^2\right) + O\left((k_y \rho_{\xi_y \xi_y})^2\right) \\
&\quad \quad \left. + O\left((k_x k_y \rho_{\xi_x \xi_y})^2\right) \right] \quad (1.37)
\end{aligned}$$

In practice, given the relative importance of  $\rho_{\xi_y \xi_y}$  with respect to  $\rho_{\xi_x \xi_x}$  and  $\rho_{\xi_x \xi_y}$ , the exponential terms associated with these quantities in the expression of the  $G_1$ -function can be neglected. Then, neglecting the terms proportional to the square wavenumber, the  $G_1$ -function can be approximated by:

$$\begin{aligned}
G_1(\mathbf{r}, \tau, \mathbf{k}) &\simeq I_0^2 e^{-k_y^2 \rho_{\xi_y \xi_y}(\mathbf{0}, 0)} \\
&\quad \times \left[ 1 + \rho_{II}(\mathbf{r}, \tau) + ik_x [\rho_{I\xi_x}(\mathbf{r}, \tau) - \rho_{I\xi_x}(-\mathbf{r}, -\tau)] \right. \\
&\quad \quad \left. + ik_y [\rho_{I\xi_y}(\mathbf{r}, \tau) - \rho_{I\xi_y}(-\mathbf{r}, -\tau)] \right] \quad (1.38)
\end{aligned}$$

The exponential term acts as a low-pass filter with a cut-off value varying with the surface wind speed and limits the SAR in detecting wave systems whose wavenumber in the azimuth direction is greater than this value. This exponential highlights the frequently strongly non-linear impact of velocity bunching, particularly for wind-seas and short waves. Still, for very long waves such as swell, the azimuthal displacements are small compared to the characteristic ocean wavelength and a quasi-linear approach is valid. Besides, the tilt and hydrodynamic modulations can be treated as linear processes. Thus, we introduce  $T_{Lin}$ , the linear MTF associated with the SAR-ocean spectrum inversion defined by:

$$T_{Lin} = T_t(\mathbf{k}) + T_h(\mathbf{k}) + ik_y T_{vb}(\mathbf{k}) + ik_x T_{rb}(\mathbf{k}) \quad (1.39)$$

In our case, the range bunching MTF is neglected, leading to the following expression of the SAR cross-image spectrum:

$$\begin{aligned}
P^S(\mathbf{k}, \tau) &\simeq I_0^2 e^{-k_y^2 \rho_{\xi_y \xi_y}(\mathbf{0}, 0)} \\
&\times \frac{1}{2} \left( |T_{Lin}(\mathbf{k})|^2 e^{-i\omega\tau} S(\mathbf{k}) + |T_{Lin}(-\mathbf{k})|^2 e^{i\omega\tau} S(-\mathbf{k}) \right) \\
&+ \hat{h}(\mathbf{k}) \sigma_n^2 \left( 1 + \rho_{II}(\mathbf{0}, 0) \right) \delta(\tau)
\end{aligned} \tag{1.40}$$

The quasi-linear approach is valid whenever condition  $k_y^2 \rho_{\xi_y \xi_y}(\mathbf{r}, \tau) \ll 1$  is verified. Thus, steep waves (with large wave height-wavelength ratio) and with a high azimuth wavenumber  $k_y$  cannot be imaged by the SAR instrument due to the strong non-linearities.

### 1.3.3 Azimuth cut-off

#### 1.3.3.1 Illustration

As described in Section 1.2.2.1, velocity bunching can lead to a constructive mechanism or to an image degradation, which manifests as an apparent blurring of the SAR image. These effects can be identified in the expression of  $G_1$ -function in the equation of the non-linear transform (equation 1.33):

- the term  $e^{k_x^2 \rho_{\xi_y \xi_y}(\mathbf{r}, \tau)}$  contributes to the coherent ocean imaging by the orbital velocities of long azimuth waves;
- the term  $e^{-k_x^2 \rho_{\xi_y \xi_y}(\mathbf{0}, 0)}$  contributes to the low-pass filter, the so-called azimuth cut-off, which is governed by the standard deviation of scatterers' motion.

On average, the azimuth cut-off starts to affect waves shorter than 200 m. For wave systems with shorter wavelengths, which are mostly wind-sea waves, this low-pass filter distorts the spectral domain by rotating and translating the detected peak.

This phenomenon is illustrated on Figure 1.13 where a wave system propagating in the azimuth direction, 150 m long (as measured given by a co-located buoy), is imaged under low and strong wind conditions. In the first case, the imaging process is quasi-linear since the standard deviation of the scatterer's movement remains small while in the second case, the azimuth cut-off wavelength equals that of the wave system<sup>5</sup>, thereby moving the peak closer to the range direction. If the azimuth cut-off wavelength is much larger than the azimuth wavelength of the image wave system, it can even be completely absent from the image spectrum.

---

5. For the estimation of this parameter, cf. paragraph 1.3.3.2, page 41.

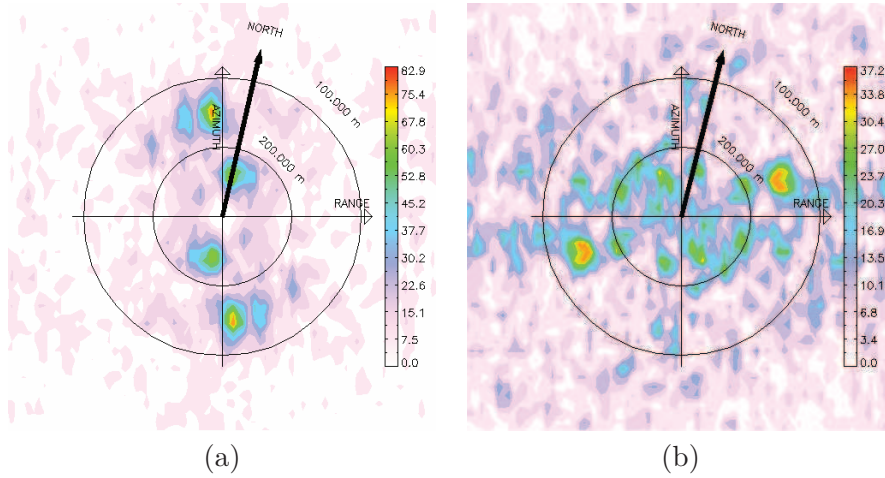


Figure 1.13: SAR image spectrum of the ocean surface imaging a wave system in the azimuth direction under low wind conditions, about  $2 \text{ m.s}^{-1}$ , (a) and strong wind conditions,  $17 \text{ m.s}^{-1}$ , (b).

The estimation of the azimuth cut-off is crucial for the exploitation of the sea surface spectrum in order to estimate which part is correctly imaged and which one is partly under-estimated or absolutely not represented. It is thus important to estimate the displacement correlation  $\rho_{\xi_y \xi_y}(\mathbf{0}, 0)$ .

### 1.3.3.2 Estimation

Several methods exist for the estimation of the azimuth cut-off. Some of them proposed by *Krogstad et al. (1994)* or *Hasselmann et al. (1996)* use the spectral domain.

As an alternative, the estimation method proposed by *Kerbaol (1997)* uses the azimuth auto-correlation function of a single image. Fitting a Gaussian to the part of this function responsible for the signal modulation yields the azimuth cut-off wavelength, as illustrated by Figure 1.14. Also, if several independent looks of the same scene are available, one can use the cross-correlation function. The resulting estimation of the azimuth cut-off wavelength is usually slightly smaller. This is partly explained by wave breaking, which significantly contributes to the standard deviation of the scatterer's movement but is filtered out by the cross-correlation method given the short lifetime of such events (*Ouchi and Cordey, 1991*).

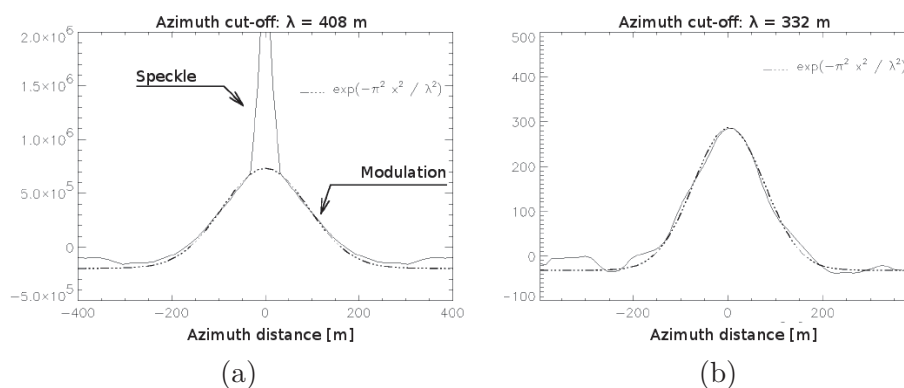


Figure 1.14: Estimation of the azimuth cut-off wavelength using the auto-correlation function (a) and the cross-correlation function (b). Adapted from *Kerbaol (1997)*.

### 1.3.4 Wave feature filtering

As often observed for SAR ocean scenes, there are numerous cases for which the measured intensity is not homogeneous. Such a phenomenon is most frequent under low wind conditions, and/or very active biological outbursts which lead to heterogeneous modifications of the backscattered signal over the SAR image. These features are illustrated on Figure 1.15-a where a SAR image under very low wind conditions is represented. It causes a modification of the backscattered signal, evidenced by the presence of dark patches. Other phenomena known to disrupt the SAR homogeneity can include internal wave signatures, rain effects, atmospheric and oceanic fronts. The spectral signatures associated with image homogeneities can be very large and can dominate at lowest wavenumbers.

To remove these undesired and aperiodic spectral contributions, a filtering analysis in the spectral domain is performed. It consists in estimating the directional continuity of the lowest wavenumber contributions. Indeed, non-wave features have rather isotropic spectral signatures which is not the case of long waves. At present, this filtering is performed using a simple constant high-pass filter. Alternatively, using morphological filters to precisely identify spectral peaks related or not to wave signatures would constitute a great improvement.

Whenever non-wave signatures are removed, the remaining SAR image spectrum is only related to wave modulation. A comparison of an inversed SAR ocean spectrum with the co-located spectrum from WAM model<sup>6</sup> is

6. Wave Action Model for sea-state prediction operated by the European Center for

shown on Figure 1.15. The wave feature filtering is performed directly on the SAR image spectra before calculating the cross-spectra described in the following subsection.

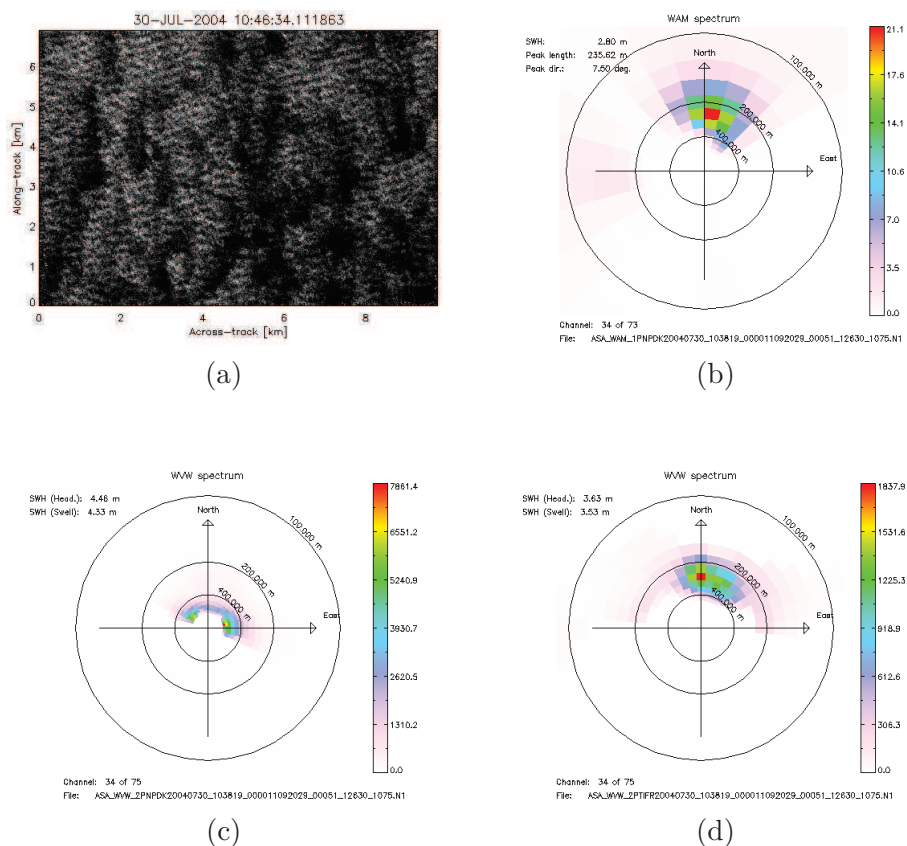


Figure 1.15: SAR image of the ocean waves in presence of non-wave features (a) and the co-located wave spectrum from WAM model (b). Subplots (c) and (d) respectively depict the inversed ocean wave spectra for cases when the low frequency signal due to non-wave features is kept or removed by the geophysical inversion.

Additionally, to make sure that the image has good contrast and homogeneity and does not contain other non-wave features like oil slicks or ships, the image normalized variance is restricted to values ranging from 1.05 to 1.5.

### 1.3.5 Cross-spectra

This technique was developed by *Engen and Johnsen* (1995) provides information on the SAR image spectrum. The advantages brought by this method are twofold:

- the image cross-spectra are shown to significantly reduce the speckle noise level while preserving the spectral shape (*Engen and Johnsen, 1995*);
- it provides information about the wave propagation direction.

These two aspects are detailed hereafter.

#### 1.3.5.1 Speckle noise

The speckle gives SAR images a grainy salt and pepper appearance. Characteristic of coherent systems, it results from constructive/destructive interferences of the backscattered signal from scatter points contained within the same resolution cell. In the absence of signal modulation, for a single-look image, the radar signal intensity standard deviation is equal to its mean. For a multi-look image, it is equal to the mean divided by the square root the number of looks. It has been thoroughly studied and characterized in the end of the last century (*Goodman, 1976; Jakeman, 1984; Arsenault and April, 1986*).

To model this noise, it is assumed that the complex signal reflected by the illuminated scene can be represented as the summation of the complex amplitude contributions from many elementary scattering areas on the rough surface. This empirical model is analogous to a classical random walk problem in the complex plane (Figure 1.16). The model then uses the two following assumptions:

- the amplitude and the phase of each elementary scatterer are statistically independent of each other and of the amplitudes and phases of all other elementary scatterers;
- the phases of the elementary contributions are equally likely to lie anywhere in the interval  $[-\pi; \pi]$ . This condition is realized when considering a rough surface, compared to the radar wavelength<sup>7</sup>.

Provided that the number of elementary contributions is large, the speckle noise can be considered as a multiplicative noise since:

- the real and imaginary parts of the complex field are independent, zero mean, identically distributed Gaussian random variables;
- the signal intensity obeys negative exponential statistics. One of its properties is that its standard deviation precisely equal its mean and thus the contrast of a speckle pattern equals one for single-look images.

---

7. Verified when the Rayleigh criterion is satisfied, cf. paragraph 1.2.1.3, page 21.

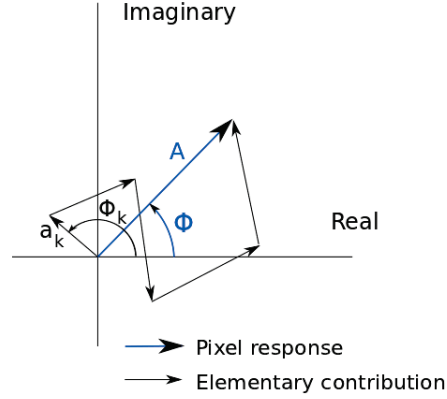


Figure 1.16: Physical origin of speckle: effect of the coherent nature of SAR resulting from the combination of elementary contributions within each pixel.

Speckle noise can be totally removed using the cross spectrum of two independent ocean scenes, separated from one another by a time  $\tau \neq 0$ . Indeed, looking at equation 1.40, the second term which is proportional to  $\delta(\tau)$  is eliminated resulting in the following relation:

$$\begin{aligned}
 P^S(\mathbf{k}, \tau) &\simeq I_0^2 e^{-k_y^2 \rho_{\xi_y \xi_y}(\mathbf{0}, 0)} \\
 &\times \frac{1}{2} \left( |T_{Lin}(\mathbf{k})|^2 e^{-i\omega\tau} S(\mathbf{k}) + \right. \\
 &\quad \left. |T_{Lin}(-\mathbf{k})|^2 e^{i\omega\tau} S(-\mathbf{k}) \right) \quad (1.41)
 \end{aligned}$$

Not only does this totally eliminate the fluctuations  $\sigma_n^2$ , due to the speckle but it also suppresses the fluctuations  $1 + \rho_{II}(\mathbf{0}, 0)$ , due to the modulation by RAR imaging. In practice, for incidence angle of  $20^\circ$ ,  $\rho_{II}(\mathbf{0}, 0)$  is of the order of 0.1 (Krogstad, 1992; Kerbaol, 1997).

### 1.3.5.2 Directional ambiguity

Inversion methods such as those proposed by *Hasselmann and Hasselmann* (1991), require an *a priori* knowledge of the sea surface spectrum, which can be given by a wave model like WAM<sup>8</sup> (WAMDIG, 1988). In most cases, the result of the wave spectrum inversion and more specifically the removal of the  $180^\circ$  direction ambiguity depends on this first guess. This information can also be assessed using the cross spectrum phase associated with the translation of the wave systems during time  $\tau$  (*Vachon and Raney*,

8. A third generation wave model based on transport equation describing the evolution of a directional ocean wave spectrum.

1991). This translation is related to the phase velocity of the propagating waves  $C(k)$ . Considering long waves for which the quasi-linear approach is valid and according to equation 1.41, the phase of the SAR cross-image spectrum  $\phi(k)$ , comes from the translation in the spatial domain of all waves with wavenumber  $k$ :

$$\phi(k) = \omega\tau = kC(k)\tau \quad (1.42)$$

The information given by the imaginary part of cross spectrum is illustrated on Figure 1.17. Its sign indicates a propagation of the main swell system in the NE direction. In a general way, if the imaginary part of the cross

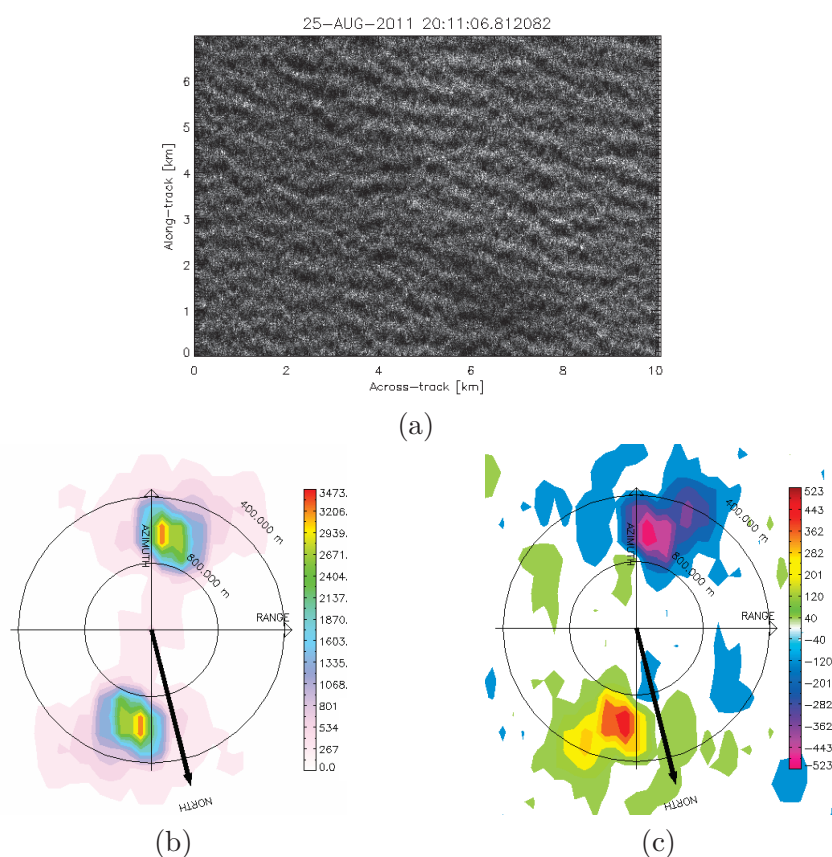


Figure 1.17: (a) SAR image of the sea surface with a 600 m swell propagating NE. (b) Associated SAR spectrum. (c) Imaginary part of the cross spectrum

spectra is above the noise floor, that means a wave motion can be detected from comparing two looks of the ocean surface. The noise floor threshold is determined empirically. In practice, the imaginary part of the cross spectra is weighted by the energy cross spectra to give more importance to the imaginary part attributed to the considered swell.

The  $180^\circ$  ambiguity can only be removed if the phase remains within the range  $[0, \pi]$ . In practice, for ENVISAT wave mode products,  $\tau$  equals 0.4 s and this condition on the phase can be expressed as a condition on the minimum period:

$$kC(k)\tau < \pi \quad (1.43a)$$

$$2\tau < T \quad (1.43b)$$

The limitation imposed on the minimum wavelength detected by the SAR due to the azimuth cut-off is about 200 m, corresponding to a period of 11 s. Therefore, the detected waves using the quasi-linear approach will always satisfy condition 1.43.

## 1.4 Conclusion

First, we have presented the SAR fundamental principles and how fine resolutions can be theoretically achieved in the range direction using an adequate signal sampling and in the azimuth direction, determined by the SAR antenna. Thus, SAR wave mode resolutions of the order of  $10 \times 10 \text{ m}^2$  and  $5 \times 5 \text{ m}^2$  for ENVISAT and Sentinel-1, respectively, could be reached but additional ocean imaging processes greatly diminish the effective resolution over the ocean.

Second, to quantify the signal backscattered from the ocean surface, we have introduced the NRCS which measures the signal intensity coming from a ground unit surface. As for the mechanisms influencing the NRCS for the range of incident angles we consider ( $20$  to  $40^\circ$ ), Bragg scattering has been thought to be the only active phenomenon for long. This mechanism results from the coherent addition of returns from adjacent waves that are in phase. The signal intensity contribution from Bragg scattering is due to centimetric waves. It is proportional to the spectrum energy in the range direction and at Bragg frequency. Even if the conditions on direction and frequency are quite precise, they are generally met since wind-waves are continuously distributed in frequency. Besides, wind-wave spectra show a rather wide angular distribution centered around the wind blowing direction which also ensures the presence of energy in the range direction, even when the wind blows in perpendicular direction.

Discrepancies with experiments in ocean and controlled wave tanks have proven that other phenomena than Bragg scattering, such as quasi-specular reflection, had to be taken into account. Its contribution to the NRCS can be related to the probability that these sea surface facets are oriented perpendicularly to the radar. Its relative contribution to the NRCS is most effective at HH polarization and at incidence angles smaller than  $20^\circ$  or for

larger incident angles in wave breaking regions.

Then, we have presented the modulation processes allowing the SAR instrument to image ocean waves. Long waves play a particularly important role since they induce variations of the local incidence angle caused by long waves' slope (tilt modulation) and they modify the short waves' dynamic along longer waves' profile (hydrodynamic modulation) which also modifies the wind stress in return. Since the theoretical models quantifying the tilt modulation do not reproduce the signal variations with long waves' direction or wind speed, an empirical backscattering model using CMOD is preferred. It establishes a relation between the NRCS, the incidence angle, the wind speed and the wave direction. However, because of the difficulty to separate the respective contribution of tilt and hydrodynamic modulations in the SAR image, this empirical method tends to over-estimate the significant wave height, especially at low winds.

On top of this, sea surface displacements caused by waves induce a Doppler shift in the backscattered signal which results in a mis-positioning of the point scatterers on the SAR image in the azimuth direction (velocity bunching). As a consequence, the final SAR image is smoother and the signal dynamic is reduced in presence of wind-waves. At moderate and high winds, this tends to compensate the significant wave height over-estimation when using CMOD. Still, the final SAR resolution is affected by this azimuth cut-off and on average, it is impossible to image ocean waves whose wavelength component in azimuth direction is smaller than 200 m. Estimations methods of the azimuth cut-off wavelength have been proposed using the auto-correlation of a SAR image or the cross-correlation of different looks of the same scene. For waves that are not filtered by the azimuth cut-off, a quasi-linear transformation can be established between the SAR image spectrum and the ocean wave spectrum. Additionally, using the SAR cross image spectrum brings crucial information on the waves' direction of propagation and totally removes speckle noise.

Given the limitations on mapping ocean waves with SAR, the instrument appears dedicated to the measurement of long waves with rather moderate wind conditions, better known as swell and described in the following chapter.

## Bibliography

- Alpers, W. R. (1983a), Imaging ocean surface waves by synthetic aperture radar: a review, *Satellite microwave remote sensing*, p. 107–109. 24
- Alpers, W. R. (1983b), Monte Carlo simulations for studying the relationship between ocean wave and synthetic aperture radar image spectra, *Journal of geophysical research*, 88(C3), 1745–1759. 24
- Alpers, W. R., and C. Brüning (1986), On the relative importance of motion related contributions to the SAR imaging mechanism of ocean surface waves, *IEEE Trans. on Geosci. and Remote Sensing*, 24, 873–885. 27
- Alpers, W. R., and C. Rufenach (1979), The effect of orbital motions on synthetic aperture radar imagery of ocean waves, *Antennas and Propagation, IEEE Transactions on*, 27(5), 685–690. 26, 34
- Alpers, W. R., D. B. Ross, and C. L. Rufenach (1981), On the detectability of ocean surface waves by real and synthetic aperture radar, *J. Geophys. Res.*, 86(C7), 6481–6498. ii, 1, 24
- Apel, J. (1987), *Principles of ocean physics*, vol. 38, Academic Pr. 21
- Arsenault, H. H., and G. V. April (1986), Information content of images degraded by speckle noise, *Optical Engineering*, 25, 662–666. 44
- Askari, F., and W. C. Keller (1994), Real aperture radar imaging of ocean waves during SAXON-FPN: A case of azimuth-traveling waves, *J. Geophys. Res.*, 99(C5), 9817–9833. 31
- Beckmann, P., and A. Spizzichino (1963), *The Scattering of Electromagnetic Waves from Rough Surfaces*, 1963, Pergamon, New York. 22
- Collard, F., F. Ardhuin, and B. Chapron (2005), Extraction of coastal ocean wave fields from SAR images, *Oceanic Engineering, IEEE Journal of*, 30(3), 526–533. 29
- COSMO-SkyMed, S. (2007), *Products Handbook*, Italian Space Agency (ASI), Rome, Italy, Doc. ASI-CSM-ENG-RS-092-A, Rev. A. 10
- Crombie, D. D. (1955), Theory of HF ground wave backscatter from sea waves, *Nature*, 175, 681–682. 17
- Curlander, J., and R. McDonough (1991), Synthetic aperture radar- Systems and signal processing(Book), *New York: John Wiley & Sons, Inc*, 1991. 10
- Duncan, J. R., W. C. Keller, and J. W. Wright (1974), Fetch and wind speed dependence of Doppler spectra, *Radio Science*, 9(10), 809–819. 17

- Elachi, C., T. W. Thompson, and D. King (1977), Ocean wave patterns under hurricane Gloria: observation with airborne synthetic aperture radar, *Science*, 198, 609–610. 11, 24
- Elfouhaily, T. M. (1997), A consistent wind and wave model and its application to microwave remote sensing of the ocean surface, Ph.D. thesis, Denis Diderot University, Paris. 38
- Engen, G., and H. Johnsen (1995), SAR-ocean wave inversion using image cross spectra, *IEEE transactions on geoscience and remote sensing*, 33(4), 1047–1056. ii, 2, 34, 37, 44
- Ericson, E. A., D. R. Lyzenga, and D. T. Walker (1999), Radar backscatter from stationary breaking waves, *J. Geophys. Res.*, 104(C12), 29,679–29,695. 23
- Feindt, F., J. Schröter, and W. R. Alpers (1986), Measurement of the ocean wave-radar modulation transfer function at 35 GHz from a sea-based platform in the North Sea, *J. Geophys. Res.*, 91(C8), 9701–9708. 30
- Fu, L., and B. Holt (1982), Seasat views oceans and sea ice with synthetic aperture radar, *NASA-JPL*, pp. 81–120. 11
- Goodman, J. W. (1976), Some fundamental properties of speckle, *Journal of the Optical Society of America*, 66(11), 1145–1150, doi:10.1364/JOSA.66.001145. 44
- Gower, J. (1983), “Layover” in Satellite Radar Images of Ocean Waves, *Journal of geophysical research*, 88(C12), 7719–7720. 33
- Hara, T., and W. J. Plant (1994), Hydrodynamic modulation of short wind-wave spectra by long waves and its measurement using microwave backscatter, *J. Geophys. Res.*, 99(C5), 9767–9784. 30
- Hasselmann, K., and S. Hasselmann (1991), On the nonlinear mapping of an ocean wave spectrum into a synthetic aperture radar image spectrum and its inversion, *Journal of Geophysical Research*, 96(C6), 10,713–10. ii, 2, 31, 34, 38, 45
- Hasselmann, K., R. K. Raney, W. J. Plant, W. R. Alpers, R. A. Shuchman, D. R. Lyzenga, C. L. Rufenach, and M. J. Tucker (1985), Theory of Synthetic Aperture Radar Ocean Imaging: A MARSSEN View, *Journal of Geophysical Research*, 90(C3), PP. 4659–4686, doi:198510.1029/JC090iC03p04659. 1, 24, 28, 34
- Hasselmann, S., C. Bruning, K. Hasselmann, and P. Heimbach (1996), An improved algorithm for the retrieval of ocean wave spectra from synthetic

- aperture radar image spectra, *Journal of Geophysical Research*, *C7*(101). 41, 86, 87, 89, 95
- Holt, B. (2004), Chapter 2. SAR Imaging of the Ocean Surface, in *Synthetic aperture radar marine user's manual*, pp. 25–79, US Department of Commerce. 19, 25
- IFREMER (1996), Off-line wind scatterometer ERS Products: User Manual, (C2- MUT-W-01-IF, Version 2.0). 32
- Jackson, C., J. Apel, and U. S. D. o. Commerce (2004), *Synthetic aperture radar marine user's manual*, US Department of Commerce. 10
- Jakeman, E. (1984), Speckle statistics with a small number of scatterers, *Optical Engineering*, *23*, 453–461. 44
- Janssen, P., H. Wallbrink, C. J. Calkoen, D. Van Halsema, W. A. Oost, and P. Snoeij (1998), VIERS-1 scatterometer model, *Journal of geophysical research*, *103*(C4), 7807–7831. 20, 23
- Keller, W. C., and J. W. Wright (1975), Microwave scattering and the straining of wind-generated waves, *Radio Science*, *10*, 139–147. 17, 30
- Kerbaol, V. (1997), Analyse spectrale et statistique vent-vague des images radar à ouverture synthétique (ROS)–application aux données des satellites ERS1/2, Ph.D. thesis, Thèse de doctorat, Rennes I, France. 2, 12, 15, 23, 27, 33, 34, 41, 42, 45
- Kerbaol, V., and B. Chapron (1997), A global comparison between AMI scatterometer data and SAR ERS-1/2 Wave Mode products, *ESA SP*, p. 1163–1168. 32
- Krogstad, H. E. (1992), A simple derivation of Hasselmann's nonlinear ocean-synthetic aperture radar transform, *J. Geophys. Res.*, *97*(C2), 2421–2425. ii, 2, 34, 36, 37, 38, 45, 242
- Krogstad, H. E., O. Samset, and P. W. Vachon (1994), Generalizations of the nonlinear oceanSAR transform and a simplified SAR inversion algorithm, *Atmosphere-Ocean*, *32*(1), 61–82, doi:10.1080/07055900.1994.9649490. 41
- Kudryavtsev, V., D. Hauser, G. Caudal, and B. Chapron (2003a), A semiempirical model of the normalized radar cross-section of the sea surface 1. Background model, *J. Geophys. Res.*, *108*(C3), 8054, doi:10.1029/2001JCOO1003. 20, 23
- Kudryavtsev, V., D. Hauser, G. Caudal, and B. Chapron (2003b), A semiempirical model of the normalized radar cross-section of the sea surface

2. Radar modulation transfer function, *J. Geophys. Res.*, 108(C3), 8055, doi:10.1029/2001JCOO1004. 24, 31, 32
- Larson, T. R., L. I. Moskowitz, and J. W. Wright (1976), A note on SAR imagery of the ocean, *IEEE Trans. Antennas Propagat.*, AP-24, 393–394. 34
- Lasswell, S. W. (2005), History of SAR at Lockheed Martin (previously Goodyear Aerospace), *Proceedings of SPIE*, 5788(1), 1–12, doi:doi:10.1117/12.603927. 10
- Long, A., and D. Trizna (1973), Mapping of North Atlantic winds by HF radar sea backscatter interpretation, *Antennas and Propagation, IEEE Transactions on*, 21(5), 680–685. 17
- Massonnet, D., and J. C. Souyris (2008), *Imaging with synthetic aperture radar*, EPFL Press. 10
- Monaldo, F., and D. Lyzenga (1986), On the Estimation of Wave Slope and Height-Variance Spectra from SAR Imagery, *Geoscience and Remote Sensing, IEEE Transactions on*, (4), 543–551. 31
- Ouchi, K., and R. A. Cordey (1991), Statistical analysis of azimuth streaks observed in digitally processed CASSIE imagery of the sea surface, *Geoscience and Remote Sensing, IEEE Transactions on*, 29(5), 727–735. 41
- Phillips, O. M. (1988), Radar returns from the sea surface—Bragg scattering and breaking waves, *J. Phys. Oceanogr.*, 18, 1065–1074. 23
- Plant, W. J. (1986), A Two-Scale Model of Short Wind-Generated Waves and Scatterometry, *Journal of Geophysical Research*, 91(C9), PP. 10,735–10,749, doi:198610.1029/JC091iC09p10735. 20
- Plant, W. J. (1990), Bragg scattering of electromagnetic waves from the air/sea interface, *Surface Waves and Fluxes*, 2, 41–108. 23
- Plant, W. J., and W. C. Keller (1983), The two-scale radar wave probe and SAR imagery of the ocean, *J. Geophys. Res.*, 88(C14), 9776–9784. 34
- Plant, W. J., and W. C. Keller (1990), Evidence of Bragg scattering in microwave Doppler spectra of sea return, *J. Geophys. Res.*, 95(C9), 16,299–16,310. 19
- Quilfen, Y., B. Chapron, A. Bentamy, J. Gourrion, T. Elfouhaily, and D. Vandemark (1999), Global ERS 1 and 2 and NSCAT observations: upwind/crosswind and upwind/downwind measurements, *J. Geophys. Res.*, 104(C5), 11,459–11,469. 23

- Romeiser, R., and W. R. Alpers (1997), An improved composite surface model for the radar backscattering cross section of the ocean surface, 2. Model response to surface roughness variations and the radar imaging of underwater bottom topography, *Journal of Geophysical Research-Part C-Oceans-Printed Edition*, 102(11), 25,251–25,267. 20
- Romeiser, R., A. Schmidt, and W. R. Alpers (1994), A three-scale composite surface model for the ocean wave-radar modulation transfer function, *J. Geophys. Res.*, 99(C5), 9785–9801. 20, 32
- Stoffelen, A., and D. Anderson (1993), ERS-1 scatterometer data characteristics and wind retrieval skill, in *ESA, Proceedings of First ERS-1 Symposium on Space at the Service of Our Environment*, vol. 1. 32
- Swift, C., and L. Wilson (1979), Synthetic aperture radar imaging of moving ocean waves, *Antennas and Propagation, IEEE Transactions on*, 27(6), 725–729. 26, 27, 34
- Thompson, D. (2004), Chapter 4. Microwave Scattering from the Sea, in *Synthetic aperture radar marine user's manual*, pp. 117–138, US Department of Commerce. 21, 22
- Tran, V. B. (1999), Contribution à l'étude des diffusiomètres NSCAT et ERS-2 par modélisation neuronale. Influence de la hauteur des vagues sur le signal diffusiométrique, Ph.D. thesis. 23
- Tucker, M. (1983), The effect of a moving sea surface on SAR imagery, *Satellite microwave remote sensing*, p. 14–154. 34
- Tucker, M. (1985), Review Article. The imaging of waves by satelliteborne synthetic aperture radar: the effects of sea-surface motion, *Remote Sensing*, 6(7), 1059–1074. 26, 27
- Ulaby, F., R. Moore, and A. Fung (1982), *Microwave remote sensing-Volume II: Radar remote sensing and surface scattering and emission theory*, Addison-Wesley Publishing Company, Reading, Massachusetts, USA. 20, 21
- Vachon, P., and R. Raney (1991), Resolution of the ocean wave propagation direction in SAR imagery, *Geoscience and Remote Sensing, IEEE Transactions on*, 29(1), 105–112. 45
- Valenzuela, G. (1978), Theories for the interaction of electromagnetic and oceanic waves—A review, *Boundary-Layer Meteorology*, 13(1), 61–85. 18
- WAMDIG (1988), The WAM Model - A third generation ocean wave prediction model, *J. Phys. Oceanogr.*, 18, 1775–1810. 45

Ward, J. F. (1969), Power spectra from ocean movements measured remotely by ionospheric radio backscatter, *Nature*, *223*, 1325–1330. 17

## Chapter 2

# Ocean swell: theory and observations

### Contents

---

2.1	Airy theory . . . . .	<b>56</b>
2.1.1	Solutions . . . . .	56
2.1.2	Phase and group velocity . . . . .	58
2.1.3	Energy and significant wave height . . . . .	59
2.1.4	Deep ocean propagation properties . . . . .	60
2.2	Generation of waves by wind . . . . .	<b>61</b>
2.2.1	Wind-wave growth observations . . . . .	61
2.2.2	Wave age and wave growth laws . . . . .	65
2.2.3	Non-linear wave-wave interactions . . . . .	66
2.3	Swell propagation in deep ocean . . . . .	<b>67</b>
2.3.1	Storm sources . . . . .	67
2.3.2	Swell energy decay . . . . .	68
2.3.3	Energy dissipation . . . . .	69
2.4	Conclusion . . . . .	<b>72</b>
	Bibliography . . . . .	<b>74</b>

---

Swell defines a series of surface gravity waves that are not generated by local wind. This definition applies for ocean waves as well as for seas or lakes. This study specifically focuses on ocean swell.

This chapter first describes the swell behavior as predicted by Airy theory, the associated dispersion relation and other properties governing the swell propagation in deep ocean. Second, going back to swell origin, the storm conditions necessary for the development of long and energetic waves are detailed. Third, non-linear processes involving wave-wave interactions are presented. Finally, we expose the general trends that emerge from the measurements of swell energy decay and dissipation.

## 2.1 Airy theory

Developed in the 19<sup>th</sup> century by Airy, this theory is named after the scientist George Biddell Airy. It applies to the case of small amplitude, free propagating oscillations of the water surface. It is also linear and thus, different solutions can be linearly added to account for the sea state. According to the first swell studies, it faithfully explains *in situ* observations of waves in the absence of wind and current (*Gain, 1918; Barber and Ursell, 1948; Munk and Snodgrass, 1957; Munk et al., 1963; Snodgrass et al., 1966*). In the following section, the mathematical equations governing swell motion are described to illustrate the properties of those linear waves.

### 2.1.1 Solutions

The particle flow is described by its coordinates in the horizontal plane  $\mathbf{x} = (x, y)$  and vertical position  $z$  as illustrated in Figure 2.1. Its speed is given by their time derivative  $\mathbf{u} = (u, v)$  and  $w$ . Displacements of the sea surface along the vertical axis are described by variable  $\zeta$ .

The wave motion is described by equation 2.1, given below. The hypothesis and full development for obtaining it, using an Eulerian approach and starting from the Navier-Stokes equations governing the wave dynamics, can be found in *Lamb (1932)*. Briefly, we recall that this development assumes an incompressible fluid, with no viscosity, without current and with a flat ocean bottom.

$$\frac{\partial^2 \phi}{\partial t^2} + g \frac{\partial \phi}{\partial z} = 0, \quad \text{for } z = 0 \quad (2.1)$$

where  $\phi$  is the speed potential and  $g$ , the Earth gravity.

Searching for the periodic solutions whose phase  $\varphi$  equals:

$$\varphi = \mathbf{k} \cdot \mathbf{x} - \omega t \quad (2.2)$$

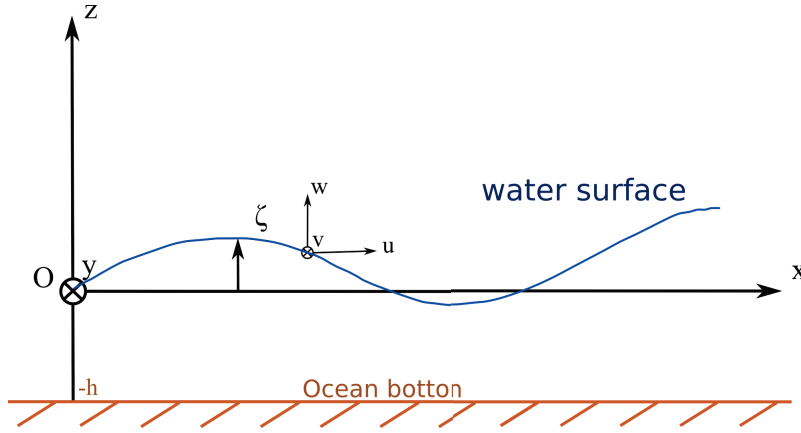


Figure 2.1: Geometry of the fluid in motion

where,  $\mathbf{k}$  is the wave vector;  
 $k$ , the wavenumber. It satisfies  $k = 2\pi/\lambda$ ;  
 $\lambda$ , the wavelength;  
 $\omega$ , the wave pulsation. It satisfies  $\omega = 2\pi/T$ ;  
 $T$ , the wave period.

This linear approach is judged valid whenever the following conditions are satisfied:

$$\varepsilon \ll 1 \quad \text{and} \quad \alpha \ll 1 \quad (2.3a)$$

with,

$$\varepsilon = ak \quad \text{and} \quad \alpha = a/D \quad (2.3b)$$

where,  $\varepsilon$  is proportional to the wave steepness  $a/\lambda$ ;  
 $a$ , the wave amplitude;  
 $\alpha$ , the relative wave amplitude with respect to the ocean depth.

In the end, the following dispersion relation is obtained:

$$\omega^2 = gk \tanh(kD) \quad (2.4)$$

where  $D$  is the water depth.

The particle motion, speed and pressure given by the periodical solutions to this equation satisfy:

$$\zeta = a \cos(\mathbf{k} \cdot \mathbf{x} - \omega t) \quad (2.5a)$$

$$\mathbf{u} = a \frac{\mathbf{k}}{k} \omega \frac{\cosh(kz + kh)}{\sinh(kD)} \cos(\mathbf{k} \cdot \mathbf{x} - \omega t) \quad (2.5b)$$

$$w = a\omega \frac{\sinh(kz + kh)}{\sinh(kD)} \cos(\mathbf{k} \cdot \mathbf{x} - \omega t) \quad (2.5c)$$

$$p = \bar{p}^H + \rho_w g a \frac{\cosh(kz + kh)}{\cosh(kD)} \cos(\mathbf{k} \cdot \mathbf{x} - \omega t) \quad (2.5d)$$

with,

$$\bar{p}^H = -\rho_w g(z - \bar{\zeta}) + \bar{p}_a \quad (2.5e)$$

where,  $\bar{p}^H$  is the mean hydrostatic pressure;  
 $p_a$ , the atmospheric pressure;  
 $a$ , the wave amplitude at the water surface;  
 $\rho_w$ , the water mass density;

The trajectory of a water particle thus approximately describes an ellipse and almost falls back to its initial position after each wave period. It is referred to as orbital motion.

### 2.1.2 Phase and group velocity

The phase velocity  $C$ , is the speed of the wave crests. Using equation 2.4, we establish the following relation:

$$C = \frac{\omega}{k} = \frac{\lambda}{T} = \left[ \frac{g}{k} \tanh(kD) \right]^{1/2} \quad (2.6)$$

This relation indicates that in deep water, long waves travel faster than short waves. On the contrary, all waves travel at the same speed in shallow waters:  $C = \sqrt{gD}$ .

The group velocity  $C_g$ , differs from the phase velocity in the way that it defines the speed at which the energy is conveyed. It is defined by  $C_g = \partial\omega/\partial k$ , which corresponds to the speed of a wave group. According to the dispersion equation 2.4, we get:

$$C_g = C \left[ \frac{1}{2} + \frac{kD}{\sinh(2kD)} \right] \quad (2.7)$$

For deep ocean, it equals half the phase velocity. In practice, an observer traveling at group velocity would record a constant wavelength and be continuously overtaken by individual waves. This interesting phenomenon is well known and was already mentioned in the Admiralty Navigation Manual (1939), Vol. III:

*If the motion of the first wave of the group is followed, it will be found that this motion dies out and that the wave next behind takes the lead. If, on the other hand, the last wave of the group is watched, another wave will be seen to appear behind it. The new waves constantly rise in the rear as rapidly and as constantly as those in the front dies out, so that the general appearance of a group of waves remains unchanged.*

The grouping phenomenon results from the superposition of waves of various yet close frequencies. Indeed, the surface elevation of two waves of same amplitude propagating in the same direction with wavenumbers and pulsations equal to  $\mathbf{k}$  and  $\mathbf{k} \pm \Delta\mathbf{k}/2$  and  $\omega$  and  $\omega \pm \Delta\omega/2$ , respectively, can be written using the elementary trigonometric formula:

$$\zeta = a \cos(\Delta\mathbf{k} \cdot \mathbf{x} - \Delta\omega t) \cos(\mathbf{k} \cdot \mathbf{x} - \omega t) \quad (2.8)$$

The second term is well known and corresponds to the main periodic signal while the first term corresponds to a slower modulation.

The dispersion works as a natural filter that separates waves according to their frequency. Therefore, after several thousand kilometers of propagation, swell spectra exhibit quite a narrow frequency width. Still, we suspect non-linear wave-wave interactions, whose effect is recognized to be very effective near the storm source region, to also modify the swell spectrum at greater distances. These interactions are discussed in Section 2.2.3. The swell modulation into wave groups has been observed using spaceborne SAR imagery by *Dankert et al.* (2003); *Borge et al.* (2004), thanks to the large wave mode dataset provided by ERS-2. Defining the run-area as the sea surface region where there are contiguous waves higher than a given threshold height, these studies have shown that the run-areas were almost always smaller than  $1 \times 1 \text{ km}^2$ , allowing the  $10 \times 5 \text{ km}^2$ -SAR wave mode products on-board ERS-2 or ENVISAT to image several entire swell groups.

### 2.1.3 Energy and significant wave height

The wave energy can be decomposed into constantly exchanging potential and kinetic components, thus explaining the name *gravity waves*. The total wave energy  $E_t$ , averaged over a wave period and integrated over the water column is equal to:

$$\begin{aligned} E_t &= E_p + E_c \\ &= \left\langle \int_0^{\zeta(\mathbf{x},t)} \rho_w g z dz \right\rangle + \left\langle \int_{-h}^{\zeta(\mathbf{x},t)} \frac{1}{2} \rho_w (|\mathbf{u}|^2 + w^2) \right\rangle \\ &= \rho_w g \langle \zeta^2 \rangle = \frac{1}{2} \rho_w g a^2 \end{aligned} \quad (2.9)$$

where  $-h$  is the ocean bottom coordinate on the vertical axis.

This total energy, expressed in  $[\text{J} \cdot \text{m}^{-2}]$ , is proportional to the square of the wave amplitude  $a$ , and independent of the water depth.

The case of a single frequency wave is over-simplified as compared to real ocean conditions whose spectrum can exhibit a rather wide frequency range,

with varying energy. Besides, one can wonder how this theoretical definition can be used in practice. The concept of significant wave height was thus developed during World War II as part of a project aiming at forecasting wave heights and periods. Studies at the Scripps Institution of Oceanography by *Munk* (1944) showed that wave height estimated by observers corresponds to the average height of the 20 to 40% highest waves. The term significant wave height then evolved to become the average of the highest one-third of the waves and noted  $H_s$  or  $H_{1/3}$ .

Presently, significant wave height is calculated from measured wave displacement. Then, if the wave spectrum has a narrow frequency range, which is the case of swell,  $H_s$  is defined as a function of the standard deviation of the sea surface displacement  $\langle \zeta^2 \rangle$  (*Hoffman and Karst, 1975*) by:

$$H_s = 4 \langle \zeta^2 \rangle^{1/2} \quad (2.10)$$

In this case, the energy is related to the significant wave height by the relation:

$$E_t = \rho_w g \frac{H_s^2}{16} \quad (2.11)$$

#### 2.1.4 Deep ocean propagation properties

Given the dispersion equation 2.4, the deep ocean is a good approximation near the sea surface as soon as  $D > \lambda/2$ . Then, in this specific case, the main wave characteristics are summarized hereafter in Table 2.1.

Phase velocity	$C = \frac{\omega}{k} = \frac{\lambda}{T} = \frac{g}{2\pi} T$
Group velocity	$C_g = \frac{\partial \omega}{\partial k} = \frac{C}{2}$
Dispersion relation	$\omega^2 = gk$
Wavelength	$\lambda = \frac{g}{2\pi} T^2$
Energy	$E = \rho_w g \langle \zeta^2 \rangle^{1/2} = \frac{1}{2} \rho_w g a^2$
Radius of particle orbit	$r = \frac{1}{2} a e^{2\pi z / \lambda}$

Table 2.1: Linear wave characteristics according to Airy theory for deep ocean, when wavelength  $\lambda$  is greater than half the water depth  $D$ .

Applying Airy theory to the case of spherical geometry, it can be shown that swells propagate on the globe following geodesics.

## 2.2 Generation of waves by wind

Long swells are generated by severe storms. During such events, the strongest winds are found in a well defined region and for a limited time, typically of the order of 12 to 24 hours. The ensemble of swell trains that were all generated by this same meteorological event is referred to as a *swell field* or *swell system*.

Swell field forecasting needs have been motivated by the colonial war (1907-1912) for the prediction of best landing conditions on the coast of Morocco (*Gain, 1918*). These military concerns were soon shared by commercial shipping. Again, these forecasting needs regained interest for similar reasons starting in 1943 for the amphibious landing on the coast of Morocco and many other locations during the end of World War II (*Sverdrup and Munk, 1947*). Following on these studies, prediction models using meteorological data were proposed by *Darbyshire (1952)* and *Gelci et al. (1957)*.

Wind-wave generation and growth mechanisms are very complex and many different theories have been and are still developed today to explain them (*Jeffreys, 1925; Phillips, 1957; Miles, 1957; West, 1982; Belcher and Hunt, 1993*). Rather than describing these different theories, we prefer to focus on the empirical results measuring the phenomenon.

### 2.2.1 Wind-wave growth observations

As indicated by experiments, ocean waves are produced by the wind. The stronger the wind, the longer it blows and the bigger the area over which it blows, the longer and the higher the waves will be. For example, larger waves can be observed on a lake than in a pond and in the ocean, waves more than 20 m-high or 700 m-long exist. The fetch defines the distance along which the wind blows with constant velocity and contributes to wave generation. It can be rather difficult to estimate unless considering offshore winds blowing perpendicularly to the coastline. Using this favorable wind configuration, the sea surface spectrum evolution with fetch was recorded during the JONSWAP campaign, in 1968. Such spectra are referred to as *fetch-limited* as their shape depends on the fetch. On the opposite, if the wind conditions remain steady for enough time, the wind-sea spectrum reaches an asymptotic shape, independent from the fetch, referred to as a *fully-developed* wind-sea spectrum. Examples of fetch-limited spectra are shown on Figure 2.2.

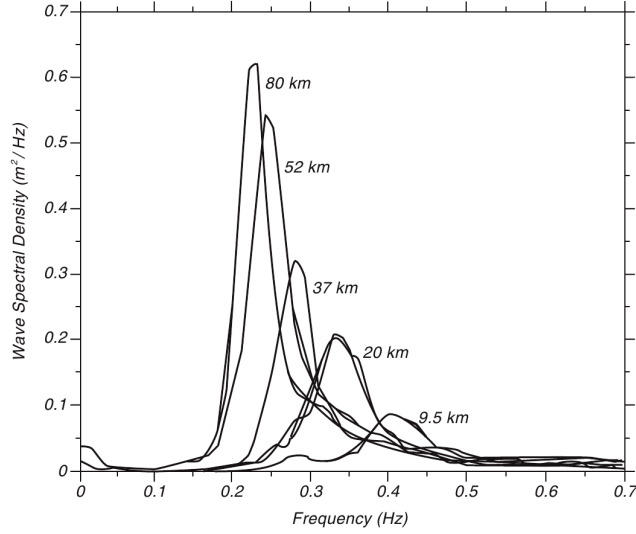


Figure 2.2: Sea surface spectra recorded on 15 September 1968 at 11Z during the JONSWAP campaign. Figures indicate the fetch in kilometers. Taken from *Hasselmann et al. (1973)*.

As expected, the wave spectrum energy increases and the peak frequency decreases with fetch. Also, for a given frequency, we observe that energy rapidly increases and reaches a maximum when it equals the peak frequency and then slowly decreases as the peak frequency keeps decreasing with fetch. The fact that the energy level at peak frequency is higher than the one given at the same frequency for a spectrum obtained for a longer fetch is called the *overshoot* (*Barnett and Sutherland, 1968*). This pattern is absent from previously proposed spectra of fully-developed wind-seas (*Pierson and Moskowitz, 1964*). *Donelan et al. (1985)* have carried out other fetch limited experiments on Lake Ontario. The parameterization of the sea surface spectrum energy they proposed reconciles the previous parameterizations made by *Pierson and Moskowitz (1964)* and *Hasselmann et al. (1973)* by representing the fetch-limited wind-sea spectrum as that of a fully-developed wind-sea spectrum modulated by a peak enhancement factor that reproduces the overshoot signal:

$$E(f) = \alpha g^2 f^{-4} f_p^{-1} \exp \left[ - \left( \frac{f}{f_p} \right)^{-4} \right] \gamma^\Gamma \quad (2.12a)$$

with,

$$\Gamma = \exp - \frac{(f - f_p)^2}{2\omega^2 f_p^2} \quad (2.12b)$$

where,  $f$  is the frequency;  
 $f_p$ , the peak frequency;  
 $\gamma$ , the peak enhancement factor;  
 $\omega$ , the peak width parameter;  
 $g$ , the Earth gravity;  
 $\alpha$ , the equilibrium range parameter.

The equilibrium range is sometimes also called the *rear face* of the spectrum and refers to the range of frequencies greater than the peak frequency. Within this range, the spectrum energy decrease proportionally to  $f^{-4}$ <sup>1</sup> Let  $\theta$  be the angle between the wind and the wave directions and  $C_p$ , the peak frequency phase velocity. Then, the aforementioned values are empirically determined and given below for values of  $U_{10} \cos \theta / C_p$  ranging from 0.83 to 5:

$$\alpha = 0.006(U_{10} \cos \theta / C_p)^{0.55} \quad (2.13a)$$

$$\omega = 0.08 \left[ 1 + \frac{4}{(U_{10} \cos \theta / C_p)^3} \right] \quad (2.13b)$$

$$\gamma = \begin{cases} 1.7, & \text{if } 0.83 < U_{10} \cos \theta / C_p < 1 \\ 1.7 + 6.0 \log(U_{10} \cos \theta / C_p), & \text{if } 1 \leq U_{10} \cos \theta / C_p < 5 \end{cases} \quad (2.13c)$$

More recently, the evolution of the peak frequency and wind-sea energy with respect to the fetch have been measured during the SHOWEX campaign that took place in North Carolina in 1999. To compare the evolution of the peak parameters they obtained to that given by other fetch-limited experiments, like JONSWAP, dimensionless parameters first proposed by *Sverdrup and Munk (1947)* are introduced. It applies to the total wind-sea energy  $E$ , the wave peak frequency  $f_p$ , the fetch  $X$ , the time for which the wind has blown  $t$ , and the 10 m-high wind speed<sup>2</sup>  $U_{10}$ :

$$X^* = \frac{gX}{U_{10}^2} \quad (2.14a)$$

$$t^* = \frac{gt}{U_{10}} \quad (2.14b)$$

$$f_p^* = \frac{U_{10}}{gT_p} \quad (2.14c)$$

---

1. This decrease was also studied by *Long and Resio (2007)* by analyzing the Currituck Sound data and found both a decrease proportionally to  $f^{-4}$  and  $f^{-5}$  depending on the frequency range in the spectrum.

2. Choosing to quantify the wind forcing with  $U_{10}$  may be criticized since the friction velocity,  $U_*$ , is expected to be more relevant. However, many more observations rather provide  $U_{10}$ .

$$E^* = \frac{g^2 E}{U_{10}^4} \quad (2.14d)$$

with,

$$E = H_s^2/16 \quad (2.14e)$$

where  $g$  is the Earth gravity and  $E$ , the wave energy.

The SHOWEX observations are shown on Figure 2.3 together with other empirical laws, given by previous datasets. They indicate that the wind-sea

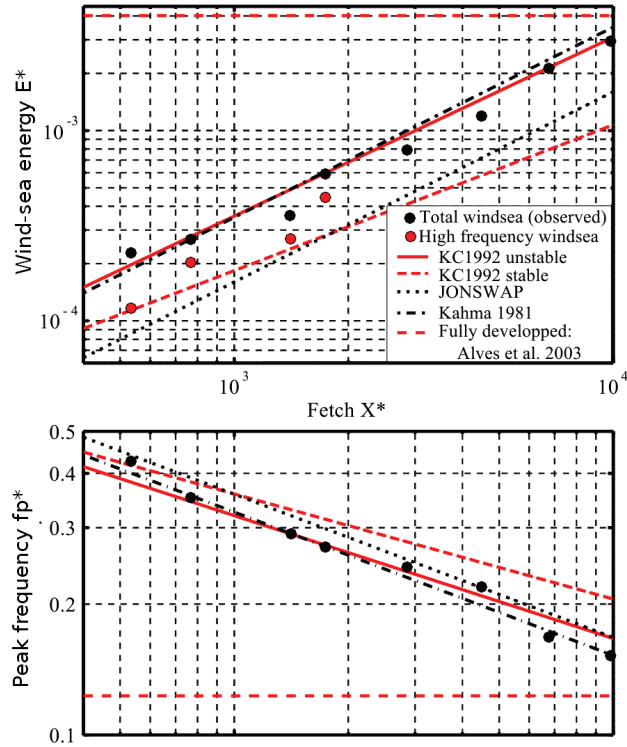


Figure 2.3: Wind-wave growth measurements with fetch from the SHOWEX campaign. The wind was not completely perpendicular to the coastline but made a  $20^\circ$  angle with respect to this direction, thereby producing a double-peak wind-sea for short fetches. Therefore, close to the coast, a high frequency part of the wind-sea, in the wind direction (red disks), can be separated from the overall wind-sea (black disks). Other empirical laws are given by *Kahma and Calcoen* (1992), the JONSWAP campaign, *Kahma* (1981) and the fully-developed wind-sea given by *Alves et al.* (2003). Taken from *Ardhuin* (2011).

total energy continuously increases and the peak frequency decreases with fetch. However, for very large values of  $X^*$ , they tend towards asymptotic

values. In practice, it is very difficult to obtain steady wind conditions over sufficiently great distances. Still, with careful data selection subsequently validated by *Alves et al.* (2003), *Pierson and Moskowitz* (1964) gave estimates of these asymptotic values:  $E^* = 0.00402$  and  $f_p^* = 0.123$ .

Many growth curve observations exist in the bibliography and only a few of them are presented here. For further details, more references can be found in *Holthuijsen* (1980).

### 2.2.2 Wave age and wave growth laws

Another and more convenient way to describe the wave development is the wave age, equal to  $C_p/U_{10}$ . As the peak frequency decreases with the fetch, so does the peak frequency phase velocity,  $C_p$ , which is equal to  $g/(2\pi f_p)$  in deep water. Thanks to this parameter, young wind-seas, with little wave age, that are still actively wind-generated can be separated from old wind-seas, whose wave age approaches 1.2 and on which the wind has almost no effect anymore. Analyses from *Pierson and Moskowitz* (1964) and *Donelan et al.* (1992) indicate that wave growth stops when  $C_p/U_{10} > 1.2$ . At this point, individual waves travel faster than the wind. Figure 2.4 gives an example of sea surface spectrum measured by an *in situ* buoy showing swells as well as young and old wind-seas.

The spectrum contains several wave systems: two swells coming from North and South-West directions with peak wavelength of 366 and 370 m, respectively, and an old and young wind-sea coming from South and South-South-East directions with peak wavelength of 151 and 77 m, respectively. At the same time, the wind is blowing from that very last direction at a speed ranging between 5 and 8 m.s<sup>-1</sup> as indicated by QuikScat measurements (wind speed buoy measurements were not available for that time). The larger directional spreading and the larger frequency width of the wind-sea spectral peak compared to that of the swells results from the shorter distance to the storm source and the longer propagation time.

Given the wind speed and the fetch over which the wind has blown, wave energy and peak frequency can be approximately estimated as follows:

$$C_p/U_{10} \simeq 1.2 \left( \min \left\{ \frac{X^*}{X_0^*}, 1 \right\} \right)^{0.33} \quad (2.15a)$$

$$H_s \simeq 0.26 \frac{U_{10}^2}{g} \left( \min \left\{ \frac{X^*}{X_0^*}, 1 \right\} \right)^{0.5} \quad (2.15b)$$

where  $X_0^* = 2.2 \times 10^4$ .

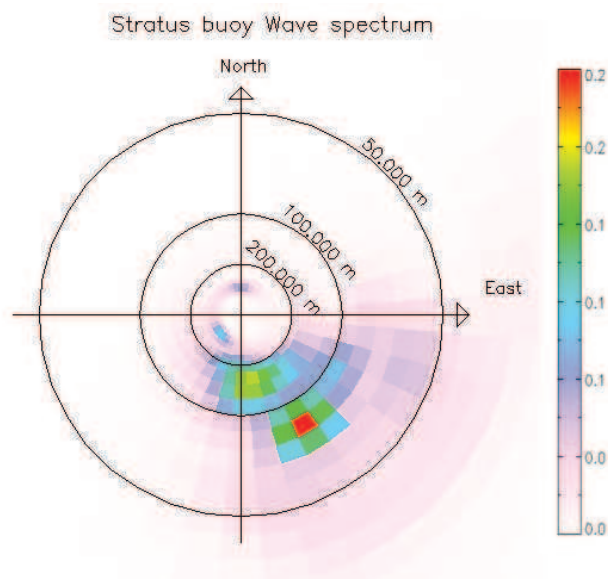


Figure 2.4: Sea surface spectrum measured by the buoy 'Stratus' (WMO 32012) operated by Woods Hole Oceanographic Institution (WHOI) and moored 1500 km off the coast of Chile, at  $-19.7^{\circ}\text{N}$ ,  $-85.5^{\circ}\text{E}$  on 6 January 2008 at 15Z.

Slightly different relations have been published and the coefficients may significantly vary from one to another (*Kahma and Calhoun, 1992*). These differences are attributed to variations of the boundary layer stability and/or to the simplified hypothesis of uniform and constant wind, whose direction is supposed perpendicular to a straight coastline but which is never completely fulfilled.

So far, only fetch limitation has been discussed but the wind-wave growth may also be limited by the time for which the wind has blown. If  $t^* < 10^5$ , then wave age and height can be approximated by replacing  $X^*$  by  $X' = (t^*/70)^{1.3}$ . Because wind-sea development can be limited by both time and fetch, one should estimate the wave age and height given by both approaches and choose the limitation giving the smaller values of peak frequency and significant swell height.

### 2.2.3 Non-linear wave-wave interactions

Ocean waves are not exactly linear. Non linear terms that were first neglected in Airy theory can indeed explain important energy transfers between the different components of the wave spectrum by wave-wave interactions (*Phillips, 1960; Hasselmann, 1961; Longuet-Higgins and Phillips, 1962;*

*Hasselmann, 1963, 1966; Zakharov, 1968*). In deep water, only interactions to the fourth order are significant. Furthermore, significant energy transfers require that the time and distance over which waves interact are large compared to the wave periods and wavelengths. These interactions between four waves are considered to be the dominant phenomenon in shifting energy to longer waves.

## 2.3 Swell propagation in deep ocean

In this section, the ability of swell systems to propagate over several thousand kilometers is exposed successively discussing the typical spectral time series signature of a swell system at a given location.

### 2.3.1 Storm sources

Using the swell dispersion properties evidenced in Section 2.1 (equations 2.6 and 2.7), arrival times records at a fixed location of the various frequency components belonging to the same swell field can indicate the distance  $D$ , separating the storm source from the observation point:

$$D = \frac{g}{4\pi} \left( \frac{\Delta f_p}{\Delta t} \right)^{-1} \quad (2.16)$$

where,  $g$  is the Earth gravity;  
 $\Delta f_p$ , the recorded peak frequency difference during the time interval  $\Delta t$ .

A typical example of sea surface spectrum evolution with a swell arrival is given on Figure 2.5.

This approach assumes a point source, that is, a small storm angular aperture as seen from the observation point, and a short storm event lifetime compared to the swell observation period. However, this may not be valid whenever close to the storm source. In such cases, *Gjevik et al. (1988)* have shown that, for a given swell field, the lowest and highest frequency measurements of the swell spectrum at a fixed location could be used to determine the storm source lifetime.

Thanks to swell dispersion and using pressure recorders placed on the sea bed, early swell observations made by *Barber and Ursell (1948)* and *Munk and Snodgrass (1957)* indicated the measured swell had been generated, in angular distance, about  $100^\circ$  and  $130^\circ$  away from the recording location, respectively. Similarly, *Munk et al. (1963)* even recorded a swell whose generation region turned out to be antipodal. Clearly, these observations indicate that swell energy can decay very slowly with propagation.

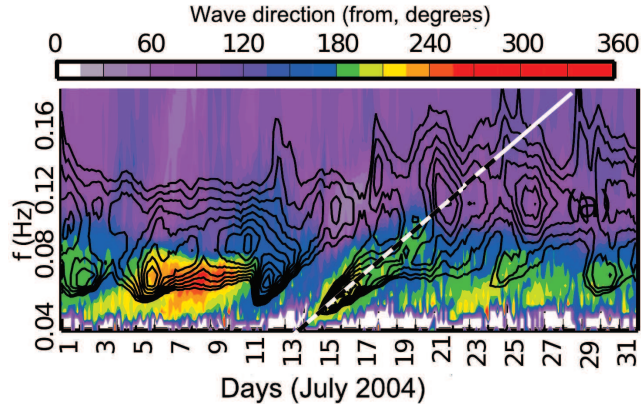


Figure 2.5: Energy and mean direction spectrum measured *in situ* by the Christmas Island buoy (World Meteorological Organization (WMO) number 51028). Contours, equally spaced from 0.1 to 1.4, indicate the natural logarithm of the spectral energy density. Colors indicate the mean arrival direction at each frequency. Main swell signal is highlighted by black and white dashed line. Taken from *Collard et al. (2009)*.

The great space and time consistency of a swell system give the possibility to observe this very same phenomenon over large time periods and/or distances.

### 2.3.2 Swell energy decay

As already mentioned, outside of island shadows and in the absence of currents, swell propagates at group velocity and along geodesics in deep water. But one can wonder how its energy varies.

Considering a dissipation-free propagation, and in the absence of currents, continents and islands, the only phenomena modifying the swell energy are angular spreading, acting in transverse direction, and frequency dispersion, acting in radial direction. *Collard et al. (2009)* have demonstrated that far enough from the storm source and given the significant swell height at an angular great-circle distance  $\alpha_0$  from the storm source, its value could be estimated at any other position,  $\alpha$ , as follows:

$$H_s^{\text{free}}(\alpha) = H_s(\alpha_0) \sqrt{\frac{\alpha_0 \sin(\alpha_0)}{\alpha \sin(\alpha)}} \quad (2.17)$$

This behavior corresponds to an asymptotic trend and it may not be well reproduced whenever too close from the storm source. In practice, for a 1,000 km-wide storm region, the threshold distance from the source for

which this energy decay model is judged valid is 4,000 km. However, this limit is expected to vary depending on the storm region extension.

### 2.3.3 Energy dissipation

In the previous description of the swell energy decay, the propagation is assumed to be dissipation-free. However, experiments indicate that swell energy can indeed dissipate during propagation. Following 13 s period swell at different locations along the swell field path, *Snodgrass et al. (1966)* measured an e-folding scale  $L_e$ , of 5,000 km meaning that the swell energy is divided by  $e = 2.718\dots$  every 5,000 km. For larger periods, *Snodgrass et al. (1966)* could only conclude that  $L_e$  was larger, possibly infinite.

First, swell propagation is limited by air viscosity. A theoretical upper bound of  $L_e$  is given by *Dore (1978)*:

$$L_{e,\max} = \frac{\rho_w g^2}{4\rho_a \omega^3 \sqrt{2\nu_a \omega}} \quad (2.18)$$

where,  $\rho_w$  and  $\rho_a$  are the water and air density, respectively;  $\nu_a$ , the air viscosity.

For a peak period of 13 s,  $L_{e,\max} = 45,000$  km which means that over a realistic propagation distance of 10,000 km, which corresponds to an angular distance of  $90^\circ$ , the energy of 13 s swells is only reduced by 25%.

Following the propagation of a fixed period swell with measurements given by the SAR wave mode of ENVISAT more than 4,000 km away from the storm source, *Collard et al. (2009)* have measured the deviation of the swell energy with respect to the expected energy decay described by equation 2.18. These deviations are attributed to a dissipation of the swell energy,  $E_s$ , at a rate  $\mu$  defined by:

$$\mu = -\frac{1}{R} \frac{(dE_s \alpha \sin \alpha) / d\alpha}{E_s \alpha \sin \alpha} \quad (2.19a)$$

then,

$$L_e = \frac{1}{\mu} \quad (2.19b)$$

and,

$$\begin{aligned} H_s(\alpha) &= H_s^{\text{free}}(\alpha) \exp\left(-\mu \frac{\alpha - \alpha_0}{2}\right) \\ &= H_s(\alpha_0) \sqrt{\frac{\alpha_0 \sin(\alpha_0)}{\alpha \sin(\alpha)}} \exp\left(-\mu \frac{\alpha - \alpha_0}{2}\right) \end{aligned} \quad (2.19c)$$

where  $R$  is the Earth radius.

Using SAR wave mode, observations of the swell field generated by a storm occurring on 12 February 2007 in the North Pacific Ocean were gathered. Significant swell height measurements of the same peak period swell along its propagation path are shown on Figure 2.6. The dissipation rate that best reproduces the energy decay can be estimated, as well as the extrapolated significant swell height at 4,000 km. For the associated dissipation rate, *Collard et al. (2009)* found  $3.1 \times 10^{-7} < \mu < 4.0 \times 10^{-7} \text{ m}^{-1}$  for a 68% confidence level. These values of  $\mu$  are more than twice larger than those reported by *Snodgrass et al. (1966)* for smaller amplitude swells. Using the same approach over 22 storm events, *Ardhuin et al. (2009)* found that  $\mu$  increases with respect to wave steepness, as shown on Figure 2.7.

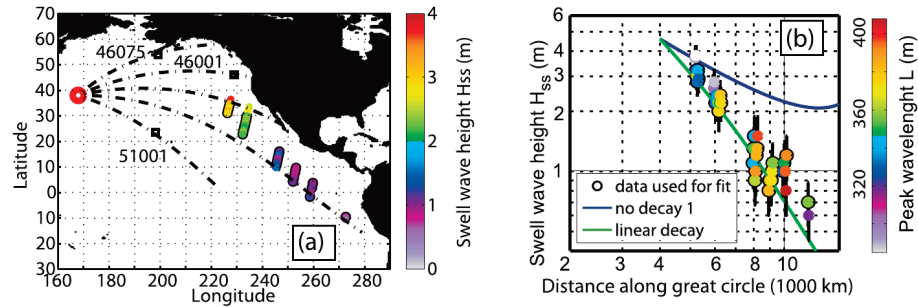


Figure 2.6: (a) Location of SAR observations with a 15 s peak period swell system corresponding to a storm occurring on 12 February 2007, with outgoing directions of 74 to 90°. The same swell was also observed at all buoys from 46075 off western Alaska to 51001 in Hawaii. The dash-dotted line represents great circles leaving the storm source with directions 42, 59, 74, 90 and 106°. (b) Observed swell wave height as a function of distance to storm source. The solid lines represent theoretical decays using no dissipation (blue) or the fitted linear dissipation (green) for swells observation of the swell field presented in (a). Outlined dots are the observations used in the fitting procedure. Error bars show one standard deviation of the expected error on each SAR measurement. Taken from *Collard et al. (2009)*.

There is no consensus on the plausible causes of the loss of swell energy (*WISE Group, 2007*). Observations suggest that some swell momentum is lost to the atmosphere (*Grachev and Fairall, 2001*) because of the reversal of the wind stress induced by swell motion relatively to the atmospheric boundary layer. The energy loss increase with wave steepness may be explained by a transition from a laminar to a turbulent flow of the air-side boundary layer (*Ardhuin et al., 2009*).

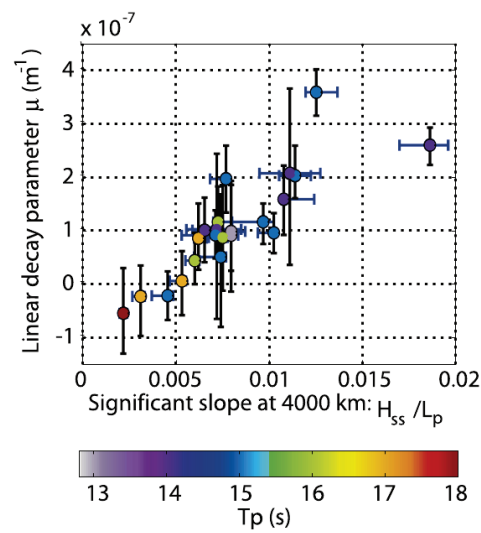


Figure 2.7: Using 22 swell events, estimated linear dissipation rate as a function of the initial significant slope, ratio of the significant swell height and peak wavelength,  $H_s/\lambda$ , taken 4,000 km from the storm center, for a variety of peak swell periods (colors). Negative values of  $\mu$  would correspond to a gain of energy. Instead, they are attributed to estimation errors due to storm shapes different from those assumed by *Collard et al.* (2009). Taken from *Ardhuin et al.* (2009).

## 2.4 Conclusion

Using Airy theory, we have shown that in the absence of currents and in deep water, gravity waves propagate following geodesics on a globe. Along their path, individual waves propagate at phase velocity which is proportional to Earth gravity and wave period, whereas wave energy is shown to propagate at group velocity, twice smaller than that of individual waves. As confirmed by early observations, this theory particularly well explains the dispersive propagation of ocean swell systems away from their storm source region.

Then, we have exposed wind-wave growth observations during fetch-limited experiments. For a given fetch, the wave spectrum energy is maximum at peak frequency and diminishes slowly when moving toward higher frequencies and rapidly toward smaller frequencies. Under the influence of non-linear wave-wave interactions and with increasing fetch, some energy is transferred toward higher and smaller frequencies. As the wind keeps on blowing and with increasing fetch, the peak period and associated energy increase as well. Parameterizations reproducing the overall shape of the 1D wave spectrum as proposed by *Long and Resio (2007)* assume the slow energy decay for frequencies higher than the peak frequency to be proportional to  $f^{-4}$ . Further, we have defined the wave age and shown that it constitutes an interesting parameter for the characterization of the waves' development stage with respect to the wind conditions. In particular, wind wave growth seems to vanish as wave age approaches 1.2 and the wave spectrum reaches an asymptotic peak period and energy that can be determined using the dimensionless approach proposed by *Sverdrup and Munk (1947)*.

Once waves have outrun their generation area, they propagate freely and are referred to as swell. Assuming a point source, their energy decay is governed by angular spreading and frequency dispersion. Far enough from their generation region, the swell energy varies proportionally to  $1/(\alpha \sin \alpha)$ , where  $\alpha$  is the spherical distance from the storm source. On top of this, SAR wave mode measurements have revealed the energy dissipation of certain swell fields with respect to this expected energy decay. The dissipation importance from one swell field to another seems to be directly related to the swell steepness which could be explained by a loss of swell momentum to the atmosphere.

The present chapter has presented the expected behavior of swell fields along their propagation assuming absence of currents, deep ocean propa-

---

gation and point source were made. Hence, for a given storm source and direction of swell propagation, it is not possible to describe swell main characteristics in island shadows even though swell may still be present in these regions because of swell refraction and/or diffraction. Additionally, the point source assumption may be quite far from reality. Indeed, long-lived and/or large extended storms are regularly observed at high latitudes in the Southern Hemisphere. Therefore, the energy decay model we use, for 1,000 km wide storm regions, may probably not be valid anymore and will need to be adapted to these particular cases. The dependency of the swell energy decay with respect to the size of the associated storm region could be studied using the 15 year-long SAR wave mode data archive we dispose of thanks to ENVISAT and ERS-2 missions and the methodology developed in Chapter 5.

## Bibliography

- Alves, J. H. G. M., M. L. Banner, and I. R. Young (2003), Revisiting the Pierson-Moskowitz asymptotic limits for fully developed wind waves, *Journal of physical oceanography*, *33*(7), 1301–1323. 64, 65
- Ardhuin, F. (2011), *Etats de mer : hydrodynamique et applications*. 64
- Ardhuin, F., B. Chapron, and F. Collard (2009), Observation of swell dissipation across oceans, *Geophys. Res. Lett.*, *36*, L06,607, doi:10.1029/2008GL037030. ii, 2, 70, 71, 152, 181, 237
- Barber, N. F., and F. Ursell (1948), The generation and propagation of ocean waves and swell. I wave periods and velocities, *Phil. Trans. Roy. Soc. London A*, *240*, 527–560. iv, 56, 67
- Barnett, T. P., and A. J. Sutherland (1968), A note on an overshoot effect in wind-generated waves, *J. Geophys. Res.*, *73*(22), 6879–6885. 62
- Belcher, S. E., and J. C. R. Hunt (1993), Turbulent shear flow over slowly moving waves, *J. Fluid Mech.*, *251*, 109–148. 61
- Borge, J. C. N., S. Lehner, A. Niedermeier, and J. Shulz-Stellenfleth (2004), Detection of ocean wave groupiness from spaceborne synthetic aperture radar, *J. Geophys. Res.*, *109*, C07,005, doi:10.1029/2004JC00298. 59
- Collard, F., F. Ardhuin, and B. Chapron (2009), Monitoring and analysis of ocean swell fields from space: New methods for routine observations, *Journal of Geophysical Research-Oceans*, *114*(C7), C07,023. ii, 2, 68, 69, 70, 71, 80, 85, 111, 152, 153, 155, 219, 239
- Dankert, H., J. Horstmann, S. Lehner, and W. Rosenthal (2003), Detection of wave groups in SAR images and radar-image sequences, *IEEE Trans. on Geosci. and Remote Sensing*, *41*(6), 1437–1441. 59
- Darbyshire, J. (1952), The generation of waves by wind, *Proceedings of the Royal Society of London. Series A, Mathematical and Physical Sciences*, p. 299–328. 2, 61, 237
- Donelan, M., M. Skafel, H. Graber, P. Liu, D. Schwab, and S. Venkatesh (1992), On the growth rate of wind-generated waves, *Atmosphere-Ocean*, *30*(3), 457–478. 65
- Donelan, M. A., J. Hamilton, and W. H. Hui (1985), Directional spectra of wind-generated waves, *Phil. Trans. Roy. Soc. London A*, *315*, 509–562. 62
- Dore, B. D. (1978), Some effects of the air-water interface on gravity waves, *Geophys. Astrophys. Fluid. Dyn.*, *10*, 215–230. 69

- Gain, L. (1918), La prédiction des houles au Maroc, *Annales Hydrographiques*, pp. 65–75. 2, 56, 61, 237
- Gelci, R., H. Cazalé, and J. Vassal (1957), Prévission de la houle. La méthode des densités spectroangulaires, *Bulletin d'information du Comité d'Océanographie et d'Etude des Côtes*, 9, 416–435. 61
- Gjevik, B., O. Rygg, H. E. Krogstad, and A. Lygre (1988), long period swell wave events on the Norwegian shelf, *Journal of Physical Oceanography*, 18(5), 724–737. 67
- Grachev, A. A., and C. W. Fairall (2001), Upward momentum transfer in the marine boundary layer, *J. Phys. Oceanogr.*, 31, 1698–1711. 70
- WISE Group (2007), Wave modelling - the state of the art, *Progress in Oceanography*, 75, 603–674, doi:10.1016/j.pocean.2007.05.005. 70
- Hasselmann, K. (1961), On the Non-Linear Energy Transfer in a Wave Spectrum, in *Ocean Wave Spectra*, p. 191–197, Prentice-Hall, Englewood Cliffs, N.J. 66
- Hasselmann, K. (1963), On the non-linear energy transfer in a gravity wave spectrum part 2. conservation theorems; wave-particle analogy; irrevesibility, *Journal of Fluid Mechanics*, 15(02), 273–281. 67
- Hasselmann, K. (1966), Feynman diagrams and interaction rules of wave-wave scattering processes, *Rev. of Geophys.*, 4(1), 1–32. 67
- Hasselmann, K., T. P. Barnett, E. Bouws, H. Carlson, D. E. Cartwright, K. Enke, J. A. Ewing, H. Gienapp, D. E. Hasselmann, P. Kruseman, A. Meerburg, P. Müller, D. J. Olbers, K. Richter, W. Sell, and H. Walden (1973), Measurements of wind-wave growth and swell decay during the Joint North Sea Wave Project, *Deut. Hydrogr. Z.*, 8(12), 1–95, suppl. A. 62
- Hoffman, D., and O. J. Karst (1975), The theory of the Rayleigh distribution and some of its applications, *Journal of Ship Research*, 19(3). 60
- Holthuijsen, L. H. (1980), *Methoden voor golfvoorspelling*, Technische adviescommissie voor de waterkeringen. 65
- Jeffreys, H. (1925), On the formation of water waves by wind, *Proc. Roy. Soc. Lond. A*, 107, 189–206. 61
- Kahma, K. K. (1981), A study of the growth of the wave spectrum with fetch, *J. Phys. Oceanogr.*, 11, 1503–1515. 64

- Kahma, K. K., and C. J. Calkoen (1992), Reconciling discrepancies in the observed growth of wind-generated waves, *J. Phys. Oceanogr.*, *22*, 1389–1405. 64, 66
- Lamb, H. (1932), *Hydrodynamics*, 6th ed., Cambridge University Press, Cambridge, England. 56
- Long, C., and D. Resio (2007), Wind wave spectral observations in Currituck Sound, North Carolina, *J. Geophys. Res.*, *112*, C05,001. 63, 72
- Longuet-Higgins, M. S., and O. M. Phillips (1962), Phase velocity effects in tertiary wave interactions, *J. Fluid Mech.*, *12*, 333–336. 66
- Amiralty Navigation (1939), *Admiralty navigation manual, 1938*, vol. 1, His Majesty's Stationery Office. 58
- Miles, J. W. (1957), On the generation of surface waves by shear flows, *J. Fluid Mech.*, *3*(Pt 2), 185–204. 61
- Munk, W., and F. Snodgrass (1957), Measurements of southern swell at Guadalupe Island, *Deep Sea Research (1953)*, *4*, 272, IN1–IN2, 273–286, doi:10.1016/0146-6313(56)90061-2. iv, 56, 67
- Munk, W. H. (1944), Proposed uniform procedure for observing waves and interpreting instrument records, *Scripts Institute of Oceanography Wave Report*, *26*. 60
- Munk, W. H., G. R. Miller, F. E. Snodgrass, and N. F. Barber (1963), Directional recording of swell from distant storms, *Philosophical Transactions of the Royal Society of London. Series A, Mathematical and Physical Sciences*, *255*(1062), 505–584. iv, 2, 56, 67, 237
- Phillips, O. M. (1957), On the generation of waves by turbulent wind, *J. Fluid Mech.*, *2*(5), 417–445. 61
- Phillips, O. M. (1960), On the Dynamics of Unsteady Gravity Waves of Finite Amplitude Part 1. The Elementary Interactions, *Journal of Fluid Mechanics*, *9*(02), 193–217, doi:10.1017/S0022112060001043. 66
- Pierson, W. J., Jr, and L. Moskowitz (1964), A proposed spectral form for fully developed wind seas based on the similarity theory of S. A. Kitaigorodskii, *J. Geophys. Res.*, *69*(24), 5,181–5,190. 62, 65
- Snodgrass, F. E., G. W. Groves, K. F. Hasselmann, G. R. Miller, W. H. Munk, and W. H. Powers (1966), Propagation of ocean swell across the Pacific, *Philosophical Transactions of the Royal Society of London. Series A, Mathematical and Physical Sciences*, *259*(1103), 431. iv, 2, 56, 69, 70, 152, 168, 192

---

Sverdrup, H. U., and W. H. Munk (1947), Wind, sea and swell: theory of relations for forecasting, *Contributions-Scripps Institution of Oceanography*, 61, 63, 72

West, B. J. (1982), Statistical properties of water waves. Part 1. Steady-state distribution of wind-driven gravity-capillary waves, *J. Fluid Mech.*, 117, 187–210. 61

Zakharov, V. E. (1968), Stability of periodic waves of finite amplitude on the surface of a deep fluid, *J. Appl. Mech. Tech. Phys.*, 2, 190–194. 67



# Chapter 3

## Validation of SAR swell measurements

### Contents

---

3.1	Buoy dataset . . . . .	<b>80</b>
3.1.1	Wave measurements . . . . .	80
3.1.2	Buoy networks . . . . .	82
3.2	SAR dataset . . . . .	<b>83</b>
3.2.1	Data quality . . . . .	83
3.2.2	Data Correction . . . . .	85
3.3	Methodology . . . . .	<b>86</b>
3.3.1	Spectral partitioning . . . . .	86
3.3.2	Integral parameter estimation . . . . .	89
3.3.3	Peak-to-peak association . . . . .	90
3.3.4	Graphical summary . . . . .	91
3.4	Statistical results . . . . .	<b>91</b>
3.4.1	Matchup criteria . . . . .	91
3.4.2	Matchup dataset . . . . .	93
3.4.3	Main statistics . . . . .	95
3.4.4	Dependences . . . . .	96
3.5	Conclusion . . . . .	<b>111</b>
	Bibliography . . . . .	<b>116</b>

---

Using the SAR-ocean wave inversion presented in Chapter 1, swell spectra can be estimated from the SAR images. The goal of this chapter is to assess the accuracy of the SAR estimated swell integral parameters, namely significant swell height, peak propagation direction and peak period, before using them for further analysis in Chapters 5 and 6. Even though previous studies by *Johnsen and Collard (2004)* and *Collard et al. (2009)* have already published these parameters estimation accuracy, we propose a more detailed error characterization and a quite different comparison method that can also be used to further validate the synthetic swell field concept exposed in Chapter 6. This way, we dispose of an homogeneous comparison methodology to estimate the statistical improvements brought by the new concept developed in that forthcoming chapter with respect to the performances of the SAR swell measurements hereafter presented.

First, the *in situ* dataset used for the validation of SAR swell measurements is presented. Second, we describe the methodology adopted for comparing directional spectra given by SAR and buoys. Third, measurement statistics are discussed and main sources of error highlighted.

## 3.1 Buoy dataset

### 3.1.1 Wave measurements

#### 3.1.1.1 Using moored buoys

Today, many instruments can be used for measuring ocean waves. Early wave heights records were done by human observers (*Navy, 1981*) but nowadays, accelerometers placed on moored buoys are the most common technology. The vertical displacement is given by the vertical acceleration double integration. For large buoys, such as the NDBC discus buoys<sup>1</sup> with additional measurements of buoy pitch and roll, east-west slope and north-south slope can be computed, allowing for wave direction estimation. These are called *heave/pitch/roll* buoys. For smaller buoys, like the Datawell Directional Waverider, this information is retrieved from the buoy precise position (using GPS or Galileo), which gives the horizontal acceleration. In addition to this, the buoy azimuth given by a compass indicates the buoy orientation with respect to the magnetic North. Then, with the magnetic declination, direction estimates with respect to true North are available. Buoy measurement main limitations come from the fact that wavelengths smaller than the buoy's diameter cannot be sensed but in our case, this is not an issue since we consider much longer waves.

---

1. Steel circular hulled buoys whose diameter comes in three sizes: 12, 10 and 3 m.

Looking at swells whose frequency ranges between 0.06 and 0.14 Hz, measurements comparison between NDBC 3-m discus buoys and Datawell Directional Waverider buoys indicates good estimates of the wave energy and directional parameters for a wide range of wave conditions *O'Reilly et al.* (1996). Though, compared to the NDBC buoys, directional spread and skewness are significantly better estimated by the Datawell buoys.

### 3.1.1.2 Data archival

Once the directional wave spectrum has been measured, the information it contains is generally summarized for archival reasons by the first Fourier coefficients and their associated energy, given for each frequency bin. Some instruments are able to provide valuable information to high order coefficients but for heave/pitch/roll buoys, the first four Fourier coefficients only are archived:  $a_1$ ,  $a_2$ ,  $b_1$  and  $b_2$ , thus providing potentially information on the two most energetic wave systems for each frequency bin. They are also called *angular moments* and obtained from the measured directional spectrum  $S(f, \theta)$ , using the following formula:

$$a_1(f) = \frac{\int_0^{2\pi} S(f, \theta) \cos \theta d\theta}{\int_0^{2\pi} S(f, \theta) d\theta} \quad (3.1a)$$

$$b_1(f) = \frac{\int_0^{2\pi} S(f, \theta) \sin \theta d\theta}{\int_0^{2\pi} S(f, \theta) d\theta} \quad (3.1b)$$

$$a_2(f) = \frac{\int_0^{2\pi} S(f, \theta) \cos 2\theta d\theta}{\int_0^{2\pi} S(f, \theta) d\theta} \quad (3.1c)$$

$$b_2(f) = \frac{\int_0^{2\pi} S(f, \theta) \sin 2\theta d\theta}{\int_0^{2\pi} S(f, \theta) d\theta} \quad (3.1d)$$

where,  $f$  is the frequency;  
 $\theta$ , the direction.

In a different way, the NDBC data are archived using the mean and principal wave directions,  $\alpha_1$  and  $\alpha_2$  and the first and second normalized polar coordinates,  $r_1$  and  $r_2$ , of the Fourier coefficients. They are related with the angular moments by:

$$a_1(f) = r_1(f) \cos \alpha_1(f) \quad (3.2a)$$

$$b_1(f) = r_1(f) \sin \alpha_1(f) \quad (3.2b)$$

$$a_2(f) = r_2(f) \cos 2\alpha_2(f) \quad (3.2c)$$

$$b_2(f) = r_2(f) \sin 2\alpha_2(f) \quad (3.2d)$$

### 3.1.1.3 Spectrum reconstruction

Then, the directional wave spectra can be then recovered from the Fourier coefficients,  $a_1$ ,  $a_2$ ,  $b_1$  and  $b_2$ , and their associated energy,  $E(f)$ , expressed in  $[\text{m}^2\text{Hz}^{-1}]$  using the Maximum Entropy Method (MEM) developed by *Lygre and Krogstad (1986)*. Compared to other estimation methods such as the Maximum Likelihood Method (MLM) developed by *Borgman (1982)*, the MEM algorithm has the advantage of conserving the Fourier coefficients given in inputs. Though, for noisy measurements, the MEM algorithm may unnaturally split energy peaks (*Benoit et al., 1997*). Post-processing techniques like spectral peaks merging or smoothing spectra may correct for it as further described (cf. Subsection 3.3.1, page 86). Up to now, the MEM algorithm is admitted to be the most accurate reconstruction method of directional spectra. Even though we are going to use the same notation,  $S(f, \theta)$ , for the reconstructed spectrum and the one originally measured by the instrument, they are not rigorously the same. This partly comes from the reconstruction algorithm and also from the fact that the instrument is only able to measure the first two angular moments. Therefore, for complex sea state situations where more than two swell systems are present, the associated reconstructed spectrum may not properly render each swell partition.

The total significant wave height is directly calculated from the buoy spectral energy as:

$$H_{\text{stot}} = 4 \left( \int E(f) df \right)^{1/2} \quad (3.3)$$

If one is interested in the significant wave height of a particular region of the spectrum,  $R_{f,\theta}$ , it can be calculated as follows:

$$H_{\text{spart}} = 4 \left( \iint_{R_{f,\theta}} S(f, \theta) df d\theta \right)^{1/2} \quad (3.4)$$

### 3.1.2 Buoy networks

For this validation, we can rely on several quality-controlled buoy networks, among which:

- NODC: the National Oceanographic Data Center, which is responsible for the National Data Buoy Center (NDBC) buoy network archival, whose buoys are located in the Atlantic and Pacific Ocean;
- CDIP: the Coastal Data Information Program, which mainly concerns coastal buoys around North America and Pacific Islands;
- UKMO: the United Kingdom Meteorological Office, whose observational buoys are located in the eastern North Atlantic Ocean;

- OPPE: the Spanish acronym for the National Harbor Organization, whose buoys are located in the vicinity of Spanish coasts.

There are known differences between measurements from different buoy networks (*Cotton, 1998; Durrant et al., 2009*). For instance, comparisons with altimetric data indicate that UKMO over-estimates the significant wave height compared to the NDBC data by 4% to 6%. These differences can difficultly be ascribed to a particular cause which could be environmental, a function of the buoy platform, or of the instrument calibration. More precisely, focusing on the NDBC discus buoys, *Cotton (1998)* proved that this variability was independent from the buoy size. The NDBC accuracy requirements are given below:

Significant wave height	0.2 m or $\pm 10\%$
Peak period	$\pm 1$ s
Energy-weighted wave direction	$\pm 10^\circ$

Table 3.1: NDBC accuracy requirements for NDBC discus buoys.

For every single buoy, directional spectral measurements are given every hour, after a 20 minute-long record.

## 3.2 SAR dataset

### 3.2.1 Data quality

The SAR dataset is composed of the SAR Level-2 wave mode products, here denoted SAR L2 products. They are obtained thanks to the ocean spectra retrieval scheme presented in Chapter 1. They are processed and archived at the Center for Satellite Exploitation and Research (CERSAT), located at IFREMER in Brest, using the processing scheme described by *Johnsen and Collard (2004)*. These products contain an estimation of SAR ocean wave directional spectra with  $10^\circ$  resolution in directions and a discretization over 24 exponentially spaced wavenumbers ranging from 30 to 800 meters.

Each spectrum comes with a quality flag, based on the propagation direction ambiguity<sup>2</sup>, the normalized variance and the value of the swell azimuth wavenumber with respect to the azimuth cut-off. The quality flag indicates how reliable the wave spectrum is:

- 0 - probably good spectrum: there is no propagation direction ambiguity, the image normalized variance is smaller than 1.5 and the

---

2. Its estimation is detailed in Chapter 1, page 45.

- swell azimuth wavenumber is smaller than 75% of the azimuth cut-off wavenumber;
- 1 - probably good spectrum but  $180^\circ$  ambiguous spectrum: the propagation direction is ambiguous but still, image normalized variance is smaller than 1.5 and swell azimuth wavenumber is smaller than 75% of the azimuth cut-off wavenumber;
  - 2 - probably bad spectrum: the propagation direction is ambiguous. Besides, either normalized variance is larger than 1.5 or swell azimuth wavenumber is larger than 75% of the azimuth cut-off wavenumber.

For this validation study, only best quality observations are considered. Figure 3.1 illustrates the percentage of spectra with the best quality flag retrieved from ASAR instrument from 2003 till the end of 2009. It indicates a quite stable number of about 62%. The remaining 38% are composed of 32% of ambiguously retrieved spectra and of 6% of bad quality wave spectra, mostly caused by non-wave signature on SAR images, among which 2% are due to partial land coverage within the image.

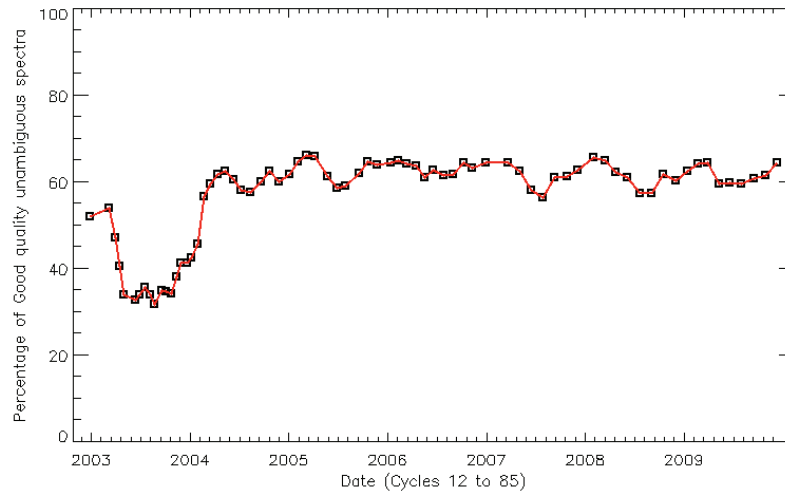


Figure 3.1: Quality levels of SAR L2 unambiguous spectra dataset for ENVISAT from 2002 to 2009. After the Wave Data Quality Report (2010), part of the GlobWave ESA funded project.

The main criticism to this data handling is that directional ambiguity is estimated over the entire swell spectrum, which would imply that a single swell system is imaged by the SAR. However, in 50% cases, a second independent swell system is imaged by the SAR. These two swells can be

spectrally separated using a partitioning algorithm<sup>3</sup>. Such methods separate a wave spectrum containing several wave systems into as many spectral parts, referred to as *partitions*. Once this operation is achieved, each spectral partition can be treated independently. Specifically, the 180° ambiguity analysis and the swell azimuth wavenumber criterion are applied for each spectral partition. Not only does it allow us to extract the additional information related to the second swell partition, but it also gives a better estimation of the azimuth wavenumber and directional ambiguity criterion. Indeed, the phase shift of the backscattered signal caused by the swell motion can be calculated for the spectral partition of interest alone and, if the swell peak directions and periods are different enough, one system's phase shift is not impacted by the presence of the other one.

SAR L2 products processed with this partition-specific approach are denoted SAR L2P products, for Level-2 *Partition* products. This operation has been applied to data from 2002 onward. For each spectrum, the percentage of partitions retrieved from the SAR L2P wave spectra with best quality flag reaches an average of 72% for the most energetic partition and 51% for the second most energetic partition. Compared to the previous approach, the number of retrieved partitions is doubled. Also, it appears that the most energetic wave partition has lower propagation direction ambiguity.

### 3.2.2 Data Correction

Previous validation studies have shown that the significant swell height was biased. For instance, *Collard et al. (2009)* noticed that it was primarily a function of the swell height and wind speed, increasing with height and decreasing with wind speed. It is estimated as follows:

$$b_H = 0.11 + 0.1H_{ss} - 0.1 \max \{0, U_{10} - 7\} \quad (3.5)$$

where,  $U_{10}$  is the 10 m-high wind speed measured by the SAR;  
 $H_{ss}$ , the significant swell height.

A more detailed analysis with an extended SAR-buoy co-located dataset has been initiated within the GlobWave project<sup>4</sup>. Comparison with the NODC buoy network indicates that the significant swell height is over-estimated for short swells. Consequently, within the GlobWave project, a corrected form of the significant swell height is proposed:

$$H'_{ss} = H_{ss} \left( 0.215 + \frac{\lambda_p}{670} \right) + 0.05 \max \{ (U_{10} - 7), 0 \} - 0.05 \quad (3.6)$$

3. Detailed in Subsection 3.3.1, page 86.

4. An initiative funded by the European Space Agency (ESA). One of its main objective is to provide a uniform, harmonized, quality controlled, multi-sensor set of satellite wave data and ancillary information, thereby allowing inter-comparison of different wave data sources.

Also, the SAR L2P validation with the GlobWave project shows that the swell wavelength is over-estimated for short swell while it is under-estimated for long swell. The following wavelength correction is thus proposed:

$$\lambda'_p = 1.14\lambda_p - 61 \quad (3.7)$$

### 3.3 Methodology

The validation process is split in three main steps: spectral partitioning, integral parameters' estimation and peak-to-peak association between partitions from SAR and buoy spectra.

#### 3.3.1 Spectral partitioning

Accumulated every hour for decades, directional ocean wave spectra archives can reach a very large amount of information. For both archival and interpretations purposes, swell integral parameters are a good solution since they considerably reduce the amount of information to store and still suitably describe the main characteristics of a wave spectrum. However, if composed of several simultaneous wave systems, the integral parameters have to be estimated over each partition rather than over the whole spectrum, which requires a previous step: spectral partitioning.

First introduced by *Gerling* (1992), further developments were brought by (*Brüning et al.*, 1994; *Brüning and Hasselmann*, 1994; *Hasselmann et al.*, 1996; *Young and Glowacki*, 1996; *Voorrips et al.*, 1997; *Hanson and Phillips*, 2001). These improved versions have proven more robust and can be a benefit to data assimilation which require spectral comparisons from different sources like *in situ* buoys and numerical models. Our approach is inspired from the method proposed by *Portilla et al.* (2009). It comes in three steps:

1. 2D noise removal,
2. Watershed algorithm,
3. Merging partitions with poor contrast.

##### 3.3.1.1 2D noise-removal

If no filtering is applied, 2D ocean wave spectra are quite noisy, which makes partitioning difficult. The proposed operation consists of a 2D discrete convolution between the spectrum and a convolution kernel, hereby averaging immediate neighbors of the central bin.

In order not to modify the spectrum energy, it is crucial to take into account the fact that frequency discretization is not necessarily even over the spectrum. Indeed, it is refined for small scales and usually follows a

geometric suite. Therefore, prior to any convolution, the ocean wave spectrum is successively multiplied by a vector  $N$  to convert the wave spectrum,  $S(f, \theta)$ , expressed in  $[\text{m}^2\text{Hz}^{-1}]$  to  $S_1(f, \theta)$ , expressed in  $[\text{m}^2]$ . It is then convoluted by  $K$  to get  $S_2(f, \theta)$  and finally multiplied by  $N'$  to obtain  $S_3(f, \theta)$ , in  $[\text{m}^2\text{Hz}^{-1}]$ . These operations are described by:

$$S_1(f, \theta) = S(f, \theta)N(f) \quad \text{with } N_j = df_j \quad (3.8a)$$

$$S_2(f, \theta) = K(m, n) \otimes S_1(f, \theta) \quad (3.8b)$$

$$= \sum_{m=-1}^1 \sum_{n=-1}^1 K(m, n)S_1(f - m, \theta - n) \quad (3.8c)$$

$$S_3(f, \theta) = S_2(f, \theta)N'(f) \quad \text{with } N'_j = 1/df_j \quad (3.8d)$$

where the operator  $\otimes$  indicates a convolution.

For  $K$ , we choose a  $3 \times 3$  kernel with 8-connectivity as opposed to 4-connectivity to further smooth the wave spectrum energy. Still, to avoid losing relevant information because of excessive smoothing, the kernel coefficients are chosen so that they enhance the central bin as shown below:

$$K = \frac{1}{a} \begin{pmatrix} 1./\sqrt{2} & 1 & 1./\sqrt{2} \\ 1 & 2 & 1 \\ 1./\sqrt{2} & 1 & 1./\sqrt{2} \end{pmatrix} \quad (3.9)$$

where  $a = 6 + 4/\sqrt{2}$ , so that the  $\sum_{ij} K_{ij} = 1$ .

As opposed to the filtering proposed by *Portilla et al. (2009)*, we perform this step only once to avoid excessive smoothing.

### 3.3.1.2 Watershed algorithm

This algorithm partitions a wave spectrum into independent wave systems in term of water catchment areas. It was first introduced by *Brüning et al. (1994)* and further developed by *Hasselmann et al. (1996)*. It is based on the idea that the wave spectrum can be seen as an inverted topography. Wave systems are then defined in the spectral domain by all the grid points whose run-off drains into local inverted peak. Mathematically speaking, a grid point is assigned to the same wave system as its immediate steepest ascent neighbors, considering 4- or 8-connectivity. In the end, a grid point whose energy is higher than all its neighbors defines a local peak and a wave system. In our approach, we choose 8-connectivity which makes the algorithm less sensitive to noise. Though, as the spectrum has already been smoothed, this choice has a very minor impact on partitioning.

The corresponding algorithm is often denoted *watershed*. The level of partitioning detail is determined by the maximum spectrum energy. Therefore, all our spectra are normalized so that their maximum equals 200 before ingestion by the watershed algorithm. Figure 3.2 illustrates this partitioning scheme.

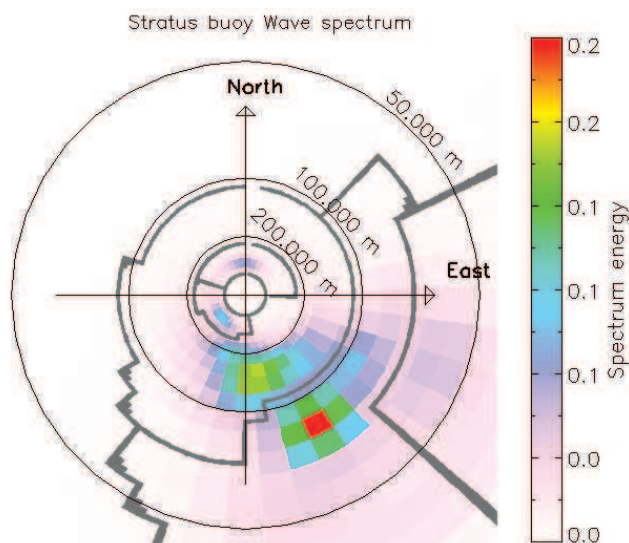


Figure 3.2: Example of a partitioned sea surface spectrum measured by the buoy 'Stratus' (WMO51028), operated by Woods Hole Oceanographic Institution (WHOI) and moored 1500 km off the coast of Chile, at  $-19,7^{\circ}\text{N}$ ,  $-85.5^{\circ}\text{E}$  on 6 January 2008 at 15Z. The spectrum partitioning, delimited by gray solid lines, exhibit five wave systems: two swells coming from North and South-West directions with peak wavelength of 366 and 370 m, respectively, and an old and two young wind-seas coming from South and South-South directions with peak wavelength of 151 and 77 and 57 m, respectively.

Even if this algorithm has sprung out from Gerling's algorithm (*Gerling, 1992*), the original one developed by Gerling was quite different. Up to now, there is no dedicated study comparing Gerling's and Hasselmann's partitioning scheme but it seems that the latter may be more robust (*Aarnes and Krogstad, 2001*) and thus more appropriate for comparing spectra measured by different instruments.

Speed of partitioning algorithm is also important, especially when applied to a wave model used for early warning applications for instance. In that case, it is relevant to look at efficient watershed algorithms such as those developed by *Vincent and Soille (1991)*.

### 3.3.1.3 Merging partitions with poor contrast

This step consists in merging partitions that have poor contrast, so as to avoid splitting a wave system because of spectral noise and/or miscellaneous spectral reconstruction caused by the MEM algorithm. More explicitly, this criterion estimates if the valley between two peaks is sufficiently pronounced or not. If it reaches a threshold percentage of the smaller peak energy, then the partitions are merged. We have chosen to fix this threshold to 85%, similarly to what is done by *Hasselmann et al. (1996)*. This process is illustrated in Figure 3.3.

### 3.3.1.4 Assumption

Looking at wave spectra such as the one displayed on Figure 3.2, we can see that the frequency width and the directional spreading can be rather large, especially when considering wind-sea partitions. Therefore, whenever several wave systems are present, their spectral domain can overlap. On the other hand, partitioning algorithms behave as if there were no intersection between each wave system's spectral domain. The boundary drawn by the watershed partitioning algorithm between two adjacent wave systems corresponds to the region where the energy components of each partitions are equal. Thus, two adjacent partitions will each contain part of the other wave system's spectral tail. We assume that this erroneously attributed energy is equal for each partition. Other studies have tried different approaches. For example, *Kerbiriou et al. (2007)* have proposed to fit a JONSWAP-like spectrum to the one measured to recover each partition spectral tail. We have chosen not to do so since such spectra are more adapted to wind-sea than to swell. Therefore, the JONSWAP parametrization may not be appropriate.

## 3.3.2 Integral parameter estimation

Now that the wave system partitions are defined, we estimate integral parameters for each of them: the significant swell height,  $H_{ss}$ , the peak direction,  $D_p$ , and the peak period  $T_p$ . The significant swell height is defined as:

$$H_{ss} = 4 \left( \iint_{R_P} S(f, \theta) df d\theta \right)^{1/2} \quad (3.10)$$

where  $R_P$  is the spectral domain of the swell partition.

The swell peak period is defined as the energy-weighted average period around  $\pm 22\%$  of the frequency of maximum energy. Likewise, the peak direction is defined as the energy-weighted average direction within  $30^\circ$  of the direction of maximum energy.

In addition to these parameters, we also retrieve the partition peak-to-boundary energy ratio, denoted  $R_{pb}$ . It is equal to the partition peak energy divided by the maximum energy met along the partition's boundary. For large values of  $R_{pb}$ , the swell partition is well isolated from other partitions or very predominant compared to them while for small values of  $R_{pb}$ , the swell system peak is not very clear and adjacent to other swell systems. We expect to better estimate swell partitions with high values of  $R_{pb}$ .

### 3.3.3 Peak-to-peak association

Once the SAR and buoy spectra have been partitioned and before comparing them, ones' instrument partition has to be associated to the corresponding one as seen by the other instrument. Indeed, SAR spectra may contain several swell partitions and it is crucial to know to which partition of the buoy spectrum it corresponds to. This association is always based on the SAR spectrum since the buoy can measure wind-sea conditions that may not be seen by the SAR because of the azimuth cut-off.

To compare two partitions,  $P_1$  and  $P_2$ , we define a spectral distance,  $S(P_1, P_2)$ :

$$S(P_1, P_2) = \frac{1}{q} \left( |D_1 - D_2| \bmod 360 + 2 \frac{|T_1 - T_2|}{T_1 + T_2} r \right) \quad (3.11)$$

with,

$$q = 60 \text{ and } r = 250$$

where,  $D_i$  refers to the peak propagation direction of each partition;  
 $T_i$ , to the peak period of each partition.

Other spectral distances have been proposed in the past (e.g. *Delpy et al.*, 2010), though, the weight given to the direction with regard to the relative frequency was not satisfactory. On the opposite, factor  $r$  gives the possibility to modulate the relative importance of the peak period with regard to the direction of propagation. Its value was chosen so that  $20^\circ$  errors in direction are equivalent to 8% errors in period, which are approximately the expected accuracies of SAR swell measurements. Other Additionally, factor  $q$  was chosen for convenience, so that a  $30^\circ$  error in direction and 12% in period give a spectral distance equal to one.

Given a SAR partition, the spectral distance is estimated for all possible buoy partition associations. The peak-to-peak association is then determined by the shortest spectral distance.

Following this association, some significant differences between the integral parameters of the SAR, and buoy associated partitions may arise due

the fact that the buoy measurements are limited to the first four Fourier coefficients. To tackle this issue, *Hanson and Phillips (2001)* have proposed to use the buoy partition and to apply it to the other wave spectrum. However, this approach assumes that the two directional spectra are available, not just their integral parameters. We have chosen not to do so because we also want to use the same comparison methodology in Chapter 6, where the integral parameters alone are available. Still, to avoid significant differences, the buoy most energetic partition only is used.

### 3.3.4 Graphical summary

An illustration of the partitioning scheme is proposed on Figure 3.3. The buoy spectrum right after its reconstruction using the MEM algorithm is shown on subplot (a). Then, it is smoothed and partitioned, exhibiting two different systems in the first place (b). Since, they have a rather small contrast, they are gathered into a single swell system (c). Similarly, the SAR spectrum contains a single swell system (d). Therefore, there is no need for any peak-to-peak association.

The buoy indicates a swell system whose significant swell height, peak wavelength and peak direction equals 1.27 m, 289 m and  $117^\circ$  respectively while the SAR indicates 1.9 m, 260 m and  $128^\circ$ .

## 3.4 Statistical results

### 3.4.1 Matchup criteria

Previous global scale SAR validations have been made in the past. *Johnsen and Collard (2004)* directly compared swell parameters, estimated from SAR L2 products and buoy measurements within 200 km and 1 hour. Significant swell height statistics gave root mean square error (RMSE) of 0.5 m, including a bias of 0.2 m. Later, another study by *Collard et al. (2006)* applied the L2 processing to  $4 \times 4$  km<sup>2</sup> tiles from narrow swath images, instead of the traditional  $10 \times 10$  km<sup>2</sup> SAR L2 wave mode products, but centered on buoy positions. Despite the four times smaller image area that should have produced larger errors due to statistical uncertainties, the significant swell height RMSE was equal to 0.37 m. This suggests that a significant part of the "errors" in SAR validation studies are due to the distance between SAR and buoy observations.

**Dynamical co-location** In order to get the best co-located SAR-buoy dataset, strict conditions on the time difference and distance are thus necessary. We choose to only consider observations with a maximum 1-hour

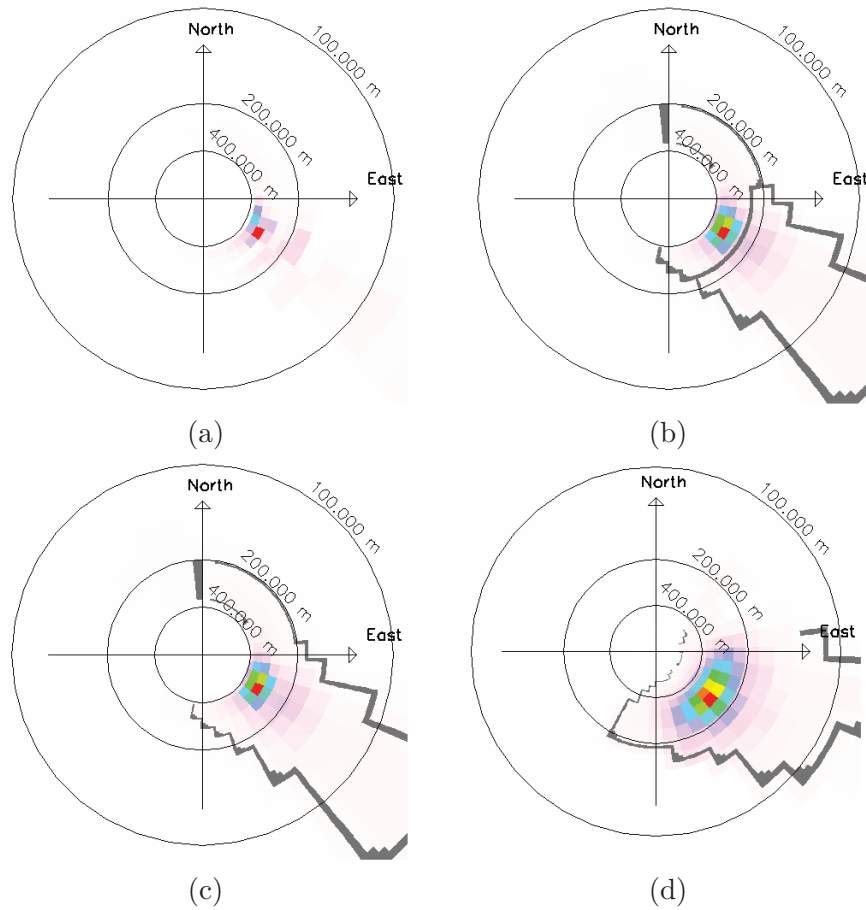


Figure 3.3: A buoy spectrum at different stages of the partitioning scheme (a), (b) and (c) and the co-located SAR spectrum (d). Subplot (a) is the buoy spectrum right after MEM reconstruction; (b), after smoothing and partitioning, partitions being contoured by the gray solid lines and (c), after merging poorly contrasted partitions.

interval and 100 km distance<sup>5</sup>. Using these parameters greatly diminishes the total co-location number and undermine our capability to statistically quantify SAR measurements' accuracy. To compensate for this effect, we take advantage of the SAR integral peak parameters. Instead of only using the measurements that are co-located in time and space, we use the peak period and direction to estimate the position of each SAR swell observation after propagating it for several hundred kilometers using linear theory (cf. Chapter 2, Section 2.1). Estimating the significant swell height while propagating the swell assumes we know the swell steepness and distance to its storm source. Here, a mean significant swell height decay is assumed because this information is not available. Using this new *dynamical co-location* method with a maximum 500 km propagation, co-locations are multiplied by a factor 5.

Unlike peak direction and period, significant swell height co-locations are only established for swell partitions propagated for a maximum distance of 150 km. Then, the associated energy decay reaches a maximum significant swell height difference of 4.5 cm compared to its value at observation time. It is consistent with previously measurements of energy decay assessed along propagation direction using the same SAR instrument.

Using linear propagation assumes that the validation buoys are located in open ocean. Since the NODC network contains most offshore buoys, it will be our main validation network. Still, we make sure that each buoy it contains is located far enough from shallow water areas and islands to avoid refraction and diffraction phenomena that should otherwise be taken into account.

### 3.4.2 Matchup dataset

As mentioned before, the dynamical co-location is established by investigating SAR and buoy data from year 2002 to 2009 measurements with a maximum 1-hour interval and 100 km distance, leading to a dataset of 22,494 co-locations. The additional restrictions for building the matchup dataset are listed hereafter:

1. SAR measurements with best quality flag, limiting the dataset to 12,332 co-locations;
2. propagated distance for SAR measurements limited to 150 km, further limiting the dataset to 1,364 co-locations;
3. SAR significant swell height greater than 30 cm;

---

5. These criteria are not strictly equivalent and it would have been wiser to fix the maximum time difference to 2H30 since this is the period required for a typical 14 s swell to cover 100 km.

4. minimum water depth of 400 m (1,306 co-locations);
5. SAR derived wind speed,  $U_{10}$ , limited to values ranging from 3 to  $9 \text{ m.s}^{-1}$  in order to remove low winds with poorly contrasted SAR images and high winds which may still cause some important azimuth cut-off and contamination of swell spectra by wind-sea spectra.
6. swell period between 12 and 18 s (551 co-locations);
7. peak-to-boundary energy ratio exceeding  $R_{pb}$  greater than five for a better peak-to-peak association (153 co-locations).
8. outliers exclusion, when peak period difference exceeds 3 s, the peak direction difference exceeds  $135^\circ$  or significant swell height difference exceeds 2 m. This finally reduces the dataset to 147 co-locations.

This dataset is denoted dataset A. Co-located buoys' ID and positions are given in Table 3.2. The dataset reduction points out that, even though numerous good quality flagged SAR L2P products are available, only 13% percent of them meet all the best observability conditions.

Buoy ID	Latitude [deg. N]	Longitude [deg. W]	Buoy ID	Latitude [deg. N]	Longitude [deg. W]
WMO46047	32.403	119.536	WMO46050	44.639	124.534
WMO46011	35.000	120.992	WMO46063	34.273	120.699
WMO46013	38.242	123.301	WMO46069	33.670	120.200
WMO46015	42.747	124.823	WMO46086	32.491	118.034
WMO46022	40.776	124.589	WMO46089	45.889	125.830
WMO46026	37.759	122.833	WMO51000	23.546	154.056
WMO46027	41.850	124.381	WMO51001	23.445	162.279
WMO46028	35.741	121.884	WMO51004	17.525	152.382
WMO46029	46.144	124.510	WMO51028	0.000	153.913
WMO46041	47.353	124.731	WMO51100	23.558	153.900
WMO46042	36.785	122.469	WMO51101	23.445	162.279

Table 3.2: Geographical location of NODC buoys used for the SAR L2P validation.

The maximum period considered only reaches 18 s, which corresponds to a 500 m-long swell. Thus, we should have accepted to consider buoys whose waters depth goes down to 250 m<sup>6</sup>. Though, we have decided to limit our dataset to a 400 m water depth since we found that this brought a significant statistical improvement. This is attributed to the fact that some

6. In Airy theory, deep water propagation can be assumed as soon as the water depth is greater than half the swell wavelength (cf. Chapter 2, Section 2.1).

coastal phenomena are expected to interfere with the propagating swell and to deviate the propagated observations from their theoretical great circle trajectory. Coastal currents are probably responsible for a major part of it.

### 3.4.3 Main statistics

Using the significant swell height correction given by equation 3.6 still gives an important bias, equal to -0.32 m, though it should have been eliminated by this correction.

This apparent discrepancy is attributed to the different data processing before statistical comparison. For instance, for the SAR L2P validation in the GlobWave project, buoy spectra are not smoothed prior to SAR spectra comparison. The spectral partitioning and peak-to-peak association is also quite different. In that study, SAR spectra are partitioned using the method proposed by *Gerling (1992)*, instead of the watershed algorithm described by *Hasselmann et al. (1996)*, and the associated buoy partition is defined as the buoy spectrum part corresponding to the spectral domain of the SAR swell partition. Thus, there is no independent buoy spectral partitioning. This has the advantage of avoiding any peak-to-peak-association but can introduce a bias in the swell comparison. Indeed, part of the buoy swell partition may not be included in the spectral domain of the SAR swell partition and therefore may be mistakenly excluded. This would explain the bias difference as the SAR energy would be higher, on average, than that of the associated buoy partition. Also, part of the other buoy swell partitions may be inside the spectral domain of the SAR swell partition and therefore may be mistakenly included.

To correct for this bias, we propose a new significant swell height correction given by:

$$H'_{ss} = H_{ss} \left( 0.38 + \frac{\lambda_p}{670} \right) + 0.05 \max([U_{10} - 7]) - 0.05 \quad (3.12)$$

The peak wavelength correction indicated by equation 3.7 is judged satisfactory and kept.

Statistics for the estimation of  $H_{ss}$ ,  $T_p$  and  $D_p$  are given in Table 3.3. The associated scatter plots are shown in Figures 3.4 and 3.5. Next to these, we show the statistics given by the wave data quality report of the GlobWave project for the same SAR L2P products, but with a slightly different comparison methodology. Since that validation focuses on the swell wavelength rather than the swell peak period, both quantities are indicated in our study. Despite the different methodology, these results are very comparable and a

		$H_{ss}$	$T_p$	$\lambda_p$	$D_p$
(a)	Bias	0.01 m	-0.12 s	-6 m	2.6°
	RMSE	0.31 m	0.70 s	30 m	16.0°
	NRMSE	22.7%	5.1%	10%	NA
	r	0.90	0.84	0.85	0.99
(b)	Bias	0.02 m	-0.14 s	-7 m	0.2°
	RMSE	0.35 m	0.75 s	32 m	13.6°
	NRMSE	21.1%	5.4%	11%	NA
	r	0.86	0.85	0.87	0.98
(c)	Bias	0.00 m	-	0 m	2°
	RMSE	0.30 m	-	36 m	17°

Table 3.3: Statistics after comparison of SAR L2P and NODC buoy spectra for two different approaches. (a) refers to the methodology we have developed, and using dataset A. (b) refers to the same dataset but for swell whose significant swell height exceeds than 1 m. (c) are statistics given by wave data quality report of the GlobWave project.

slight improvement can even be noticed for the peak wavelength estimation.

### 3.4.4 Dependences

#### 3.4.4.1 Relevant parameters

Here is a list and brief reminder of the various parameters, most of which have been described in Chapter 1, that are expected to significantly influence the data quality of each swell observation:

- image normalized variance,  $NV$ : it is estimated over the SAR sea surface image. High variances are linked to non-wave features (slicks, ships..) that can contaminate the wave spectra whereas small variances are linked to low winds, resulting in poorly contrasted SAR images;
- 10 m-high SAR wind speed,  $U_{10}$ : Given at observation time, using a CMOD algorithm and the SAR sea surface backscatter, it is estimated for each wave mode acquisition. A minimum wind speed is necessary for the development of Bragg waves on the longer wave profile. Otherwise, the sea surface backscatter stays within noise level and leads to poorly contrasted SAR images. Also, high winds can cause some important azimuth cut-off and contamination of swell spectra by wind-sea spectra;
- partition peak-to-boundary energy ratio,  $R_{pb}$ : this is defined for a given swell partition as the ratio between the peak energy and the

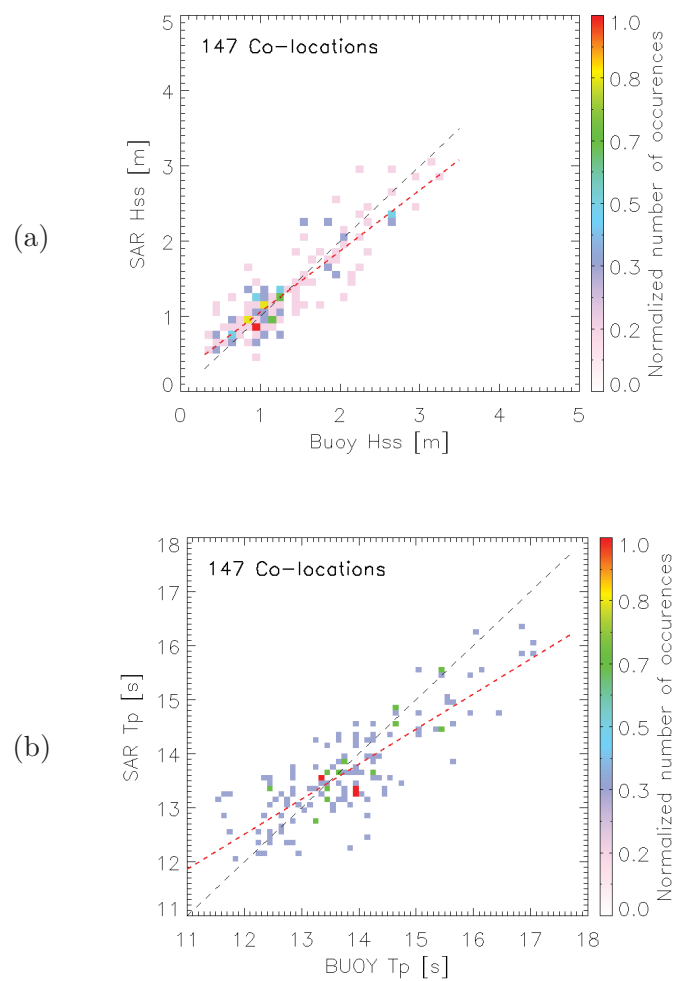


Figure 3.4: Scatter plots for the significant swell height,  $H_{ss}$ , (a) and peak period,  $T_p$ , (b) established between 147 buoy and SAR co-located swell observations. The black dashed line corresponds to the median between the ordinates and the abscissa axis whereas the red dashed line corresponds to the data point linear regression.

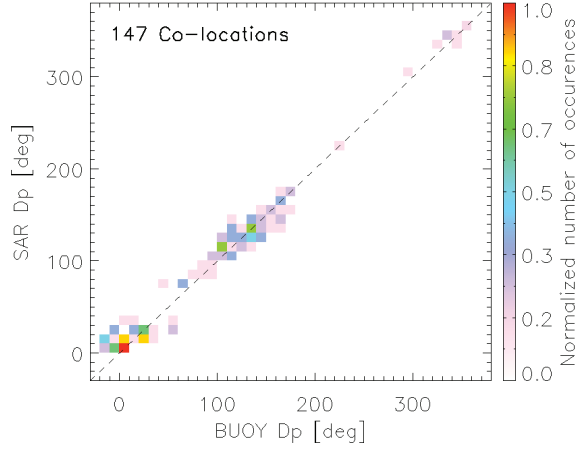


Figure 3.5: Scatter plots for the peak direction,  $D_p$ , established between 147 buoy and SAR co-located swell observations. The black dashed line corresponds to the median between the ordinates and the abscissa axis.

partition boundary maximum energy. High values represent well defined swell partitions while values close to one are explained by very smooth/unclear swell peak or energetic adjacent swell partitions which can lead to erroneous partitioning or peak-to-peak association;

- azimuth cut-off: intrinsic to the SAR measurement, short waves' motion during the SAR integration time causes an azimuthal smearing on the sea surface image, resulting in an apparent contrast loss. It prevents from imaging small scale features in the azimuth direction. The azimuth cut-off wavelength quantifies the scale above which this phenomenon disappears and, on the opposite, becomes constructive. Imaging swell with an azimuth peak wavelength close to the azimuth cut-off wavelength may lead to the under-estimation of the high frequency part of the swell partition. This can also displace the SAR estimated peak wavelength to higher values and the peak direction in the range direction;
- ambiguity factor: Using the sign of the phase difference between two different looks of the same scene acquired during the SAR integration time, one can determine the swell propagation direction. This technique is limited by the integration time. Indeed, for ENVISAT wave mode acquisition, the integration time is only a fraction of the swell period, typically 0.5 s. The higher the ambiguity factor, the stronger the confidence in propagation direction;
- propagation time: the time that separates an observation from its propagated position. This parameter is not related to the observation itself

but to its treatment in the post-processing stages. As the swell observation is propagated using linear theory, the confidence we have in its propagated position is expected to decrease with the increasing time for which it has been propagated because of the estimation errors in peak period and direction. For instance, considering a 14 s swell whose peak period and direction are estimated with errors of 0.5 s and  $10^\circ$ , respectively, they induce altogether a mis-location of the propagated point of 170 and 850 km after one and five days of propagation, respectively.

To estimate these parameters' impact on swell characteristics' accuracy, we need to soften the co-location conditions to increase the dataset size, as opposed to the very restrictive conditions given to build dataset A. Five additional datasets, B, C, D, E and F are defined. The conditions defining each dataset are summarized in Table 3.4. As they are less restrictive, the associated bias and RMSE are not as good as those given for dataset A. However, we do not focus on their absolute value but on their evolution with respect to the aforementioned parameters. We successively tackle each of them. Whenever relevant, it is accompanied by a graphical representation of the integral parameter measurement errors. For instance, for the study of the wind speed impact, the wind speed range is split into several subranges equally divided in co-location number for which associated bias and RMSE are calculated and represented. For each subset, the amount of co-locations is also indicated and may vary slightly differ among the different integral parameters because of different outlier's rejection.

#### 3.4.4.2 Integral parameters

The previous statistics results from the best co-locations. In reality, we wish to use a lot more than just 13% of all the best quality flag SAR L2P products. To get an idea of the statistics from a more comprehensive dataset, we define dataset E as described in Table 3.4. The associated scatter plots for the estimation of  $H_{ss}$ ,  $T_p$  and  $D_p$  are given in Figures 3.6 and 3.7.

**Significant swell height** First, looking at the SAR significant swell height estimation, we can see that there is a clear bias that tends to over-estimate small heights and under-estimate large ones. Small swell over-estimation reaches 0.30 m for significant swell heights around 0.5 m and large swell under-estimation reaches -0.26 m for significant swell height above 2 m. Still, this is for swell observations whose peak-to-boundary energy ratio is larger than 3 for both the SAR and the buoy partitions. Removing this condition, this bias reaches -0.51 m.

Besides, the accuracy decreases with increasing swell height. It is smaller than 0.4 m for swell whose significant height is smaller than 1 m and reaches 0.58 m for the those larger than 2 m. Obviously, the bigger the swell, the

Conditions on...	A	B	C	D	E	F
Maximum distance difference [km]	100	idem	idem	idem	idem	idem
Maximum time difference [hour]	1	idem	idem	idem	idem	idem
SAR L2P quality flag	0	idem	idem	1	idem	idem
Minimum $H_{ss}$ [cm]	30	idem	idem	idem	idem	idem
SAR $T_p$ [s]	$12 < T_p < 18$	idem	idem	idem	idem	idem
$NV$	$1.05 < NV < 1.5$	idem	idem	idem	idem	idem
$U_{10}$ [m.s <sup>-1</sup> ]	$3 < U_{10} < 9$	-	-	-	-	-
Minimum buoy $R_{pb}$	5	3	5	3	3	
Minimum SAR $R_{pb}$	5	3	-	3	3	
Max. SAR swell propag. dist. [km]	150	300	300	300	500	1,000
Data counts	147	604	580	662	1070	2590

Table 3.4: Data counts and required conditions for dataset A, B, C , D, E and F.

bigger the potential error. Consequently, we rather use the relative significant swell height, which is more representative when comparing various swell heights. The normalized root mean square error (NRMSE) is defined by:

$$NRMSE = \frac{\left\langle \left( H_{ss}^{SAR} - H_{ss}^{Buoy} \right)^2 \right\rangle^{1/2}}{\left\langle H_{ss}^{Buoy} \right\rangle} = \frac{RMSE}{\left\langle H_{ss}^{Buoy} \right\rangle} \quad (3.13)$$

The relative significant swell height is much smaller for swell whose relative significant height is larger than 2 m (21%) than for those smaller than 0.5 m (more than 55%). The effect of using dataset E instead of dataset A is quite clear. While the significant swell height NRMSE given by dataset A equal 22.7%, it is equal to 36% for dataset E.

**Peak period** For the peak period, the most accurate results are given for values ranges between 12 and 13.6 s, with RMSE and bias absolute value smaller than 0.75 s and 0.28 s, respectively. On a general trend, the peak period tends to be under-estimated for long swell and away from this period range, the bias reaches -1.1 s for swell whose period is larger than 15.5 s.

**Peak direction** The peak direction measurement errors with respect to the peak direction are disregarded as no significant evolution is found. Still, quite interesting patterns can be noticed: around the two mainly observed propagating directions, due to northern and southern swells, the scatter plot of the SAR-buoy peak direction difference with respect to the buoy peak direction exhibit ridges. Their slope is negative and their absolute value equals one, which indicate that the peak direction differences are mainly attributed to buoy measurements. This shows that they have a high variability, probably caused by the presence of several simultaneous wave systems.

#### 3.4.4.3 Normalized variance

Looking at all the co-located SAR-buoy data, 23,537 in total, we can establish an empirical relation between the normalized variance, the SAR total significant swell height,  $H_{ss_{tot}}$ , and the SAR wind speed. The scatter plots in Figure 3.8 indicates that, for a given total significant swell height, the wind speed decreases when the normalized variance increases. As we expect the mean NRCS to increase with increasing wind speeds, this shows that the NRCS modulation does not increase as fast as its mean value when the wind speed increases. Also, for a given SAR wind speed, the SAR total significant swell height increases with increasing normalized variance since, for a given wavelength, larger slopes lead to larger NRCS modulation. These variations are observed whenever the swell spectrum only contains a single

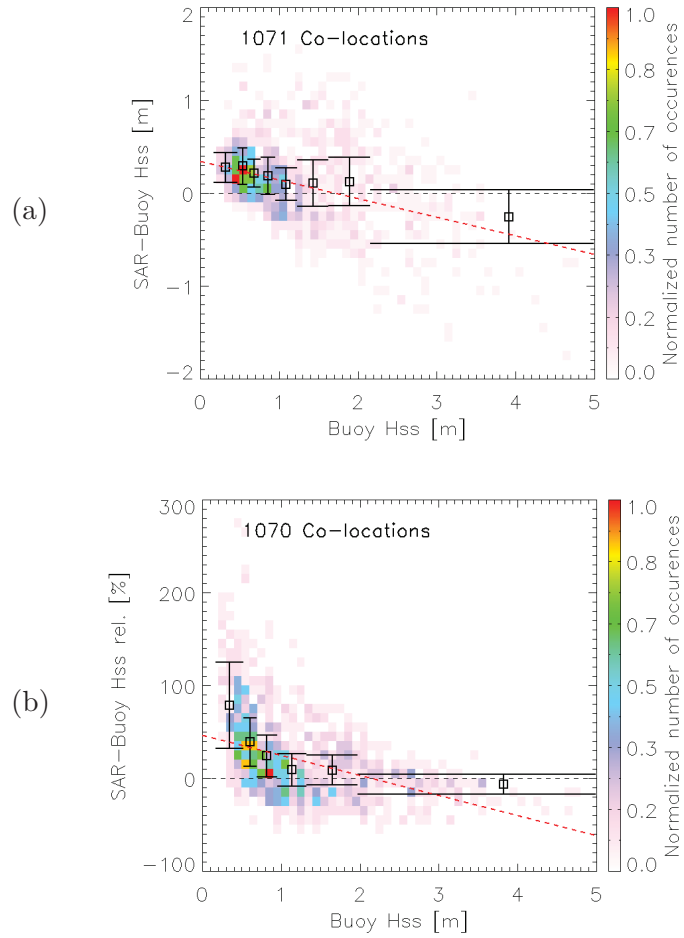


Figure 3.6: Significant swell height (a), relative significant swell height (b) measurement errors against SAR wind speed. RMSE (a), NRMSE (b) and bias are respectively indicated for each subrange by the vertical extent of the solid line segments and their central vertical value, represented by a square.

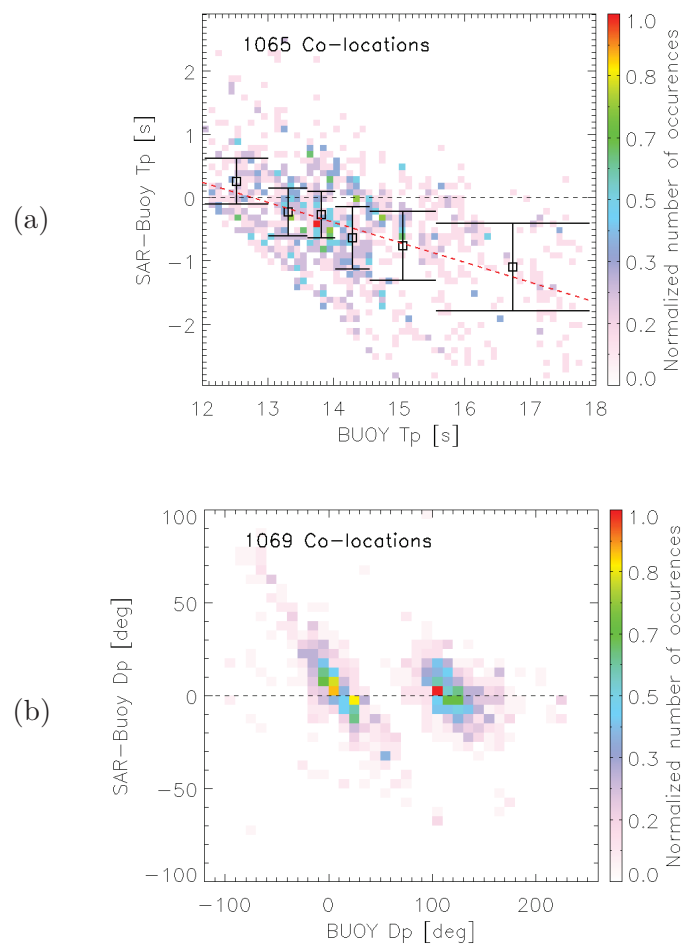


Figure 3.7: Peak period measurement errors against SAR wind speed. For the peak period, RMSE and bias are respectively indicated for each subrange by the vertical extent of the solid line segments and their central vertical value, represented by a square.

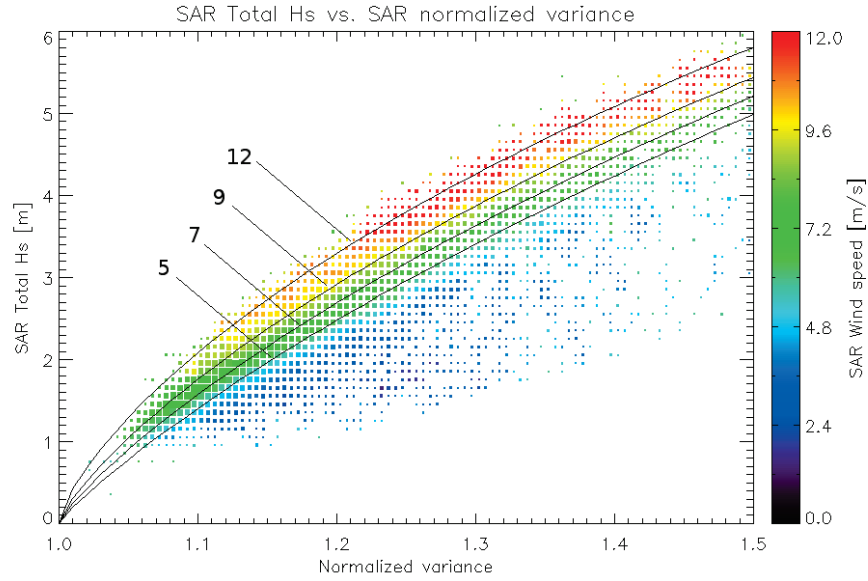


Figure 3.8: Graph showing the variation of total significant swell height with normalized variance ( $NV$ ) and wind speed together with a proposed law for  $H_{s_{stot}}$  evolution with respect to  $NV$ , for different wind speeds (5, 7, 9 and 12  $m.s^{-1}$ ).

swell partition.

Here, this empirical behavior is used to verify the quality of the SAR swell measurements. This behavior is modeled by the following equation:

$$H_{s_{stot}} = [11. \log(NV)]^{(4.97U_{10}-0.12)/5}. \quad (3.14)$$

Its variations are given for different wind speeds on Figure 3.8. The logarithmic function reproduces the total significant swell height evolution with respect to normalized variance whereas the power reproduces the wind speed dependence.

As this function seems to follow the general trend faithfully, we study the significant swell height error with respect to the difference between the total significant swell height expected value given by equation 3.14 and that measured by the SAR. It is important to note that it would not make sense to compare total significant swell height values given by the SAR to that given by a buoy. Indeed, an important part of the wave spectrum measured by buoys can come from short waves that the SAR cannot image. Using dataset B, significant swell height measurement errors with respect to the difference between expected and SAR measured total significant swell height

is represented in Figure 3.9 (a). Smallest bias and RMSE are given for differences close to zero, which certifies that our criterion is relevant. The impact on the peak period measurement errors does not show any clear trend.

As well, the normalized variance dependency is represented on Figure 3.9 (b). It indicates that the smallest bias and RMSE are given for small values of the normalized variance, between 1.1 and 1.2 and errors increase with increasing normalized variance. Thus, using a criterion based on the maximum acceptable normalized variance would tend to privilege small waves since we noticed on Figure 3.8 that the significant swell height increases with that parameter. For instance, limiting the normalized variance to 1.25 would remove all waves whose total significant wave height is larger than 4 m. On the contrary, using the difference between the measured and the modeled total significant swell height given in equation 3.14 does not prefer a specific range of swell height range. It thus concerns a more homogeneous swell dataset.

#### 3.4.4.4 Partition peak-to-boundary energy ratio

Here, we use dataset C, based on dataset B except the condition on the partition peak-to-boundary energy ratio,  $R_{pb}$ , is removed for SAR partitions and increased for buoys to keep a good quality dataset. The impact on all integral parameters is shown in Figures 3.10 and 3.11.

For all integral parameters, the data quality clearly increases with  $R_{pb}$ . For the significant swell height, the RMSE decreases very rapidly, from 0.70 cm to 0.46 cm for  $R_{pb}$  values smaller and larger than 4, respectively. Similarly, the peak period RMSE equals 1.2 for small  $R_{pb}$  values and reaches 0.7 for values above 9. The peak direction RMSE equals  $31^\circ$  for small  $R_{pb}$  values and reaches  $14^\circ$  for values above 9.

The sharp statistics improvement with  $R_{pb}$  is very likely due to a better partitioning and peak-to-peak association. Besides, we remind that our spectral partitioning is based on the assumption that the spectral tail's energy of two neighboring partitions outside their spectral domain is equal. Thus, for large  $R_{pb}$  values, this energy is much smaller relatively to the partition's energy and generate smaller significant swell height errors whenever our assumption does not hold.

#### 3.4.4.5 Wind speed

This parameter's impact is estimated using dataset B, which does not have any restriction on SAR wind speed. This parameter clearly impacts the significant swell height (Figure 3.12) while the wind speed dependence

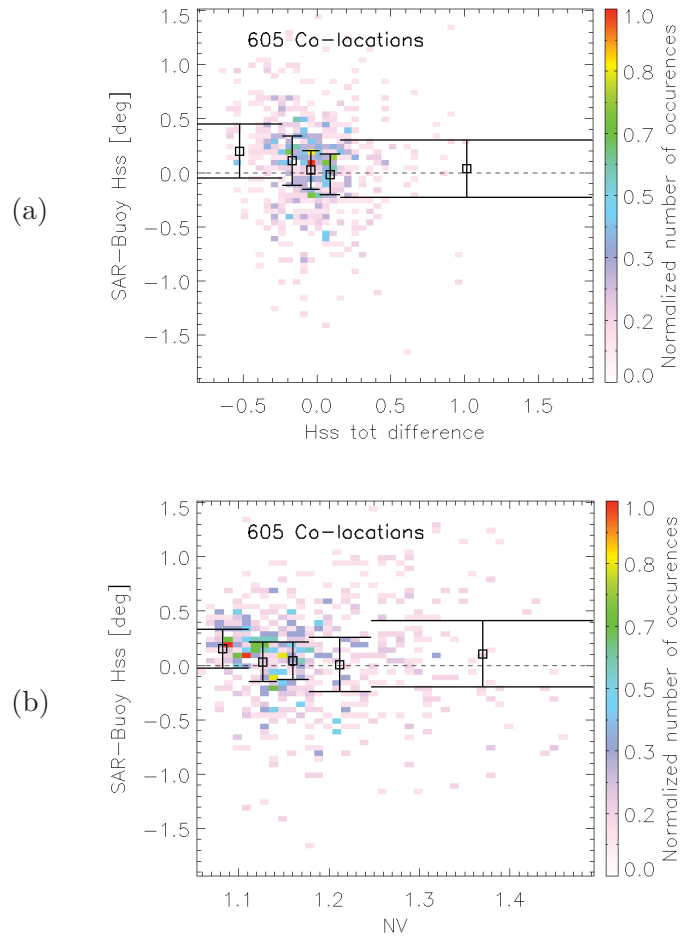


Figure 3.9: Significant swell height measurement errors against the difference between expected and measured total significant wave height (a) and against image normalized variance (b). RMSE and bias are respectively indicated for each of the five subranges by the vertical extent of the solid line segments and their central vertical value, represented by a square.

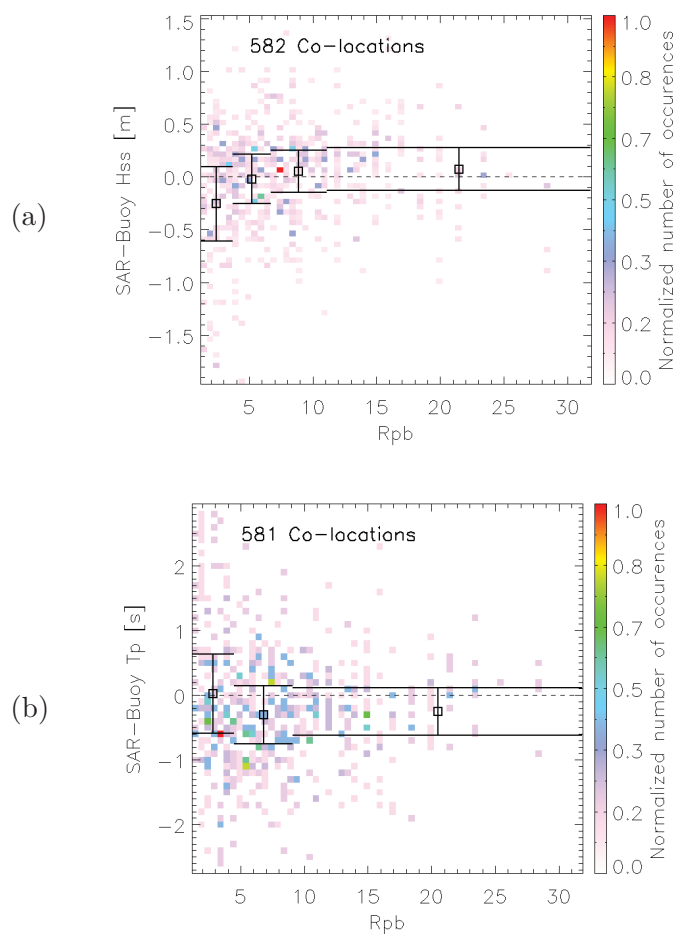


Figure 3.10: Significant swell height (a) and peak period (b) measurement errors against partition peak-to-boundary energy ratio. RMSE and bias are respectively indicated for each of the three subranges by the vertical extent of the solid line segments and their central vertical value, represented by a square.

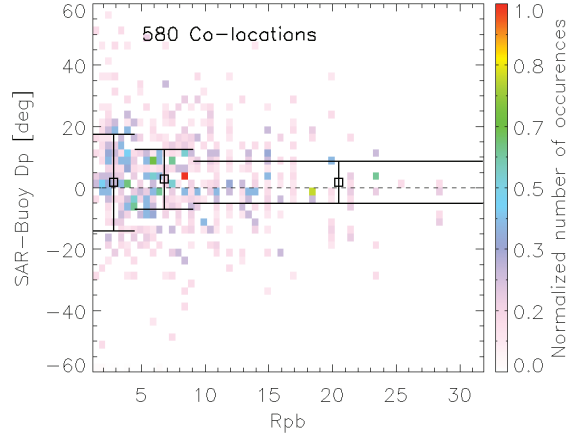


Figure 3.11: Peak direction measurement errors against partition peak-to-boundary energy ratio. RMSE and bias are respectively indicated for each of the three subranges by the vertical extent of the solid line segments and their central vertical value, represented by a square.

cannot be clearly brought out for other integral parameters. For wind speeds less than  $8 \text{ m}\cdot\text{s}^{-1}$ , the RMSE does not vary significantly with the SAR wind speed and stays equal to 0.41 m. On the contrary, it increases for higher wind speeds and reaches 0.57 m.

A significant positive bias of 0.16 m is observed for very small wind speeds. This is most probably due to the fact that the swell spectra estimation is based on a CMOD backscattering model, established using scatterometer data, which are conventional radars. Given their coarse resolution, of the order of 50 km compared to the 10 m resolution of the SAR wave mode, the normalized sea surface roughness they measure is averaged over wide areas over which very low wind conditions are only scarcely met. This results in a reduced NRCS dynamic and artificially increases the significant swell height.

#### 3.4.4.6 Ambiguity factor

Here, we use dataset D, based on dataset B except peak direction outliers are kept and the threshold condition on the minimum ambiguity factor is removed. The effect of an erroneous SAR swell  $180^\circ$  ambiguity removal on the statistics depend on the situation. Whenever both the SAR and the buoy swell spectrum contain a single partition, the direction error equals  $180^\circ$ . On the contrary, if several swell systems are present in one of these two spectra,

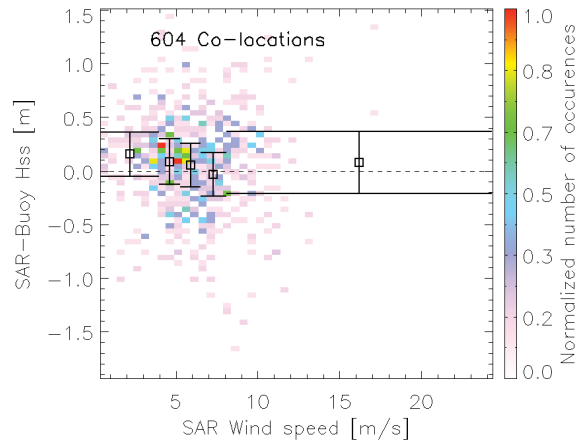


Figure 3.12: Significant swell height measurement errors against SAR wind speed. RMSE and bias are respectively indicated for each of the five sub-ranges by the vertical extent of the solid line segments and their central vertical value, represented by a square.

the peak-to-peak association chooses the two closest peaks. Still, the statistical error increases except in the fortuitous case that buoy partition has a peak period to that of the SAR and a peak direction opposite to that of the SAR, which is quite unlikely.

As shown in Figure 3.13, the measurement error decreases with increasing ambiguity factor. Maximum RMSE, equal to  $35^\circ$ , are given for smaller ambiguity factor and the errors tends to diminish, reaching  $16^\circ$ , for large ambiguity factors.

Still, large errors are noticed for the largest ambiguity factor values. Such uncertainties are probably the consequence of buoy's poor directional sensitivity to low amplitude waves. Indeed, after closer inspection, we notice that large ambiguity factors are given by the longest waves. These waves also have larger phase velocity and move for a greater distance during the time separating two SAR looks of the ocean scene. Additionally, these waves also have a smallest amplitude. The mean significant swell height for waves whose ambiguity factor lies between 0.08 and 0.12 equals 1.46 m. On the contrary, waves whose ambiguity factor is greater than 0.15 have a mean significant swell height of 1.04 m. It is assumed that the associated direction measured by the heave/pitch/roll buoys is noisier because of the much smaller steepness these waves have. It also shows that intrinsic limitations to wave measurements by moored buoys previously described in Section 3.1 can

account for the high errors encountered for large ambiguity factors. Since only the two most energetic peaks can be identified by the buoy, low energy swell systems can be absent from the buoy spectrum and the SAR partition then associated to another swell system.

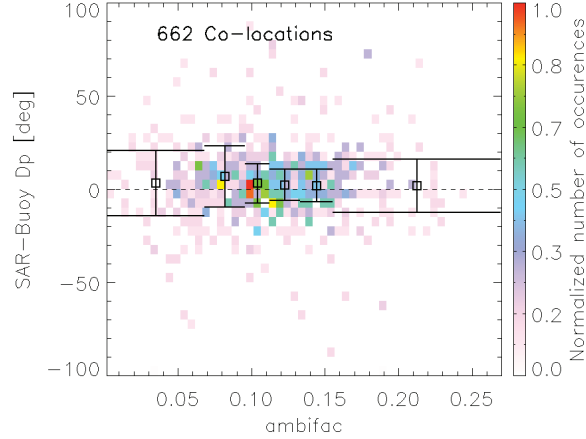


Figure 3.13: Peak direction measurement errors against ambiguity factor. RMSE and bias are respectively indicated for each of the six subranges by the vertical extent of the solid line segments and their central vertical value, represented by a square.

#### 3.4.4.7 Azimuth cut-off

The azimuth cut-off is expected to have a significant effect on the swell spectrum estimation whenever its wavenumber value is close to the swell azimuth wavenumber. The swell azimuth wavenumber  $k_a$ , is the projection of the swell wavenumber along the azimuth axis. It is given by the formula:

$$\lambda_a = \frac{2\pi}{\lambda_p} \cos(D_p - \phi) \quad (3.15)$$

where,  $\lambda_p$  is the peak wavelength;  
 $D_p$ , the peak direction;  
 $\phi$ , the satellite track-angle which is the angle between the North and the satellite azimuth direction.

Let  $k_c$  be the azimuth cut-off wavenumber, then we define the ratio  $R_{az} = k_a/k_c$ . It is limited to values smaller than 0.75 in the best quality flag. Differences affecting the integral parameters estimates with respect to this ratio are illustrated in Figure 3.14 using dataset B.

As expected, the significant swell height bias decreases with increasing values of  $R_{az}$ , moving from 19 cm for smallest values of  $R_{az}$  to -14 cm for largest values. This is due to the fact that, whenever the swell azimuth wavenumber is close to the azimuth cut-off wavenumber, part of the swell partition's energy belongs to short waves that cannot be imaged. As for peak period, its bias increases with increasing values of  $R_{az}$ , moving from -0.77 s for smallest values of  $R_{az}$  to 0.07 s for largest values. This is also foreseen since the energy cut-off in short periods moves the partition peak toward higher periods.

Also, one would expect the significant swell height and peak period bias to be close to zero for low values of  $R_{az}$ . Though, the significant swell height was corrected so that its mean bias reaches zero. For the peak period, low values of  $R_{az}$  are most often related to very long swell, which explains the importance negative bias. Indeed, very long swell period are largely underestimated as evidenced in paragraph 3.4.4.2, page 101.

#### 3.4.4.8 Propagation time

The effect of the propagation time on data quality is estimated using dataset F, based on dataset B except we accept to propagate the swell observations for up to 1,000 km before they reach the buoy vicinity. This distance is converted in time using the group velocity in deep ocean. As expected, the RMSE increases with increasing time (Figures 3.15 and 3.16). After 24 hours of propagation, the RMSE increase reaches 62%, 48% and 28% for the peak period, significant swell height and peak direction, respectively, as compared to the time of observation.

### 3.5 Conclusion

In this chapter, we have proposed a validation method of the SAR swell measurements using comparison with measurements of directional spectra from moored buoys belonging to the NODC network. This method is quite different from the ones that have been previously used to validate SAR measurements (*Johnsen and Collard, 2004; Johnsen et al., 2006; Collard et al., 2009*). This very same method will be further used to estimate the accuracy of the Level-3 SAR products. Also, to increase the total number of co-locations, we propose a dynamical co-location method. Using the linear propagation theory, SAR observations are propagated for up to 500 km, increasing the co-location dataset by a factor 5 and allowing for a better data characterization and the statistical results. Still, keeping strict criteria for best data quality, the total number of co-locations for years 2002 to 2009

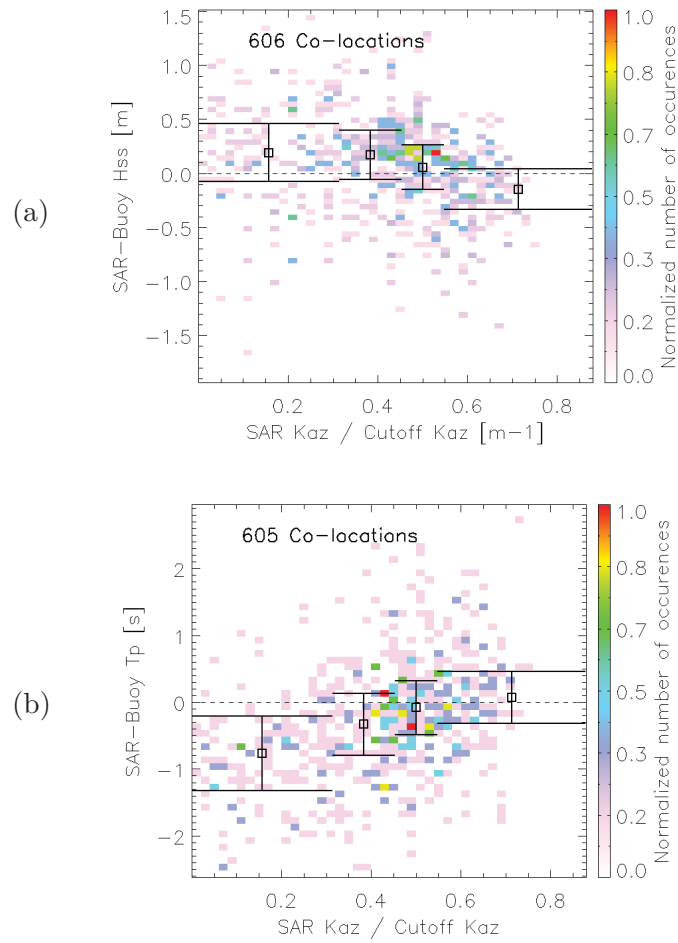


Figure 3.14: Significant swell height (a) and peak period (b) measurement errors against the ratio between SAR azimuth wavenumber and azimuth cut-off wavenumber. RMSE and bias are respectively indicated for each of the four subranges by the vertical extent of the solid line segments and their central vertical value, represented by a square.

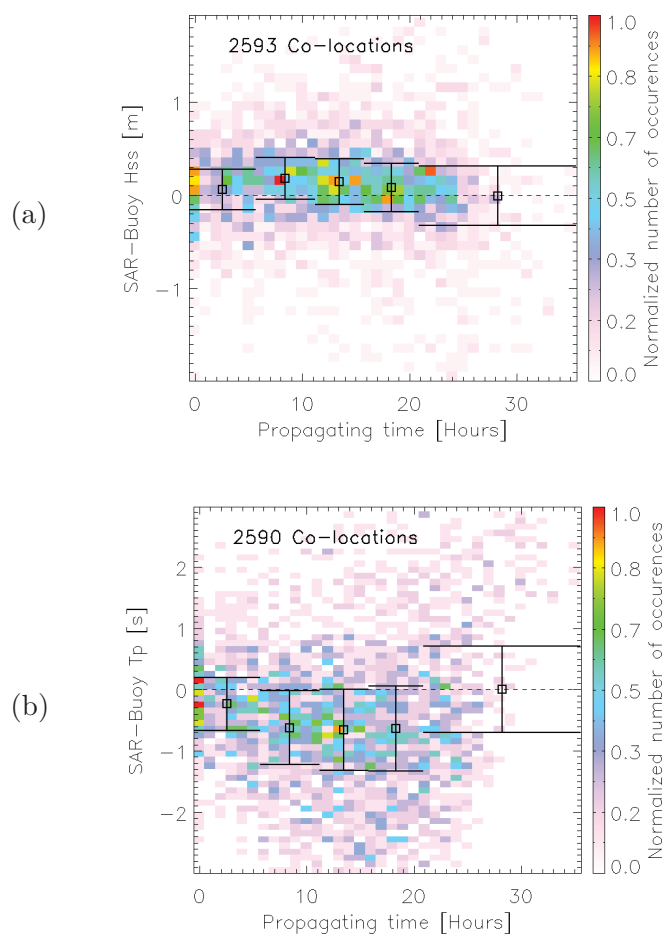


Figure 3.15: Significant swell height (a) and peak period (b) measurement errors against the propagating time separating the SAR observation from its virtual position when propagated to the buoy. RMSE and bias are respectively indicated for each of the four subranges by the vertical extent of the solid line segments and their central vertical value, represented by a square.

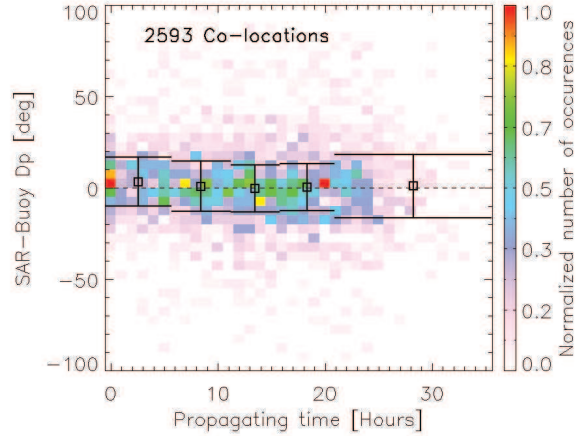


Figure 3.16: Peak direction measurement errors against the propagating time in hours that separates the SAR observation from its virtual position when propagated to the buoy. RMSE and bias are respectively indicated for each of the four subranges by the vertical extent of the solid line segments and their central vertical value, represented by a square.

falls from 22,494 down to 147.

In order to remove the bias on significant swell height, we have proposed a new bias correction which depends on the peak wavelength, sea surface wind speed and wave height. Statistics indicate RMSE of 31 cm for the significant swell height, 0.70 s for the peak period and  $16^\circ$  for the peak direction. SAR estimates of significant swell height and peak period seem to have a weaker dynamic than *in situ* measurements. For instance, for values larger than 2 m, mean under-estimation of SAR significant swell height reaches 0.51 m and for values larger than 15.5 s, mean under-estimation of SAR peak period reaches 1.1 s.

Finally, the impact of several parameters on the accuracy of the SAR swell measurements was estimated. This study is important for it will be the base of the data confidence estimation in each SAR observation used for SAR products of higher levels, as proposed in Chapter 6.

Investigating the dependences on normalized variance, we have introduced a criterion faithfully reproducing the behavior of the SAR total significant swell height with respect to the SAR wind speed and the SAR image normalized variance.

Also, we have introduced the partition peak-to-boundary energy ratio which, estimated for each SAR and buoy partition, appears to be a very

good quality flag. SAR integral parameters' accuracy increases with that quantity.

Wind speed dependence indicates best SAR estimations are given for sea surface wind speeds between 4 and 8 m.s<sup>-1</sup> and slight increases of SAR bias and RMSE away from this range.

As for the ambiguity factor which is an indicator of the confidence in the SAR direction of propagation, the accuracy clearly increases with that parameter. However, we suspect that for longest swell, which have very small steepness and for which the ambiguity factor is very large, buoy peak direction estimates are noisier due to other simultaneous wave systems of larger steepness.

Then, the influence of the azimuth cut-off is estimated looking at the ratio between the swell azimuth wavenumber and the azimuth cut-off wavenumber. As expected, the biases on the SAR significant swell height and peak period respectively increases and decreases as this ratio gets closer to zero.

The influence of the propagation time is also quite clear and the measurement errors clearly increase with respect to this parameter, especially for the peak period.

This validation study confirms the expected behavior of the SAR swell inversion described in Chapter 1. For instance, the effects of intense winds and the associated azimuth cut-off are clearly visible and quantified. They seem to well explain the important under-estimation of greatest SAR significant swell heights and on average, are still visible for values of the SAR peak wavelength twice larger than the azimuth cut-off wavelength. Even if bias corrections can be applied to the significant swell height estimates afterwards, there is still a need for further improvements of the SAR swell inversion. In addition, some unexpected and systematic bias are highlighted. This is the case of the large peak period under-estimation of longest swells. We are led to think that this partly results from an inappropriate spectral filtering which was initially meant to remove low wavenumber signal originating from non-wave features. Yet, it is very difficult to correct for these systematic errors without increasing the estimation errors. Certainly, we do not dispose of enough SAR measurement co-locations to properly characterize them. This task shall be facilitated by the further developments proposed in Chapters 5 and 6.

## Bibliography

- Aarnes, J. E., and H. E. Krogstad (2001), Partitioning sequences for the dissection of directional ocean wave spectra: A review, *Part of work package, 4*, 2001–00,017. 88
- Ash, E., D. Carter, and F. Collard (2010), Wave data quality report, phase 1 - globwave project, *Globwave deliverable*. 84
- Benoit, M., P. Frigaard, and H. A. Schäffer (1997), Analyzing multidirectional wave spectra: a tentative classification of available methods, in *Proceedings of the 1997 IAHR conference, San Francisco*, p. 131–158, The Johns Hopkins University Press, Baltimore. 82
- Borgman, L. E. (1982), Maximum-entropy and data-adaptive procedures in the investigation of ocean waves, *Maximum-Entropy and Bayesian Methods in Inverse Problems*, D. Reidel, Dordrecht, p. 429–442. 82
- Brüning, C., and S. Hasselmann (1994), Extraction of wave spectra from ERS-1 SAR wave-mode spectra by an improved SAR inversion scheme, *European Space Agency - Publications - ESA-SP, 365*, 45–45. 86
- Brüning, C., S. Hasselmann, K. Hasselmann, S. Lehner, and T. Gerling (1994), First evaluation of ERS-1 synthetic aperture radar wave mode data, *Global Atmos. Ocean Syst*, 2(1), 61–98. 86, 87
- Collard, F., B. Chapron, F. Ardhuin, H. Johnsen, and G. Engen (2006), Coastal ocean wave retrieval from ASAR complex images, in *Proceedings of OceanSAR*, Saint John's, Canada. 91
- Collard, F., F. Ardhuin, and B. Chapron (2009), Monitoring and analysis of ocean swell fields from space: New methods for routine observations, *Journal of Geophysical Research-Oceans*, 114(C7), C07,023. ii, 2, 68, 69, 70, 71, 80, 85, 111, 152, 153, 155, 219, 239
- Cotton, P. D. (1998), A feasibility study for a global satellite buoy intercalibration experiment, *SOC Research and consultancy report*, (26). 83
- Delpey, M., F. Ardhuin, F. Collard, and B. Chapron (2010), Space-time structure of long swell systems, *J. Geophys. Res.*, 115, C12,037, doi:10.1029/2009JC005885. ii, 2, 90, 152, 180, 186, 189, 192, 241
- Durrant, T. H., D. J. M. Greenslade, and I. Simmonds (2009), Validation of jason-1 and envisat remotely sensed wave heights, *Journal of Atmospheric and Oceanic Technology*, 26(1), 123–134. 83

- Gerling, T. W. (1992), Partitioning sequences and arrays of directional ocean wave spectra into component wave systems, *Journal of Atmospheric and Oceanic Technology*, 9(4), 444–458. 86, 88, 95
- Hanson, J. L., and O. M. Phillips (2001), Automated analysis of ocean surface directional wave spectra, *J. Atmos. Ocean Technol.*, 18, 277–293. 2, 86, 91, 152, 192
- Hasselmann, S., C. Bruning, K. Hasselmann, and P. Heimbach (1996), An improved algorithm for the retrieval of ocean wave spectra from synthetic aperture radar image spectra, *Journal of Geophysical Research*, C7(101). 41, 86, 87, 89, 95
- Johnsen, H., and F. Collard (2004), ASAR wave mode processing-validation of reprocessing upgrade, *Tech. rep.*, technical report for ESA-ESRIN under contract 17376/03/I-OL, Tech. Rep. 168, NORUT. ii, 80, 83, 91, 111
- Johnsen, H., G. Engen, F. Collard, V. Kerbaol, and B. Chapron (2006), ENVISAT ASAR wave mode products-quality assessment and algorithm upgrade, *Proceedings of SEASAR*. ii, 2, 111
- Kerbiriou, M., M. Prevosto, C. Maisondieu, A. Babarit, and A. Clément (2007), Influence of an improved sea-state description on a wave energy converter production, in *Proceedings of the 26th International Conference on Offshore Mechanics and Arctic Engineering*. 89
- Lygre, A., and H. E. Krogstad (1986), Maximum entropy estimation of the directional distribution in ocean wave spectra, *Journal of physical oceanography*, 16, 2052–2060. 82
- Navy, U. S. (1981), US navy marine climate atlas of the world IX, worldwide means and standard deviations, *Nav. Oceanogr. Command Detachment, Asheville, NC*. 80
- O'Reilly, W. C., T. H. C. Herbers, R. J. Seymour, R. T. Guza, et al. (1996), A comparison of directional buoy and fixed platform measurements of pacific swell, *Journal of Atmospheric and Oceanic Technology*, 13(1), 231–238. 81, 224
- Portilla, J., F. Ocampo-Torres, and J. Monbaliu (2009), Spectral partitioning and identification of wind sea and swell, *Journal of Atmospheric and Oceanic Technology*, 26(1), 107–122. iii, 86, 87
- Vincent, L., and P. Soille (1991), Watersheds in digital spaces: an efficient algorithm based on immersion simulations, *IEEE transactions on pattern analysis and machine intelligence*, p. 583–598. 88

Voorrips, A. C., V. K. Makin, and S. Hasselmann (1997), Assimilation of wave spectra from pitch-and-roll buoys in a north sea wave model, *J. Geophys. Res.*, *102*(C3), 5829–5849. 86

Young, I. R., and T. Glowacki (1996), Assimilation of altimeter wave height data into a spectral wave model using statistical interpolation, *Ocean Eng.*, *23*(8), 667–689. 86

# Chapter 4

## Swell stroboscopic imaging

### Contents

---

4.1	Stroboscopic imaging principle . . . . .	<b>120</b>
4.1.1	The phenomenon . . . . .	120
4.1.2	Classification . . . . .	121
4.1.3	Stroboscopic swell configurations . . . . .	127
4.1.4	Case examples of SI . . . . .	127
4.2	Probability of missing a swell system . . . . .	<b>132</b>
4.2.1	Considering ascending and descending passes alone . . . . .	132
4.2.2	Considering a full orbit . . . . .	137
4.3	Case of Sentinel-1 . . . . .	<b>138</b>
4.3.1	Stroboscopic swell configurations . . . . .	141
4.3.2	Probability of missing a swell system considering a full orbit . . . . .	145
4.4	Conclusion . . . . .	<b>148</b>
	Bibliography . . . . .	<b>150</b>

---

The present chapter focuses on the dynamical behaviors of a swell field and the SAR instrument ground track with respect to one another to study their impact on ocean swell sampling. As mentioned in Chapter 2, a swell field is composed of a coherent system of waves of different periods propagating in different directions. As will be seen, certain directions and periods may lead to peculiar space and time sampling of the ocean surface by the SAR instrument for which a swell region may always or never be observed. Studying the occurrence of such conditions contributes to a better understanding of the forthcoming attempt to reconstruct ocean swell fields using SAR measurements (cf. Chapter 5).

First, the phenomenon leading to steady imaging of a swell region by a spaceborne satellite is described before identifying the conditions of occurrences. Second, using these conditions, the probability that a swell is not imaged by the satellite is calculated when considering ascending and descending passes alone and then combined. Finally, the previous study is reproduced taking the example of the future SAR mission Sentinel-1 and show how the different orbits induce significant changes.

## 4.1 Stroboscopic imaging principle

### 4.1.1 The phenomenon

The present chapter focuses on SAR instruments placed on-board satellites with sun-synchronous orbits. As an example, ENVISAT satellite ground tracks are given on Figure 4.1. In this case, from one day to the next and at  $40^\circ$  latitude, the satellite ground track is located around 600 km to the east of that of the previous day. This also corresponds to the group velocity of 9 s swells<sup>1</sup>. In this situation, these swells, whenever traveling eastward, may repeatedly or never be imaged by the satellite depending on their phasing with the satellite passes. This phenomenon is referred to as *stroboscopic imaging*, hereafter denoted *SI*.

In the first case, the same swell would be imaged at different times along its propagation. Even though it could be interesting to verify that the swell period is constant while observing conditions may change for validation purposes, this case does not bring much information on the overall swell field. In the second case, no information at all is available on the propagating swell. For these reasons, the occurrence of SI conditions is a major handicap for ocean swell imaging.

The previously described case example is especially interesting since, in the North Atlantic Ocean, this situation is frequent near Cap Farewell. Indeed, studies by *Moore and Renfrew (2005)* using Seawinds instrument

---

1. For group velocity calculation, cf. Chapter 2, Subsection 2.1.4.

on-board QuikSCAT have shown high wind speed events were common in this region with wind speed above  $25 \text{ m.s}^{-1}$  more than 15% of the time. This shows that in addition to the identification of SI conditions, a study of the mean wave conditions is necessary to determine how frequent SI conditions can be met in reality. The goal of this chapter is to identify the configurations favorable to SI, and see how they can affect SAR capability to monitor ocean swells.

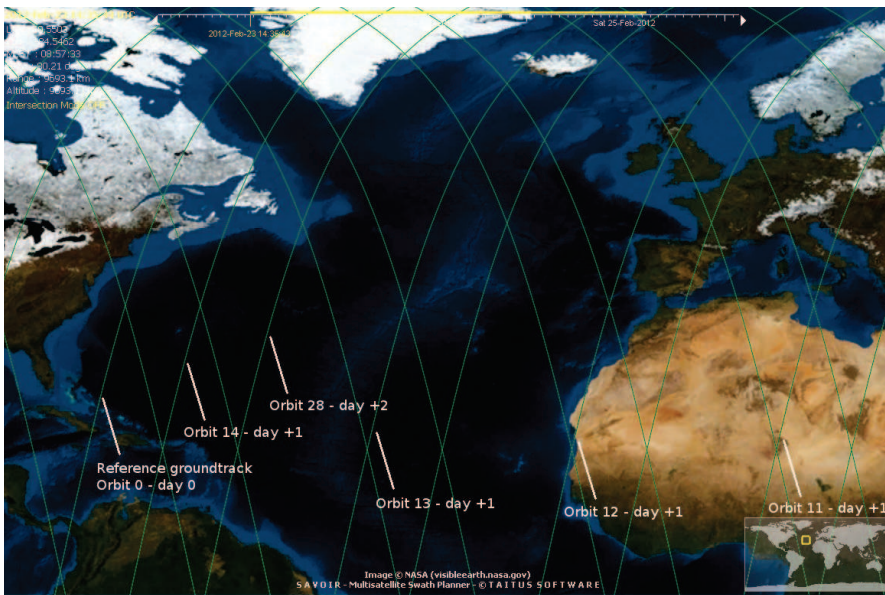


Figure 4.1: ENVISAT satellite ground track over 3 days during the extended orbit period. Given a reference track, the orbit number and day are indicated for different ones other. Screenshot acquired from SAVOIR software.

#### 4.1.2 Classification

Assuming that the look angle of the SAR wave mode is fixed<sup>2</sup>, ASAR wave mode coverage can easily be obtained from acquired data or orbit and pointing parameters. Basically, it is equivalent to the satellite ground track except it is sampled every 100 km and it is shifted several hundreds kilometers off-track due to the right-side look angle of the instrument.

Given a starting latitude and a propagation direction, a virtual swell is placed at a wave mode sampling point. Then, the swell trajectory is calculated following the linear theory (cf. Chapter 2, Section 2.1). The intersec-

<sup>2</sup>. This is the case in practice even though, technically, ENVISAT satellite is able to acquire wave mode data at different look angles.

tion between the swell propagation trajectory and the SAR wave mode track determines a propagation distance and duration. The group velocity corresponding to this distance and duration can be estimated and corresponds to a given swell period that would be imaged a second time. Given the new propagation direction and location of the virtual swell, this process is iterated over a 5-day period. For each step, the period at which the swell would be re-imaged by the satellite from one to the next is calculated. Whenever the calculated periods are close enough from one another, SI conditions are fulfilled.

In this example, SI conditions are met for eastward propagating swell. AS illustrated in Figure 4.11, for a propagation direction parallel to the equator, the distance between a starting wave mode track and the eastern track of the next day equals around 1050 km at the equator whereas it equals 1800 km when considering the western wave mode track of the next day. Only extremely long swells, with periods exceeding 25 s, can cover this distance in 24 hours. As it is not currently possible to observe such swells with ASAR, only eastward propagating swell cases are investigated.

In practice, for a better analysis and understanding, ascending and descending passes<sup>3</sup> are first treated separately. Propagation directions investigated are ranging from 0 to 180°, starting clockwise from the North with a 11.25° bin size.

SI occurrences are classified in three categories:

- SI: the range of periods at which the swell are be re-imaged by the satellite from one to the next, estimated for 5 successive days, is smaller than 1 s;
- near SI: the range of periods at which the swell are be re-imaged by the satellite from one to the next, estimated for 5 successive days, is greater than 1 s and smaller than 2 s;
- no SI: the range of periods at which the swell are be re-imaged by the satellite from one to the next, estimated for 5 successive days, is greater than 2 s.

This classification has been evaluated for all propagation directions and, once every two bins, the most *stroboscopic* conditions out of these three is indicated by a color code and the mean stroboscopic swell period is indicated for each direction on Figures 4.2 and 4.3.

**SI conditions:** They are given by the following quadruplet:

- orbit phase: descending or ascending;

---

3. For sun-synchronous satellites, ascending ground tracks stretch from SE to NW whereas descending ground tracks stretch from NE to SW.

- starting latitude;
- starting propagation direction;
- swell period.

All the SI quadruplets are explicitly given in Tables 4.1 and 4.2 and a graphical summary of these results is proposed in Figures 4.2 and 4.3. They were estimated for starting latitudes ranging from  $-50$  to  $50^\circ$ , placed every  $10^\circ$ . Quite hopefully, a North-South symmetry is found (not shown): the SI configurations given for ascending passes in the Northern Hemisphere are the same for descending passes in the Southern Hemisphere. Therefore, swell propagation in the North Hemisphere only is further considered.

Starting latitude	Period [s]	Starting propagation direction [deg.]
50°N	[7.5, 8.5]	[56.25, 67.5]
	[8, 9]	[67.5, 78.75]
40°N	[9, 10]	[56.25, 67.5]
	[9.5, 10.5]	[67.5, 78.75]
30°N	[10.5, 11.5]	[56.25, 67.5]
	[10.5, 11.5]	[67.5, 78.75]
20°N	[11.5, 12.5]	[56.25, 67.5]
	[12, 13]	[67.5, 78.75]
	[12.5, 13.5]	[78.75, 90]
	[13.5, 14.5]	[90, 101.25]
10°N	[12, 13]	[56.25, 67.5]
	[12, 13]	[67.5, 78.75]
	[13, 14]	[78.75, 90]
	[13.5, 14.5]	[90, 101.25]
0°N	[12.5, 13.5]	[56.25, 67.0]
	[12.5, 13.5]	[67.5, 78.75]
	[13, 14]	[78.75, 90]
	[13.5, 14.5]	[90, 101.25]

#### ASCENDING PASSES

Table 4.1: Conditions on starting latitude, swell peak period and starting propagation direction leading to stroboscopic imaging when considering ENVISAT ascending passes only.

Starting latitude	Period [s]	Starting propagation direction [deg.]
50°N	[8, 9]	[78.75, 90]
	[8.5, 9.5]	[90, 101.25]
40°N	[9.5, 10.5]	[78.75, 90]
	[10, 11]	[90, 101.25]
30°N	[11, 12]	[78.75, 90]
	[11, 12]	[90, 101.25]
20°N	[11.5, 12.5]	[78.75, 90]
	[12, 13]	[90, 101.25]
10°N	[12.5, 13.5]	[78.75, 90]
	[12, 13]	[90, 101.25]
	[12.5, 13.5]	[101.25, 112.5]
	[13, 14]	[112.5, 123.75]
	[14, 15]	[123.75, 135]
	[15, 16]	[135, 136.25]
0°N	[14.5, 15.5]	[56.25, 67.5]
	[13.5, 14.5]	[67.5, 78.75]
	[13, 14]	[78.75, 90]
	[12.5, 13.5]	[90, 101.25]
	[12.5, 13.5]	[101.25, 112.5]
	[12.5, 13.5]	[112.5, 123.75]

## DESCENDING PASSES

Table 4.2: Conditions on starting latitude, swell peak period and starting propagation direction leading to stroboscopic imaging when considering ENVISAT descending passes only.

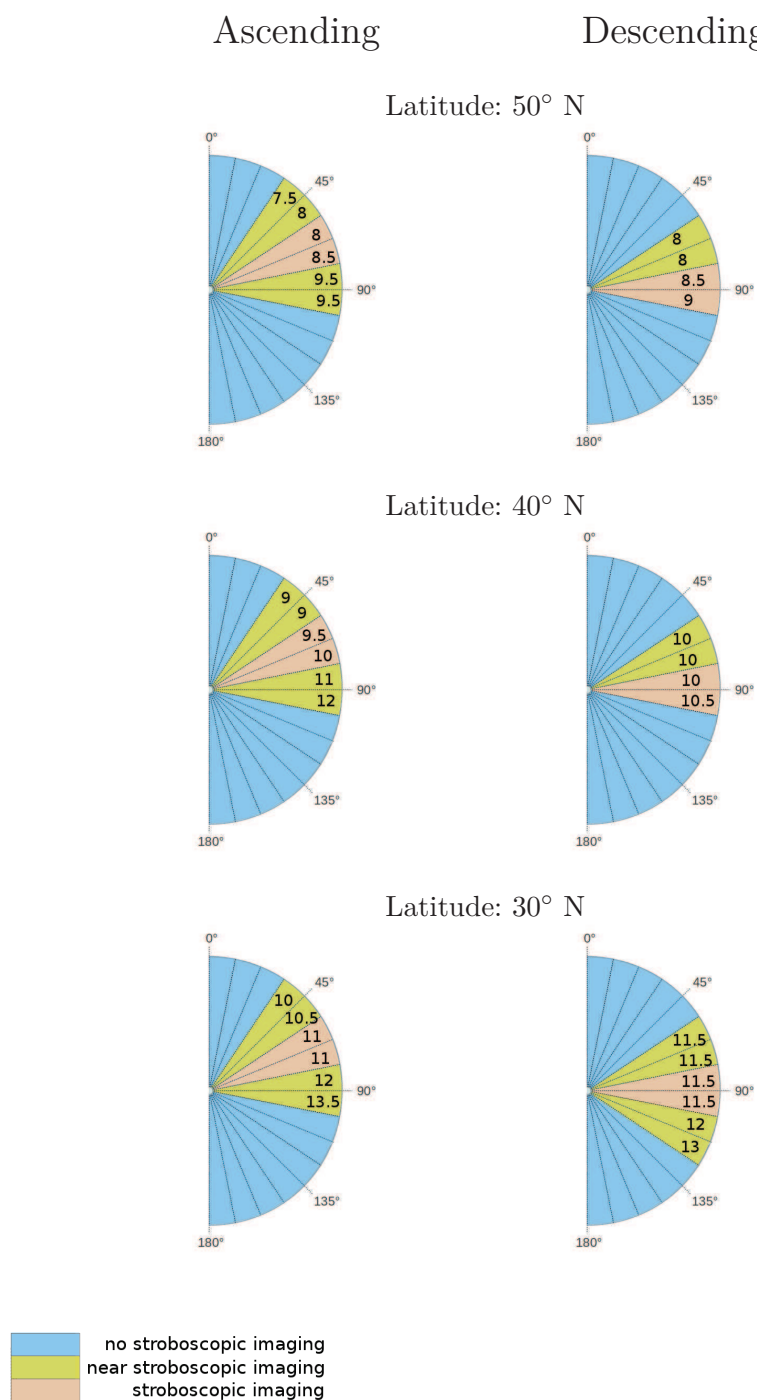


Figure 4.2: SI occurrences with mean re-imaging period calculated over a 5-day period for swell propagating from starting latitude of 50, 40 and 30° with starting propagation direction ranging from 0 to 180°. Left and right column correspond to the results using ascending and descending passes of ENVISAT, respectively.

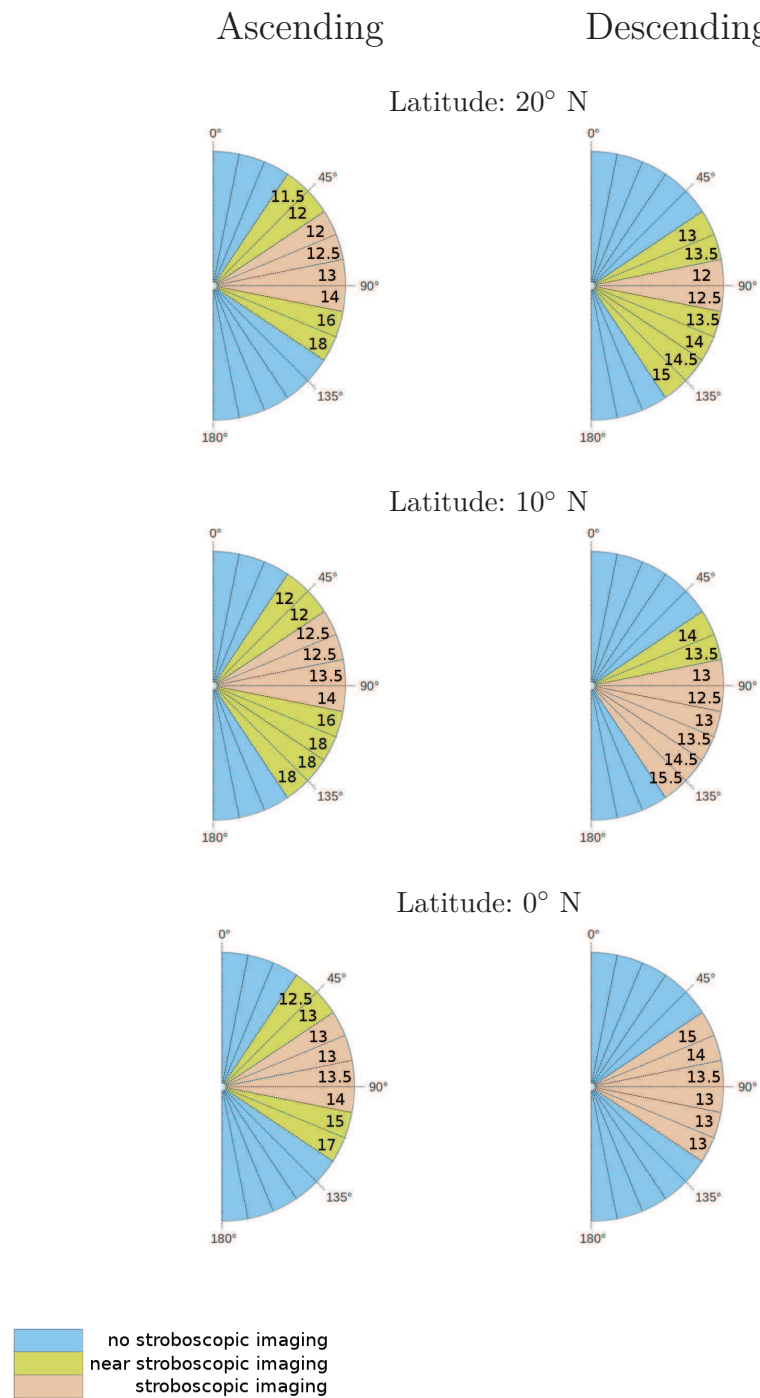


Figure 4.3: SI occurrences with mean re-imaging period calculated over a 5-day period for swell propagating from starting latitude of 20, 10 and 0° with starting propagation direction ranging from 0 to 180°. Left and right column correspond to the results using ascending and descending passes of ENVISAT, respectively.

### 4.1.3 Stroboscopic swell configurations

For ascending passes, the SI main direction is ENE and rather constant with respect to the starting latitude. The SI period increases with a decreasing latitude, reaching up to 14 s at the equator. For instance, at 50° latitude, SI conditions are obtained in two cases:

$$\begin{aligned} 7.5 \text{ s} < T < 8.5 \text{ s} \quad \text{and} \quad 56.25^\circ < D_s < 67.5^\circ \\ 8 \text{ s} < T < 9 \text{ s} \quad \text{and} \quad 67.5^\circ < D_s < 78.75^\circ \end{aligned} \quad (4.1)$$

where  $T$  is the swell period and  $D_s$ , the starting propagation direction.

For descending passes, the SI main direction behavior is quite similar: oriented to the East and rather constant with respect to the starting latitude. Similarly as for ascending passes, the SI period increases with a decreasing latitude, reaching up to 15 s at the equator. This behavior can be explained by the fact that the distance between two points at the same latitude and located on two successive orbit paths increases with decreasing latitude. For instance, at 50° latitude, SI conditions are obtained in two cases:

$$\begin{aligned} 8 \text{ s} < T < 9 \text{ s} \quad \text{and} \quad 78.75^\circ < D_s < 90^\circ \\ 8.5 \text{ s} < T < 9.5 \text{ s} \quad \text{and} \quad 90^\circ < D_s < 101.25^\circ \end{aligned} \quad (4.2)$$

### 4.1.4 Case examples of SI

Typical cases where the SI effects are visible on the SAR propagated observation distribution is shown on Figures 4.4, 4.5, 4.6 and 4.7. They are representations of SAR swell measurements belonging to the same swell system and whose positions at the given time are extrapolated using linear theory (cf. Chapter 2, Section 2.1). The methodology allowing for the association of isolated SAR swell measurements into coherent swell fields is further detailed in Chapter 5.

Particularly visible on Figure 4.4, the propagated observations are irregularly distributed and exhibit ridge-like structures parallel to the transverse direction. Among the propagated positions of the swell measurements, the ground tracks of those acquired during the ascending passes intersect for swell frequencies and directions given by SI conditions. At the considered time step, this phenomenon occurs around 18°S, 105°W for wavelength around 270 m, corresponding to periods of 13.2 s, and direction of 75°. Since it is located in the Southern Hemisphere, that would correspond in the Northern Hemisphere to the observation of descending passes, with swell directions of 105° and identical periods. Effectively, it corresponds to the expected SI conditions given at the latitudes around 10 and 20°N.

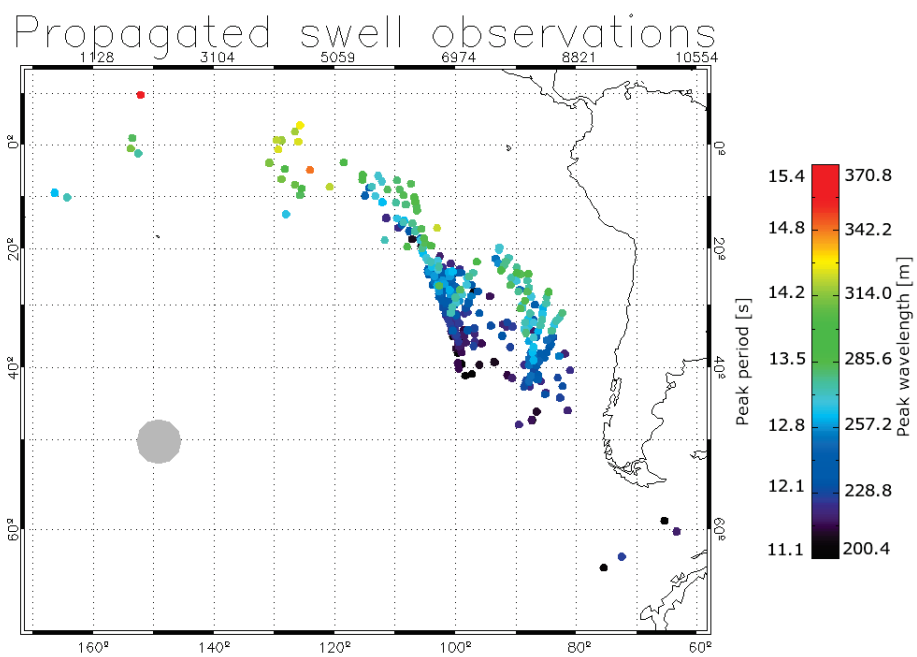


Figure 4.4: Distribution of the propagated SAR observations during ascending and descending passes of a swell field generated by a storm that occurred in the South Pacific Ocean on 29 August 2008. Storm source region is represented by a gray disk.

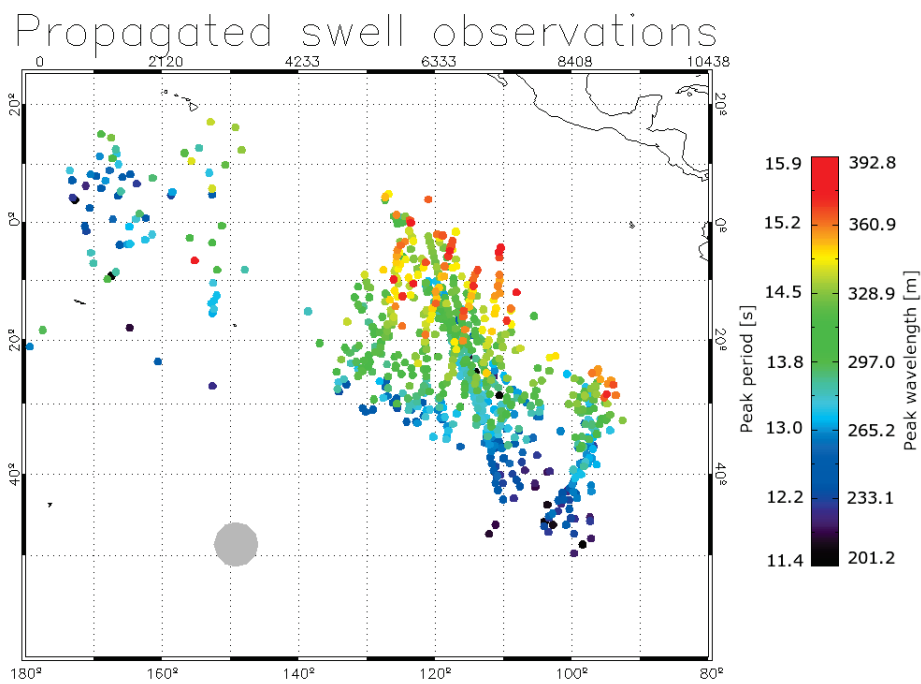


Figure 4.5: Distribution of the SAR propagated observations during ascending and descending passes of a swell field generated by a storm that occurred in the South Pacific Ocean on 1 September 2008. Storm source region is represented by a gray disk.

## Propagated swell observations

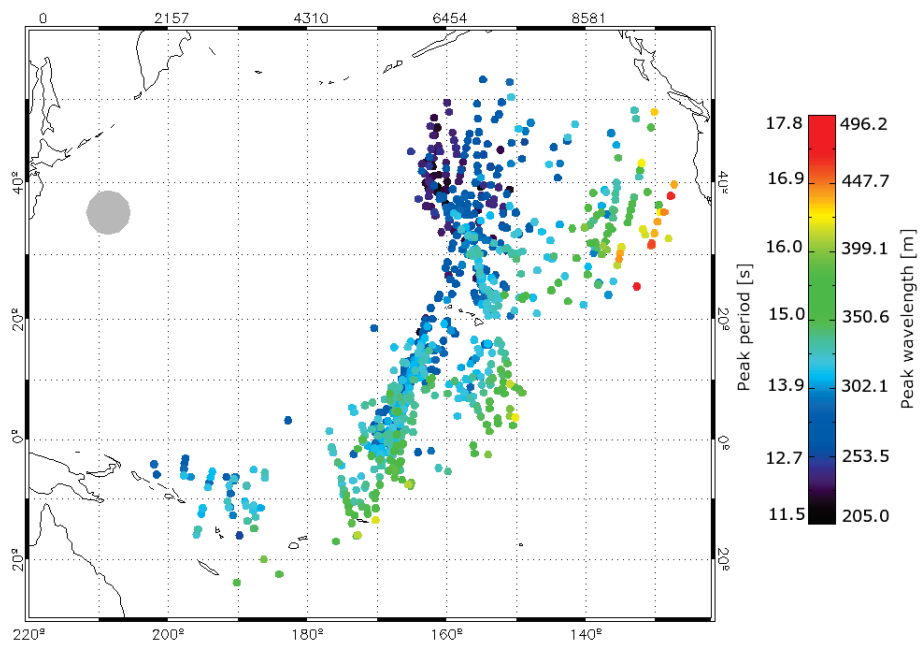


Figure 4.6: Distribution of the SAR propagated observations during ascending and descending passes of a swell field generated by a storm that occurred in the North Pacific Ocean on 26 December 2008. Storm source region is represented by a gray disk.

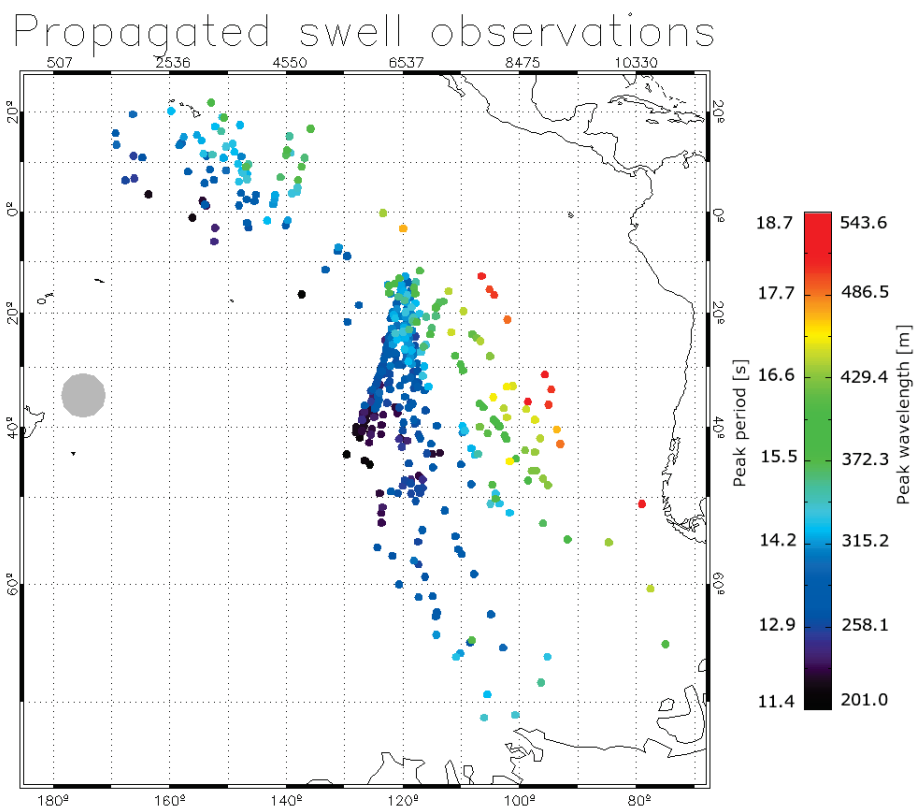


Figure 4.7: Distribution of the SAR propagated observations during ascending and descending passes of a swell field generated by a storm that occurred in the South Pacific Ocean on 27 July 2008. Storm source region is represented by a gray disk.

## 4.2 Probability of missing a swell system

In this section, the probability that a swell system is not imaged by the SAR instrument over a 5-day period is estimated whenever SI conditions presented in the previous section are met.

### 4.2.1 Considering ascending and descending passes alone

#### 4.2.1.1 General formulation

First, we consider ascending or descending passes alone for all SI quadruplets. Also, that probability dependence on swell period is addressed.

For a simplified analysis, the swell packet is monochromatic (all swells have the same period) and originate from a storm region modeled by a disk of diameter  $D_{\text{source}}$ . Reminded that the group velocity  $C_g$ , of a swell of period  $T_p$  propagating in deep ocean is given by  $C_g = g/(4\pi)T_p$ , there is no dispersion for the swell packet. Hence, its size does not vary while propagating. As illustrated in Figure 4.8,  $D_{\text{orbit}}$  and  $l$  are defined as follows:  $D_{\text{orbit}}$  is the great-circle distance between the points defined by the intersections of an orbit and of the closest eastward orbit of the next day with the swell trajectory and  $l$ , the great-circle distance between the points intersecting two successive orbits and the swell trajectory.

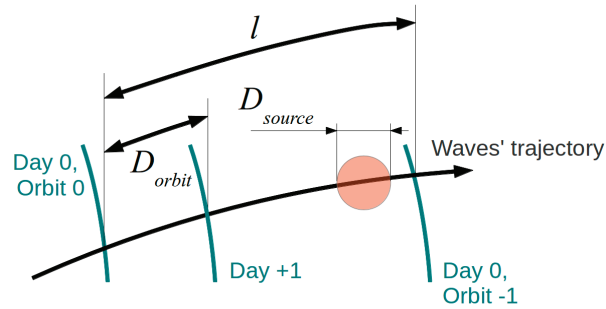


Figure 4.8: Geometry of the satellite ground track, for ascending passes, imaging a swell system located within the red disk and whose trajectory is symbolized by a black line.

Given the time between these two satellite passes  $\Delta t$ , the exact period satisfying SI conditions,  $T_{SI}$ , is given by:

$$T_{SI} = \left(\frac{4\pi}{g}\right)^{-1} \frac{D_{\text{orbit}}}{\Delta t} \quad (4.3)$$

The analysis focuses on swell whose period  $T_p$  is close to  $T_{SI}$  and, more precisely, satisfying the following condition:

$$\frac{4}{5} < \frac{T_p}{T_{SI}} < \frac{6}{5} \quad (4.4)$$

As regards the left-side relation, when  $T_p$  is smaller than  $T_{SI}$ , the distance covered by the propagating swells during  $\Delta t$  is smaller than  $D_{\text{orbit}}$ . The threshold on the swell period is then obtained when this delay, accumulated after 5 days, reaches  $D_{\text{orbit}}$ , corresponding to the fact that the satellite ground track has caught up the slow-moving swells. Similarly, the right-side relation is obtained for swells with a period larger than  $T_{SI}$ . In this case, the threshold on the swell period is obtained when the accumulated advance reaches  $D_{\text{orbit}}$ , corresponding to the fact that the fast-moving swell has caught up the next satellite ground track.

It might be thought that  $D_{\text{orbit}}$  depends on the starting latitude and propagation direction. For directions parallel to the equator,  $D_{\text{orbit}}$  is obviously a constant. Though, apart from such cases, considering a direction corresponding to SI conditions, this distance remains the same along the swell trajectory. This is due to the fact that the variation of  $D_{\text{orbit}}$  with the latitude are compensated with the propagation direction variations along the swell trajectory.

Let  $C$  be the proposition: "the propagating swell system of diameter  $D_{\text{source}}$  and swell period  $T_p$  is not imaged over a 5-day period, by one of the ascending or descending passes alone". Then, if  $T_p = T_{SI}$ , this probability is given by:

$$P(C) = 1 - \frac{D_{\text{source}}}{l + D_{\text{source}}} \quad (4.5)$$

It corresponds to the probability that a point randomly chosen along a path of length  $l + D_{\text{source}}$  does not fall within a segment of length  $D_{\text{source}}$ .

Now,  $P(C)$  is estimated considering that  $T_p$  is not necessarily equal to  $T_{SI}$  but that it fulfills the condition given by relation 4.4. Figure 4.9 illustrates how to calculate this probability: the five daily positions of the propagated swell source region are placed on an  $\mathbf{Ox}$  axis. Their abscissa is equal to their distance from their initial position modulo  $D_{\text{orbit}}$ . Then, several scenarios emerge:

1. all propagated regions are occupying the exact same location: this corresponds to the case when  $T_p = T_{SI}$ , as shown on Figure 4.9 (c).
2. when swell periods are close to  $T_{SI}$ , all propagated regions occupy a wider area. This corresponds to cases (a) and (b) on Figure 4.9.

3. swell period are so different from  $T_{SI}$  that, or they occupy the entirety of the space left between orbits of two successive days, or the space they occupy is equal to five times their individual extent if  $l > 5D_{\text{source}}$ . For sun-synchronous satellites such as ENVISAT, at the equator, in the eastward direction,  $l$  is about 2800 km.

The probability for the swell system to be imaged by the instrument at least once equals the total distance of occupied segments along the  $\mathbf{Ox}$  axis divided by  $l + D_{\text{source}}$ . Applying this to the last three aforementioned cases, probability  $P(C)$  is given by:

$$P(C) = 1 - \frac{\min\{5D_{\text{source}}, l\}}{l + D_{\text{source}}} \quad (4.6)$$

For the first case,  $P(C)$  has already been given in equation 4.5. As for intermediate cases, the probability varies linearly between these two extreme values.

#### 4.2.1.2 Occurrence in real conditions

Now that the conditions that are unfavorable to swell SAR observation have been identified, it is necessary to quantify the probability that such conditions are met in reality. To do so, the swell information given by the spectral wave model WAVEWATCH III<sup>®</sup> is used, further referred to as WW3<sup>4</sup>. Focusing on overall year 2008 and for the investigated latitudes, swell partitions were retrieved from the swell spectra which are provided every three hours on a worldwide  $0.5^\circ$  grid. Wind-sea partitions were voluntarily excluded from the analysis as only swell observations are considered. Also, only swell with significant swell height above 30 cm are kept.

Then, two distinct cases are defined:

- $A$ : the model indicates a swell for which one of the starting latitude and swell direction conditions given by the SI quadruplet configurations given in Tables 4.1 and 4.2 are fulfilled;
- $B$ : the condition given by relation 4.4 is satisfied, implying that the swell period is close to  $T_{SI}$ .

Consequently,

- $A \cap B$ : the starting latitude and swell direction satisfy one of the SI quadruplet configurations while the swell period satisfies relation 4.4;
- $A|B$ : among the swells whose period satisfies relation 4.4, starting latitude and swell direction conditions given by the SI quadruplet configurations are fulfilled.

---

4. A third generation wave model developed at NOAA/NCEP by *Tolman* 1999; 2009 in the spirit of WAM model used by ECMWF (*Hasselmann et al.*, 1988; *Komen et al.*, 1994).

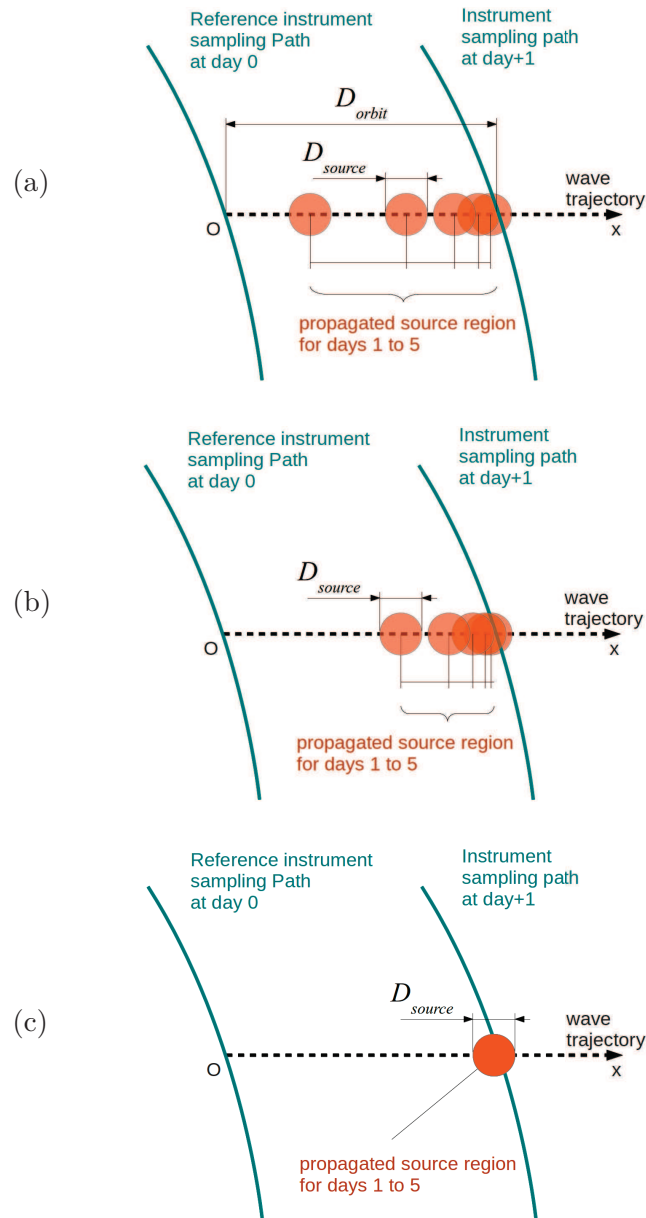


Figure 4.9: Daily position of the propagated swell source region for swells traveling eastward for 5 days. Their abscissa along the  $\mathbf{Ox}$  axis equals their distance from their initial position after one to five days of propagation, modulo  $D_{orbit}$ , the  $\mathbf{Ox}$  distance between two ascending passes at day 0 and day 1. Subplots (a) corresponds to the case where  $T_p$  is very different from  $T_{SI}$ . Subplots (b) corresponds to the case where  $T_p$  is a little closer to  $T_{SI}$ . Subplot (c) corresponds to the case where  $T_p = T_{SI}$ .

Latitude	0°	10°	20°	30°	40°	50°
$A$ [%]	1.3	11.4	2.1	4.7	19.8	32.0
$B$ [%]	37.9	56.5	54.1	61.2	68.3	59.4
$A B$ [%]	0.4	12.2	1.1	2.9	17.1	24.3
$A \cap B$ [%]	0.1	6.9	0.6	1.8	11.7	14.4

Table 4.3: Percentage of occurrence of  $A$ ,  $B$ ,  $A|B$  and  $A \cap B$  at different latitudes. Results concern the combination of ascending and descending passes for ENVISAT.

It is important to understand that numerous occurrences of  $A \cap B$  means that it is likely that swells will always or never be imaged by the satellite which, in both cases, bring very few information for the global observation of ocean swell.

Occurrences of  $A$ ,  $B$ ,  $A|B$  and  $A \cap B$  are presented in Table 4.3 for latitudes ranging from 0 to 50°. For instance, at 40° latitude, the percentage of occurrences of  $A|B$  equals 17.1%. It concerns swells modeled by WW3 with a significant swell height above 30 cm and meeting one of the following conditions:

- a direction within [56.25, 67.50] and a period within [7.6, 11.4] (ascending pass);
- a direction within [67.50, 78.75] and a period within [8, 12] (ascending pass);
- a direction within [78.75, 90] and a period within [10, 12] (descending pass);
- a direction within [90, 101.25] and a period within [8.4, 12.6] (descending pass).

Globally, swell is mostly generated by eastward traveling extra-tropical storms, driven by the westerlies and located at intermediate latitudes. Hence, at mid-latitudes, these swells mostly propagate to the East, while around the tropics, it is mostly South-East in the North Hemisphere and North-East in the South Hemisphere. Consequently, occurrences of  $A|B$  which concerns eastward traveling swell are mostly encountered for mid-latitudes. Given the fact that the direction bins are 11.25°-wide, if their propagation directions were isotropic, the expected average value of  $A|B$  would be 3.1%. Though, a significantly higher probability occurs for mid-latitudes: around 11.7% at 40° and 14.4% at 50° latitude. High values of  $A|B$  at 10° latitude are mostly related to South-East propagating swells.

### 4.2.1.3 Numerical applications

Hereafter, numerical applications of the general formula given in Section 4.2.1.1 are presented. Only latitudes with greatest occurrences of A|B are considered, that is 10, 30, 40 and 50° (cf. Table 4.3).

Proposition C is reminded: "the propagating swell system of diameter  $D_{\text{source}}$  and swell period  $T_p$  is not imaged over a 5-day period, by one of the ascending or descending passes alone". Then,  $P(C)$  with respect to the swell period, is given for mean directions where SI conditions are met, that is, according to Tables 4.1 and 4.2, 67.75°, 90° for ascending and descending passes, respectively. This applies for starting latitudes of 30, 40 and 50°. When the starting latitude equals 10°, directions given by the SI quadruplets in Tables 4.1 and 4.2 range from 56.25 to 146.25°. Though, as mentioned before, only swells propagating at 135° significantly occur in real conditions. SI conditions are encountered at this latitude in this direction for descending passes. In the end, investigated directions are 67.75, 90 and 135°.

The required inputs,  $D_{\text{orbit}}$ ,  $\Delta t$  and  $l$  are calculated using ENVISAT nominal orbit (detailed in Table 4.4). Analytical results are presented in solid line in Figure 4.10. The probability  $P(C)$  reaches minimum and maximum values of 0.7 and 0.85, respectively, depending how close the swell period is from  $T_{SI}$ .

The choice of the time period of investigation, 5 days, is arbitrary and impacts all the probabilities previously calculated. Other choices could have been made but the general trend, from one latitude to another, is expected to be the same. A minimum number of days is necessary to expect a swell field to be imaged at least once, given the satellite orbit. Then, because of the finite extent of ocean basin, a realistic upper boundary of 5 days was chosen. For instance, it takes more than 3 days for a 12 s swell to travel from the Labrador Sea to Brittany coastline and more than 6 days for the same period swell to travel from the south of New Zealand to French Polynesia<sup>5</sup>.

## 4.2.2 Considering a full orbit

Up to this point, ascending and descending passes have been considered separately. Obviously, combining the ascending *and* the descending passes (full orbit) diminishes the probability that a swell is not seen by the wave mode but to which extent?

To answer this question, the propagation of a swell region emanating from the same storm area of diameter  $D_{\text{source}}$  is simulated over a 5-day pe-

---

5. These are very common observed cases as discussed in Chapter 5, page 173.

riod at various frequencies satisfying relation 4.4. Again, two swell directions are investigated, each corresponding to the SI direction for the ascending and the descending passes. Considering latitudes of 30, 40 and 50°, the associated directions are 67.5 and 90° for the ascending and descending orbit paths, respectively. For each period, the source region starting location has been moved along the same latitude to explore all the different timings of the swell propagation with respect to the satellite orbit. For all these different positions, the number of cases when the propagating swell region was never imaged, neither during the descending nor during the ascending passes, is counted. In the end, this value divided by the number of different tested positions gives the probability that the source region at the given swell period is not imaged at all.

First, in order to test the validity of this approach, the previous analytical results have been tested. Results are presented for the different starting directions and latitudes in Figure 4.10 in dashed lines and they indicate that the two approaches well agree.

As for the combination of the two orbit phases, the mean probability that a swell region is never imaged is smaller than that given considering a single orbit phase. Besides, the probability dependence to the swell period remains the same, with a maximum for swell periods close to  $T_{SI}$ . Away from this value, the probability seems to decrease symmetrically. Still, the probability cutting-down is always less pronounced for starting propagation direction equal to 67.5°, no matter the starting latitude. Indeed, as Figure 4.2 recalls, this direction corresponds to conditions of exact and near SI for the ascending and descending passes, respectively, with associated values of  $T_{SI}$  that are very close. Specifically, for 40° latitude, these values are equal (Figure 4.2 and 4.3). Thus, the SI conditions can be met simultaneously for both the ascending and descending passes, thus explaining the particularly high probability, with values of  $P(C)$  equal to 0.75 for 10 s swells.

### 4.3 Case of Sentinel-1

To illustrate the impact of a different orbit on the swell imaging capability, the case of next European SAR mission Sentinel-1 is investigated. Expected to be launched in 2014, it follows a sun-synchronous orbit like ENVISAT but its repeat cycle is quite different as shown on Table 4.4. This directly impacts the values  $D_{orbit}$ ,  $\Delta t$  and  $l$ . A graphical comparison of Sentinel-1 and ENVISAT wave mode ground track is shown on Figure 4.11.

As can be seen, the distances  $D_{Sentinel-1}$  and  $D_{ENVISAT}$ , between orbits at two successive days, are very different. It equals 1050 and 1600 km for EN-

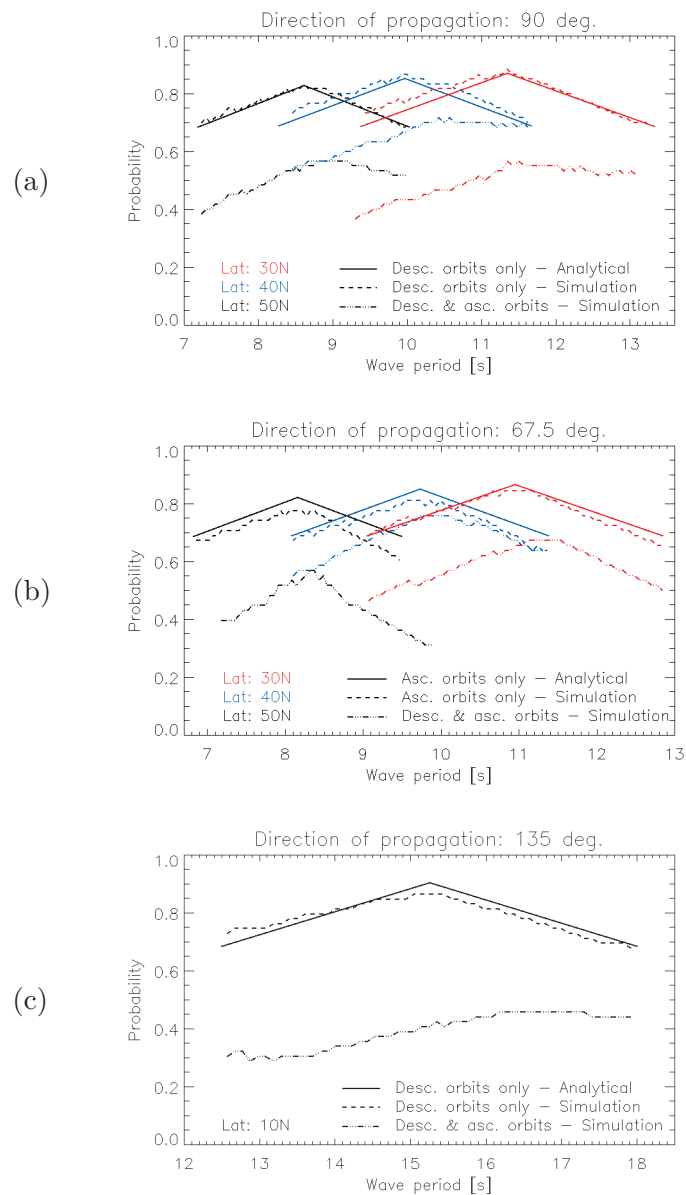


Figure 4.10: Probability that a swell region with a 400 km diameter is not imaged by ENVISAT wave mode during a 5-day period of propagation. Subplots (a), (b) and (c) refer to starting propagation direction of 90, 67.5 and 135°, respectively. For each subplots, the continuous line indicates results using the simulation and only considering one of the ascending or the descending passes alone; the dashed line gives the same information but using analytical calculation; the dash dotted line considers the combination of the ascending and descending passes.

Orbit of satellite	ENVISAT		Sentinel-1
	Nominal orbit	Extension orbit	
Altitude [km]	800	782	693
Repeat cycle [days]	35	30	12
Orbital period [min]	100.6	100.2	98.6
Revolutions per cycle	501	431	175
Mean local solar time at ascending node	22:00	$\simeq$ 22:04	18:00

Table 4.4: Orbital characteristics of the ENVISAT and Sentinel-1.

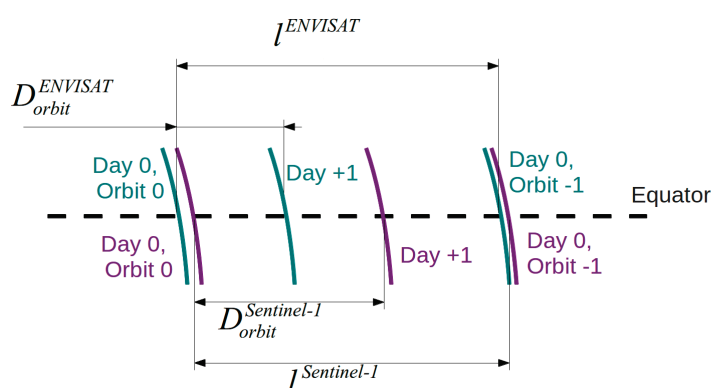


Figure 4.11: Wave mode ground track for ENVISAT (blue) and Sentinel-1 (magenta) at the equator.  $l_{ENVISAT}$  and  $l_{Sentinel-1}$  are very close, around 2800 km while  $D_{ENVISAT}$  and  $D_{Sentinel-1}$  are equal to 1050 and 1600 km, respectively. For ENVISAT, the nominal orbit is used.

VISAT and Sentinel-1, respectively, when considering a swell propagation to the East and 1750 and 1200 km for ENVISAT and Sentinel-1, respectively, when considering a swell propagation to the West. As this distance increases, the period of the swell that will cover this distance within the same time increases as well. With Sentinel-1 orbit, the calculation of the conditions leading to SI was performed, similarly to what was done in Section 4.1. In the end, among the different starting latitudes, the minimum swell period for which SI conditions are found equals 24 seconds, for eastward propagating swells.

First of all, such swell conditions are very scarce and second, such swells usually have very low amplitudes, seldom more than a few centimeters, conditions which undermines the SAR ability to detect such swells. Still, that is

in case of eastward traveling swell. Now, considering swells propagating from East to West, the distance for which SI conditions are met equals 1200 km. This rather concerns swell period between 10 and 16 seconds, which better corresponds to the swell observability domain of the SAR wave mode. Thus, the case of westward traveling swells is investigated similarly to what was done before with eastward traveling swells for ENVISAT.

### 4.3.1 Stroboscopic swell configurations

Studying westward traveling swells, SI quadruplets (orbit phase, starting latitude, starting direction and swell period) are explicitly given in Tables 4.5 and 4.6 and a graphical summary of these results is proposed in Figures 4.12 and 4.13.

Starting latitude	Period [s]	Starting propagation direction [deg.]
30°N	[14, 15]	[-101.25, -90]
	[13.5, 14.5]	[-90, -78.75]
20°N	[16, 17]	[-123.75, -112.5]
	[15.5, 16.5]	[-112.5, -101.25]
	[15, 16]	[-101.25, -90]
	[14.5, 15.5]	[-90, -78.75]
10°N	[16, 17]	[-123.75, -112.5]
	[15.5, 16.5]	[-112.5, -101.25]
	[15.5, 16.5]	[-101.25, -90]
	[15.5, 16.5]	[-90, -78.75]
0°N	[15.5, 16.5]	[-123.75, -112.5]
	[15.5, 16.5]	[-112.5, -101.25]
	[15.5, 16.5]	[-101.25, -90]
	[15.5, 16.5]	[-90, -78.75]
	[17, 18]	[-78.75, -67.5]
	[18, 19]	[-67.5, -56.25]

#### ASCENDING PASSES

Table 4.5: Conditions on starting latitude, swell peak period and starting propagation direction leading to stroboscopic imaging when considering Sentinel-1 ascending passes only.

In order to estimate how frequently SI conditions occur for Sentinel-1, the swell conditions provided by the model WW3 over year 2008 are used. Results are given in Table 4.7 and compared to that of ENVISAT. In this

Starting latitude	Period [s]	Starting propagation direction [deg.]
40°N	[11, 12]	[-78.75, -67.5]
	[10.5, 11.5]	[-67.5, -56.25]
30°N	[13, 14]	[-78.75, -67.5]
	[12, 13]	[-67.5, -56.25]
20°N	[16, 17]	[-101.25, -90]
	[14.5, 15.5]	[-90, -78.75]
10°N	[16.5, 17.5]	[-101.25, -90]
	[15.5, 16.5]	[-90, -78.75]
	[14.5, 15.5]	[-78.75, -67.5]
	[14.5, 15.5]	[-67.5, -56.25]
0°N	[18.5, 19.5]	[-123.75, -112.5]
	[17, 18]	[-112.5, -101.25]
	[16, 17]	[-101.25, -90]
	[15.5, 16.5]	[-90, -78.75]
	[15.5, 16.5]	[-78.75, -67.5]
	[15.5, 16.5]	[-67.5, -56.25]

## DESCENDING PASSES

Table 4.6: Conditions on starting latitude, swell peak period and starting propagation direction leading to stroboscopic imaging when considering Sentinel-1 descending passes only.

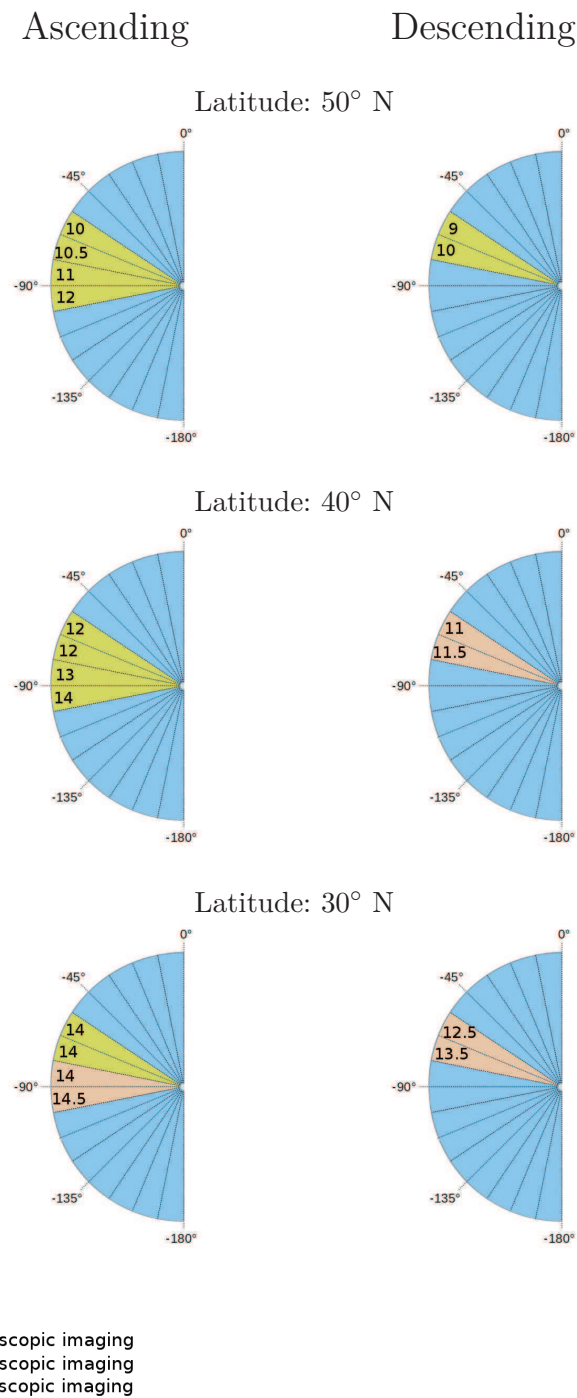


Figure 4.12: SI occurrences with mean re-imaging period calculated over a 5-day period for swell propagating from starting latitude of 50, 40 and 30° with starting propagation direction ranging from -180 to 0°. Left and right column correspond to the results using ascending and descending passes of Sentinel-1, respectively.

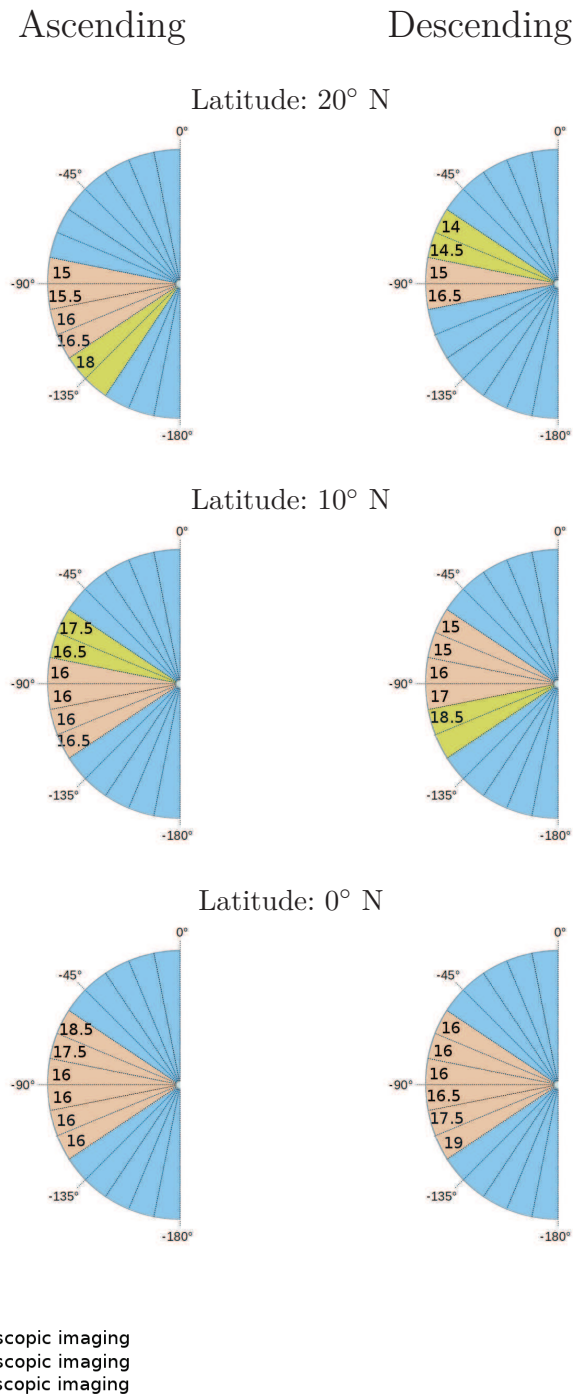


Figure 4.13: SI occurrences with mean re-imaging period calculated over a 5-day period for swell propagating from starting latitude of 20, 10 and 0° with starting propagation direction ranging from -180 to 0°. Left and right column correspond to the results using ascending and descending passes of Sentinel-1, respectively.

Satellite	Latitude	0°	10°	20°	30°	40°	50°
ENVISAT	B [%]	37.9	56.5	54.1	61.2	68.3	59.4
	$A B$ [%]	0.4	12.2	1.1	2.9	17.1	24.3
	$A \cap B$ [%]	0.1	6.9	0.6	1.8	11.7	14.4
Sentinel-1	B [%]	21.3	32.9	26.3	47.3	56.8	NA
	$A B$ [%]	0.7	0.2	0.9	5.6	9.1	NA
	$A \cap B$ [%]	0.2	0.1	0.2	2.7	5.1	NA

Table 4.7: Percentage of occurrence of  $A$ ,  $B$ ,  $A|B$  and  $A \cap B$  at different latitudes. Results concern the combination of ascending and descending orbit paths for ENVISAT and Sentinel-1.

Table, the acronym NA means *Not Applicable*. It comes from the fact that no SI conditions are met at 50° latitude.

First of all, fewer configurations are favorable to SI for 40 and 50° latitudes for Sentinel-1 as opposed to ENVISAT. Second, westward traveling swell seldom occur compared to eastward traveling swell. For these reasons, occurrences of  $A \cap B$  are a lot more numerous for ENVISAT than for Sentinel-1, meaning that swells are less likely to be missed by Sentinel-1, thus making Sentinel-1 wave mode more appropriate for ocean swell observation.

### 4.3.2 Probability of missing a swell system considering a full orbit

Similarly to what was done before with ENVISAT, Sentinel-1 orbit is used to simulate the probability  $P(C)$ , that a swell system emanating from a 400 km wide storm region is not observed by the SAR. This is only done for configurations for which SI conditions are met, that is directions equal to  $-67^\circ$  for descending passes and  $-90^\circ$  for ascending passes. As before,  $P(C)$  is evaluated for descending and ascending passes alone and then, considering the combination of both. Results are given on Figure 4.14.

The investigated swell period range is chosen according relation 4.4. As observed for ENVISAT, the combination of the ascending and descending decreases the mean level of probability  $P(C)$ . Besides, this cutting-down is more pronounced for directions not parallel to the equator. Indeed, the sampling is less regular for the non-SI orbit phase and better complements the other one. Maximum values of  $P(C)$  reached for the combination of two orbit phases and for a single incidence angle reaches 0.6, while it reached 0.75 in case of ENVISAT.

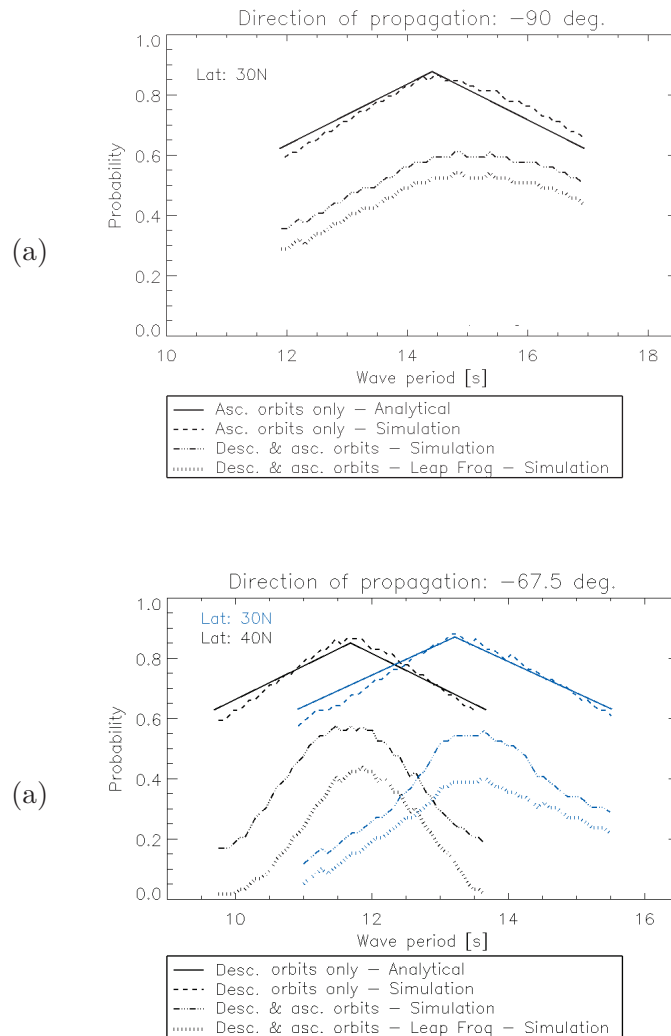


Figure 4.14: Probability that a swell region with a 400 km diameter is not imaged by Sentinel-1 wave mode during a 5-day period of propagation. Subplots (a) and (b) refer to starting propagation direction of  $-90$ ,  $-67.5^\circ$  respectively. For each subplots, the continuous line indicates results using the simulation and only considering one of the ascending or the descending passes alone; the dashed line gives the same information but using analytical calculation; the dash dotted line considers the combination of the ascending and descending passes and the dotted line considers the leap frog feature of Sentinel-1.

Satellite	Latitude	0°	10°	20°	30°	40°	50°	
ENVISAT	$A \cap B$ [%]	0.1	6.9	0.6	1.8	11.7	14.4	
	$E$ [%] <	-	3.1	-	1.1	8.6	8.3	
Sentinel-1	$A \cap B$ [%]	0.2	0.1	0.2	2.7	5.1	0.0	
	- No leap frog -	$E$ [%] <	-	-	-	1.6	3.1	-
	- Leap frog -	$E$ [%] <	-	-	-	1.1	2.4	-

Table 4.8: Percentage of occurrence of  $A \cap B$  and  $E$  at different latitudes.  $A \cap B$  refers to the cases when, for the given latitude, swells satisfying the SI conditions are encountered (from spectral ocean swell model WW3).  $E$  refers to the case, over time, when a swell is missed because of the SI effect.

In addition, the Sentinel-1 wave mode will operate in a new *leap frog* configuration for which each wave mode acquisition is alternatively acquired at incidence angles of 23 and 36.5°, separated by 200 km in the range direction (cf. Table 1.1 in Chapter 1, page 16). Thus, the SAR instrument swell field sampling will be further improved by this additional feature. The impact of this additional operating mode on  $P(C)$  was also estimated. It is presented on Figure 4.14. Clearly,  $P(C)$  further diminishes. For -90° propagation direction, corresponding to 30° starting latitude, the maximum value reached by  $P(C)$  goes from 0.62 down to 0.53. For -67.5° propagation direction, corresponding to 40 and 30° starting latitude, it goes from 0.58 down to 0.43 and from 0.55 to 0.4, respectively.

In the end, it is also interesting to estimate the percentage of occurrences in time  $E$ , when a swell system is not observed. This combines the probability that a swell satisfying the SI conditions is present and the probability that such a swell is not imaged. Since, these two events are clearly independent, the resulting probability is equal to their product. For this calculation, an upper-bound of  $P(E)$  can be estimated for each configuration using the maximum value given by  $P(C)$  rather than the full period-probability profile. Results are given in Table 4.8. They indicate that for Sentinel-1, swell can be missed because of SI phenomenon only 1.1% of the time at 30° latitude and 2.4% of the time at 40° latitude. On the contrary, ENVISAT exhibits much higher values reaching more than 8% at 40 and 50° latitude. Thus, the SI limitation hardly applies for Sentinel-1 wave mode showing a much more favorable swell sampling than ENVISAT.

## 4.4 Conclusion

The present chapter highlights the ability and limitations of SAR instruments operating in wave mode to sample ocean swell fields, focusing on the dynamical trajectory of a swell system with respect to the instrument sampling, directly related to the satellite orbit and the instrument incidence angle. Over a 5-day propagating period, certain swells with specific periods and eastward propagation directions can be systematically missed by the ASAR instrument. Given the conditions of realization, we have entitled the phenomenon *swell Stroboscopic Imaging* (SI).

Considering ascending and descending passes alone first, we have identified the Stroboscopic Imaging (SI) conditions under which this phenomenon occurs, determined for a given orbit and incidence angle by the quadruplet of the swell peak period, its starting propagation direction, the starting latitude and the orbit phase (ascending or descending). More precisely, taking the example of ASAR, the phenomenon occurs for swells with ENE mean propagation direction and periods ranging from 8 and 14 s for ascending passes, and for swells with eastward mean propagation direction and periods ranging from 9 and 15 s for descending passes. Using data provided by WW3 wave model over year 2008, such swell conditions were proven to be significantly met in open ocean.

The probability  $P(C)$ , that a swell system could be missed by the SAR instrument was first estimated using an analytical method. It indicates that for each descending or ascending passes alone and each considered latitude, this probability reaches maximum values of 0.9 when the swell period equals that of SI,  $T_{SI}$ , and linearly decreases to 0.7 as the swell period approaches  $\frac{4}{5}T_{SI}$  and  $\frac{6}{5}T_{SI}$ . Then, we have simulated the multiple phasing configurations of a swell system with respect to the instrument sampling. Doing so, the probability of swell non-observability combining ascending and descending passes could be estimated. It indicates that the conditions of swell non-observability due to a single orbit phase can be compensated by the other orbit phase and maximum values of  $P(C)$  are down to 0.6. This is unless the two orbit phases have very close SI conditions, in which case this probability remains high, reaching 0.75. This occurs for swell propagating in ENE directions at mid-latitudes ( $\simeq 40^\circ$ ) whose period is close to 10 s.

Finally, taking the example of the future Sentinel-1 mission, we tackle the influence of a different SAR satellite repeat cycle on SI phenomenon. Results show that the Sentinel-1 orbit offers a much better swell sampling. SI conditions are met for westward traveling swell, as opposed to eastward traveling swell in case of ENVISAT. Using WW3 ocean wave spectra simulations, we conclude that SI conditions for Sentinel-1 are four times less

likely in average than that for ENVISAT. Besides, the swell sampling will be further improved by the new leap frog feature, alternating between two incidence angles.

## Bibliography

Hasselmann, S., K. Hasselmann, E. Bauer, P. Janssen, G. J. Komen, L. Bertotti, P. Lionello, A. Guillaume, V. C. Cardone, J. A. Greenwood, et al. (1988), The WAM model—a third generation ocean wave prediction model, *Journal of Physical Oceanography*, 18, 1775–1810. 134

Komen, G. J., L. Cavaleri, M. Donelan, K. Hasselmann, S. Hasselmann, and P. A. E. M. Janssen (1994), *Dynamics and modelling of ocean waves*, Cambridge University Press, Cambridge. 134

Moore, G. W. K., and I. A. Renfrew (2005), Tip jets and barrier winds: A QuikSCAT climatology of high wind speed events around greenland, *Journal of Climate*, 18(18), 3713–3725, doi:10.1175/JCLI3455.1. 120, 173

Tolman, H. L. (1999), User manual and system documentation of WAVEWATCH III version 1.18. tech, *Tech. rep.*, Note 166, NOAA/NWS/NCEP/OMB. 134

Tolman, H. L. (2009), User manual and system documentation of WAVEWATCH-III version 3.14, *Technical note, MMAB Contribution*, (276). 134

# Chapter 5

## Swell field reconstruction

### Contents

---

5.1	Dataset Description . . . . .	<b>153</b>
5.1.1	Wind field data . . . . .	153
5.1.2	StormWatch database . . . . .	154
5.1.3	Wave data . . . . .	154
5.2	Methodology . . . . .	<b>155</b>
5.2.1	Retro-propagation . . . . .	156
5.2.2	Refocusing . . . . .	157
5.2.3	Swell observations' association . . . . .	161
5.2.4	Swell observations' filter . . . . .	162
5.2.5	Swell field analysis . . . . .	163
5.2.6	Virtual buoy and swell field association . . . . .	163
5.3	Results . . . . .	<b>168</b>
5.3.1	StormWatch co-location . . . . .	169
5.3.2	Single cases . . . . .	169
5.3.3	Yearly analysis . . . . .	173
5.4	Discussion . . . . .	<b>178</b>
5.5	Conclusion . . . . .	<b>180</b>
	Bibliography . . . . .	<b>182</b>

---

The validation of SAR swell measurements from the ENVISAT mission in Chapter 3 has proven that swell integral parameters can be retrieved from individual SAR images of the sea surface. The development of applications using these measurements is motivated by the future launch of the two Sentinel-1 missions in 2013 and 2014, together with the accumulation of a 20 year-long archive with satellites ENVISAT and ERS-1 and 2.

In the past chapters, SAR swell measurements have been treated as independent measurements but, as was shown in Chapter 2, swell can propagate for thousands of kilometers and, under deep water and no current assumptions, its trajectory and speed can be estimated using linear theory. For instance, (*Hanson and Phillips, 2001*) have advantageously used this swell persistency to identify and group swell measurements from a moored buoy related to the same swell systems. Additionally, swell persistency can also compensate for the track-based and relatively sparse sampling of the SAR swell measurements to capture the evolution of ocean swells as they spread away from their original storm as shown by *Collard et al. (2009)*. The global monitoring of ocean swell fields they propose appears promising for the better understanding of ocean swell processes. Indeed, using a high number of SAR observed swell fields (*Ardhuin et al., 2009*) has brought new measurement methods and empirical model for swell dissipation. Not only has this progress contributed to a better understanding of air-sea fluxes in low wind conditions but it also benefited wave model parametrization (*Ardhuin et al., 2008*).

Monitoring ocean swell requires the analysis of a large SAR swell observation database. With ENVISAT wave mode, more than fifty thousands points are accumulated every month on a global scale. An automated process is thus necessary, especially if targeting at developing real-time applications in preparation of the next Sentinel-1 missions. This supposes the development of robust routines that can handle the large variety of storm and swell events. For instance, complex storm scenarios of long lasting or fast succeeding events bring new issues and question the validity of point source assumption on which previous studies rely. If these problems are not addressed, they lead to a miscellaneous gathering of swell observations and cause incorrect estimations of swell arrival times and energy decay. Indeed, *Delpey et al. (2010)* noticed for a storm that occurred on 24 February 2004 in the western part of the North Pacific Ocean that the afterglow<sup>1</sup> of the storm may have been the time where most energy was attributed to the shorter swell, 18 hours after the longer one. Already, *Snodgrass et al. (1966, Section 7)* explained the important role of the storm afterglow, which was

---

1. The afterglow of a storm is defined as the time period following the storm maximum intensity and during which the maximum wind speed keeps on decreasing.

held responsible for the slow decay of swell energy at a fixed period compared to its rapid increase upon arrival.

With the attention to bring the use of SAR wave mode data to its full potential, it is important to propose automated methods to describe swell field spatio-temporal evolution from sparse observations using the most accurate storm identification. Thereby, the present chapter extends the methods previously proposed by *Collard et al. (2009)* for a finer description of the ocean swell field. Particular attention is given to complex storm cases, for which previous hypothesis of a point storm source in space and time may not apply for swell system reconstruction methods. First, a brief description of the different data sources used in this paper is given in Section 2. Then, the methodology for the SAR swell field reconstruction is detailed in Section 3. Finally, it is followed by a presentation and discussion of results going through individual examples as well as analysis of a full year.

## 5.1 Dataset Description

In this section, the different data sources used in this chapter are presented.

In order to gather SAR swell observations belonging to the same swell systems, it is necessary to identify their origin. This information on the storm locations is assessed using surface wind field data from the National Center for Environmental Prediction (NCEP) and the StormWatch database, developed by IFREMER. It can also be retrieved from the sea states given by the numerical wave model WW3. Then, wave related data is described: wave spectra extracted from SAR L2 products, already detailed in Chapter 3 at page 83, and *in situ* measurements of directional buoy spectra available through NDBC website.

### 5.1.1 Wind field data

The surface wind field data comes from the NCEP Re-Analysis 2 (NCEP RA-2) and is freely available through the NCEP website. It contains the 10 m-high wind speed provided on a global  $2.5^\circ$  grid with a 6 hour time resolution, as four 'instantaneous' global snapshots per day at UTC 00, 06, 12 and 18Z. Wind field inputs come from multiple satellites, up to six depending on the time period, including scatterometers (QuikSCAT), SSM/Is, TMI and AMSR-E observations. The blended winds are then decomposed into (u,v) components using the NCEP RA-2 and finally interpolated onto the blended wind speed grid.

Potentially, other wind data could have been used like the Climate Forecast System Reanalysis (CFSR) winds since it comes with better time and space resolution ( $0.5^\circ$  and 1 H) and extreme winds are more accurate (*Saha et al.*, 2010). However, at the time this study was conducted, we did not dispose of the additional time necessary to develop the scheme to ingest this data.

### 5.1.2 StormWatch database

The StormWatch database was developed in 2006 for CERSAT in IFREMER, in order to promote the use of ERS data archive (*De Joux*, 2006). It is intended to track hurricane-force winds, retrieve associated information and can be used to compare them to the information given by the SAR analysis. Identification of extreme events is based on the strong wind region detection. Wind information can be retrieved from atmospheric model or directly from scatterometer measurements. Though, model offers a more complete spatio-temporal description of the cyclone extension since it is not limited to satellites' swath. However, it is sometimes not a good representation of the sea truth.

Detection is defined by a minimum wind threshold. Since both scatterometer or model significantly under-estimate high wind speeds (*Quilfen et al.*, 2007), instead of choosing the conventional hurricane force wind speed limit of  $32 \text{ m.s}^{-1}$ , the minimum threshold was chosen as the minimum wind speed of the 1% highest quality checked wind speed in the wind speed inputs, which approximately equals  $20 \text{ m.s}^{-1}$ . The extension of the storm is then defined as the region around the recorded maximum where the wind speed continuously decreases and remains higher than  $15 \text{ m.s}^{-1}$ .

Each storm event thereby detected is then saved together with geophysical parameters such as the maximum wind speed, associated wind direction, time and geographical location, total wind power over the storm area and its vorticity. In the end, this dataset is a concatenation of all the records of extreme events records but successive observations of the same storm along its life cycle are not linked.

### 5.1.3 Wave data

#### 5.1.3.1 Observations: SAR L2P wave mode products

This study is based on the SAR L2P wave mode products, obtained after processing the SAR wave mode products acquired by the Advanced Synthetic Aperture Radar (ASAR) instrument on-board ENVISAT satellite using the scheme described in Chapter 3. Latest validation performances

	$H_{ss}$	$T_p$
Bias	0.02 m	0.32 s
RMSE	0.29 m	1.07 s
Scatter Index	22.4%	7.3%
NRMSE	22.5%	7.7%
r	0.92	0.64

Table 5.1: Statistical errors for swell observations of significant swell heights and peak period derived from SAR L2 wave mode data against buoy-derived data extracted from *Collard et al. (2009)*. Co-locations are restricted to SAR observations for which a maximum distance to the buoy equals 100 km and the 10-m wind speed as measured by the SAR in  $[\text{m}\cdot\text{s}^{-1}]$ ,  $U_{10}$ , satisfies the conditions is  $3 \leq U_{10} \leq 8$ . RMSE for directions equals  $20^\circ$  and is bias-free.

detailed by (*Collard et al., 2009*) are presented in Table 5.1 but for a more complete investigation, it is recommended to refer to Chapter 3.

### 5.1.3.2 Observations: Stratus buoy

*In situ* wave measurements used for comparison come from the directional buoy 'Stratus', operated by Woods Hole Oceanographic Institution (WHOI). Moored 1500 km off the coast of Chile, at  $-19,7^\circ\text{N}$ ,  $-85.5^\circ\text{E}$ , this buoy has been recording ocean waves from October 2007 until now with only a few discontinuities. It is equipped with the Wave and Meteorological Data Acquisition System (WAMDAS) designed by NDBC. Data is collected by NDBC and quality-controlled before being posted on the NDBC web site. It is available at URL <http://www.ndbc.noaa.gov/>.

## 5.2 Methodology

This section presents the methodology through which isolated SAR swell measurements can be gathered into clusters corresponding to different swell systems. For a given swell system, the main difficulty is to be able to gather as many measurements of this swell event among all the SAR measurements without incorporating measurements from other swell events. This can be particularly difficult when looking at closely succeeding storm events.

The main thrust behind the algorithm is that observations at various times and locations of the same swell field all originate from the same source region. Inversely, storm regions are defined in our approach by the regions where a significant amount of back-traced swell observations converge. The swell field reconstruction principle is rather simple: swell observations tra-

jectories are traced back in the past and they converge to their storm source region. Then, these converging retro-propagated observations are associated and define a new swell field. Its spatio-temporal properties are described by these observations propagating from the storm source region until shallow water is encountered. The overall methodology can be split in six steps:

1. Retro-propagation: tracing the swell observations trajectories back in the past;
2. Refocusing: swell sources are defined by the region where retro-propagated swell observations converge;
3. Swell observation association: all the retro-propagated observations within the previously detected region are gathered into a set defining the new swell field. The generation time and region is the same for all observations;
4. Swell observations' filter: the spatio-temporal coherence of the swell field is used to reject swell partitions originating from neighboring storms but erroneously associated to the considered swell system;
5. Swell field analysis: generation time and region are re-estimated for each observation belonging to the new swell field;
6. Swell field association: in the end, previously detected swell fields that were split into separate refocusing events but actually belong to the same event are gathered. It is based on a spectral distance criterion.

In the following pages, these steps are described in more details.

### 5.2.1 Retro-propagation

This is the first step of storm source identification. The required inputs are the peak period and direction of propagation given by the SAR L2P products. Then, all observations past-positions are calculated following geodesics at group velocity in the direction opposite to the direction of propagation until land is reached and for a maximum time of 14 days. Group velocity is estimated from dominant wavelength using linear dispersion relation, valid for swell with small steepness.

Along this past trajectory, the fact that the generation region is detected depends on two conditions. First, a minimum number of swell observations have to converge to this region. This condition is referred to as *refocusing* and it is further detailed afterwards. Second, the local sea surface wind speed has to reach a threshold value compatible with the swell wavelength. Indeed, a wave of peak period  $T_p$  requires a threshold wind speed  $U_{\min}$  around  $0.12gT_p$  to be generated, where  $g$  is the Earth gravity. This ancillary wind information is given by the maximum 10 m wind speed indicated by NCEP RA-2 wind model within 500 km of the swell propagated observation.

In practice, because of the inability of input wind data to describe the highest wind speed range, we consider a limit wind speed equal to two-thirds of  $U_{\min}$ . Thanks to this wind speed threshold, cross sea regions occurring under calm wind conditions are rightfully rejected from the following storm detection.

### 5.2.2 Refocusing

The global behavior of the refocusing algorithm is described by the sequential graph on Figure 5.1 and further detailed hereafter. It is based on the analysis of retro-propagated swell density-maps over time. These density-maps are 2D histograms indicating, for a given time step, the number of retro-propagated observations whose threshold wind speed condition is fulfilled within each cell. The density-map geographical extension covers all longitudes, and goes from 74°S to 74°N with  $2 \times 2^\circ$  cells. This resolution is justified by the limited precision on the swell retro-propagated observations' location, caused by the error on the swell peak period and direction measurements (cf. Chapter 3, Section 3.4) and the resulting mis-positioning after retro-propagation. In order to be able to compare density-map cells at different latitudes, each cell value is normalized by the cell surface.

#### 5.2.2.1 Scheme

The next two paragraphs described the recursive search among the density-maps time series allowing for the identification of storm events.

**Analysis with decreasing peak period** An example of density-map time sequence is given on Figure 5.2 where maximum refocusing region is circled in red. Clearly, a region of convergence is located south-east of New Zealand and reaches its maximum density on 11 April 2008. Only observations with peak period above 16 seconds are considered here. Indeed, the highest periods give the most precise convergence for they require the strongest wind conditions. Though, as the highest swell field peak periods varies from one event to another, an iterative process is adopted, for which the minimum peak period,  $T_{max}$ , of the swell observations to take into account for the density-maps estimation decreases in order to get the most precise refocusing for all storm events.

**And with decreasing time step** Looking at one single retro-propagated observation, the main stake is to identify when this swell was most probably generated along its past trajectory and among the segments for which the threshold wind speed condition is fulfilled. Several scenarios may occur: if only one storm event is encountered along the retro-propagated trajectory, then, the refocusing algorithm will automatically define the swell generation

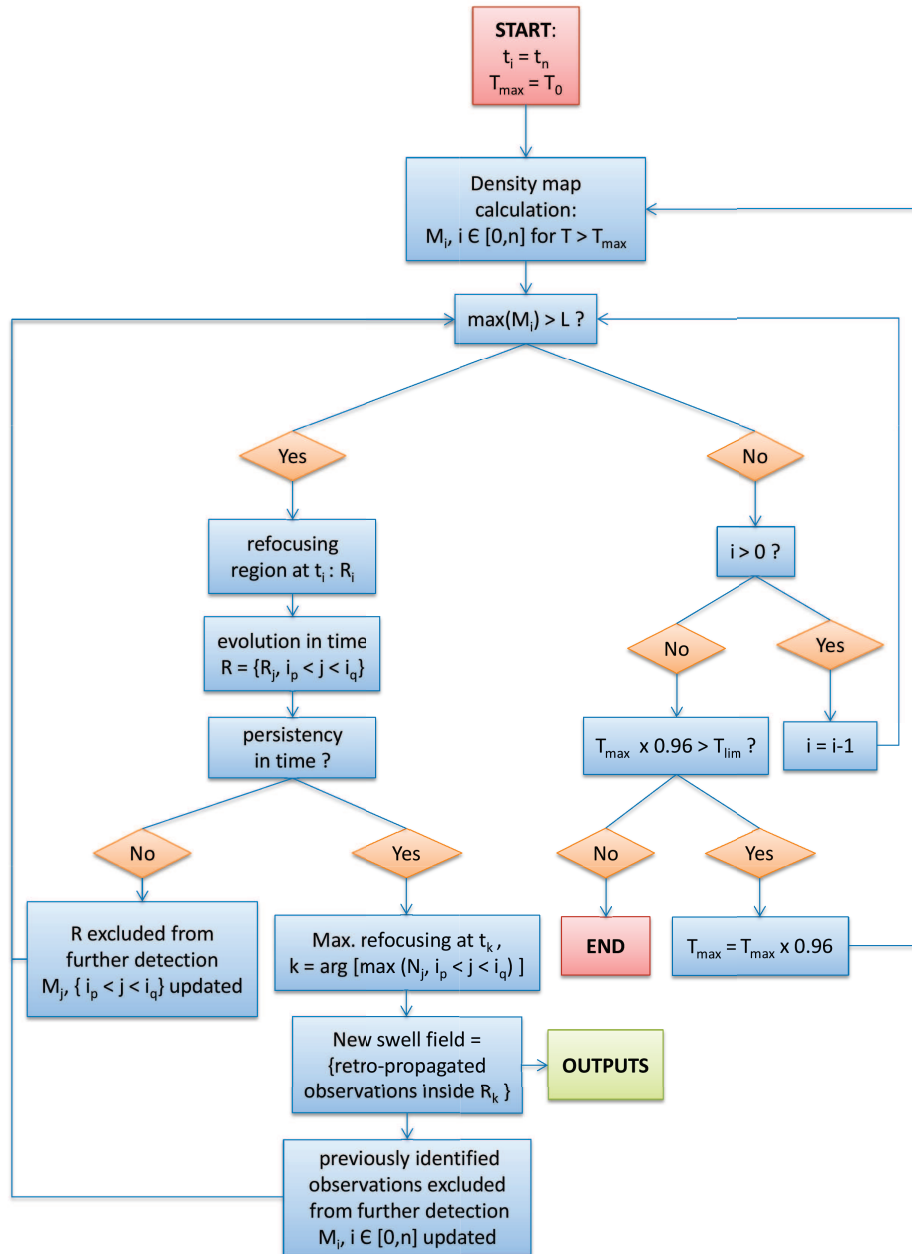


Figure 5.1: Detailed flow diagram of the refocusing algorithm.

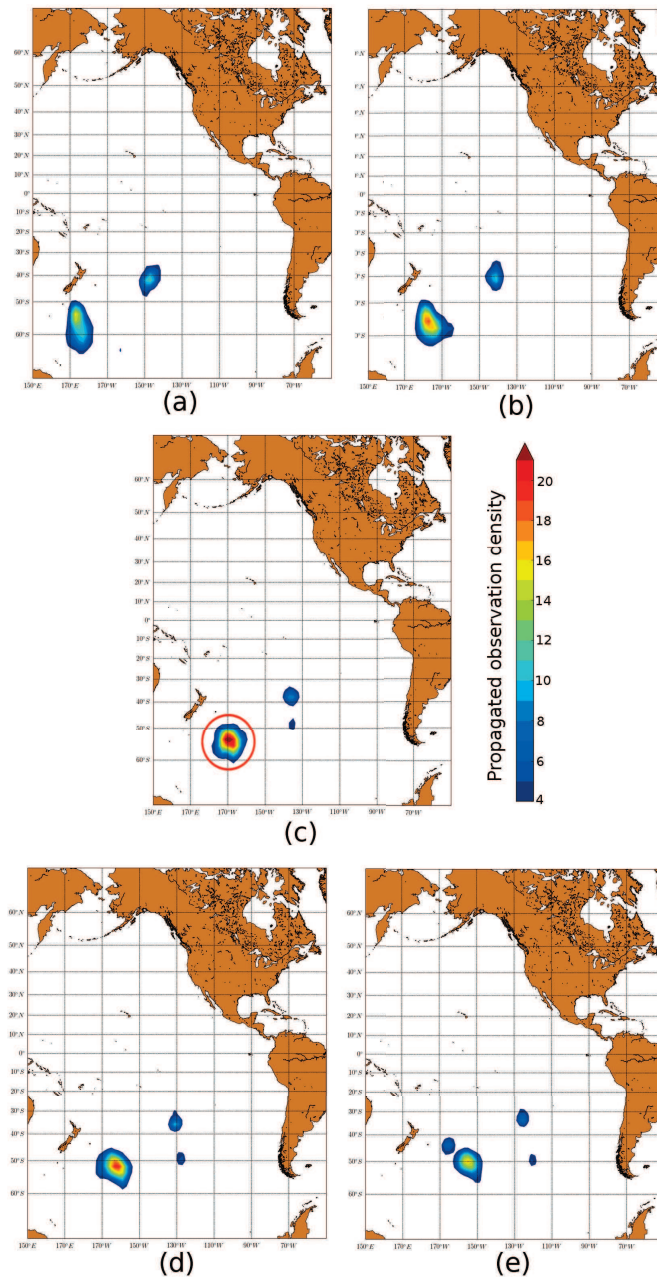


Figure 5.2: Density-maps at successive time steps showing the refocusing region displacement on 10 April at 00Z (a), 10 April at 12Z (b), 11 April at 00Z (c), 11 April at 12Z (d) and 12 April at 00Z (e). Maximum refocusing is reached on 11 April 2008. Density maps contain an absolute maximum, related to the storm event occurring on 11 April 2008, and one or several local maxima, related to another storm event, that occurred on 10 April 2008.

time as the time of maximum convergence. If several storm events are present along the retro-propagated trajectory, the swell observation may result from the successive forcing of several of them or only from the last one. In the latter case, the presence of previous storm regions along the hypothetical past trajectory is just a coincidence. In the first case, different choices are possible. We choose as a convention to consider that the storm source is the most recent storm event for which enough swell observations converge and the threshold wind speed condition is fulfilled. For this reason, given an threshold peak period as described in the previous paragraph, the density-map analysis follows an iterative process and the time series are inspected going backward in time.

Now that the density-map inspection scheme is set and given the regions of converging swell retro-propagated measurements as illustrated in Figure 5.2, a criterion is needed to precisely define the time and location of the underlying storm event. This is the refocusing criterion.

### 5.2.2.2 Refocusing region ensemble

Once  $T_{max}$  is fixed, the algorithm looks for the maximum density-map value above the threshold noise level,  $M_{noise}$ , skimming through the time period of interest, starting from last time step and going back in time.

$$(x, y) = \arg(\max M_i) , \text{ where } M_i(x, y) > M_{noise} , \text{ at } t = t_i \quad (5.1)$$

Whenever this condition is met, the density-map  $M_i$  is separated in regions of convergence using a watershed delineation transform analogous to our partitioning algorithm. Its use is motivated by the need to clearly delimit successive neighboring refocusing regions related to different storms. Otherwise, swell observations could be attributed to the wrong storm events. Then, the refocusing region  $R_i$  is defined as the partition domain around the identified peak, at  $(x, y)$ . The maximum density reached over region  $R_i$  is denoted  $\max \{M_i(R_i)\}$ . Afterwards, the evolution of this region is evaluated going forward and backward in time using a feature tracking algorithm. It defines a refocusing region ensemble,  $R = \{R_j, i_p < j < i_q\}$ . We stop the evaluation at time step  $t_{i_p}$  and  $t_{i_q}$ , whenever the maximum density reached at these times,  $M(R_{i_p})$  and  $M(R_{i_q})$ , is smaller than half the maximum density reached for intermediate time steps. This can be expressed as follows:

$$R = \{R_j, i_p \leq j \leq i_q\} , \text{ with } \max_{j \in (i_q, i_p)} \{M_j(R_j)\} \geq \frac{1}{2} \max_{i_p \leq j \leq i_q} \{M_j(R_j)\} \quad (5.2)$$

**Note** Density-map values above the threshold noise level,  $M_{noise}$ , may be reached if the swell measurements acquired during the ascending phase of

the satellite are located close enough to the measurements from the previous swell measurements acquired during the descending phase of the satellite less than 24 hours after. However, this does not necessarily corresponds to the presence of a storm region. Therefore, the refocusing region ensemble  $R$ , is only considered valid if it is persistent for more than 24 hours.

### 5.2.2.3 Refocusing criteria

Once the refocusing region ensemble is defined, the storm source region and time, respectively  $R_m$  and  $t_m$ , are chosen when both the convergence and the number of propagated observations inside the refocusing region are maximum. They are given by the argument maximizing the criterion  $N$ , that we define as:

$$N_k = A_k B_k, \text{ where } \begin{cases} A_k = \max_{(x,y) \in R_k} M_k(x, y) \\ B_k = \sum_{(x,y) \in R_k} M_k(x, y) \end{cases} \quad (5.3)$$

Other criteria have been tested, such as  $N_k = A_k$ , but results have shown it was not as robust as the previous one and refocusing was occurring too early compared to maximum storm development.

### 5.2.2.4 Application to WW3 model

The previously described refocusing algorithm aims at detecting swell source time and location. These are theoretically co-located with ocean storms, which can be characterized by maxima of total significant wave heights. In order to further verify this assumption with independent data (cf. Section 5.3.3, page 173), the refocusing algorithm can be adapted to the use of WW3 data. The estimation of the storm source time and location relies on the same principles. This is based on the analysis of total significant wave height maps instead of density-maps. Here, the refocusing criterion is the time and location of maximum total significant wave height and the threshold significant wave height equals 10 m. The criteria kept for the storm source identification using the SAR and the model may not be strictly equivalent but should still target the most energetic events. This is further discussed in the latter presented results.

## 5.2.3 Swell observations' association

The new swell field is defined as the group of observations, *all* period considered, whose position falls inside region  $R_m$  at  $t_m$ , the maximum refocusing time.

### 5.2.4 Swell observations' filter

The statistical errors of the integral parameters estimation using by SAR are given in Table 5.1. As a direct consequence of the wrong estimation of the peak periods and/or directions, all the retro-propagated partitions converging in space and time to a common storm source region may not have been generated by that storm but by a neighboring one instead. In order to reject these outliers, we use the spatio-temporal coherence of the reconstructed swell field.

As mentioned before, for each swell field detected by the refocusing algorithm, the storm source region is estimated focusing on longest swell observations since they give the most precise convergence. Therefore, those long waves are less likely associated to an erroneous refocusing region than shorter waves, whose converging regions can be much wider. Therefore, the proposed filtering aims at rejecting short waves originating from another storm source but associated to the considered swell system, using the longest swell as a spatio-temporal reference. At a given time step,  $t_{\text{Filter}}$ , and given the location of the propagated SAR observations, we estimate for each of them their expected wavelength considering a point source. Its geographical coordinates are given by the mean location of all propagated partitions at refocusing time. Then, if the difference between the expected wavelength and the actual one exceeds a certain threshold,  $\Delta\lambda_{\text{thresh}}$ , the propagated SAR observations are excluded. To estimate this threshold, we assume that in open ocean, outside of island shadows and in the absence of currents, differences between the observed and the expected values result from measurement uncertainties and the extension of the storm source region. The larger the storm source, the bigger the potential difference. The peak wavelength difference arises from the fact that the observed swells have covered different distances during the same time, as illustrated on Figure 5.3.

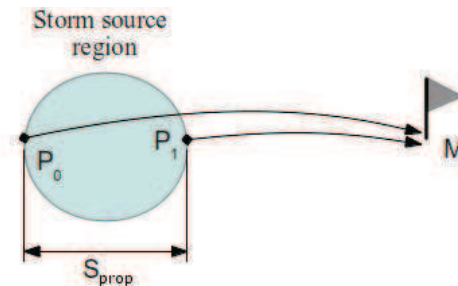


Figure 5.3: Illustration of two waves belonging to the same swell field but with slightly different wavelengths at point  $M$  because of the storm source geographical extension in propagation direction,  $S_{\text{prop}}$ .

In the end, the threshold is estimated as follows:

$$\Delta\lambda_{\text{thresh}} = \left[ \lambda_{\text{max}}^{1/2} - \left( \frac{8\pi}{g} \right)^{1/2} \frac{S_{\text{prop}}}{\Delta t} \right]^2 + \Delta\lambda_{\text{prec}} \quad (5.4)$$

where,  $\lambda_{\text{max}}$  is the peak wavelengths' ninth decile<sup>2</sup>;  
 $g$ , the Earth gravity;  
 $S_{\text{prop}}$ , the storm source dimension in the propagation direction, given by the size of the convergence region in the refocusing step;  
 $\Delta t$ , the time difference between the swell generation and the time of estimation;  
 $\Delta\lambda_{\text{prec}}$ , the RMSE of the peak wavelength<sup>3</sup>, equal to 36 m.

Empirical tests have proven that best estimation of this threshold criterion were given for  $\Delta t=2$ . This threshold is applied to a case example, presented in Figure 5.4. On subplot (a), the position of all the propagated swell observations are plotted 7 days after their generation, south-east of New Zealand. Because of the swell dispersion relation, the wavelengths should increase with the distance from the source. However, some patches show abnormally low values with respect to the general trend. Using the threshold condition given by equation 5.4, those patches are detected and plotted in brown on subplot (b). Further analysis of the meteorological situation shows that these observations were generated by a previous storm, very close in space and time to the investigated one.

### 5.2.5 Swell field analysis

In the previous step, we have considered that all observations belonging to the same swell field were generated at the same time and in the same region. Nevertheless, all waves do not necessarily leave the storm region at the same time and therefore may escape at different times and locations along the storm path, as illustrated on Figure 5.5. Here, we assume that these differences can be related to the peak period or wavelength of the observed swell. The purpose of this additional step is thus to let out the swell field to enable different times and regions of refocusing depending on the swell period.

As shown on Figure 5.6, this is done similarly to Step 2, using the same refocusing algorithm but only taking the previously set of retro-propagated observations for inputs.

### 5.2.6 Virtual buoy and swell field association

In certain cases, the swell source is so spread in space and/or time that a single swell event may be split into several refocusing events. They need to

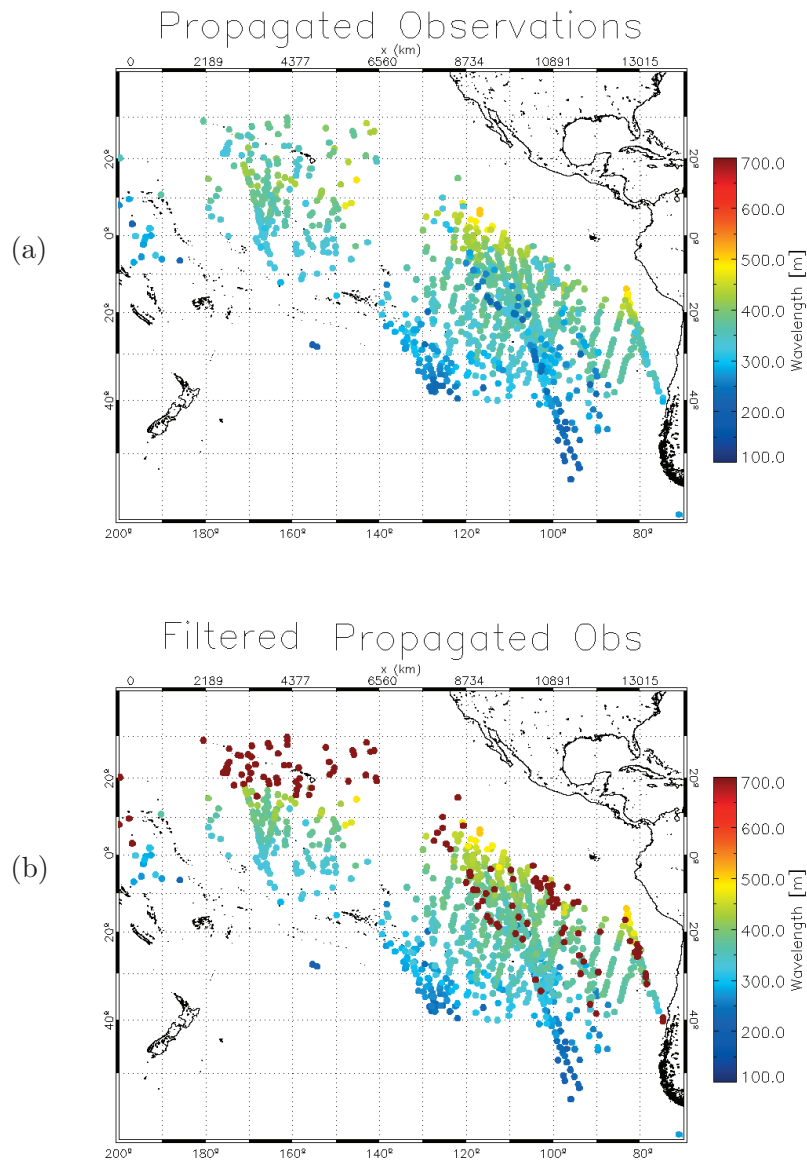


Figure 5.4: Propagated swell observations seven days after their generation by a powerful storm event that occurred on 23 August 2011, south-east of New Zealand (a). On subplot (b), partitions excluded using criterion given by equation 5.4 are represented by a maroon disk.

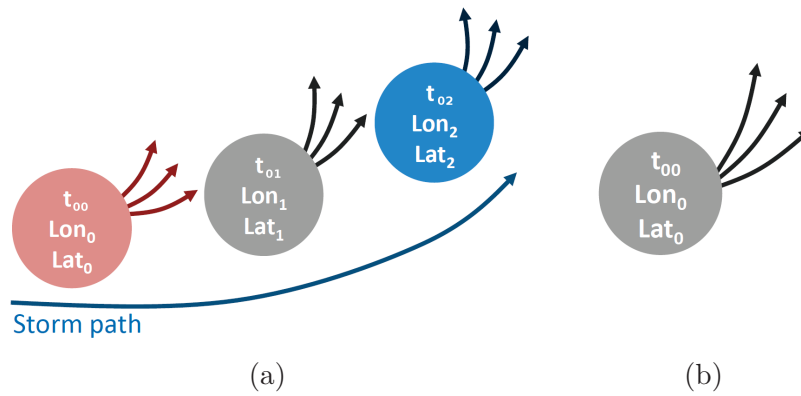


Figure 5.5: Illustration of the new storm source parametrization allowing for different times and locations of refocusing along the storm path (a) as opposed to a point source parametrization (b).

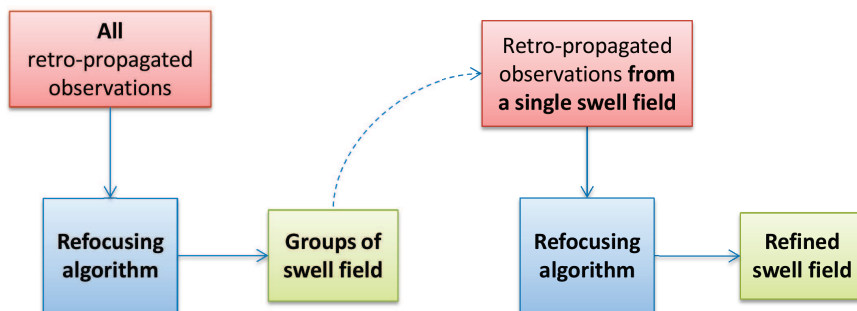


Figure 5.6: Different uses of the refocusing algorithm for raw swell field identification in first place and refined identification then.

be gathered in order to avoid summing significant swell height measurements of the same swell field for the calculation of the total significant swell height.

As the swell field passes by a given observation point, the virtual buoy, the peak period and propagation direction are estimated. To do so, each propagated observation's position with respect to the virtual buoy is indicated by longitude,  $\varphi_i$ , measured in the local coordinate system associated with the storm source region, as illustrated in Figure 5.7. This parametrization is justified by the expected isotropic distribution of the peak period and propagation direction. Then, the peak period and propagation direction estimation are given by a weighted interpolation whose weights depend on two parameters: the time difference between the time of interest and the swell measurement observation time, and  $\varphi_i$ . This calculation uses all the propagated observations inside region  $\Omega_V$ , defined as the space between the rings whose distance to the storm source equals that of the virtual buoy to the storm source  $\pm 100$  km. Besides, to prevent from extrapolating virtual buoy parameters too far from swell trajectories, region  $\Omega_V$  is limited in longitude to  $\pm 3\sigma_\varphi$  and no information is given whenever values of  $\varphi_i$  within this range all have the same sign, which can be the case in island shadow for instance. The source is defined as the mean geographical position of all the swell propagated observations composing the swell field at maximum refocusing time.

The virtual buoy peak period,  $T^V(t_j)$ , is calculated following the equation :

$$T^V(t_j) = \frac{\sum_{i, P_i \in \Omega_V} c_i(t_j) T_i(t_j)}{\sum_{i, P_i \in \Omega_V} c_i(t_j)} \quad (5.5a)$$

with,

$$c_i(t_j) = \mathcal{N}_{0, \sigma_t^2}(t_{i_0} - t_j) + \mathcal{N}_{0, \sigma_\varphi^2}(\varphi_i(t_j)) \quad (5.5b)$$

where,  $\mathcal{N}_{0, \sigma_t^2}$  is a normal distribution centered on zero, with a standard deviation  $\sigma_t$  equal to two days;  
 $t_{i_0}$ , the acquisition time of the  $i^{th}$  swell observation;  
 $\mathcal{N}_{0, \sigma_\varphi^2}$ , a normal distribution centered on zero, with a standard deviation  $\sigma_\varphi$  equal to five longitude degrees;  
 $\varphi_i(t_j)$ , the  $i^{th}$  swell observation longitude in the local coordinate system at time step  $t_j$ .

The virtual buoy propagation direction,  $D^V(t_j)$ , is given by the azimuth from the virtual buoy.

Similarly to what is proposed in Chapter 3, Subsection 3.3.3, we define a spectral distance,  $S$ , between two storm events of indexes 1 and 2, calculated

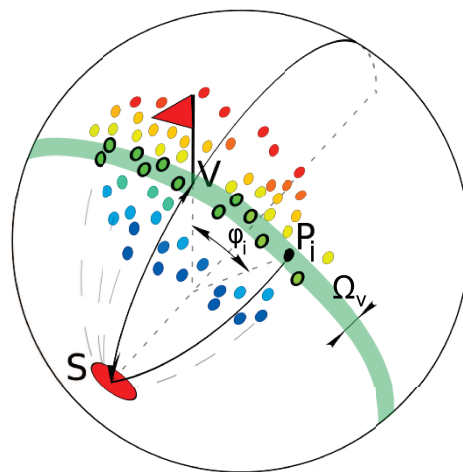


Figure 5.7: Calculation of the virtual buoy peak parameters using the set of propagated observations  $P_i$  belonging to the same swell system, originating from source  $S$ . Virtual buoy is placed in  $V$  (red flag) and estimation uses all the observations whose position falls in region  $\Omega_V$ , distinguished by the solid black line encircling them.  $\varphi_i$  correspond to longitude of  $P_i$  in the local coordinate system whose origin corresponds to source  $S$ . The color of each propagated partition, drawn using a rainbow color palette, gives information on its wavelength (shorter swell in blue to longer swell in red).

at time step  $t_j$  as follows:

$$S^V(t_j) = \frac{1}{q} \left( |D_1^V(t_j) - D_2^V(t_j)| + 2 \frac{|T_1^V(t_j) - T_2^V(t_j)|}{T_1^V(t_j) + T_2^V(t_j)} r \right) \quad (5.6)$$

with,

$$q = 60 \text{ and } r = 250$$

Two separate swell events detected by the refocusing algorithm are concatenated if their mean spectral distance is smaller than 0.6, which corresponds to a difference of  $18^\circ$  in direction and 7% in period). One of the particularities of this method is that the comparison is bound to a specific location instead of being global. In practice, several virtual buoys are placed in the middle of each ocean basin, in the deep ocean regions through which most swell fields propagates. In addition, if specific locations are investigated, for further validation against buoy measurements for instance, the swell field association is also performed at these locations.

As a reminder, the performances of the SAR estimated integral parameters upon observation are presented in Table 5.1. It indicates a root mean square error of 1.07 s and  $20^\circ$  respectively for peak period and propagation direction. The estimated position accuracy of each propagated observation decreases as it is virtually propagated away from its observation point. Though, because no bias is present, these errors are evenly distributed. On average, refocusing regions gather around a thousand propagated observations and their mis-geolocation are thus expected to compensate. Nevertheless, mis-geolocation of individual propagated observations results in the inability to gather to the new swell field those located outside the refocusing region. In addition to direction estimation errors, scattering caused by islands as mentioned by *Snodgrass et al.* (1966), or currents, also contributes to ray back-tracing errors.

## 5.3 Results

The refocusing algorithm has been run for the entire year 2008 on a global scale and more than 700 swell events were identified. This section is separated in three main parts. First, using the StormWatch database, we test the validity of the refocusing algorithm's prime hypothesis: that storm sources can be identified as the regions where a significant number of converging retro-propagated observations. Second, we focus on a two case examples of long-lived storm events and show that the complex storm source parametrization we have proposed in Subsection 5.2.5 is necessary. Third, looking at all storms detected over the year, we estimate the percentage of storms that benefit from this parametrization. Then, we verify that the

storm distribution given by the SAR analysis over a year corresponds to that indicated by wave climatology and WW3 data.

### 5.3.1 StormWatch co-location

For each storm detected by the refocusing algorithm, the StormWatch database is investigated to test whether or not it contains a co-located storm event. For this specific test only, the refocusing algorithm did not use any ancillary wind information to apply a threshold speed condition (Step 1). Using the StormWatch database with QuikSCAT surface winds, detected regions of intense winds are co-located with refocusing regions in 96% cases under following limitations: 700 km distance between the location of maximum of wind speed and of refocusing, direction of the maximum wind speed vector within  $60^\circ$  of displacement direction of the refocusing region and 3-hour interval. The remaining 4% can be explained by wave sampling of the satellite instrument aside the strongest wind conditions.

### 5.3.2 Single cases

Hereafter, we focus on a two interesting cases identified by the refocusing algorithm in the Pacific Ocean.

#### 5.3.2.1 11 April 2008 - SW Pacific

From the SAR analysis, a major storm event was identified on 11 April 2008 in western South Pacific Ocean, around  $165^\circ\text{W}$  -  $55^\circ\text{S}$ . The NCEP blended wind model indicates wind blowing over  $30\text{ m}\cdot\text{s}^{-1}$  for more than 30 hours. In addition to the maximum refocusing location and time given by the SAR analysis, it appears interesting to look at the path of the refocusing center before and after the  $L$  criterion reaches its maximum. Clearly, it follows the direction in which most swell energy propagates. As Figure 5.8 illustrates, for each time step, co-located StormWatch results are represented by wind barbs whose color indicates time. The depression center, south-eastward the maximum wind speed location, follows the same pattern (not shown). The SAR information offers a continuity between the independent StormWatch outputs. This relation is of great interest since it gives the possibility to independently establish a link between a swell system and the history of the extreme wind conditions that have actively contributed to its generation. Such a dataset can greatly benefit to the understanding of swell generation mechanisms.

Further results from Step 4, previously detailed in Methodology Section, give information about the refocusing time with regard to the swell period. As Figure 5.9 indicates, shorter swell refocuses after longer swell, during the afterglow of the storm. The different wavelength groups are all refocusing

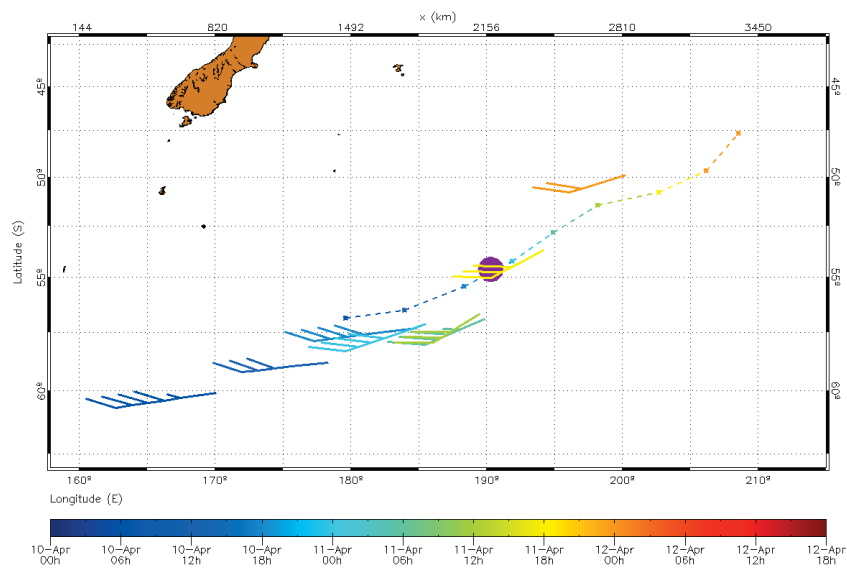


Figure 5.8: Displacement of the refocusing center from the SAR analysis (dashed line). The purple disk indicates the maximum refocusing location. Its position along the dashed line indicates a maximum refocusing occurring on 11 April 00H. Wind barbs indicate in surface wind speed (in [m/s]) and direction. Time is indicated by the color scale.

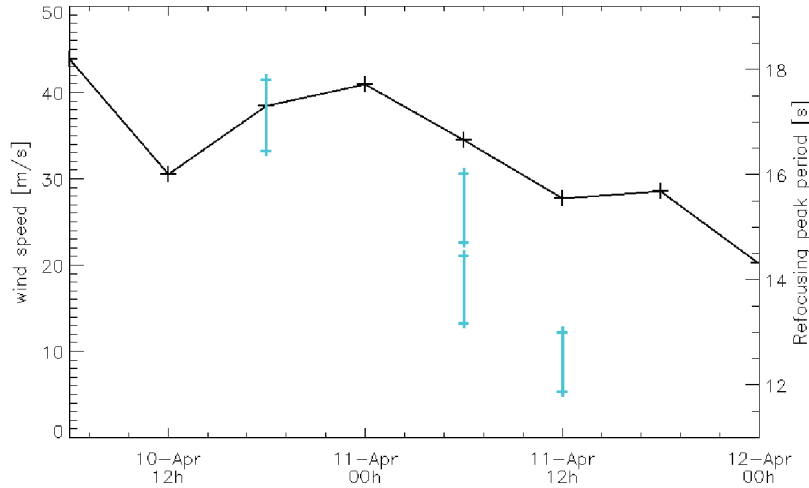


Figure 5.9: Highest surface wind speed time series measured by NCEP blended model (black line) near the refocusing center. SAR swell field given by Step 3 was separated into 4 sub-sets, whose refocusing time was calculated. They are indicated by the cyan segments, together with the wavelength range of these sub-sets. Graph indicates shorter swell refocuses during the storm decay.

within the same region, represented by a purple disk, about 500 km downwind the region where the strongest wind area has slowed down its path, on 11 April. Furthermore, the average wave age at refocusing time is approximately 1.25.

Using *in situ* data from moored buoy WMO32012, the frequency time series of the corresponding swell field was deduced from the hourly-recorded directional wave spectra. After smoothing and partitioning, retrieving the peaks related to this swell event was relatively easy since no other significant swell condition was present during its arrival. Mean direction of arrival is in good agreement with the one expected from the SAR analysis ( $5^\circ$  difference) and the significant swell height is of the order of one meter. Figure 5.10 presents the frequency time series of the swell system in gray solid line and its smoothed curve in dashed black. On top of it, the red solid line represents the expected arrival time based on the distance to the source given by the SAR. Its slope was calculated using equation 2.16 which can also be written as follows:

$$\frac{df}{dt} = \frac{g}{4\pi D} \quad (5.7)$$

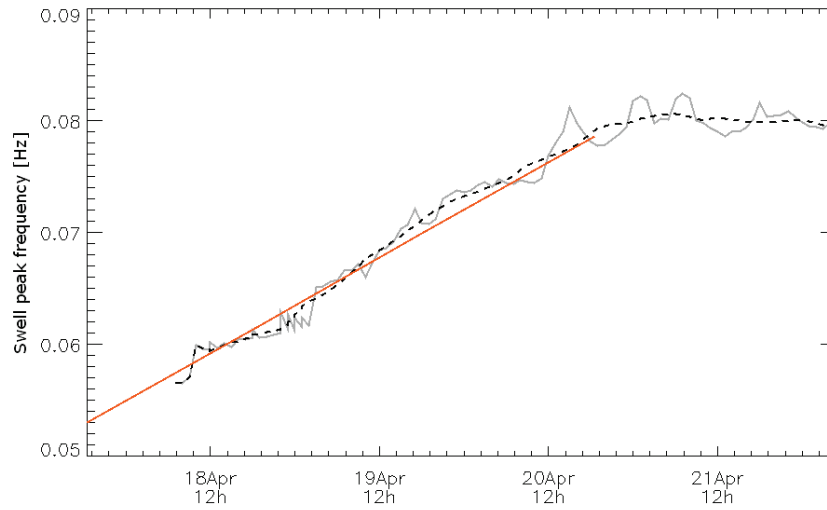


Figure 5.10: Swell peak frequency hourly time series given by buoy WMO32012 in gray solid line and the smoothed time series in dashed black. The solid red line represents the swell expected arrival time based on the storm distance to the buoy.

where,  $g$  is the Earth gravity;  
 $D$ , the distance between the buoy and the storm source.

The differential arrival time given by the SAR fits to that measured by the buoy for low frequencies. Though, for the higher frequency part of the swell field, around 0.08 Hz, the peak frequency signal is still present after the expected arrival time and up to 18 hours after, which is in good agreement with the varying refocusing times found by Step 4.

### 5.3.2.2 15 December 2008 - NE Pacific

This long-lived storm sets up in less than 12 hours and reaches its maximum power on 13 December morning with surface wind speeds over  $25 \text{ m.s}^{-1}$  as measured by QuikSCAT (Figure 5.11). Then, it slowly decreases and the mean flow turns north to north-east until it dies out on 17 December while the storm drives south (not shown). Despite this late move, the storm can be considered to remain at the same location during its most significant activity, setting up a fetch of 1500 km for 3 days. According to *Kitaigorodskii* (1962), non-dimensional fetch is over  $10^4$  and full development is expected. As wave generation theory describes, the wave spectrum peak frequency decreases going down-fetch and swell escapes from the storm region when its phase speed gets close to 1.3.

Accordingly, for wind speed of 18-20 m.s<sup>-1</sup>, we expect peak periods equal of 15-16.7 s, corresponding to wavelengths of 350-435 m. This is in good agreement with the longest SAR recorded swell. Indeed, the ninth wavelength decile of all the SAR observations associated to this storm event equals 346 and highest value 420 m. Then, as the maximum wind power available decreases, the reachable peak frequency of the full developed sea should decrease as well. In our case, the shorter swell refocusing time happens 48 hours after that of the longer swell and at the same location. For a matter of fact, this time difference was so important that this swell event was initially split in two different ones which were then gathered thanks to Step 6.

### 5.3.3 Yearly analysis

Among the 700 storms detected using the SAR analysis, more than 250 exhibit different refocusing times depending on swell peak period. Even though scenarios are multiple, the swell of larger period refocuses strictly before the smaller one in 63% cases and for these situations, the average refocusing time difference equals 14 hours with a standard deviation of 12 hours.

#### 5.3.3.1 Global storm distribution

Figure 5.12-a presents the normalized smoothed 2D histogram of all SAR detected storms for year 2008, so that it indicates the percentage of SAR detected storms encountered in the surrounding 2×2° cells during year 2008. It mainly exhibits extra-tropical storms, rather well distributed in longitude even though they are most present in the western part of each ocean basin.

Several regions clearly arise from this map: western South Pacific Ocean, region between New Zealand and the Ross Sea, North Pacific Ocean near the Aleutian Islands, southern tip of Greenland (Cap Farewell) in the North Atlantic Ocean and in the south-west Indian Ocean, around the Kerguelen Islands. These regions are well known for their frequent storm activity (*Jones and Simmonds, 1993; Moore and Renfrew, 2005; Zhu et al., 2007*). They are all located within the prevailing westerlies band and specific regional effects can intensify the potential storm activity. They are of interest from both a severe weather and climate perspective.

#### 5.3.3.2 Refocusing time vs. time of escape

In the attempt to explain the results of the SAR analysis, it is first important to point out that the refocusing time corresponds to the time at

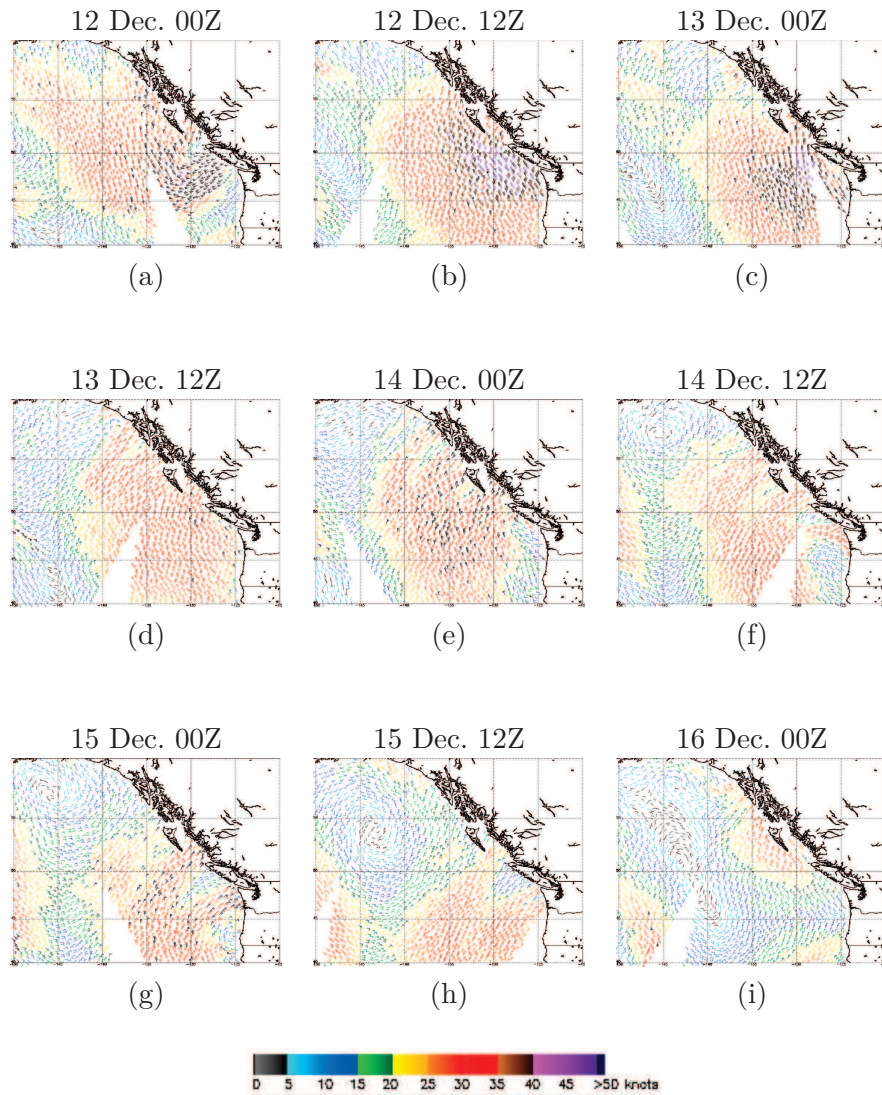


Figure 5.11: Wind field time series measured by QuikSCAT in knots off the coast of the state of British Columbia, Canada. Map (a) starts on 12 December 2008 and goes on every 12 hours.

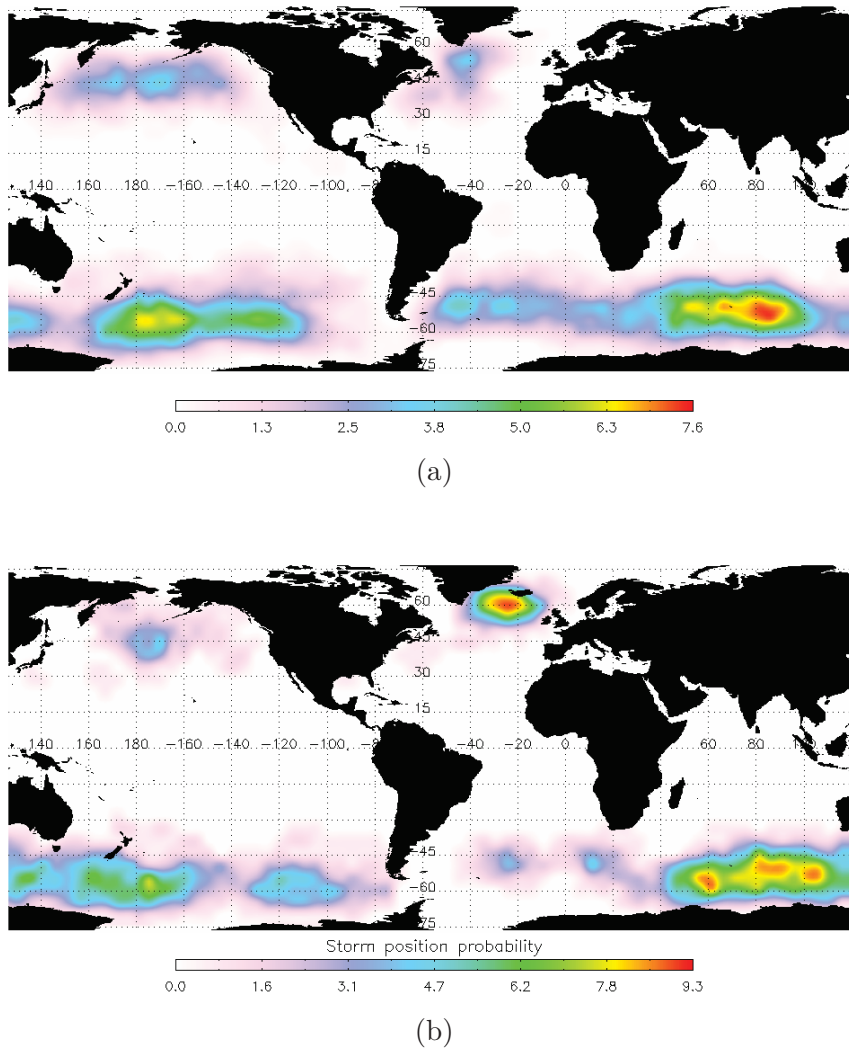


Figure 5.12: Normalized smoothed 2D histogram of all SAR detected storms (a) and all storms for which the maximum significant wave height given by WW3 model was larger than 10 m (b) during year 2008. The colorbar indicates the percentage of detected storms encountered in the surrounding  $2 \times 2^\circ$  cells during year 2008.

which the swell escapes from the storm region. Indeed, on average, the refocusing region is located downwind the maximum surface wind speed location and wave age equals 1.4 at maximum refocusing (0.3 standard deviation). Therefore, the term 'refocusing time' or 'time of refocusing' should be understood as 'time of escape'. This is relevant when comparing the storm sources location given by the SAR analysis to that of the wave model. In the latter case, the storm source identification is given by the time of maximum total significant swell height which, on average, comes sooner than the time given by the SAR analysis.

### 5.3.3.3 Geographical distribution comparison

As already mentioned in paragraph 5.2.2.4, the storm source identification can be applied to WW3 data. Comparing the storm source geographical distribution given by these two different datasets over year 2008 (Figure 5.12), Cap Farewell region appears under-represented by the SAR analysis. These distribution can also be compared in terms of events per ocean basins as proposed on Figure 5.13. In this histogram, the storm distribution obtained with the current version of the SAR refocusing algorithm is represented under label SAR V1 while SAR V2 refers to another version detailed further down and WW3 represents the distribution obtained using WW3 data. It shows that the current refocusing algorithm over-estimates the number of storms occurring in the South Atlantic Ocean and the North Pacific Ocean while it under-estimates them in the South Pacific Ocean, the North Atlantic Ocean and the Indian Ocean.

This difference can be explained by different factors. First, it is partly introduced by the refocusing algorithm. Indeed, swell fields that have more time to propagate and be imaged by the SAR instrument before they reach the coast are better sampled. As the refocusing algorithm detects storm events for which a minimum number of swell observations converge, these are detected first. Therefore, among different ocean basins, swell fields that propagate in wide deep oceans, with limited effects of island blocking, are favored. Also, within the same ocean basin, since most detected swell fields originate from extra-tropical westward moving depression, swell fields that are generated in the western side of ocean basin are biased as well. Second, the geographical distribution of the SAR swell measurements is not the same over all ocean basins. For instance, over the eastern North Atlantic Ocean, many wave mode measurements are not available over year 2008 because the SAR instrument was operated in wide swath/low resolution mode for a higher priority project, the CleanSeaNet project<sup>4</sup>. As a result, the refocus-

---

4. CleanSeaNet is a near-real-time satellite-based oil spill and vessel monitoring service provided to European Union member states that entered into operation on 16 April 2007

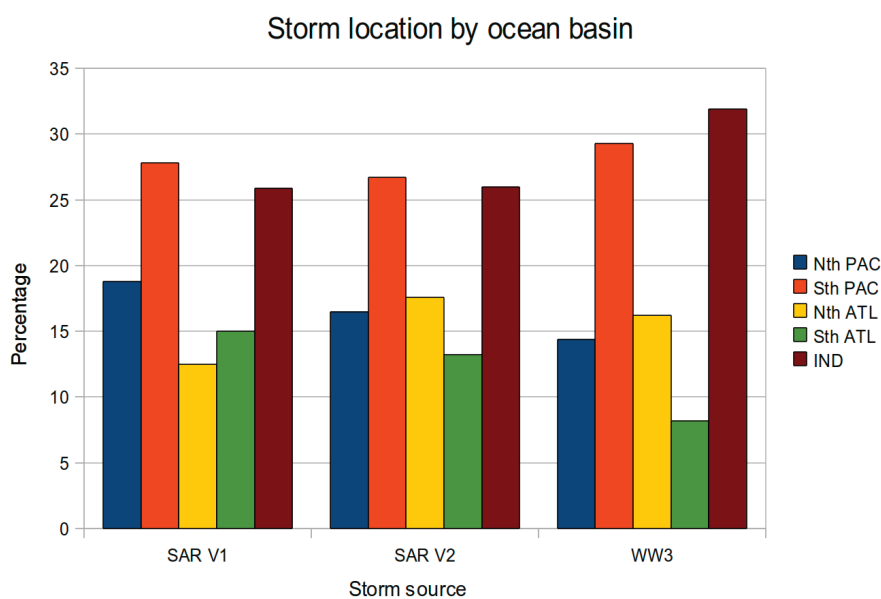


Figure 5.13: Storm repartition among ocean basins for year 2008. SAR V1 and SAR V2 respectively refer to the raw and modified version of the refocusing algorithm using SAR data while WW3 designates the WW3 model. Storm repartition given by SAR V2 algorithm is closer to that of WW3 than SAR V1 for North Pacific, North Atlantic Ocean and South Atlantic Ocean. General shape is in better agreement as well. Still, even for SAR V2 algorithm, repartitions for Indian Ocean and South Atlantic Ocean are significantly different. This difference is attributed to the different storm estimation method that tend to locate storms sooner for WW3, thereby locating some Indian Ocean storms in the South Atlantic Ocean.

ing algorithm suffers from fewer observations points in such regions.

In the attempt to test these hypothesis and correct the bias introduced by the refocusing algorithm, a new version of the refocusing algorithm has been tested. It differs in the calculation of the density-maps: now, the weight of each propagated swell observation no longer equals 1 but varies to compensate for the probability of each propagated swell observation to be imaged from its propagated position on to the shore, given the geographical distribution of the SAR observations during the last satellite orbit cycle. Still, each density-map cell is normalized by its surface. In the end, storm geographical repartition among the different ocean basins is presented in Figure 5.13 under label SAR V2.

Storm distribution given by SAR V2 algorithm is closer to that of WW3 than SAR V1 for North Pacific Ocean, North Atlantic Ocean and South Atlantic Ocean. General shape is in better agreement as well. Still, even for SAR V2 algorithm, significant differences exist for Indian Ocean and South Atlantic Ocean that are respectively over and under-estimated. This difference is most probably due to their permeability to storms passing from the South Atlantic Ocean to the Indian Ocean and different storm estimation methods. Indeed, because storm events given by the model tend to be detected earlier than those detected by the SAR, the same storms, whenever traveling westward and at the limit between these two oceans might be counted in different ocean basins.

## 5.4 Discussion

Results showing that for a given swell field, low frequency swell escapes before the high frequency part might seem counterintuitive for the wave peak frequency decreases during the wave generation process. Although, the whole difference remains in the fact that we consider waves inside *or* outside their generation region. Case of 15 December 2008 shall serve as an example. It is preferred to case of 11 April 2008 as it is a simpler case to analyze for several reasons. First, it can be considered to be almost stationary. Furthermore, the storm location, off the coast of the state of British Columbia, Canada, together with a mean wind field blowing offshore, provide good observation conditions. It assures that the emanating swell only results from this storm. In the end, we believe that the main reason explaining the refocusing time evolution with regards to the frequency is that the early generation of high frequency waves inside the fetch feeds the further development of longer waves until full development or end of fetch is reached. After that, its period remains constant and swell escapes from the storm region. It can even be considered as a footprint of the wind and wave

forcing integrated all along its path inside the storm region.

The explanation given above for the observed scenario may seem oversimplified. Obviously, it describes a general pattern and intentionally skips a few aspects. For instance, during the set-up of the fetch region, waves leaving the area will have received less energy than those that will have traveled through it all. In our case, this transient state is neglected since there is a clear asymmetry of the wind power evolution developed by the storm, opposing a rapid set up to a long storm decay.

Finally, it is unrealistic to model the previous storm by a point source given the large generation time difference of two days. Though, among the swell field sub-sets given by Step 4 (Swell field analysis), this hypothesis can only be made at sufficient distance from its refocusing point. Among these, the refocusing region area increases with the decreasing mean peak period of the associated swell field sub-set. Indeed, their generation require weaker winds and shorter fetches, conditions that can be met over wider areas. This phenomenon even tackles the question of whether the refocusing algorithm makes sense past a certain period threshold. This is the main reason why we choose to restrict the refocusing approach to waves whose wavelength exceeds 250 meters.

Determining the correct time of escape for a given observation can have a significant impact on the propagated information. Indeed, in the absence of energy dissipation, swell energy evolution is mainly driven by frequency dispersion and geometrical spreading and approaches the asymptote described by the following equation:

$$H_s(\alpha) = H_s(\alpha_0) \sqrt{\frac{\alpha_0 \sin(\alpha_0)}{\alpha \sin(\alpha)}} \quad (5.8)$$

where,  $\alpha$  is the spherical distance between the swell and its storm source;  
 $\alpha_0$ , the spherical distance at swell observation time and  $H_s(\alpha)$ ;  
 $H_s(\alpha_0)$ , the corresponding significant swell height.

Using the example of 11 April 2008, changes are significant if one considers that all the propagated partitions were generated at the same time instead of being spread over 24 hours. Measuring height 4,000 km away from the storm source, it would result in a significant swell height over-estimation by an average 7%. Similarly, dissipation is expected to vary since it depends on the swell slope, but to a lesser extent. Also, it is expected to vary with the directional aperture of the swell spectrum. This dependency shall be investigated in future studies using the size of the refocusing regions.

## 5.5 Conclusion

Ever since 1978, SAR instruments have been imaging the ocean and our ability to understand the imaging process and to retrieve ocean wave spectra has now reached a mature point. The European Space Agency has shown during ENVISAT mission that these spectra could be processed and made available in near real-time.

Using these partitioned Level-2 wave mode products, a methodology has been developed to enable the automatic association of swell observations into reconstructed swell field. Taking advantage of swell persistency, it is based on the assumption that, whenever back-traced, long swell observations converge to their generation area. This process has been applied to all year 2008, worldwide. Comparisons with NCEP blended surface winds have confirmed this hypothesis, showing quasi-systematic co-location of the swell origins with hurricane force extra-tropical cyclones. Besides, this method offers an independent association of a swell field to the intense surface winds that have contributed to its generation. Provided for overall year 2008, such a dataset will give information on the total energy transferred from the atmosphere to the ocean and can improve our understanding of wave generation processes.

Most importantly, following the observations made by *Delpey et al. (2010)*, we proposed a method to study the validity of the point source hypothesis for each swell event. Looking at the yearly analysis, long swell leaves the storm region before the shorter one on average. This is observed in more than 63% cases. For these situations, the average time difference equals 14 hours, with a standard deviation of 12 hours. Most often, we observe a rapid set-up of the storm conditions with a slow decay that plays an important role in the swell generation.

The refined swell field reconstruction method proposed in this chapter is specifically designed for the study of swell emanating from long-lived storms for which swell will escape at different time and/or locations from the storm and for complex scenarios where closely succeeding storms require careful partitioning of the different storm sources and swell measurements' filtering. As the example of 15 December 2008 illustrates, the long storm decay seems to be responsible for the 48 hour difference between the time of escape of long and short swell. These results bring the light on the necessity to reconsider the point source hypothesis for long lasting storm events. Not considering this varying time and region of generation within a single swell field can lead to a mis-calculation of the estimated swell energy decay of 10% and lead to incomplete swell reconstruction.

Finally, the concatenation of all storm locations over year 2008 exhibits ocean regions well known for their frequent storm activity. The comparison of the storm location distribution given by the SAR analysis to that given by the analysis of WW3 model results has revealed a bias in the SAR swell field detection related to the swell lifetime. A second version of the refocusing algorithm correcting for this effect was thus developed and showed that the detected storm distribution among ocean basins is closer to that extracted from WW3.

The automation of refined swell field reconstruction provides a rush of information. It could be used to better estimate the dissipation parameter given by *Ardhuin et al. (2009)* and study its dependency on other parameters such as the swell directional aperture. In the end, these improvements together with the data continuity insured by the forth-coming Sentinel-1 mission will contribute to the increasing quality of SAR swell field representation. Looking back at the long ESA wave mode products record that has been continuously operated from 1991 to 2012, this swell reconstruction could also find applications in climatological studies, calculating storm location and storm energy densities at a global scale and followed potential trends.

We now dispose of SAR swell measurements organized in coherent swell fields, for which all three integral parameters are available far enough from the storm source. Furthermore, a virtual buoy method has been proposed to retrieve information on one of these integral parameters at a precise location for each swell system. Still, this information relies on the presence of propagated SAR swell measurements in close vicinity of the point of interest. As studied in Chapter 4, they can have very irregular geographical distributions, with regions of thousands of kilometers showing very few propagated swell measurements. In such cases, the virtual buoy methodology would not be applicable although, for example, the large scale distribution of wavelength propagated measurements seems to deliver useful information. Additionally, several types of measurement errors were identified in Chapter 3. Being able to retrieve a large scale distribution for each integral parameters would thus enable a better detection of these outliers and improve out estimations of swell field characteristics. These issues are addressed in the following chapter.

## Bibliography

- Ardhuin, F., F. Collard, B. Chapron, P. Queffelec, J.-F. c. Filipot, and M. Hamon (2008), Spectral wave dissipation based on observations: a global validation, in *Proceedings of Chinese-German Joint Symposium on Hydraulics and Ocean Engineering, Darmstadt, Germany*, p. 391–400, ISBN: 3-936146-23-3. 2, 152
- Ardhuin, F., B. Chapron, and F. Collard (2009), Observation of swell dissipation across oceans, *Geophys. Res. Lett.*, 36, L06,607, doi:10.1029/2008GL037030. ii, 2, 70, 71, 152, 181, 237
- Collard, F., F. Ardhuin, and B. Chapron (2009), Monitoring and analysis of ocean swell fields from space: New methods for routine observations, *Journal of Geophysical Research-Oceans*, 114(C7), C07,023. ii, 2, 68, 69, 70, 71, 80, 85, 111, 152, 153, 155, 219, 239
- De Joux, R. (2006), Catalogue des evenements extremes a partir de l'archive du diffusiometre d'ERS, *Rapport d'etude BO-015-IFR-0609-RF*, BOOST-Technologies. 154
- Delpy, M., F. Ardhuin, F. Collard, and B. Chapron (2010), Space-time structure of long swell systems, *J. Geophys. Res.*, 115, C12,037, doi:10.1029/2009JC005885. ii, 2, 90, 152, 180, 186, 189, 192, 241
- Hanson, J. L., and O. M. Phillips (2001), Automated analysis of ocean surface directional wave spectra, *J. Atmos. Ocean Technol.*, 18, 277–293. 2, 86, 91, 152, 192
- Jones, D., and I. Simmonds (1993), A climatology of southern hemisphere extratropical cyclones, *Climate Dynamics*, 9(3), 131–145. 173
- Kitaigorodskii, S. A. (1962), Applications of the theory of similarity to the analysis of wind-generated wave motion as a stochastic process, *Izv. Geophys. Ser. Acad. Sci., USSR*, 1, 105–117. 172
- Moore, G. W. K., and I. A. Renfrew (2005), Tip jets and barrier winds: A QuikSCAT climatology of high wind speed events around Greenland, *Journal of Climate*, 18(18), 3713–3725, doi:10.1175/JCLI3455.1. 120, 173
- Quilfen, Y., C. Prigent, B. Chapron, A. A. Mouche, and N. Houti (2007), The potential of QuikSCAT and WindSat observations for the estimation of sea surface wind vector under severe weather conditions, *J. Geophys. Res.*, 112, C09,023, doi:10.1029/2007JC004163. 154
- Saha, S., S. Moorthi, H.-L. Pan, X. Wu, J. Wang, S. Nadiga, P. Tripp, R. Kistler, J. Woollen, D. Behringer, H. Liu, D. Stokes, R. Grumbine, G. Gayno, J. Wang, Y.-T. Hou, H.-y. Chuang, H.-M. H. a. J. S. Juang,

M. Iredell, R. Treadon, D. Kleist, P. V. Delst, D. Keyser, J. Derber, M. Ek, J. Meng, H. Wei, R. Yang, S. Lord, H. v. d. Dool, A. Kumar, W. Wang, C. Long, M. Chelliah, Y. Xue, B. Huang, J.-K. Schemm, W. Ebisuzaki, R. Lin, P. Xie, M. Chen, S. Zhou, W. Higgins, C.-Z. Zou, Q. Liu, Y. Chen, Y. Han, L. Cucurull, R. W. Reynolds, G. Rutledge, and M. Goldberg (2010), The NCEP climate forecast system reanalysis, *Bull. Amer. Meteorol. Soc.*, *91*, 1015–1057. 154

Snodgrass, F. E., G. W. Groves, K. F. Hasselmann, G. R. Miller, W. H. Munk, and W. H. Powers (1966), Propagation of ocean swell across the pacific, *Philosophical Transactions of the Royal Society of London. Series A, Mathematical and Physical Sciences*, *259*(1103), 431. iv, 2, 56, 69, 70, 152, 168, 192

Zhu, X., J. Sun, Z. Liu, Q. Liu, and J. E. Martin (2007), A synoptic analysis of the interannual variability of winter cyclone activity in the Aleutian low region, *Journal of Climate*, *20*(8), 1523–1538, doi:10.1175/JCLI4077.1. 173



# Chapter 6

## Synthetic swell field

### Contents

---

6.1	Synthetic swell field estimation . . . . .	<b>187</b>
6.1.1	Surface fitting . . . . .	187
6.1.2	Iterative filtering . . . . .	202
6.2	Validation . . . . .	<b>210</b>
6.2.1	Methodology . . . . .	213
6.2.2	Tested configurations . . . . .	213
6.2.3	Statistical results . . . . .	214
6.2.4	Single cases . . . . .	216
6.2.5	Dependences . . . . .	219
6.2.6	Rejected Data . . . . .	227
6.3	Comparison with the numerical wave model . . . . .	<b>229</b>
6.3.1	Methodology . . . . .	229
6.3.2	Statistical results . . . . .	230
6.4	Conclusion . . . . .	<b>231</b>
	Bibliography . . . . .	<b>235</b>
6.A	GRL publication: Revealing forerunners on ASAR . . . . .	<b>237</b>

---

In the previous chapter, we demonstrated the possibility to associate isolated swell measurements into coherent swell fields. However, stroboscopic imaging phenomena described in Chapter 4 often lead to heterogeneous sampling which undermines our capability to retrieve swell information on significant swell height, peak period and direction at point of interest even though the large scale distribution could provide useful information. Exploiting these distributions could also allow a better outlier detection. Besides, looking forward to developing downstream applications with a view to make the best use of future Sentinel-1 missions, it appears crucial to try to provide regularly sampled swell information and estimate the quality of these estimations.

A similar work was undergone by *Delpey et al. (2010)* with a specific focus on the energy distribution in the direction perpendicular to the propagation of the swell field, the transverse direction. Among others, it relies on the hypothesis that outside of land influence, the swell field energy distribution in the transverse and the propagation direction were independent. The study of long-lived storms in Chapter 5 has shown that they could not be considered as point source since the swell can sometimes continuously radiate from the storm region for 48 hours. For this reason, such hypothesis appear over-simplified and we prefer to develop an observation based swell model by minimizing the constraints on the overall shape of the swell field.

Here, for each reconstructed swell field provided by the refocusing algorithm, we investigate the possibility to combine the discrete and irregularly sampled swell information provided by the propagated SAR observations into another set, filtered and regularly sampled over space and time, called synthetic swell field.

On average, a reconstructed swell field contains around a thousand propagated observations and a smart selection and combination of the most accurate ones is possible, by discarding erroneous measurements. We choose to tackle this issue together with the estimation of swell parameter of the entire swell field region through an iterative combined use of outliers filtering and surface fitting.

First, the synthetic swell field estimation method is described, including the data confidence estimation based on the results from Chapter 3 and the iterative steps of surface fitting and outliers filtering. In particular, two different least-square minimization methods are investigated: a direct weighted fit using 2D polynomial regression and Kriging. Second, this methodology is applied to a year-long dataset of reconstructed swell fields and the swell integral parameters' accuracy given by the previous methodology is estimated using *in situ* measurements. One of the main issues is to verify to which extent irregular sampling caused by stroboscopic imaging phenomena

can be compensated by interpolations methods. Third, synthetic swell field estimates are compared to the numerical wave model WW3 to identify the immediate benefit our observation based model can bring to classical models. Finally in the Appendix, we propose an application of an early version of the synthetic swell field: we show how swell signatures in seismic noise can be reproduced and how, the other way around, the seismic noise information can be used to help recover the extremely long swell signal present in SAR images but absent from the SAR L2P products. This paper (cf. Appendix, page 237) was accepted and published in Geophysical Research Letters (GRL).

## 6.1 Synthetic swell field estimation

This section presents the overall methodology for the estimation of the synthetic swell field starting from the reconstructed swell fields produced using the refocusing algorithm (cf. Chapter 5). In the first place, we justify the use of linear least square estimation problems and propose a coordinate system, followed by the two different surface fit methods being tested: a 2D polynomial regression and Kriging. While the former has the advantage of being time efficient and of taking data confidence into account, the latter should provide a better surface fit, provided that input parameters are properly set. In the second place, the successive steps of the iterative filter are exposed in details. It is based on the alternate use of the previously obtained surface fits and outlier rejection. Although, the overall scheme and the outlier filters are not the same for all integral parameters (height, period, direction) and therefore detailed for each of them.

### 6.1.1 Surface fitting

#### 6.1.1.1 Linear least square minimization

At a given time, the propagated swell observations associated to a reconstructed swell field can be considered as discrete and irregularly sampled estimations of the integral parameters' spatial distribution. From there, several surface fitting techniques can be applied to recover the overall distribution such as inverse distance interpolation, polynomial regression, bicubic splines, modified Shepard's interpolation, Kriging or radial basis functions. Among these, two different kinds of interpolation can be distinguished: those for which the fitted surface estimation at a certain point is influenced by all the measurements, as for a polynomial regression, and those for which only the measurements within the point vicinity are taken into account, as for Kriging.

All these interpolation techniques belong to the family of linear least

squares estimation algorithms. In that sense, they provide a mathematical model of the data in cases where the idealized values provided by the model are expressed linearly in terms of the unknown model parameters. The resulting fitted model can be used to summarize the data or predict unobserved values.

Linear least square methods solve over-determined systems of linear equations, where the best approximation is defined by minimization of the sum of squared differences between the data values and their corresponding modeled values, referred to as *residuals*. The minimized function can be represented as follows:

$$f(\mathbf{A}) = \sum_{c=0}^p r_c^2(\mathbf{A}) \quad (6.1)$$

where,  $\mathbf{A} = (a_0, a_1, \dots, a_n)$ , is a vector;  
 $f$ , the objective function;  
 $r_c$ , the residuals, functions from  $\mathbb{R}^n$  to  $\mathbb{R}$ .

Such problems are convex and have a closed-form solution that is unique, provided that the number of data-points used for fitting equals or exceeds the number of unknown parameters ( $p \geq n$ ). In contrast, non-linear least squares problems generally must be solved by an iterative procedure and the problems can be non-convex with multiple optima for the objective function.

Because least square methods use  $l_2$  norm, they are a lot more sensitive to outliers than methods using  $l_1$  norms<sup>1</sup>. Still, least square minimization methods are much more time efficient.

The main objective is obviously the best agreement of the fitted surface with *in situ* measurements, but the calculation cost has to be taken into account as well. Indeed, for operational application purposes, global scale SAR swell field analysis encompassing swell field reconstruction and synthetic swell field estimation is to be launched several times a day. Besides, for each analysis, the average amount of swell fields to be processed is around 50, corresponding to all swell fields found by refocusing in the last two weeks. If each of these swell fields is propagated for two weeks and results are needed every three hours then, the average number of calculated surface fits reaches 5,600. Considering that the number of surface fit iteration for each time step equals 5, one has to calculate about 28,000 surface fits each time the global scale SAR swell field analysis is launched. Thus, time efficiency can be critical and shall be estimated, depending on the methods

---

1. The  $l_2$ -norm of a vector  $\mathbf{x}$  is denoted  $|\mathbf{x}|_2$  and defined as follows:  $|\mathbf{x}|_2 = \sqrt{\sum_{i=0}^n x_i^2}$  while the  $l_1$ -norm,  $|\mathbf{x}|_1$ , is defined as:  $|\mathbf{x}|_1 = \sum_{i=0}^n |x_i|$ .

and the number of points in the reconstructed swell field.

Under these considerations, we selected least square methods for time efficiency reasons. However, as these methods are more sensitive to outliers, we use an iterative process during which surface fits alternate with outlier exclusion in order to remove most outliers from the final surface estimation. The criteria qualifying swell measurements as such are detailed in the next section. Prior to this, we need to expose the coordinate system used to describe the synthetic swell field.

### 6.1.1.2 Swell field coordinate system

As mentioned in introduction, our attempt to derive a synthetic swell field from SAR swell propagated observations is similar to the study of the swell field structures undergone by *Delpey et al. (2010)*. We adopt the same swell field parametrization, defining a propagation and a transverse direction. The propagation coordinate,  $r$ , is defined as the great-circle distance to the reference storm source point and the transverse coordinate,  $\theta$ , is defined as the angle between the North, the reference storm source point and the geographical point of interest. The  $(r, \theta)$  grid is illustrated in Figure 6.9-b, together with an example case of the peak wavelength spatial distribution of the propagated SAR observations at a given time in Figure 6.9-a. Resolution equals 150 km and 2.5° in in propagation and transverse direction, respectively.

The synthetic swell fields will be estimated along a time period ranging from 5 to 13 days after swell generation, with a 3-hour time step. The 5 day-limit is explained by the fact that significant swell height estimates cannot be realistically made to close to the storm source (cf. Chapter 2, Section 2.3). The 13 day-limit is arbitrary. It is mostly justified by the fact that after this propagation time, swells' energy is of the order of a few decimeters and is therefore becoming negligible.

### 6.1.1.3 Polynomial regression

Using a polynomial regression allows us to fit a polynomial surface to the swell measurements spread over the  $(r, \theta)$  grid. The principle of the polynomial regression is first recalled. Then, because the expected shape of the function models differs depending on the integral parameter of interest, polynomial orders are further discussed for each one of them.

Even though the polynomial regression fits a non-linear model to the data, the estimation problem itself is linear in the way that it linearly depends on the polynomial coefficients. Thus, assessing the swell integral parameter's spatial distribution by a direct 2D polynomial regression to

the scattered propagated observations has the advantage of being very fast. Besides, the contribution of each propagated observation relatively to the others can easily be taken into account by assigning weights, which are representative of the confidence in the propagated information.

Let  $P$  be the 2D polynomial function chosen to represent the integral parameters' spatial distribution over variables  $r$  and  $\theta$ :

$$P(r, \theta) = \sum_{i=0}^m \sum_{j=0}^n a_{ij} r^i \theta^j \quad (6.2)$$

where  $a_{ij}$  are the polynomial coefficients to determine.

We can also describe the problem using matrices as detailed below: let  $\mathbf{W}$  be the vector whose elements  $w_c$  are the weights assigned to each measurement;  $\mathbf{Y}$ , the vector whose elements  $y_c$  are the measurements and of coordinates  $(r_c, \theta_c)$  with  $0 \leq c \leq p$ . We further define  $\mathbf{X}$  and  $\mathbf{A}$  as:

$$\mathbf{X} = \begin{pmatrix} 1 & \cdots & \theta_0^n & r_0 & \cdots & r_0 \theta_0^n & \cdots & r_0^m \theta_0^n \\ \vdots & \ddots & \vdots & \vdots & \ddots & \vdots & \ddots & \vdots \\ 1 & \cdots & \theta_p^n & r_p & \cdots & r_p \theta_p^n & \cdots & r_p^m \theta_p^n \end{pmatrix}, \quad \mathbf{A} = \begin{pmatrix} a_{00} \\ \vdots \\ a_{0n} \\ a_{10} \\ \vdots \\ a_{1n} \\ \vdots \\ a_{mn} \end{pmatrix} \quad (6.3)$$

Then, the problem can be solved by minimizing the objective function:

$$f(\mathbf{A}) = \sum_{c=0}^p r_c^2 \quad (6.4)$$

where the residuals are defined by:

$$r_c = w_c \left( y_c - \sum_{i=0}^m \sum_{j=0}^n a_{ij} r_c^i \theta_c^j \right) \quad (6.5)$$

The polynomial function is finally given by:

$$\tilde{\mathbf{A}} = \left( \mathbf{X}^T \mathbf{W} \mathbf{X} \right)^{-1} \mathbf{X}^T \mathbf{W} \mathbf{Y} \quad (6.6)$$

The polynomial function degree has to be high enough to allow the model to faithfully reproduce the data evolutions. However, excessive freedom can induce the fitted surface fluctuations to follow the data errors rather than the

data overall trend. Therefore, the polynomial degree has to be discussed according to the expected data evolution. If the polynomial degree is too high, it results in an improper fit, easily evidenced by a high RMSE. Therefore, we start with a low polynomial degree and successively try higher degrees, calculating the associated RMSE for each. It is expected to decrease until it reaches a minimum when the model polynomial function best describes the integral parameter's spatial distribution.

One of the advantages of using a polynomial regression is that once the polynomial coefficients are known, the surface fit can be estimated at any location without any further calculation.

**Wavelength** As already presented in Chapter 2, considering a single swell system at a given time, the peak period is expected to increase linearly as one moves away from the storm source because of dispersion. If the storm source was punctual in space and time, the peak period distribution would be a plane in our geometry. As the peak wavelength is proportional to the squared peak period, its distribution in the propagation direction would be quadratic while there would be no transverse direction dependency. Though, as discussed in Chapter 5, this point of view can be inadequate for long-lived and/or fast moving storms, even far away from the generation area. Therefore, the peak wavelength distribution in the transverse direction is expected to vary significantly and the distribution in propagation direction to be more complex than just quadratic.

To estimate the model function for the wavelength spatial distribution, we choose a 2D polynomial function whose degree is superior or equal to 2.

**Direction** Similarly, if the storm source was punctual in space and time, the peak direction distribution would vary linearly in the transverse direction and there would be no propagation direction dependence. Following the same considerations for the representation of complex distributions emanating from long-lived and/or fast moving storms, we choose to estimate the model function for the wavelength spatial distribution with a 2D polynomial function whose degree is greater or equal to 2.

**Significant swell height** As for the significant swell height, the distribution in the propagation direction can be assessed with *in situ* data using a single point observation like moored buoys or pressure recorders. Still, such approaches are a little different since they observe the significant swell height evolution in time and in the propagation direction while we look at the spatial distribution at a given time. Main difference is that energy propagation

and associated dispersion and dissipation have to be taken into account to obtain the spatial distribution at a given time.

Previous studies focusing on individual swell systems (*Snodgrass et al.*, 1966; *Hanson and Phillips*, 2001; *Kerbiriou*, 2008) indicate that, from a given observation point, the significant swell height increases with the arrival of the swell front, reaches a maximum and then decreases. Still, the peak period at which this maximum occurs varies from one event to another and it may not even be seen by the SAR if it occurs at a peak wavelength outside the wavelength observability range of the SAR wave mode instrument. Significant swell height distribution in the transverse direction is scarcely documented. Still, *Delpey et al.* (2010) have shown that the transverse structure could be assessed using SAR measurements and that, in deep ocean and outside from island shadows, it was conserved during the swell propagation between the intermediate and the far field. It usually exhibit a clear principal propagation direction in which the significant swell height is several times higher than that propagating in adjacent directions. As opposed to the peak wavelength and direction distributions, its distributions in propagation and transverse directions are not expected to be monotonic. Because of this rather more complex distribution, this integral parameter's spatial distribution is estimated with 2D polynomial function whose degree is greater or equal to 4.

**Summary** In the end, using equation 6.2 and taking account the parametrization given in the previous paragraphs, the spatial distribution of each integral parameters is expressed as follows:

$$P(r, \theta, t) = \sum_{i=0}^m \alpha_i(t)r^i + \sum_{i=1}^m \beta_i(t)\theta^i + \sum_{\substack{i,j>0 \\ i+j<m}} \gamma_{ij}(t)r^i\theta^j \quad (6.7)$$

where,  $\alpha_i(t)$ ,  $\beta_i(t)$  and  $\gamma_{ij}(t)$  are the polynomial coefficients to determine,

$m \geq 2$  for the peak wavelength or direction,

$m \geq 4$  for the significant swell height.

The fact that the degree associated to coefficients  $\gamma_{ij}(t)$  is non-null is motivated by the supposed correlation between the integral parameters evolution in the transverse and propagation direction. We believe that storm source history, including intensity, dimension and storm tracks, is responsible for most of it when considering swell propagation outside of land influence. For example, the peak wavelength distribution of a reconstructed swell field is represented on Figure 6.1-a. Subplot (b) shows the difference between this distribution and the theoretical one that would have been obtained considering a punctual storm source. The fact that the difference is anisotropic is most probably a consequence of the eastward storm displacement during the swell generation (not shown).

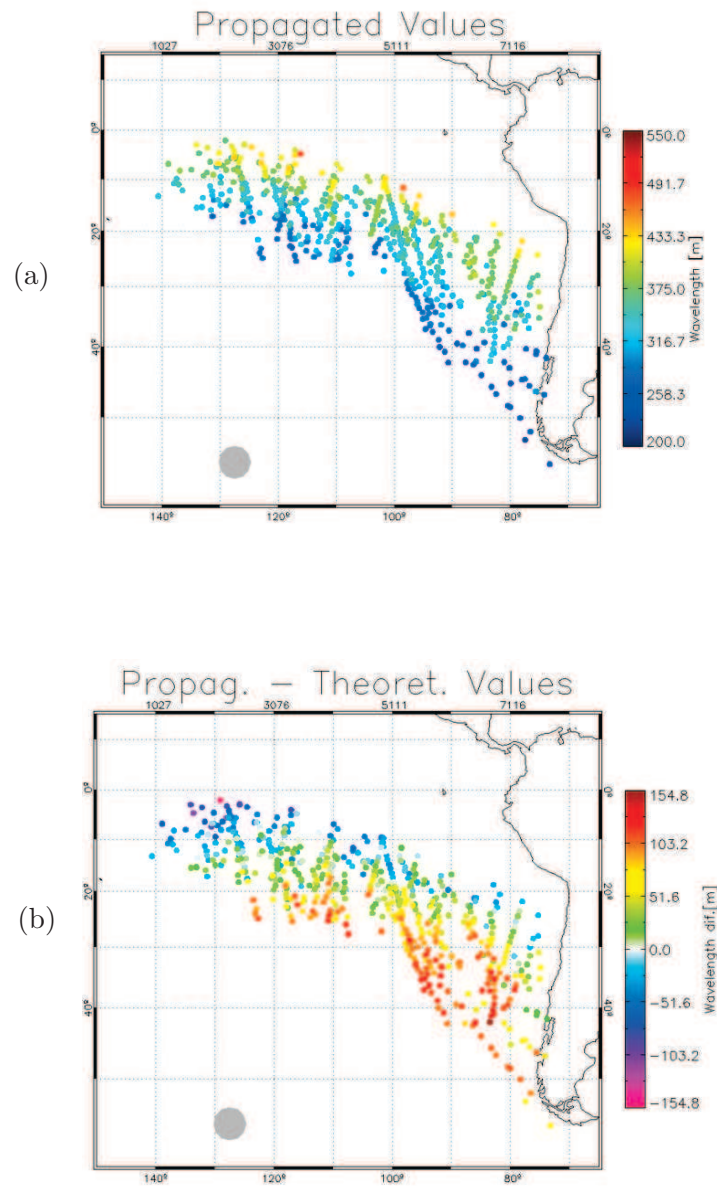


Figure 6.1: Illustration of the peak wavelength distribution of a reconstructed swell field (a) and of the difference between this distribution and the theoretical one that would have been obtained considering a punctual storm source (b).

### Data density correction: a test case

We are now going to test the capability of the present polynomial fit to solve typical swell integral parameters' spatial distribution starting from heterogeneous propagated observation density. However, instead of using actual propagated swell observations, we use a simulated distribution modeled by a 2D polynomial function to which a Gaussian noise is added. This function is obtained by a previously calculated surface fit<sup>2</sup>. Therefore, the present step can be seen as a test of robustness of the polynomial regression with respect to noisy input data. As the original simulated field before noise addition is given by a 2D polynomial function, a perfect match with the fitted surface is theoretically possible. Therefore, any difference between the two is attributed to our fitting method. Specifically, the effect of heterogeneous data density in the  $(r, \theta)$  grid on the fitted surface is investigated. It is further shown that it introduces a significant bias in the final fitted surface. We thus propose to correct for this effect by introducing weight coefficients to the input propagated swell measurements depending on the data density. The new fitted surface shows better agreement with the expected result.

As a typical case example, we choose to focus on the swell generated by a storm that took place on 2 January 2012. On Figures 6.2 and 6.3, all three integral parameters' spatial distribution are given six days after the swell was generated. The simulated swell field values are given at the location of the propagated SAR observation. Only their value has been changed so that the data density remains the same.

Even though the accuracy of the integral parameter's spatial distribution to reproduce is not the main topic of this section, it is still important to use realistic conditions. It will be further shown in the results section that the simulated spatial distribution of the integral parameters obtained by this polynomial regression is satisfying. Already, it can be noticed that the peak wavelength increases with the distance from the storm source and the peak direction variations in transverse direction is consistent.

The significant swell height exhibit hill-like shape. Its variations in transverse direction indicate the swell energy predominantly propagates South-East. These three spatial distributions are modified by the addition of a Gaussian noise whose variance is chosen in accordance with the typical RMS differences met between the integral parameters values given by the propagated SAR observations and their fitted surface. They are equal to 30 m for the peak wavelength,  $16^\circ$  for the peak direction and 60 cm for the significant swell height.

---

2. The estimation methodology is developed in the next section.

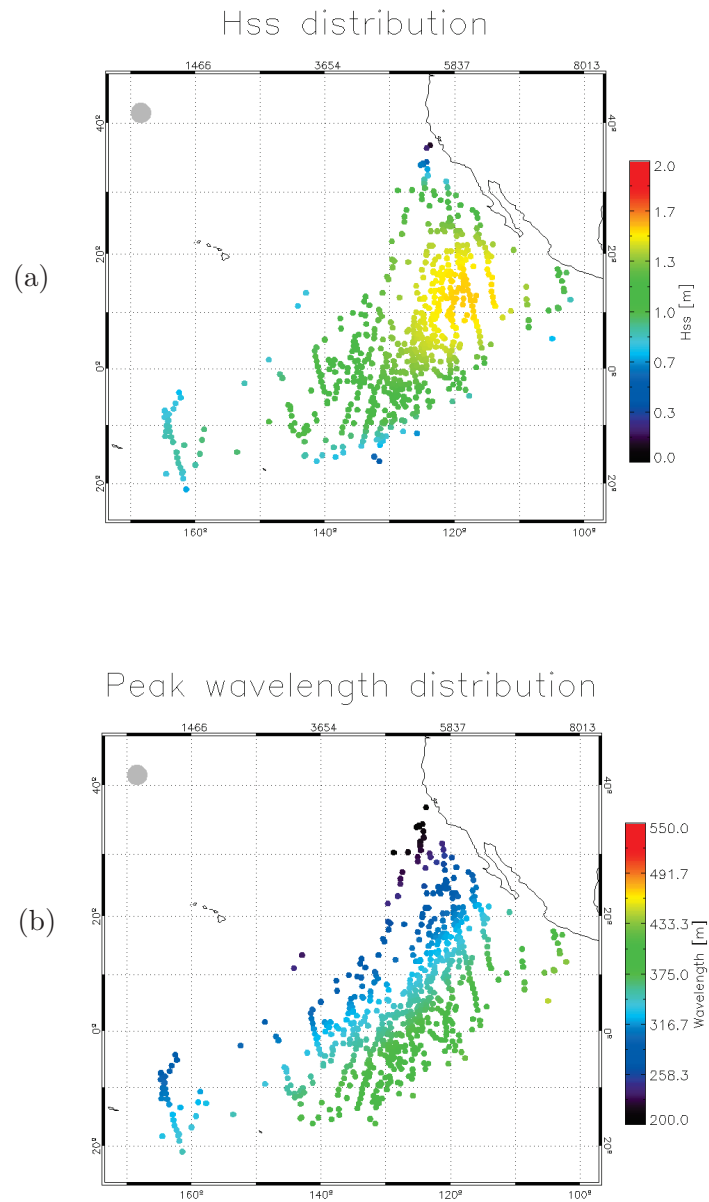


Figure 6.2: Noise-free input distributions of significant swell height and peak wavelength of a swell field observed 6 days after its generation by a storm in the North Pacific Ocean, on 2 January 2012. The storm location is evidenced by a gray disk in the upper left side.

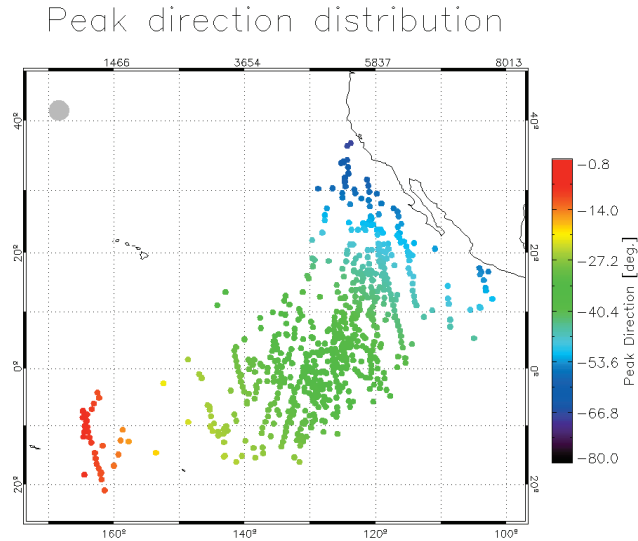


Figure 6.3: Noise-free input distributions of peak direction of a swell field observed 6 days after its generation by a storm in the North Pacific Ocean, on 2 January 2012.

The data density significantly varies within the set of propagated swell observations. This is due to several factors:

- the swell detection in the propagation direction is limited by the frequency range of SAR observable waves. Indeed, swell whose period is larger than 18 s or smaller than 12 s cannot be easily detected;
- swell whose significant swell height is below the minimum 30 cm threshold stay within the noise level and are therefore not observable. For a given swell field, this mostly limits swell detection in transverse directions far away from the swell field main propagation direction since it received less energy from the storm. This limitation also applies in the propagation direction when the 30 cm threshold is only reached for periods smaller than 18 s;
- the stroboscopic swell imaging effect can give rise to very inhomogeneous data density (cf. Chapter 4).

This irregular data density can have unwanted side effects. Typically, the geographical region with highest data density will have much more impact on the polynomial function estimation than the surrounding area. For instance, this is expected to undermine the synthetic field ability to accurately estimate swell whose period is close to the 12 and 18 s since such waves are located at the edges of the peak wavelength spatial distribution.

In order to correct for the effects, we test the effect of weight correction,

	$L_p$ [m]		$D_p$ [deg.]		$H_{ss}$ [cm]	
	No	Yes	No	Yes	No	Yes
Density correction	No	Yes	No	Yes	No	Yes
$l_\infty$	15.3	13.5	10.3	7.0	64.2	48.5
RMSE	3.66	3.07	3.16	1.65	10.7	6.6
Bias	-1.93	-1.8	-2.0	-1.0	-3.1	-2.1

Table 6.1: Effect of the density correction on the polynomial regression for each of the peak wavelength,  $L_p$ , peak direction,  $D_p$ , and significant swell height,  $H_{ss}$ .

which consist in multiplying each propagated observation's weight by a value inversely proportional to the local data density. This correction, is expected to minimize the  $l_\infty$  norm, which is the maximum absolute difference between the noise-free input and the result of the polynomial regression. Results are given in Table 6.1.

Not only does the density correction give better results when considering the  $l_\infty$  norm, but it is also the case for the  $l_2$  norm as the RMSE improvement indicates. Applying this weight correction, the polynomial regression does not depend on the data density anymore and the surface fit better represents the input data in regions with low data density, which explains the  $l_\infty$  decrease. Besides, because each integral parameter's spatial distribution is continuous, this also has a positive impact on the overall fit, leading to a better RMSE.

### Data confidence

The previous data density correction has shown that weighting input data could diminish the effects of heterogeneous data distribution and lead to a better the polynomial regression. Similarly here, we investigate the potential improvements of using the weights attributed to each propagated swell measurements to take into account their expected accuracy based on the validation of the SAR swell observations (cf. Chapter 3).

Several parameters have been shown to significantly influence the data quality and can be used to give a global quality index to each propagated observation. This global quality index is defined as a combination of the quality indexes related to each impacting parameter, namely image normalized variance, SAR wind speed, partition peak-to-boundary energy ratio, azimuth cut-off, ambiguity factor and propagation time. Their impact on data quality differs: for instance, studying the impact of partition peak-to-boundary energy ratio on the significant swell height accuracy in Chapter 3,

we showed the RMSE could vary by as much as 100% depending on the considered range of partition peak-to-boundary energy ratio. On the contrary, the RMSE varies by less than 30% when considering the effect of surface wind speed. Consequently, each quality indexes associated to the impacting parameters are weighted by a coefficient taking into account their impact on data quality. The relation between these quality indexes  $Q_i$ , and the global quality index  $Q$ , all of them being real numbers, is given below:

$$Q = \frac{Q_t w_{NV} Q_{NV} + w_{U_{10}} Q_{U_{10}} + w_{R_{pb}} Q_{R_{pb}} + w_{R_{az}} Q_{R_{az}} + w_{A_f} Q_{A_f}}{2 (w_{NV} + w_{U_{10}} + w_{R_{pb}} + w_{R_{az}} + w_{A_f})} \quad (6.8)$$

where,  $w_{NV}$  and  $Q_{NV}$  are respectively the weight and quality index attributed to a propagated swell observation according to its image normalized variance;  
 $w_{U_{10}}$  and  $Q_{U_{10}}$ , the values that depend on the 10 m-high wind speed measured by the SAR;  
 $w_{R_{pb}}$  and  $Q_{R_{pb}}$ , the values that depend on partition peak-to-boundary energy ratio;  
 $w_{R_{az}}$  and  $Q_{R_{az}}$ , the values that depend on the ratio between the azimuth cut-off wavenumber and the swell azimuth wavenumber;  
 $w_{A_f}$  and  $Q_{A_f}$ , the values that depend on the ambiguity factor;  
 $Q_t$ , the quality index that depends on the propagation time.

In the next paragraph, we explain how these coefficients and quality indexes are estimated. Yet, some differences with the general calculation rule given below exist for some integral parameters. They are further detailed in the following paragraph.

**Main rule** The quality indexes range from 0 to 1. Their value decreases with the increasing RMSE of the significant swell height with respect to the impacting parameter. The quality index equals zero when the RMSE is maximal, one when it is minimal and varies linearly for intermediate values.

The quality indexes are estimated according to the significant swell height accuracy regardless of which integral parameter is being estimated in the synthetic swell field. The only exception is for the ambiguity factor, for which the propagation direction accuracy is used instead of the significant swell height since that integral parameter appears more relevant. Otherwise, referring to the significant swell height accuracy is justified by the fact that the error evolution with respect to each impacting parameter appear to follow the same overall behavior for all integral parameters. Only does the range between the maximum and minimum error significantly varies from one integral parameter to another. This difference is then taken into account when estimating the global rate, assigning weights  $w_i$  to each of these quality indexes.

As a general rule, the weight is set to highest value for the impacting parameter that offers the maximum improvement between the lowest and the highest RMSE values of the evaluated integral parameter.

**Adjustments** Complementary to this rule, certain adjustments are made for the following impacting parameters:

- SAR wind speed: the quality index is set to zero when the SAR wind speed is lower than  $1 \text{ m.s}^{-1}$  or larger than  $12 \text{ m.s}^{-1}$ , hereby strengthening the conditions on the acceptable SAR wind speed range and still setting few data points to zero (12% on average);
- azimuth cut-off: this parameter has more influence on the bias than on the RMSE of the estimated integral parameter. Statistics indicate best bias are normally obtained for lowest values of  $R_{az}$ : the ratio between the azimuth cut-off wavenumber  $k_c$ , and the swell azimuth wavenumber<sup>3</sup>,  $k_a$ . However, validation study undertaken in Chapter 3, page 110, reveals that the bias is not equal to zero for lowest values of  $R_{az}$ . Therefore, the relevant criteria kept for the estimation of azimuth cut-off quality index is the difference between the significant swell height bias and the bias obtained for lowest values of  $R_{az}$ ;
- ambiguity factor: the quality index is set to zero when the ambiguity factor is lower than 0.09;
- propagation time: as mentioned before in Chapter 3, page 96), this parameter is mostly expected to amplify the observation errors. Therefore, rather than summing the corresponding quality index to the other ones, it makes more sense to multiply it by the weighted mean of the other ones as indicated in equation 6.8. For this reason, instead of setting the quality index range to  $[0,1]$ , which would drastically reduce the global quality index of many propagated SAR observations, we rather set it to  $[1,2]$ . As the propagation time effect on data accuracy was only estimated for up to 30 hours in Chapter 3, we rather choose to set to the minimum quality index observations that have been propagated using Airy theory in past or future, for more than 5 days instead of 30 hours. Otherwise, too many data points would have their quality index set to the minimum value and their would not be enough dynamic among the different propagated observation quality indexes. Finally, the quality index linearly decreases from 2 to 1 when the propagation time goes from 0 to 5 days.

#### 6.1.1.4 Kriging

In the following part, another linear least square method is presented, starting with an overall description of the method, followed by theory and

---

3. Cf. Chapter 3, equation 3.15, for the definition of swell azimuth wavenumber.

application to our case.

Kriging is a linear least square method for interpolation and extrapolation developed by Georges Matheron based on the Master's thesis of Daniel Gerhardus Krige (*Matheron, 1969, 1971*). This method was originally developed for the purpose of geostatistics applications and, presently, is widely used in numerous disciplines, among which remote sensing or hydrology, for the spatial interpolation of various physical quantities given a number of spatially distributed measurements (*Isaaks and Srivastava, 1989; Webster and Oliver, 2007*).

As all interpolation, Kriging can be seen as an interpolation based on regression against measured values of surrounding data points. Although, it is different from inverse distance squared, splines, radial basis functions or triangulation algorithms in the way the weights are attributed according to a data-driven weighting function rather than an arbitrary decreasing weight with increasing separation distance. Main advantages brought by Kriging are given below:

- it helps to compensate for the effects of irregular data sampling or data clustering by assigning less weight to individual points within a cluster than isolated data points. No additional density correction is therefore needed;
- along with the estimates of interpolated variable, the estimation error, also called the Kriging variance, can be returned.

However, it still is an interpolation method and for this reason, the results it returns may be very similar to other interpolation methods. In particular:

- if the propagated data location are uniformly distributed and fairly dense throughout the region of interest, estimations are fairly good regardless of interpolation algorithm;
- if the data locations fall in a few clusters with large gaps in between, then one get unreliable estimates within these gaps regardless of the interpolation algorithm;
- almost all interpolation algorithms will over-estimate the lows and under-estimate the highs, which is inherent to low-pass filtering. Indeed, there is a trade-off to accept between high-pass filters following outliers and low-pass filters with excessively smooth signals.

Kriging estimators can be seen as basic linear regression estimator  $\tilde{Z}(u)$  defined as:

$$\tilde{Z}(\mathbf{u}) - m(\mathbf{u}) = \sum_{\alpha=1}^{n(\mathbf{u})} \lambda_{\alpha} (Z(\mathbf{u}_{\alpha}) - m(\mathbf{u}_{\alpha})) \quad (6.9)$$

where,  $\mathbf{u}$  and  $\mathbf{u}_\alpha$  are location vectors for estimation point and neighboring data points indexed by  $\alpha$ ;  
 $n(\mathbf{u})$ , the number of data points in the local neighborhood for the estimation of  $\tilde{Z}(\mathbf{u})$ ;  
 $Z(\mathbf{u})$ , the value at the location vector  $\mathbf{u}$ ;  
 $m(\mathbf{u})$  and  $m(\mathbf{u}_\alpha)$ , the expected values of  $Z(\mathbf{u})$  and  $Z(\mathbf{u}_\alpha)$ ;  
 $\lambda_\alpha(\mathbf{u})$ , the Kriging weight assigned to datum  $Z(\mathbf{u}_\alpha)$  for estimation location  $\mathbf{u}$ .

The same datum will receive different weights for different estimation location.

$Z(\mathbf{u})$  is treated as a random field with a trend component,  $m(\mathbf{u})$ , and a residual component,  $R(\mathbf{u}) = Z(\mathbf{u}) - m(\mathbf{u})$ . Kriging estimates residual at  $\mathbf{u}$  as the weighted sum of residuals of surrounding data points. Kriging weights,  $\lambda_\alpha$ , are derived from the covariance function, as described further down.

**Kriging variants:** The three main Kriging variants, simple, ordinary, and Kriging with a trend (also called universal Kriging), differ in their treatments of the trend component,  $m(\mathbf{u})$ . For simple Kriging, the trend component is supposed constant while ordinary Kriging assumes that it is only constant in the local neighborhood of each estimation point rather than over the entire domain. Finally, universal Kriging is much like ordinary Kriging except that instead of fitting just a local mean in the neighborhood of the estimation point, we fit a linear or higher-order trend in the 2D coordinates of the data points. In our case, we use simple Kriging.

The goal is to determine weights,  $\lambda_\alpha$ , that minimize the variance of the estimator:

$$\sigma_E^2(\mathbf{u}) = \text{Var} \left\{ \tilde{Z}(\mathbf{u}) - Z(\mathbf{u}) \right\} \quad (6.10)$$

with the unbiasedness constraint  $E \left\{ \tilde{Z}(\mathbf{u}) - Z(\mathbf{u}) \right\} = 0$ .

The random field  $Z(\mathbf{u})$  is decomposed into residual and trend components,  $Z(\mathbf{u}) = R(\mathbf{u}) + m(\mathbf{u})$ , with the residual component treated as a random field with a null stationary mean and a stationary covariance  $C_R$ , function of the lag  $\mathbf{h}$ :

$$E \{ R(\mathbf{u}) \} = 0 \quad (6.11a)$$

$$\text{Cov} \{ R(\mathbf{u}), R(\mathbf{u} + \mathbf{h}) \} = E \{ R(\mathbf{u}) R(\mathbf{u} + \mathbf{h}) \} = C_R(\mathbf{h}) \quad (6.11b)$$

This covariance function can be decomposed as follows:  $C_R(\mathbf{h}) = C_R(\mathbf{0}) - \gamma(\mathbf{h})$ , where  $C_R(\mathbf{0})$  is called the *sill* and  $\gamma(\mathbf{h})$  is called the *semivariogram*. Indeed, it can be shown that:

$$\gamma(\mathbf{h}) = \frac{1}{2} \text{Var} \{ R(\mathbf{u} + \mathbf{h}) - R(\mathbf{u}) \} \quad (6.12)$$

The covariance function is generally derived from the semivariogram given as an input. In principle,  $\gamma(\mathbf{h})$  can assume different behaviors depending on the direction of vector  $\mathbf{h}$ , leading to anisotropic spatial distribution. In such case, one has to use the so called *universal Kriging* (Matheron, 1969; Delhomme, 1976, 1978). For simplified reasons though, we assume isotropic spatial distribution and scale the input data instead depending on the considered direction. The most commonly used models of isotropic semivariograms are shown in Figure 6.4 and detailed hereafter:

- polynomial semivariogram:

$$\gamma(\mathbf{h}) = \omega \mathbf{h}^\alpha, \quad \text{with} \quad 0 < \alpha < 2$$

- exponential semivariogram:

$$\gamma(\mathbf{h}) = \omega(1 - e^{-\mathbf{h}/\alpha})$$

- Gaussian semivariogram:

$$\gamma(\mathbf{h}) = \omega(1 - e^{-(\mathbf{h}/\alpha)^2})$$

- spherical semivariogram:

$$\gamma(\mathbf{h}) = \begin{cases} \frac{1}{2}\omega \left( \frac{3\mathbf{h}}{\alpha} - \frac{\mathbf{h}^3}{\alpha^3} \right), & \text{if } |\mathbf{h}| < \alpha \\ \omega, & \text{if } |\mathbf{h}| > \alpha \end{cases}$$

In our case, the semivariogram model selected is the exponential one since it gives the most satisfying surface fits. Its variations are shown on Figure 6.4 along a single dimension. The parameter  $\alpha$  is called the *range*. It controls the shape of the covariance function and thus, the weights of each data point according to their distance to the estimation point. First, in order to define this range distance for both the propagation and transverse direction, the input coordinates have to be scaled relatively to the other. Several scalings have been tested. Second, once this scaling is done, the range parameter should depend on the mean data density and the noise level of the reconstructed swell field considered.

The major drawback in using Kriging is that it cannot take into account weights attributed to each propagated SAR measurements, whether used for data density correction or as quality index, as opposed to a polynomial regression.

### 6.1.2 Iterative filtering

This step aims at excluding from the reconstructed swell field the propagated SAR observations that are too different from the overall integral

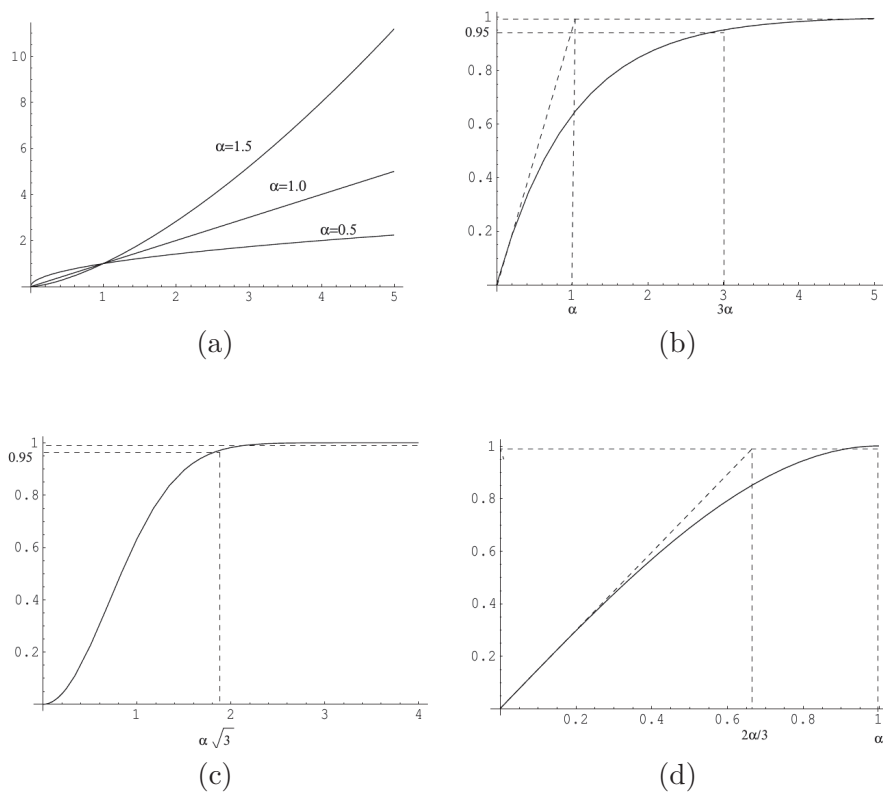


Figure 6.4: Different semivariogram models showing the evolution of  $\gamma$  with respect to  $h$ : polynomial (a), exponential (b), Gaussian (c) and spherical (d).

parameter's spatial distribution. For each of them, the previously described surface fit is estimated and outliers are rejected using the criteria described hereafter. The iterative filtering stops when the mean difference between the surface fit and the remaining input points starts increasing, when the maximum number of iterations is reached or when no more data points is excluded. After this, the final surface fit is calculated and results are restricted to the valid region of estimation defined hereafter.

Outliers are rejected using the peak wavelength distribution first and then using the peak direction and significant swell height distributions. Once excluded by one of the integral parameter filters, outliers are not taken into account in the next processing steps.

#### 6.1.2.1 Rejection process

Here, the successive steps allowing for the rejection of outliers are exposed. As they differ among the integral parameters, they are described separately.

**Peak wavelength and propagation direction** The first filtering step is applied to peak wavelength and propagation direction distributions because these are expected to be more consistent than the significant swell height distribution. This is due to the SAR swell field reconstruction. Indeed, all propagated observations originate from the same storm region, thereby pre-filtering the peak wavelength and propagation direction measurements. As the swell field propagates away from its generation region, swell angular spreading and frequency dispersion causes the directional aperture  $\beta_d$ , and the frequency width  $\beta_f$ , of a swell peak partition (illustrated on Figure 6.5) to decrease. Therefore, we expect the swell field spatial distribution given by the propagated observations to be better arranged and outliers more evident whenever looked at many days after the storm event. For this reason, the iterative filtering is applied at a single time step. Once outliers of peak wavelength and propagation direction distribution are detected and removed, the final surface fits can be calculated at each time step.

On average, among all the reconstructed swell fields treated over year 2008, 4% of the input propagated swell measurements are rejected.

**Significant swell height** As opposed to the previous case, outliers detection are applied at each time step. Indeed, this integral parameter varies during the swell propagation according to a dispersion and dissipation model (cf. Chapter 2, Section 2.3). This model may introduce errors, partly due to mis-estimation of the storm source location, invalid hypothesis of free-propagation or of punctual storm source. Thus, the significant swell height information for a single observation may be inaccurate after several days of

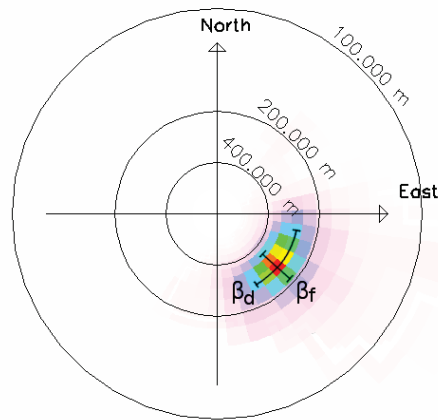


Figure 6.5: Illustration of the directional aperture  $\beta_d$ , and frequency width  $\beta_f$ , for a swell spectra measured by the SAR instrument. We can define these values as the direction and frequency range around the partition peak, along which the energy remains higher than half the peak energy.

propagation although its value corresponded to the real swell conditions at observation time. For this reason, it makes more sense to detect outliers in significant swell height spatial distribution at each time step.

On average, among all the reconstructed swell fields treated over year 2008, 25% of the input propagated swell measurements are rejected.

### 6.1.2.2 Free propagation assumption

As the reconstructed swell field propagates, less and less propagated observations remain. First reason is that many have totally dissipated when reaching the coast. Second reason is that they have reached shallow waters regions for which linear propagation theory does not apply anymore. This phenomenon has several implications:

- this could potentially cause significant discontinuities from one time step to the next. In addition, this would diminish the spatial data density of the propagated SAR swell observations, which is expected to degrade the synthetic swell field estimations;
- as outliers of the peak wavelength and peak direction distribution are detected at a single time step, long after the swell generation, outliers absent from the set of remaining propagated SAR observations at this time step would not be rejected. Thus, they would be taken into account for the estimation of the final surface fits for earlier time steps.

To tackle this issue, land-blocking is not applied anymore and the information that propagated SAR swell observations convey is taken into account even if they have reached land several days before the time of interest. Following this rule, the detection of outliers from the peak period and propagation direction spatial distributions can be done many days after swell generation. In practice, it is done 12 days after.

### 6.1.2.3 Region of estimation

In order to limit the synthetic swell field estimates to deep ocean regions, an isotropic swell propagation is simulated, starting from the storm source region and a mask of open ocean propagation is created. This mask is set to one for all points in the  $(r, \theta)$  coordinates for which no land or islands were met along propagation. Also, since storm source is not a point source but rather spread over a few hundreds kilometers, sometimes thousands, this mask is obtained by the intersection of the masks estimated starting from several distant points in the storm source region. A case example of this mask is presented in Figure 6.6. Starting from the distribution of propagated observations without land-blocking shown on Subplot (a), the open ocean mask is deduced and represented on Subplot (b).

Besides, we suppose that the synthetic swell field estimation is only valid over regions for which the density of propagated observations is larger than a minimum threshold. The main goal of this step is to get rid of isolated observations that have been associated to the reconstructed swell field because their retro-propagated trajectories were fortuitously passing by the refocusing region at the appropriate time even though they do not belong to the swell field<sup>4</sup>. In most cases, these observations propagate in directions very different from the swell main propagation direction. In practice, we choose not to consider propagated observations located in regions where the data density is lower than the first decile, which defines another mask of valid data. Still, this mask is dilated using morphological operations in order not to reject propagated observations belonging to the swell field of interest but that are located at the swell front or behind most propagated observations in the propagation direction, corresponding to longest or shortest swell. Also, its shape may be quite irregular in the transverse direction because of the data sampling. To fill the blanks, we apply a succession of dilatation and erosion with the following kernels:

$$\mathbf{K}_{\text{dilat}} = \frac{1}{3} \begin{pmatrix} 0 & 1 & 0 \\ 0 & 1 & 0 \\ 0 & 1 & 0 \end{pmatrix}, \quad \mathbf{K}_{\text{erod}} = \frac{1}{3} \begin{pmatrix} 0 & 0 & 0 \\ 1 & 1 & 1 \\ 0 & 0 & 0 \end{pmatrix} \quad (6.13)$$

---

4. For the refocusing algorithm description, cf. Chapter 5, Section 5.2.

where,  $\mathbf{K}_{\text{dilat}}$  is the kernel used for dilatations;  
 $\mathbf{K}_{\text{erod}}$ , the kernel used for erosions.

A case example of this mask is given in Figure 6.6-c. In the end, the synthetic swell field is estimated over the region where both masks, represented on Subplots (b) and (c), are valid, as shown on Subplot (d).

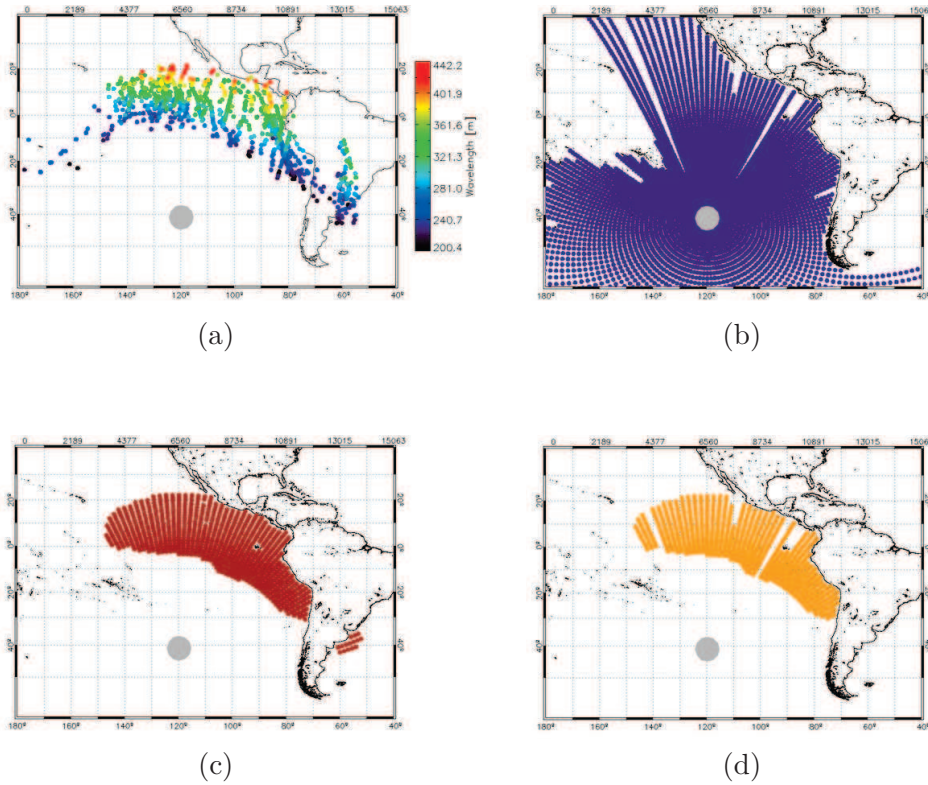


Figure 6.6: Illustration of the estimation of the synthetic swell field valid region. (a) Peak wavelength distribution of observations whose propagated positions are estimated without land-blocking. (b) Open ocean mask, determined by the storm source location and the land mask. (c) Data density mask. (d) synthetic swell field region of estimation, determined by the intersection of masks (b) and (c).

#### 6.1.2.4 Peak wavelength filtering

As previously indicated, this filtering is done using the peak wavelength spatial distribution of the propagated swell observations 12 days after the swell generation. Once the weighted polynomial regression is estimated, we define a criterion to reject or not individual measurements from all successive steps, including the synthetic swell field estimation.

This criterion is based on the size of the storm source region. This parameter was previously estimated during the refocusing step and is equal to the size of the refocusing region<sup>5</sup>. Here, we assume that in open ocean, outside of island shadows and in the absence of currents, the frequency width of a swell partition at a given location only depends on the geographical extension of the storm source and the distance to it. Therefore, swell measurements with slightly different peak wavelengths may be observed. Under this consideration, given an observed wavelength  $\lambda_0$ , the maximum acceptable difference for another wavelength  $\lambda_1$ , related to the same swell field is given by:

$$\left[ \lambda_0^{1/2} - \left( \frac{8\pi}{g} \right)^{1/2} \frac{S_{\text{prop}}}{\Delta t} \right]^2 \leq \lambda_0 - \lambda_1 \leq \left[ \lambda_0^{1/2} + \left( \frac{8\pi}{g} \right)^{1/2} \frac{S_{\text{prop}}}{\Delta t} \right]^2 \quad (6.14)$$

where,  $g$  is the Earth gravity;  
 $S_{\text{prop}}$ , the storm source dimension in the propagation direction;  
 $\Delta t$ , the time difference between the swell generation and the time of estimation (12 days in our case).

This wavelength difference is due to the fact that the two considered swells have traveled different distances but in the same time period, as illustrated on Figure 6.7.

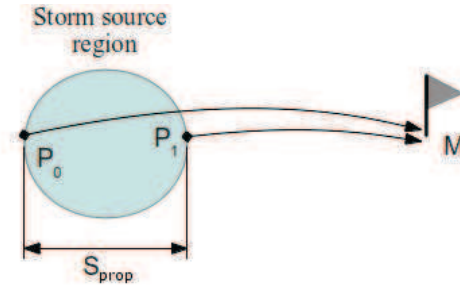


Figure 6.7: Illustration of two waves belonging to the same swell field but with slightly different wavelengths at point  $M$  because of the storm source geographical extension in propagation direction,  $S_{\text{prop}}$ .

The threshold criteria given by equation 6.14 are estimated for each propagated SAR swell observation. Whenever the wavelength difference between the peak wavelength of fitted surface  $\lambda_0$ , and the peak wavelength of the propagated swell observation  $\lambda_1$ , is higher than the threshold values, the

5. For the refocusing algorithm description, cf. Chapter 5, Section 5.2.

propagated swell observation is rejected. This operation is repeated up to five times, a new surface fit being estimated between each rejection step.

#### 6.1.2.5 Peak direction filtering

As previously indicated, this filtering is done using the peak direction spatial distribution of the propagated swell observations 12 days after the swell generation.

Similarly to the peak wavelength filtering, we define a criterion to reject swell observations whose propagation direction difference with the distribution obtained by the polynomial regression exceeds a threshold value  $\theta_{\max}$ . Given the hypothesis of open ocean propagation, outside of island shadows and in the absence of currents, the directional aperture of the swell spectrum at a given location only depends on the geographical extension of the storm source and the distance to it. Therefore, swell measurements with slightly different peak directions may be observed as illustrated in Figure 6.8.

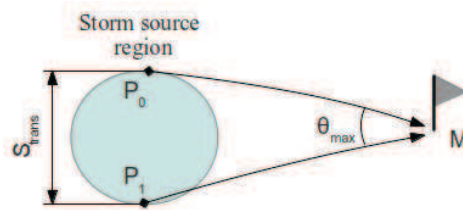


Figure 6.8: Illustration of two waves belonging to the same swell field but with slightly different propagation directions at point  $M$  because of the storm source geographical extension in transverse direction,  $S_{\text{trans}}$ .

The maximum direction difference  $\theta_{\max}$ , is calculated for each propagated swell observation, given their position with respect to their storm source. Whenever the difference between their peak direction and that of the fitted surface is larger than  $\theta_{\max}$ , the propagated SAR observation is rejected. This operation is repeated up to five times, a new surface fit being estimated between each rejection step.

#### 6.1.2.6 Significant swell height filtering

As previously indicated, this filtering is done using the significant swell height spatial distribution of the propagated swell observations at each time step.

As opposed to the peak propagation direction and wavelength, the significant swell height has not been pre-filtered by the refocusing step. The propagated swell measurements spatial distribution is therefore much noisier for the significant swell height parameter.

As shown in Chapter 3 (cf. page 99), the NRMSE of the SAR significant swell height measurements with respect to that of *in situ* buoys is more stable over the overall range of measured waves than the absolute RMSE. In order to have an homogeneous criterion for all wave heights, we therefore choose to exclude data points based on the NRMSE rather than the absolute RMSE. Besides, we have noticed that within the set of propagated observations, numerous significant swell height measurements were largely under-estimated as compared to the *in situ* measurements. In order to reject those under-estimated data points, the NRMSE is calculated relatively to the input data rather than the fitted surface. Data points whose relative difference is higher than twice the NRMSE are rejected. This operation is repeated up to ten times.

**Final step** After the data points have been filtered, we obtain for each time step the 2D polynomial function describing the final surface fit. Then, the synthetic swell field can be estimated anywhere over the  $(r, \theta)$  grid. Results are restricted to the valid region of estimation. Examples of synthetic swell field estimations starting from the initial propagated SAR swell observations of the peak wavelength and significant swell height are given on Figures 6.9 and 6.10, respectively.

The irregular sampling caused by stroboscopic imaging (cf. Chapter 4) are clearly visible on subplot (a). Also, island shadow are well depicted by the absence of peak wavelength estimation on subplot (b). Finally, it is interesting to notice that peak wavelength distribution is not isotropic and seems to follow the easterly displacement of the original storm source.

## 6.2 Validation

In this section, we estimate the accuracy of synthetic swell field integral parameters using *in situ* measurements over the whole year 2008. First, the comparison method is presented. Then, the different configurations tested for the estimation of the synthetic swell field are detailed. Third, the statistical results obtained for each of them are discussed. It is accompanied by two swell field examples, for which we show the integral parameters evolution as the swell fields pass the recording buoy. Then, parameters impacting the accuracy of the synthetic swell field estimations such as the input data density and the storm source characteristics are presented. Finally, the detected outliers are inspected and we highlight a specific error in SAR measurements.

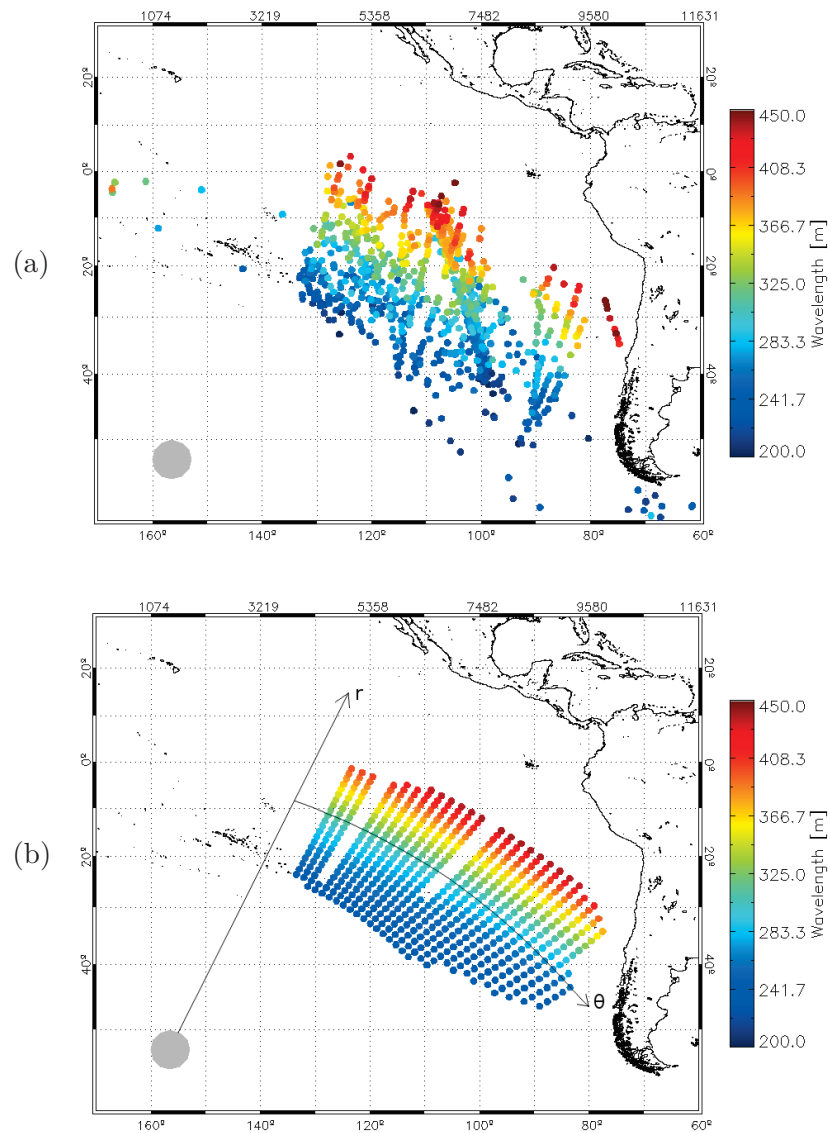


Figure 6.9: (a) Original spatial distribution of the peak wavelength as given by the propagated SAR swell observations and (b) the corresponding estimation of the synthetic swell field estimate using the 2D polynomial regression. The  $(r, \theta)$  grid is also depicted on subplot (b). This example corresponds to swell field situation on 19 January 2008, at 09Z. It originates from a storm that occurred on 13 January and whose location is represented by a gray disk.

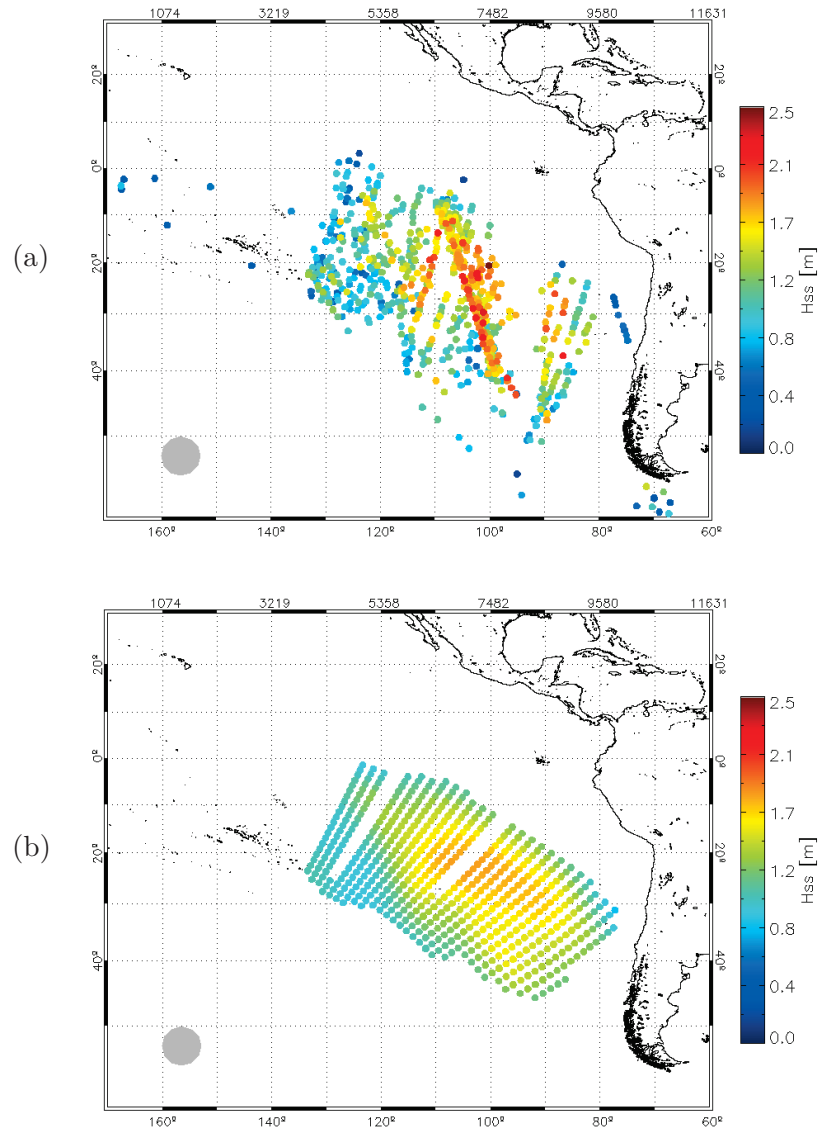


Figure 6.10: (a) Original spatial distribution of the significant swell height as given by the propagated SAR swell observations and (b) the corresponding estimation of the synthetic swell field estimate using the 2D polynomial regression. This example corresponds to swell field situation on 19 January 2008, at 09Z. It originates from a storm that occurred on 13 January and whose location is represented by a gray disk.

### 6.2.1 Methodology

Similarly to the swell observation validation presented in Chapter 3, the synthetic swell field validation is based on the comparison with *in situ* measurements. However, since the synthetic swell field method provides a lot more co-locations with buoys, we do not have to use an entire buoy network as done previously with the NDBC network but a single buoy is used, called *Stratus* (WMO51028), which has the advantage of being located in the most favorable location: placed at 19.691°S and 85.567°W, more than a thousand kilometers off the coasts of Peru, at a depth of 4540 m. Besides, this buoy is not located in any island shadow and is placed at a sufficiently low latitude so that it can measure swells coming from both hemispheres. It is maintained by the WHOI. It was deployed in October 2007 and is still operating today.

The comparison of the swell propagation directions given by this buoy and synthetic swell field estimates obtained over the whole year 2008, revealed that there was a bias of the order of  $-10^\circ$ . After a series of test for confirmation, we contacted WHOI and learned that the *Stratus* buoy magnetic declination was biased by  $-11.9^\circ$ . The magnetic declination is the difference between the true North and the magnetic North, which is the reference direction for such buoys. Because this mistake could only be corrected on site, the change was made one year after deployment, in October 2008. The previously acquired data has not been corrected by NDBC and we applied our own correction. However, as we do not know the exact day at which the buoy magnetic system was corrected, there may still be a minor bias in the propagation direction comparison.

The only difference between the currently exposed methodology and the one in Chapter 3 is that several synthetic swell field estimates may be given at the buoy location at the same moment. Whenever this is the case, the peak-to-peak association step is modified in the way it calculates a cross-spectral distance between each partition of the *in situ* measurements and the synthetic swell field estimates. Partitions with shortest spectral distance are associated.

Here, we give a local point of view of the swell field propagation. This method can be seen as a virtual buoy estimator.

### 6.2.2 Tested configurations

Different synthetic swell field estimation methods are tested. In addition to comparing the performances of these different methods, we also specifically focus on the capability to estimate energetic swell, whose significant

swell height is above 1.5 m. Here is the list of the different configurations we evaluate:

- P0: All three integral parameter's distribution are estimated using a weighted polynomial regression, with density correction;
- P1: All three integral parameter's distribution are estimated using a polynomial regression, with density correction, but without weighting;
- K0: Only peak wavelength and peak direction distribution are estimated using a weighted polynomial regression. The significant swell height is estimated using Kriging and the range parameter,  $\alpha_0$ , in  $(r, \theta)$  coordinates, equals:

$$\alpha_0 = \left( \text{median} \{r\} / 3 \quad 9^\circ \right) \quad (6.15)$$

- K1: Identical to K0 except the range parameter,  $\alpha_1$ , is changed to:

$$\alpha_1 = \left( \text{median} \{r\} / 12 \quad 67^\circ \right) \quad (6.16)$$

Besides, we differentiate two cases: those with high average data density and high confidence in the propagated swell observations, referred to as case  $C_{\text{High}}$ , and the general case, for which all values are considered, referred to as case  $C_{\text{Gen}}$ . Performances are given in Tables 6.2.

### 6.2.3 Statistical results

**Polynomial regression configurations** The statistics obtained by configurations P0 and P1 shows that using the weighted regression based on data confidence gives slightly better results for both the significant swell height and the peak direction and identical results for the peak wavelength.

**Kriging configurations** When comparing statistics obtained by configurations K0 and K1, it appears that configuration K0, which uses more information in the transverse direction and less in the propagation direction than configuration K1, gives better results in case  $C_{\text{High}}$ . However, results are best correlated for configuration K1 when considering lower data density ( $C_{\text{Gen}}$ ). The reason is that, between the two configurations, the increase of the range parameter in the transverse direction is not of the same order as the decrease in the propagation direction. Indeed, this changes the interpolation process in the way that it does not use the same number of data points. Therefore, configuration K1 tends to interpolate over more data points than K0. For low density data, this tends to be an advantage since it is more robust but probably loses dynamic for high density data.

The effect of data point number on the estimation should be further investigated. It could be interesting to test the improvement brought by a procedure where the range parameter would be scaled according to the data

		P0		P1	
Config.		C <sub>High</sub>	C <sub>Gen</sub>	C <sub>High</sub>	C <sub>Gen</sub>
	RMSE [m]	0.30	0.43	0.31	0.43
	any $H_{ss}$ NRMSE [%]	20.8	28.1	20.9	28.0
	Bias [m]	-0.07	-0.20	-0.09	-0.20
	Correl.	0.92	0.82	0.88	0.82
(a)	RMSE [m]	0.35	0.53	0.36	0.53
	$H_{ss} > 1.5\text{m}$ NRMSE [%]	17.8	26.2	18.1	26.1
	Bias [m]	-0.26	-0.42	-0.27	-0.42
	Correl.	0.83	0.63	0.78	0.64
	RMSE [s]	0.40	0.58	0.40	0.58
	$T_p$ NRMSE [%]	2.9	4.2	2.9	4.2
	Bias [s]	-0.1	-0.1	-0.1	-0.1
	Correl.	0.95	0.91	0.95	0.91
	RMSE [deg]	11.2	16.0	12.0	16.1
	$D_p$ Bias [deg]	-2.9	-1.9	-1.7	-2.0

		K0		K1	
Config.		C <sub>High</sub>	C <sub>Gen</sub>	C <sub>High</sub>	C <sub>Gen</sub>
	RMSE [m]	0.33	0.49	0.35	0.49
	any $H_{ss}$ NRMSE [%]	22.0	31.9	23.2	31.4
	Bias [m]	-0.10	-0.22	-0.15	-0.26
	Correl.	0.87	0.75	0.87	0.80
(b)	RMSE [m]	0.40	0.60	0.43	0.61
	$H_{ss} > 1.5\text{m}$ NRMSE [%]	20.0	29.9	21.9	30.0
	Bias [m]	-0.28	-0.48	-0.33	-0.50
	Correl.	0.72	0.49	0.71	0.59

Table 6.2: Statistics given by the comparison between *in situ* measurements from the Stratus buoy and synthetic swell field estimation using configurations P0 and P1 (a) and K0 and K1 (b). The statistics obtained for configurations K0 and K1 concerning the peak period and propagation are the same as those given for P0 and P1.

density of the considered swell field. Besides, the algorithm for neighbor data points selection can have at least as much influence on the estimate as the interpolation algorithm itself. Here, we have used a simple nearest neighbor search. A couple of alternatives include quadrant and octant searches, which look for data points within a certain distance in each quadrant or octant surrounding the data point. Still, the time required for synthetic swell field estimation using Kriging is almost prohibitive as compared to the instantaneous polynomial regression, which also undermines our ability to test many different configurations. An alternative could be to use parallel computations of the surface fits on different processors. Still, the processing time will remain of the same order which is still making real-time applications unrealistic.

**Kriging against polynomial configurations** Configuration P0 gives better statistics than all other configurations and for all integral parameters. We believe that this is due to the great coherence of the swell field. Using all data points instead of only the ones located in the vicinity of the point of interest seems to bring more information. We have noticed that this was particularly true for swell fields with irregular data density. The polynomial regression proves more robust than Kriging when interpolating in such cases.

For the synthetic swell field estimates, we further refer to configuration P0 even if it is not explicitly mentioned.

#### 6.2.4 Single cases

Comparison examples between *in situ* measurements and synthetic swell field estimations for a single swell field as it passes by the Stratus buoy are given on Figure 6.11 and 6.12. They are related to storm events that took place in the South Pacific on 6 June and 27 August 2008, respectively.

The main patterns of the buoy measurements and the synthetic swell field estimates compare well: the peak wavelength decreases, the swell energy increases and then decreases whereas the peak direction remains rather constant. Apart from these, the buoy measurements exhibit significant high frequency variations around these main trends. However, it is difficult to judge whether such variations are related to noise measurements, erroneous partitioning or if they represent the actual swell conditions.

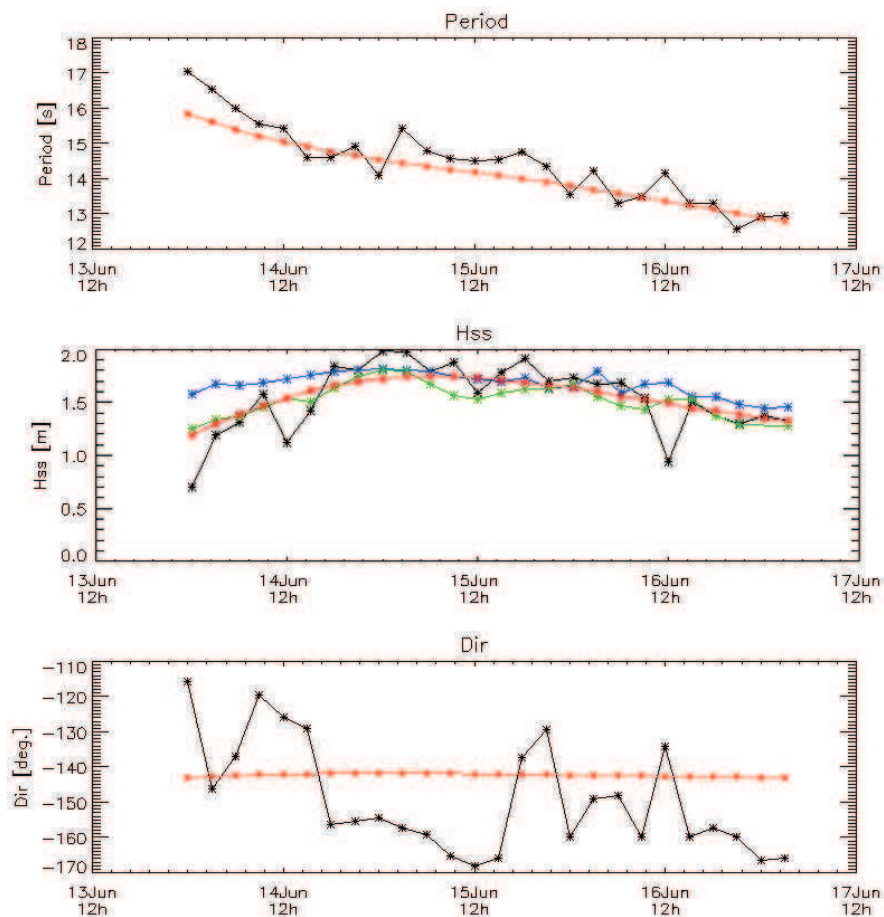


Figure 6.11: Peak period, significant swell height and peak direction evolution as estimated by the synthetic swell field with configurations PO (red line), K0 (blue line), K1 (green line) and measured by the Stratus buoy (black line). The swell field was generated by a storm that took place on 6 June 2008 in the South Pacific Ocean.

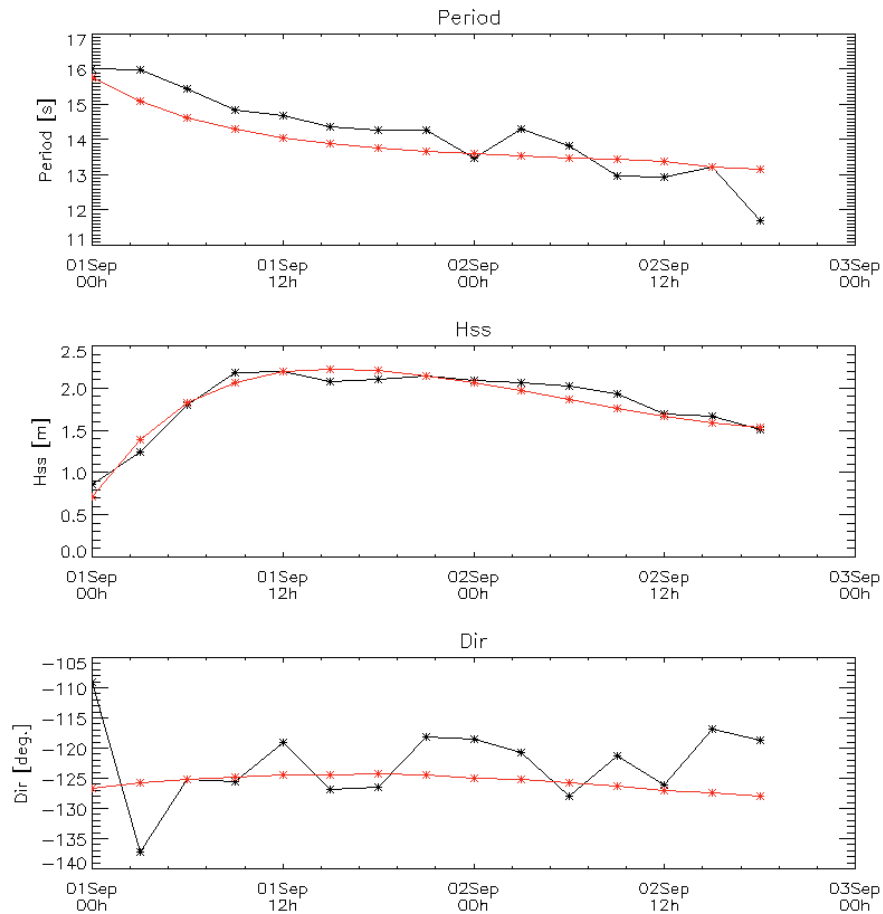


Figure 6.12: Peak period, significant swell height and peak direction evolution as estimated by the synthetic swell field (red line) and measured by the Stratus buoy (black line). The swell field was generated by a storm that took place on 27 August 2008 in the South Pacific Ocean.

### 6.2.5 Dependences

Assessing the parameters that influence the synthetic swell field accuracy and to which extent, is important for further applications such as assimilation in numerical wave models. Here, we investigate the accuracy dependence on the density of propagated observations composing the reconstructed swell field. Also, the impact of the storm source characteristics is investigated. Since this study requires numerous co-locations, we will be using case  $C_{\text{Gen}}$ .

#### 6.2.5.1 Data density

As Table 6.2 indicates, the synthetic swell field accuracy increases with the average data density and confidence. Even though the statistics are slightly better when setting a minimum threshold on both quantities, they are almost equivalent as they are very closely correlated. Indeed, their Pearson correlation coefficient equals 0.996. Thus, we will only refer to the data density in the future. Statistics dependence on the data density is estimated for all integral parameters, as shown in Figures 6.13 and 6.14.

Clearly, the synthetic swell field accuracy increases with the data density for all integral parameters. For the significant swell height, the RMSE goes from 0.56 cm for lowest densities down to 0.32 for highest values. Similarly, the relative significant swell height goes from 34.3 to 23%, the peak period from 0.84 to 0.46 s and the peak direction from 22.1 to 12.7°. Still, the highest scores are obtained for cases  $C_{\text{High}}$  indicated in Table 6.2.

#### 6.2.5.2 Integral parameters

The evolution of the synthetic swell field error for each integral parameter is estimated using *in situ* measurements. Results are represented on Figures 6.15 and 6.16 and discussed hereafter.

**Significant swell height** First of all, swell whose significant swell height is smaller than 1 m have quite unsatisfying statistics. They have a high RMSE and bias. This can be explained by several factors. Main reason is the measurement's errors. Indeed, the general trend in significant swell height bias is the same as for observations: over-estimating small swell and under-estimating large ones.

Then, the second most important part of this bias is attributed to the energy dispersion model we use and its validity very far from the storm source. As described in *Collard et al. (2009)*, the swell energy follows the asymptote  $1/(\alpha \sin \alpha)$ . However, that is according to a swell dispersion model neglecting dissipation caused continent and island blocking. In this case, the initial swell energy refocuses at the antipode of the storm source. The estimated swell

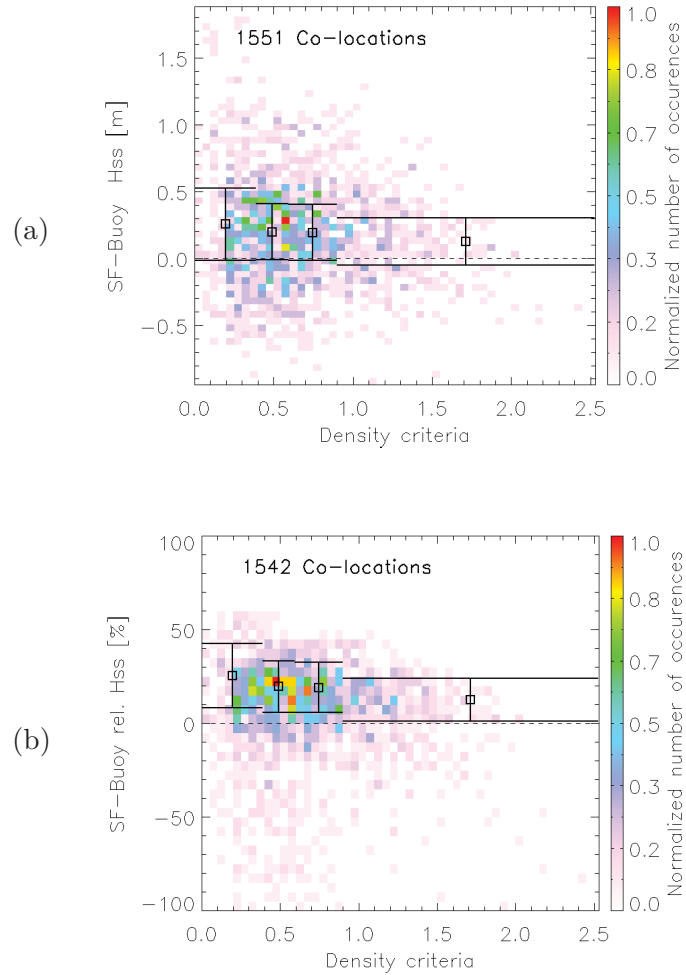


Figure 6.13: Significant swell height (a) and relative significant swell height (b) synthetic swell field errors against the reconstructed swell field density of propagated observations at the virtual buoy location. RMSE (a), NRMSE (b) and bias (both) are respectively indicated for each subrange by the vertical extent of the solid line segments and their central vertical value, represented by a square. The red dashed line corresponds to the data points linear regression.

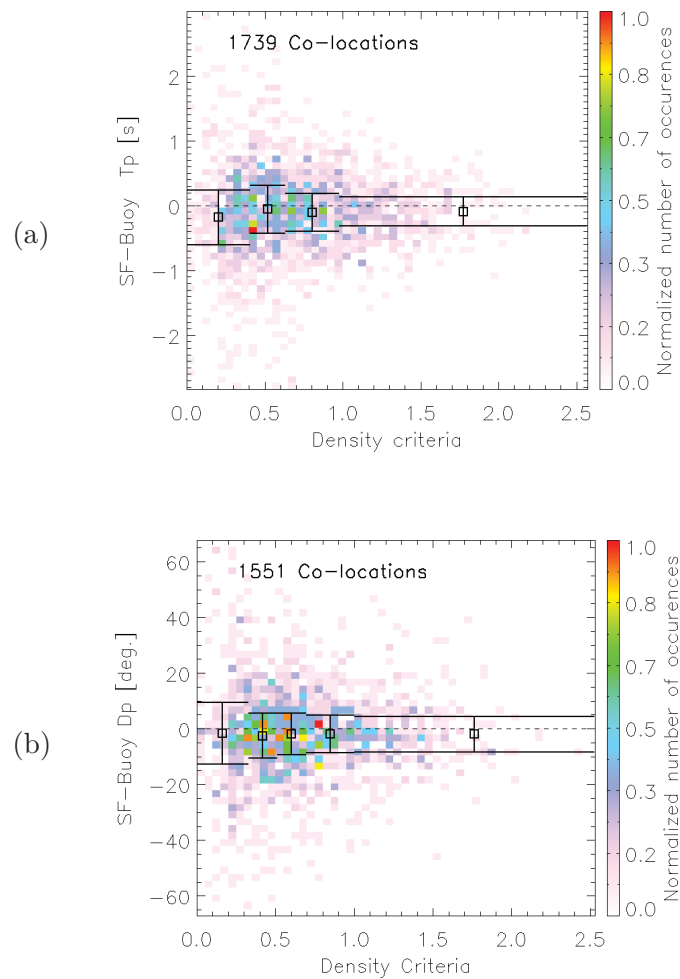


Figure 6.14: Peak period (a) and peak direction (b) synthetic swell field errors against the reconstructed swell field density of propagated observations at the virtual buoy location. RMSE and bias are respectively indicated for each subrange by the vertical extent of the solid line segments and their central vertical value, represented by a square. The red dashed line corresponds to the data points linear regression.

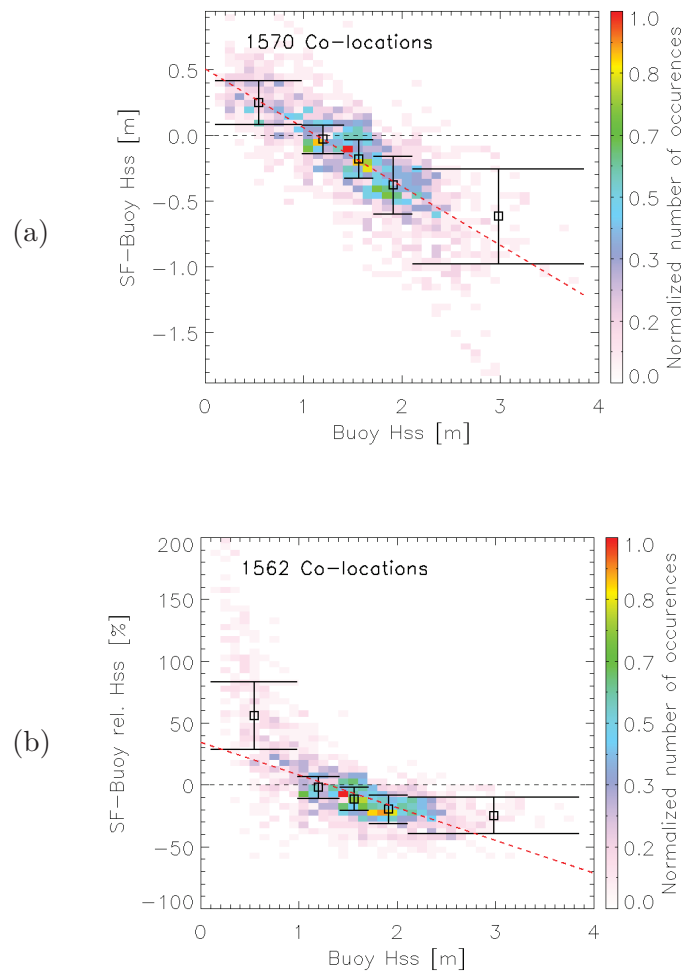


Figure 6.15: Significant swell height (a) and relative significant swell height (b) synthetic swell field errors against the corresponding parameter as measured by the buoy. RMSE (a), NRMSE (b) and bias (both) are respectively indicated for each subrange by the vertical extent of the solid line segments and their central vertical value, represented by a square.

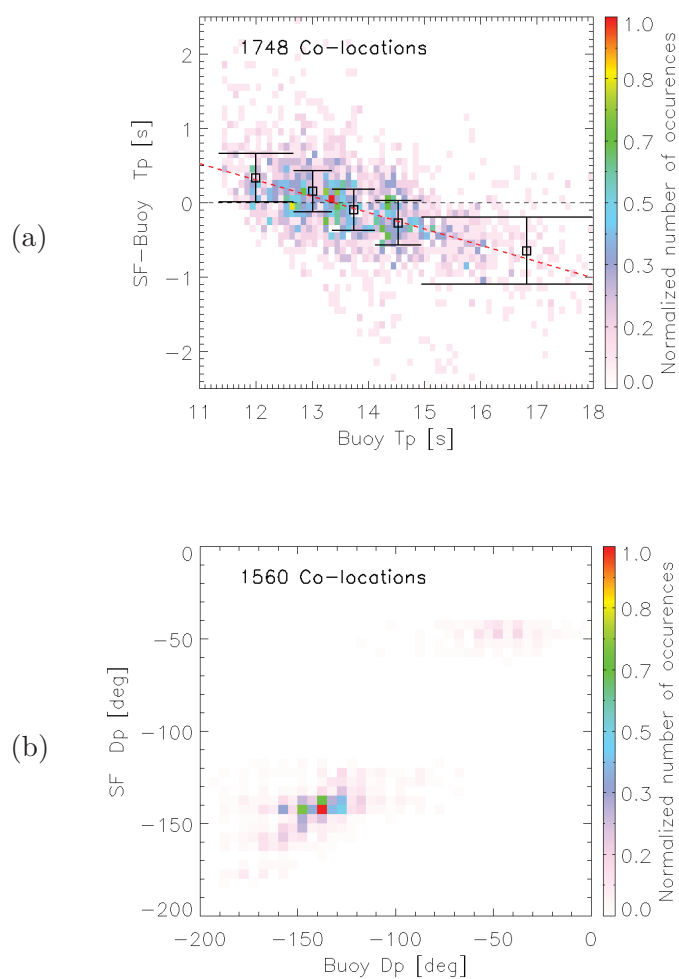


Figure 6.16: Peak period (a) and peak direction (b) synthetic swell field errors against the corresponding parameter as measured by the buoy. Except for the peak direction, RMSE and bias are respectively indicated for each subrange by the vertical extent of the solid line segments and their central vertical value, represented by a square.

energy is therefore larger than reality when the spherical distance covered by the swell after generation is larger than  $90^\circ$ , about 10,000 km. Indeed, looking at two sets of synthetic swell field estimates located less than 9,000 and more than 11,000 km away from their storm source and with equal mean significant swell height, significant swell height statistics have a bias of 0.22 and 0.36 cm, respectively. Future improvements shall therefore look for a refined version of the energy dispersion model very far away from the storm source.

Additionally, a small part of small wave over-estimation can be explained by the fact that these estimations coincide with very low data density. Indeed, swell whose significant swell height measured by the buoy is smaller than 1 m coincide with low data density in the synthetic swell field estimation in 44% cases while, for wave heights above 1 m, this percentage equals 38%.

Also, for energetic swell, the significant swell height is under-estimated and both the RMSE and the NRMSE increase with increasing wave height. However, as previously indicated by Table 6.2, the NRMSE decreases with increasing wave height for high data density. Hence, the NRMSE increases when all data densities are considered.

**Peak period** Looking at the peak period, largest errors are obtained for longest and smallest swells. The reason is that such swells are the maximum and minimum period, respectively, that the SAR can image. Within a given swell field, these swell estimates are thus located in region with lower data density, which gives the worse statistics. It can also be noticed that longest swells are largely under-estimated. This was already noticed in the SAR observation validation and therefore, it is a consequence of the swell inversion rather than of the synthetic swell field estimation.

**Peak direction** Two main directions can be distinguished, corresponding to swell systems arriving from the Northern and Southern Hemisphere. As already mentioned in subsection 6.2.4 (page 216), peak directions measured by the buoy exhibit more variations than those given by the synthetic swell field, as already observed in Chapter 3 (cf. page 101). We believe that this is due the important spread in direction measurements of the NDBC discus buoys, already highlighted by (*O'Reilly et al., 1996*).

Also, direction differences between the SAR and the buoy could result from swell deviations with respect to the expected linear propagation along great circles. Such modifications could be due to peculiar ocean and/or atmospheric conditions met along the swell propagation. The potential effect of diffraction caused by islands or surface currents should be investigated as well. Indeed, such phenomenon could cause the swell to deviate from its expected path in regions where our approach is supposed to be valid.

### 6.2.5.3 Storm source characteristics

We study here the influence of the storm source characteristics on the synthetic swell field. Storm source location impact is first investigated, followed by storm source extension

**Storm source location** We only consider storm events that occurred in the Southern Hemisphere in order to compare swell fields that have propagated for distances not too different from one another. Measurement errors are shown by scatter plots with associated RMSE and NRMSE for all data density on Figure 6.17.

Clearly, the RMSE, the NRMSE and the bias absolute value all decrease with the decreasing latitude. As the latitude decreases, the storm source is closer to the Stratus buoy and the mean significant swell height is expected to increase as well. Indeed, the mean significant swell height measured by the buoy for each of the three latitude ranges in Figure 6.17 equals 1.17, 1.32 and 1.29 m, in order of decreasing latitudes. According to Table 6.2, the statistical improvement with respect to the storm source latitude does not result from the increasing significant swell height since, contrary to what is observed, the RMSE and the bias absolute value are expected to increase with increasing significant swell height.

We believe that these statistical errors are partly related to the storm source geographical extension.

**Storm source extension** The storm source area, as estimated by the refocusing algorithm, was compared for different latitudes. Storm events of various sizes can be found at every latitude but the size of the largest storm events exhibit a very clear trend. Considering the 10% most extended storms, the mean diameter for each of the three latitude ranges indicated in Figure 6.17 equals 2700, 2300 and 1600 km, in order of decreasing latitudes, respectively. However, no clear dependency can be established between the measurement errors and the size of the original storm source. Therefore, we rather investigate the angular aperture of the storm source region, as seen from the virtual buoy.

To estimate the influence of the storm source region angular aperture on the synthetic swell field accuracy, all data points are split in three sets corresponding to small, mid and high angular aperture. Although, the statistics for each set cannot be calculated straight. Indeed, the mean significant swell height naturally tends to increase with increasing angular aperture. This is because numerous cases of high angular aperture come from source storms that are close to the virtual buoy. The resulting statistics would thus be biased as we know that the RMSE increases with increasing significant swell height. To bypass this problem, the different sets are harmonized in such a

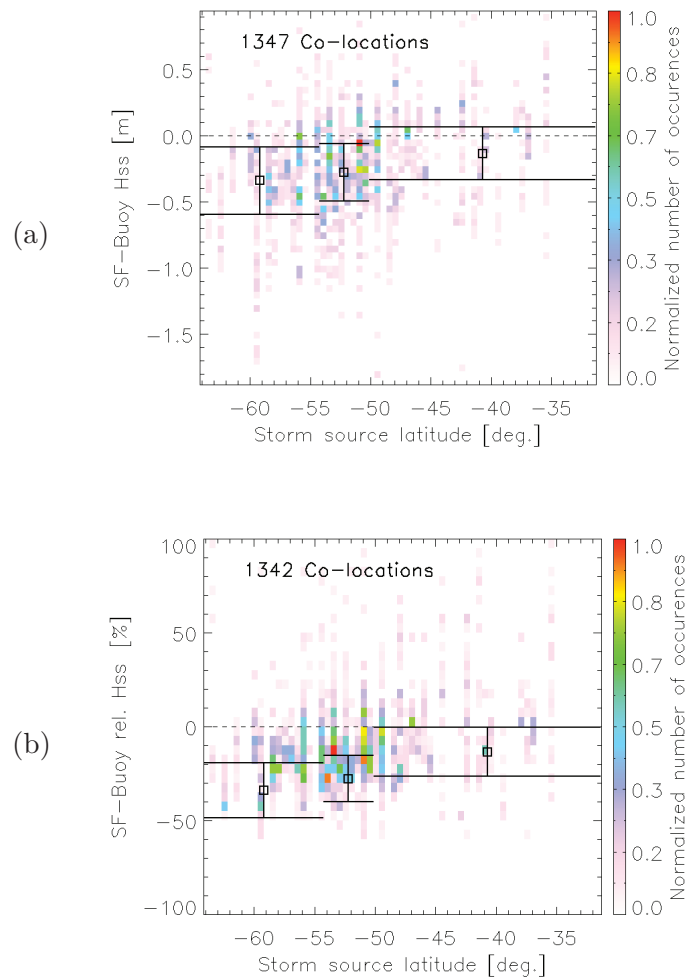


Figure 6.17: Significant swell height (a) and relative significant swell height (b) measurement errors against the latitude of the storm source at the origin of the swell from which the synthetic swell field was estimated. RMSE (a), NRMSE (b) and bias (both) are respectively indicated for each of the three subranges by the vertical extent of the solid line segments and their central vertical value, represented by a square.

way that their significant swell height distribution are the same. Measurement errors obtained for each set are shown on Figure 6.18.

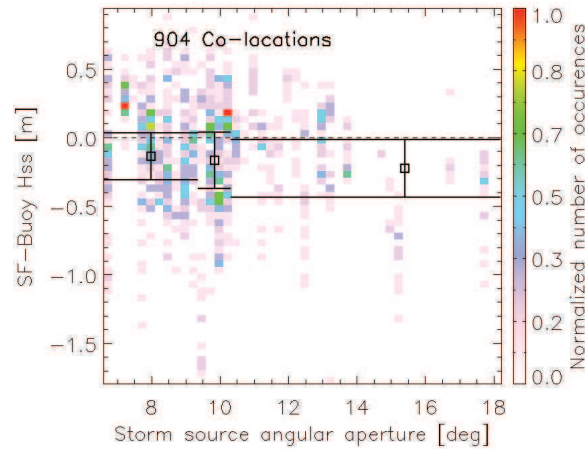


Figure 6.18: Significant swell height measurement errors against the latitude of the storm source at the origin of the swell. RMSE and bias are respectively indicated for each of the three subranges by the vertical extent of the solid line segments and their central vertical value, represented by a square.

The RMSE increases with increasing angular aperture, going from 0.34 for small values to 0.42 m for larger ones. Again, this result could be explained by limited validity of the energy dispersion model. This model is assumed to be valid when considering a storm whose diameter equals 1,000 km and more than 4,000 km away from it. As a comparison, this threshold corresponds to an angular aperture equal to  $14^\circ$ . Considering a refined version of this dispersion model closer to the source may therefore improve the synthetic swell field estimates.

### 6.2.6 Rejected Data

Analyzing the swell propagated observations that have been rejected during the iterative filtering, we can detect estimation errors due to the propagation model or to the swell observations. For a given reconstructed swell field, more than 15% of all SAR observations are rejected during the significant swell height filtering. Once these observations are set aside, we look for the reasons explaining their rejection. In addition to the previously identified sources of measurement error, we have noticed the influence of swell propagation direction with respect to the satellite azimuth direction. This value is assessed measuring the difference between the swell direction and the satellite track angle.

---

Descending orbit
ASA_WVW_2PNPDK20080112_164550_000013342065_00069_30684_6984.N1
Ascending orbit
ASA_WVW_2PNPDE20080113_050625_000015442065_00076_30691_5506.N1

---

Table 6.3: L2 wave mode products for which the significant swell height estimations exhibit an important bias. Specifically, the descending track is pointed out in Figure 6.19.

As noticed in several cases, it seems that the significant swell height can be largely under-estimated whenever its propagating direction is close to that of the azimuth direction. As illustrated in a case example in Figure 6.19, co-located significant swell height measurements acquired during an ascending orbit and the descending one, 12 hours after, exhibit a persistent negative bias all along the instrument track that reaches more than 70 cm in absolute value. The descending instrument tracks are circled in magenta. On average, among the seventeen rejected observations belonging to these two descending tracks, the angle difference between the swell propagation direction and the satellite track angle equals  $30^\circ$ . These measurements can be compared to the ones given by the next ascending orbit pass, 12 hours later. This type of comparison offers a new validation method, for which the significant swell height measurements given by successive orbits can be compared. The SAR L2 reference name of the ascending and descending orbits giving the most striking evidence of this discrepancy are indicated in Table 6.3, with their orbit phase.

This is the first time that the significant swell height error dependency on the swell direction with respect to the SAR azimuth is clearly observed. In our case, it took us more than a year to notice this bias, reason being that whenever the significant swell height distribution of the propagated observations was inspected, data points were plotted on top of each other by increasing order of swell height. Therefore, because of the high data density, the under-estimated points were hidden by the other ones. Ever since, we systematically inspect the data distribution plotting the data points in increasing and decreasing order of significant swell height.

Going back to the SAR swell observation validation presented in Chapter 3, we investigate the SAR significant swell height estimation with respect to the difference between the swell propagation direction and the satellite track angle. Two different cases are investigated:  $C_{Az}$ , for which the absolute

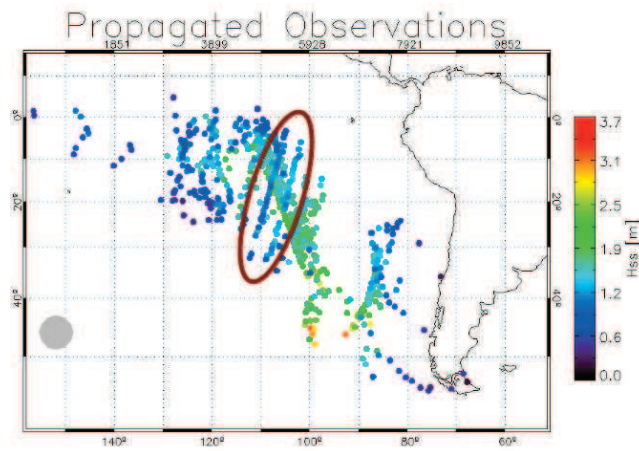


Figure 6.19: Significant swell height of the propagated swell observations associated to a storm event to take place in the western South Pacific Ocean on 7 January 2008. The represented distribution corresponds to the swell field state on 13 January 2008, at 00Z. Original storm source region is represented by a gray disk.

difference ranges from 0 to  $60^\circ$  and  $C_{Rg}$ , for which the absolute difference ranges from 60 to  $120^\circ$ . The bias difference between datasets  $C_{Az}$  and  $C_{Rg}$  equals  $-15$  cm, which confirms our first qualitative observations that swells whose propagation direction are close to the azimuth are statistically underestimated.

### 6.3 Comparison with the numerical wave model

In the present section, we compare the performance of the synthetic swell field estimates with that of the numerical wave model WW3. We briefly describe the methodology used for comparison and then describe the statistical results.

#### 6.3.1 Methodology

In addition to the ocean wave spectrum, WW3 model can also provide partitions' integral parameters, separating the swell from the wind-sea. Similarly to the partitioning scheme we used for the integral parameters' retrieval from the SAR swell spectra, the model uses an inverse water catchment algorithm for spectral partitioning. This allows us to directly compare the integral parameters.

During the peak-to-peak association, synthetic swell field estimates were

co-located with buoy partitions. The wave model can provide several swell estimates. Therefore, the minimum cross spectral distance with the previously co-located buoy partition indicate which model partition is to associate. In the end, for each time step, we have three co-located integral parameters given by the model, the buoy and the synthetic swell field.

### 6.3.2 Statistical results

Using configuration P0, the performances of the synthetic swell field are compared to those of WW3 (Table 6.4). The distinction is made between the case  $C_{\text{High}}$  for which the average SAR data density is high and case  $C_{\text{Gen}}$ , for which all co-located data points are considered, no matter what the data density. As the SAR and buoy dataset are not the same for these two cases, the differentiation also applies for comparison with the model. These conditions concern the SAR data only but they influence the statistics obtained with the SAR-buoy-model co-located dataset.

	Config.	SAR		Model	
		$C_{\text{High}}$	$C_{\text{Gen}}$	$C_{\text{High}}$	$C_{\text{Gen}}$
any $H_{ss}$	RMSE [m]	0.30	0.43	0.28	0.33
	NRMSE [%]	20.8	28.1	18.9	21.4
	Bias [m]	-0.07	-0.20	0.03	0.08
	Correl.	0.92	0.82	0.91	0.87
$H_{ss} > 1.5\text{m}$	RMSE [m]	0.35	0.53	0.23	0.31
	NRMSE [%]	17.8	26.2	11.3	15.5
	Bias [m]	-0.26	-0.42	-0.03	-0.00
	Correl.	0.83	0.63	0.84	0.73
$T_p$	RMSE [s]	0.40	0.58	0.78	0.85
	NRMSE [%]	2.9	4.2	5.7	6.1
	Bias [s]	-0.1	-0.1	0.6	0.5
	Correl.	0.95	0.91	0.92	0.88
$D_p$	RMSE [deg]	11.2	-16.0	12.3	15.5
	Bias [deg]	-2.9	-1.9	-5.5	-4.4

Table 6.4: Statistics given by the comparison between *in situ* measurements from the Stratus buoy and synthetic swell field estimates (SAR) and the same *in situ* measurements and WW3 model for two datasets: all cases and cases of high data density in the SAR reconstructed swell fields,  $C_{\text{Gen}}$  and  $C_{\text{High}}$ , respectively.

First, the significant swell height estimated by WW3 are in better agreement with *in situ* measurements in all cases. For important swell heights,

this comes from the average under-estimation of the synthetic swell field. On the contrary, the peak period is always better estimated by the SAR-based synthetic swell field hereafter referred as SAR. For cases of high data density, this RMSE obtained with the model is almost twice larger than the one obtained with SAR. This could be partly explained by the peak period over-estimation of the model. The tendency of numerical wave models to over-estimate peak periods was already pointed out by (*Bidlot et al., 2002*). This may indicate that the swell arrival time predicted by the model is in advance, which was confirmed by their analysis. As for peak propagation directions, SAR is also more accurate than WW3 model, even though the performance improvement is not as drastic as for the peak period.

At first sight, the SAR seems not to bring more accurate information on the significant swell height than the model. Some configurations show the opposite. We have noticed that certain estimation conditions were less favorable than others: swells whose storm source is located further south of 55°S, swells whose distance to the source is larger than 10,000 km and swells with high storm source angular aperture. Now, SAR and model performances are compared for swells whose storm source is located in the Southern Hemisphere and north of 50°S latitude. Statistical results are presented in Table 6.5. The significant swell height of the considered co-locations equals 1.6 m on average and ranges from 0.65 to 2.70 m. Two different cases are investigated: cases when data density is high and cases when it is above the average in the SAR reconstructed swell fields,  $C_{\text{High}}$  and  $C_{\text{Mid}}$ , respectively.

In such favorable conditions, the significant swell height estimations given by the synthetic swell field give much better statistical results than the model for both mid and high data density. This mis-estimation from the model is most probably related to the strong wave height bias. We believe that it results from an under-estimated swell energy dissipation despite the last changes brought by *Ardhuin et al. (2008)*. Therefore, modeled wave heights of swell originating from nearby storm sources tend to be over-estimated. The fact that this bias is nearly absent from the global scale comparison (cf. Table 6.4) is attributed to the under-estimation of the largest wave heights that results from weak wind forcing.

## 6.4 Conclusion

In the previous chapter, we demonstrated the possibility to monitor swell field propagation using reconstructed SAR swell fields. Still, many issues were to tackle such as the accuracy of the virtual buoy estimates, the possibility to solve the issue raised by the lack of measurements caused by het-

	Config.	SAR		Model	
		C <sub>High</sub>	C <sub>Mid</sub>	C <sub>High</sub>	C <sub>Mid</sub>
any $H_{ss}$	RMSE [m]	0.26	0.33	0.37	0.38
	NRMSE [%]	16.6	21.6	23.9	25.3
	Bias [m]	-0.04	-0.02	0.26	0.26
	Correl.	0.87	0.82	0.86	0.87
$T_p$	RMSE [s]	0.46	0.49	0.62	0.66
	NRMSE [%]	3.4	3.5	4.5	4.7
	Bias [s]	-0.2	-0.2	0.43	0.43
	Correl.	0.86	0.92	0.86	0.89
$D_p$	RMSE [deg]	16.4	-16.2	16.9	17.4
	Bias [deg]	-2.4	-3.7	-7.3	-8.5

Table 6.5: Statistics given by the comparison between *in situ* measurements from the Stratus buoy (WMO51028) and the synthetic swell field estimation (column SAR) and the same *in situ* measurements and WW3 model (column model) for two datasets: cases when data density is high or above the average in the SAR reconstructed swell fields, C<sub>High</sub> and C<sub>Mid</sub>, respectively.

erogeneous data sampling or the possibility to retrieve swell information on a regular space and time grid. The methodology developed in the present chapter for the estimation of synthetic swell fields addresses all these problems.

The estimation methodology is based on an iterative process during which, successively, a surface fit is applied to the propagated swell observations and outliers with respect to this intermediate synthetic swell field are rejected. For the moment, this approach is restricted to regions with a minimum density of propagated observations, to deep ocean, away from island shadows and in the absence of currents. Thanks to these assumptions, we were able to define a criteria for each integral parameter indicating the maximum acceptable difference between an isolated swell observation and the overall swell field trend, thereby rejecting those not satisfying one of these criteria.

Two different surface fit methods have been presented: a rather simple 2D polynomial regression and a more elaborate Kriging method. The latter is based on an input semivariogram model which requires a careful parametrization, ideally specific to each swell field. It is also quite expensive to use since reconstructed swell field are composed of a thousand observations on average, which prevents from testing many different parametriza-

tions for each synthetic swell field estimation. On the contrary, polynomial regression are almost instantaneous and the degree of the polynomial function is determined as the highest degree which minimizes the standard deviation between the integral parameter of the isolated propagated observations and of the corresponding surface fit. Additionally, the confidence in each propagated observations can be taken into account by the regression. Those quality flags have been determined according to the parameters that most influence the integral parameters' accuracy of the propagated SAR swell observations, namely the SAR estimated wind speed, the time separating the SAR observation from the time of propagation, the SAR partition contrast within the observed swell spectrum, the SAR azimuth cut-off with respect to the swell azimuth wavenumber and the confidence in the propagation direction.

Comparing the integral parameters' estimates of the synthetic swell fields to the co-located buoy spectra, partitions with minimum spectral distance are associated. Calculated over year 2008, the statistical results indicate best estimations are given by the weighted polynomial regression. Besides, we have shown that the density of the propagated SAR swell observations at location and time of estimates was a very good quality flag for the accuracy of the synthetic swell field. For such dense configurations, RMSE of the peak period equals 0.4 s and  $11.2^\circ$  for the peak directions. Compared to the estimation errors obtained for the best SAR-buoy co-located observations presented in Chapter 3, they represent statistical improvements of 43 and 30 % for the peak period and the peak direction, respectively. As concerns the significant swell height, the RMSE equals 30 cm (20.8%) and 35 cm (17.8%) for swell whose height exceeds 1.5 m. These errors are approximately the same as those obtained for the best quality SAR observations. However, those best quality data points only represent a small percentage of the total number of SAR observations, especially when considering the wave height measurements. Thus, the improvement brought by the use of numerous and coherent swell observations in the synthetic swell field is compensated by the fact that many of the propagated SAR observations are not necessarily trustful estimates.

Investigating the possible sources of error measurements, we have exhibited for the first time the dramatic influence of the wave direction with respect to the satellite azimuth direction leading to strong negative bias for waves propagating at angles of more than  $30^\circ$  with the range direction. Also, the influence of the original storm source was highlighted. It is probably due to the fact that, for largest storm, the hypothesis of a point source assumed for the calculation of the swell energy decay with propagation is not valid anymore.

Finally, performances of the synthetic swell field were compared to that of WW3 model taking, each time SAR and buoy partitions were co-located, the modeled partitions closest to the buoy partition. This comparison reveals that SAR estimated peak period are twice as accurate as the model estimates. Also, direction estimates indicate slightly better estimates for SAR. On the contrary, significant swell heights given by synthetic swell field estimates are generally not as good even though, at certain distances from the storm source, this behavior reverses.

Comparisons with numerical wave models have highlighted several interesting points. As it is known, a large part of wave estimates' errors come from the input wind forcing which tends to be under-estimated for strongest wind conditions. For this reason, *in situ* comparisons of largest waves should indicate under-estimation by numerical models. However on average, this bias seems to be absent from our statistical comparison. Looking at closer details, the modeled significant swell heights tend to be over-estimated close to the storm region and under-estimated far from it which could indicate an incorrect energy decay or dissipation despite the latest upgrade brought by *Ardhuin et al.* (2008). In addition, we have exposed the systematic peak period over-estimation, 0.6 s on average, to which we still look for an answer.

Because swell evolution, away from their storm region, is independent from the wind as opposed to wind-seas, numerical models could greatly benefit from data assimilation. As directional buoys are still very sparsely distributed in deep oceans, the synthetic swell field approach appears to be a very promising source of valuable swell information. Still, most of the bias in the synthetic swell field estimates comes from the SAR swell inversion used to generate the SAR L2P wave mode products and our synthetic method would greatly benefit from their improvement.

## Bibliography

- Ardhuin, F., F. Collard, B. Chapron, P. Queffelec, J. F. Filipot, and M. Hamon (2008), Spectral wave dissipation based on observations: a global validation, in *Proceedings of Chinese-German Joint Symposium on Hydraulics and Ocean Engineering, Darmstadt, Germany*, p. 391–400. 231, 234
- Bidlot, J.-R., D. J. Holmes, P. A. Wittmann, R. Lalbeharry, and H. S. Chen (2002), Intercomparison of the performance of operational ocean wave forecasting systems with buoy data, *Weather and Forecasting*, 17, 287–309. 231
- Collard, F., F. Ardhuin, and B. Chapron (2009), Monitoring and analysis of ocean swell fields from space: New methods for routine observations, *Journal of Geophysical Research-Oceans*, 114(C7), C07,023. ii, 2, 68, 69, 70, 71, 80, 85, 111, 152, 153, 155, 219, 239
- Delhomme, J. P. (1976), Applications de la théorie des variables régionalisées dans les sciences de l'eau, Ph.D. thesis, Université Pierre et Marie Curie. 202
- Delhomme, J. P. (1978), Kriging in the hydrosiences, *Advances in water resources*, 1(5), 251–266. 202
- Delpey, M., F. Ardhuin, F. Collard, and B. Chapron (2010), Space-time structure of long swell systems, *J. Geophys. Res.*, 115, C12,037, doi:10.1029/2009JC005885. ii, 2, 90, 152, 180, 186, 189, 192, 241
- Hanson, J. L., and O. M. Phillips (2001), Automated analysis of ocean surface directional wave spectra, *J. Atmos. Ocean Technol.*, 18, 277–293. 2, 86, 91, 152, 192
- Isaaks, E. H., and R. M. Srivastava (1989), *Applied geostatistics*, vol. 2, Oxford University Press New York. 200
- Kerbiriou, M. A. (2008), Energie des vagues: estimation du potentiel récupérable en regard du potentiel naturel du site. 192
- Matheron, G. (1969), Le krigeage universel (universal kriging). vol. 1, *Cahiers du Centre de Morphologie Mathématique, Ecole des Mines de Paris, Fontainebleau*, 83pp. 200, 202
- Matheron, G. (1971), *The theory of regionalized variables and its applications*, vol. 5, École nationale supérieure des mines. 200
- O'Reilly, W. C., T. H. C. Herbers, R. J. Seymour, R. T. Guza, et al. (1996), A comparison of directional buoy and fixed platform measurements

of pacific swell, *Journal of Atmospheric and Oceanic Technology*, 13(1), 231–238. 81, 224

Snodgrass, F. E., G. W. Groves, K. F. Hasselmann, G. R. Miller, W. H. Munk, and W. H. Powers (1966), Propagation of ocean swell across the pacific, *Philosophical Transactions of the Royal Society of London. Series A, Mathematical and Physical Sciences*, 259(1103), 431. iv, 2, 56, 69, 70, 152, 168, 192

Webster, R., and M. A. Oliver (2007), *Geostatistics for Environmental Scientists*, John Wiley & Sons. 200

# Appendix

## 6.A GRL publication: Revealing forerunners on ENVISAT's wave mode ASAR using the Global Seismic Network

R. Husson,<sup>6</sup> F. Ardhuin,<sup>7</sup> F. Collard,<sup>6</sup> B. Chapron,<sup>7</sup> A. Balanche<sup>7</sup>

Received 3 May 2012; revised 22 June 2012; accepted 26 June 2012;  
Geophys. Res. Lett., doi:10.1029/2012GL052334, in press.

**Abstract** Swells radiating across ocean basins are fingerprints of the large ocean storms that generated them, which are otherwise poorly observed. Here we analyze the signature of one swell event in the seismic noise recorded all around the Pacific and we show that it is a natural complement to the global coverage provided by the Synthetic Aperture Radar wave mode data from ENVISAT. In particular the seismic stations are much more sensitive to low frequency and amplitude signals than buoys and SAR, capturing swell forerunners a couple of days before they can be detected from space or *in situ* data. This information helps detect in the SAR measurements the presence of very long swell, with periods of 22 s in our case example, that were otherwise excluded.

### Introduction

Waves with periods larger than 13 s are routinely observed to propagate all the way across ocean basins from the area of high winds that generated them (*Gain, 1918; Darbyshire, 1952; Munk et al., 1963; Young, 1999*). These swells are today still poorly predicted (*Ardhuin et al., 2010*) in spite of a better knowledge of their dissipation (*Ardhuin et al., 2009*). Indeed, these long swells radiate from the most intense and long-lived storms, which are still poorly observed. There is thus a clear need for more swell observations, be

---

6. CLS, Plouzane, France

7. IFREMER, Plouzane, France

it for navigation safety in coastal areas, or a better understanding of air-sea fluxes at low winds, in particular in the tropics (e.g. *Edson et al., 2007*). In order to complement the sparse and spectrally limited coverage provided by satellite altimeters and space-borne Synthetic Aperture Radars, and the very few *in situ* measurement by buoys, especially in the Southern Hemisphere, we wish to advocate the potential complementarity use of seismic noise records from the Global Seismic Network.

Indeed, the strongest source of seismic noise are the hydrodynamic interactions of waves with nearly equal periods and nearly opposite directions which leads to a fast-propagating pressure signal that generates noise, in particular seismic Rayleigh waves (e.g. *Hasselmann, 1963*). This explains why the dominant recorded seismic noise has periods that are half of that of the interacting wave trains (*Bernard, 1941*). As a result, important noise sources are associated with sea states that contain a significant amount of energy radiating at the same frequency and in opposite directions. For seismic periods larger than 8s, corresponding to ocean waves with periods larger than 16 s, this is most often the result of wave reflection from the shoreline (*Haubrich et al., 1963; Bromirski et al., 1999; Ardhuin et al., 2011b*).

Only occasionally the noise recorded on land at these long periods is dominated by the interaction of swell from a remote storm with the local wind sea or another swell (*Zopf et al., 1976; Kedar et al., 2008; Ardhuin et al., 2011b, 2012*) even though it can be persistent when considering shorter periods (*Stehly et al., 2009; Kedar, 2011*). The seismic noise record from a land-based station thus provide a very clear detection, that is generally unambiguous, of the swell arriving at the nearest shoreline.

The seismic source is actually dominated by contributions from water depths larger than 1000 m, due to the seismic generation process (*Longuet-Higgins, 1950*), over regions that typically span hundreds of kilometers, or even more for mid-oceanic islands (*Ardhuin et al., 2011b*). However, the wave interaction only occurs when the incident swells interact with the reflected swells. Because the group velocity on a typical shelf is not very different from that in deep water, the maximum of noise generation should indeed occur when the incident swell energy is maximum right at the shoreline.

Waves heights and periods, and the full frequency spectrum, may then be estimated from seismic records (*Bromirski et al., 1999; Ardhuin et al., 2010*). This should even be easier when applied exclusively to long period swells because there is little contribution of sources not associated to shoreline reflection (*Ardhuin et al., 2012*). Besides, the swells have a distinctive time-evolution of the frequency spectrum with a gradual decrease of the peak period over a few days. This was particularly well demonstrated by *Barruol*

*et al.* (2006), who analyzed swells from seismic stations in Polynesia. These stations are now analyzed in real time for local marine forecasts and high surf advisories. The existing long record of seismic observations, together with the good coverage of the Global Seismic Network in both hemispheres is a compelling argument for generalizing this quantitative use of seismic data, and blending it with remote sensing data and numerical wave models.

*Collard et al.* (2009) already highlighted the ability to monitor ocean swell fields from space as they propagate through ocean basins. Taking the example of a powerful ocean storm that peaked on April 11th, 2008 South-East of New-Zealand, we take advantage of the synoptic view of the swell propagating across the ocean basin provided by the SAR. The analysis of SAR data is described in Subsection 2, leading to the estimation of swell parameters time series in the deep ocean, in the vicinity of each GSN stations. Both seismic and SAR data are compared in Subection 3.

### Analysis of SAR data

SAR instruments can be used to image the propagation of an ocean swell field (e.g. *Holt et al.*, 1998; *Heimbach and Hasselmann*, 2000). Latest quality assessment of the SAR wave measurements indicates estimations of the peak period and direction with root mean square errors of 1.07 seconds and  $20^\circ$ , respectively *Collard et al.* (2009). Yet, these swell measurements are still limited to waves with peak period less than 18 s and significant wave height larger than 30 cm. Therefore, the longest period swells that propagate ahead of the most energetic swell components, called forerunners by *Munk* (1947), are excluded from the SAR present algorithm.

Using the methods proposed by *Collard et al.* (2009), the swell event is reconstructed gathering backward propagated swell observations that converge in space and time to the generation region. Over deep ocean and away from islands, the emanating swell field is defined by that group of swell observations propagated on from this area, using linear propagation theory. Figure 6.20 represents the trajectory of all the swell observations associated to the April 2008 storm. Numerical wave hindcasts provided by the IOWAGA project (*Ardhuin et al.*, 2010, 2011a) give a total significant wave height reaching 14 m, when using ECMWF analysis winds, with mean wave direction oriented to the North-East. The swell field then swept all over the East Pacific for the next two weeks. Buoys located in Alaska, more than 10 000 km away from the storm source, recorded swell heights around 0.4 m.

The SAR dataset can be used to estimate swell parameters time series at any given location. The estimated swell peak direction is given by the azimuth to the generation region. The swell peak period is estimated for any

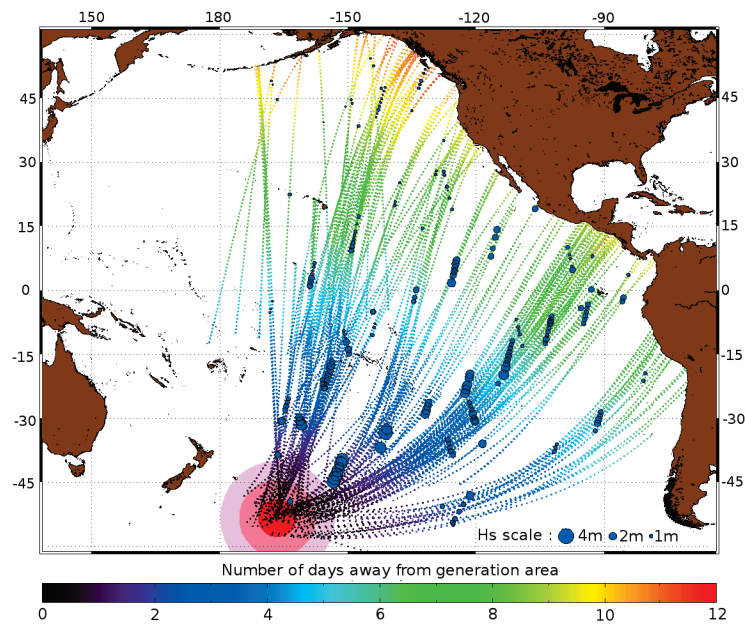


Figure 6.20: Trajectories of all the swell observations given by the SAR wave mode and associated to the storm of 11 April 2008, South-East of New-Zealand. The generation region is symbolized by a red disk and the color along the trajectories indicates the days of travel since generation. Blue disks are placed at observation locations. Their size indicates the significant swell height at this moment.

chosen time by fitting a second-order polynomial function of the distance to the source and distance to the swell field main direction of propagation. This fit gives more weight to observations with higher confidence. This 2<sup>nd</sup> order function reproduces the spatial distribution of wavelengths better than a linear function. Indeed, wave generated by long-lived and/or fast moving storm events have been proven to leave the storm generation region at different times and location depending on their wavelength (*Delpey et al.*, 2010).

Using this principle, wave peak period and direction evolution is estimated at various locations. In our example, this is first done at the buoy 'Stratus' (WMO32012), maintained by the Woods Hole Oceanographic Institution (WHOI) and moored off the coast of Peru in 4440 m of water. The same processing is then applied at ocean locations close to land-based seismometers. In that case the resulting data is shifted in time by the propagation time, estimated from linear theory, between the chosen oceanic point and the coast, and the estimated frequencies are multiplied by two for a direct comparison with the seismic data.

### Complementarity of SAR and seismic data

Seismic noise observations overlaid with results from the SAR analysis are presented on Figures 6.21 and 6.22. They show wave spectra time series integrated over directions for buoy Stratus and seismic noise spectra time series of stations RPN (Rapa Nui, Easter Island), KIP (Kipapa, Hawaii), NNA (Nana, Lima, Peru), UNM (Mexico City, Mexico) and JTS (Las Juntas de Abangares, Costa Rica). Their position is indicated on Figure 6.23.

Comparison with the Stratus buoy indicates that the swell arrived within 12 hours of our estimate based on SAR data. The swell arrives from South-West and in four days, the frequency where the energy is maximum gradually increases from 0.055 to 0.08 Hz. After partitioning the ocean wave spectra, the peak period and direction estimated by the SAR give root mean square errors of 0.34 seconds and 23°, with bias of -0.01 seconds and -3.6°, respectively.

As it is well known (*Haubrich et al.*, 1963), the swell frequency is expected to increase linearly in time and so does its seismic noise signature at primary and secondary, *i.e.* double, frequency. Here, the secondary frequency increase is observed at every seismic stations and can be followed up to 0.14 Hz, corresponding to 0.07 Hz ocean waves. The level of this signal compared to other noise sources is particularly high at continental stations compared to island stations thanks to the larger shoreline extension that intercepts the incoming wave flux.

The fact that the noise is generated by coastal reflection is confirmed by the presence of noise at primary frequency (*Haubrich et al., 1963*), which here is shown only for JTS. This signal is specific to shallow waters and results from the interaction of ocean swell with a shoaling ocean bottom (*Oliver, 1962; Hasselmann, 1963*).

Compared to the buoy and seismic-detected swells, the SAR estimations of swell frequencies are very consistent. SAR data provides a record of swell frequencies from 0.06 to 0.08 Hz while seismic noise data corresponds to 0.04 to 0.07 Hz. Seismic noise data, as already noted by *Haubrich et al. (1963)*, offers a nice extension to low frequencies of conventional wave measurements at a fixed point with pressure recorders. Here we show that this is even more true for SAR data excluding very long swell, usually around 17 s, from its measurements. In the present example, the frequency of the longest buoy-detected swell is 0.055 Hz and only the seismic stations can measure 0.04 Hz swell.

The full Global Seismic Network data can also be used alone to triangulate the storm source location and time. For each seismic station, the double frequency ridge slope is automatically estimated by maximizing the energy encountered along a straight line placed on the ridge. Then, the distance to the expected storm source is determined according to equation 6.17.

$$D = \frac{g}{8\pi} \left( \frac{df_s}{dt} \right)^{-1} \quad (6.17)$$

where,  $f$  is the seismic noise frequency;  
 $t$ , the time of arrival;  
 $g$ , the Earth gravity;  
 $D$ , the seismic station distance to the expected storm source.

As evidenced on Figure 6.23, the seismic source location based on longer period waves and the SAR source location are in general agreement.

Once the storm source location is found and the presence of very long swell is proven by seismic noise measurements, its expected arrival time is calculated using linear theory. Using this information, at appropriate times and locations, we look for this long swell signature on the SAR image spectra directly, as opposed to the SAR ocean spectra. Indeed, for such waves, under light to moderate wind speeds, a quasi-linear imaging mechanism is a valid assumption (*Krogstad, 1992*). This way, swell with peak frequency equal to 0.045 Hz is detected 3 days after the storm in the South Pacific Ocean, as shown on Figure 6.24. The induced very long scale modulation is visible on the SAR image, depicting a long wave group.

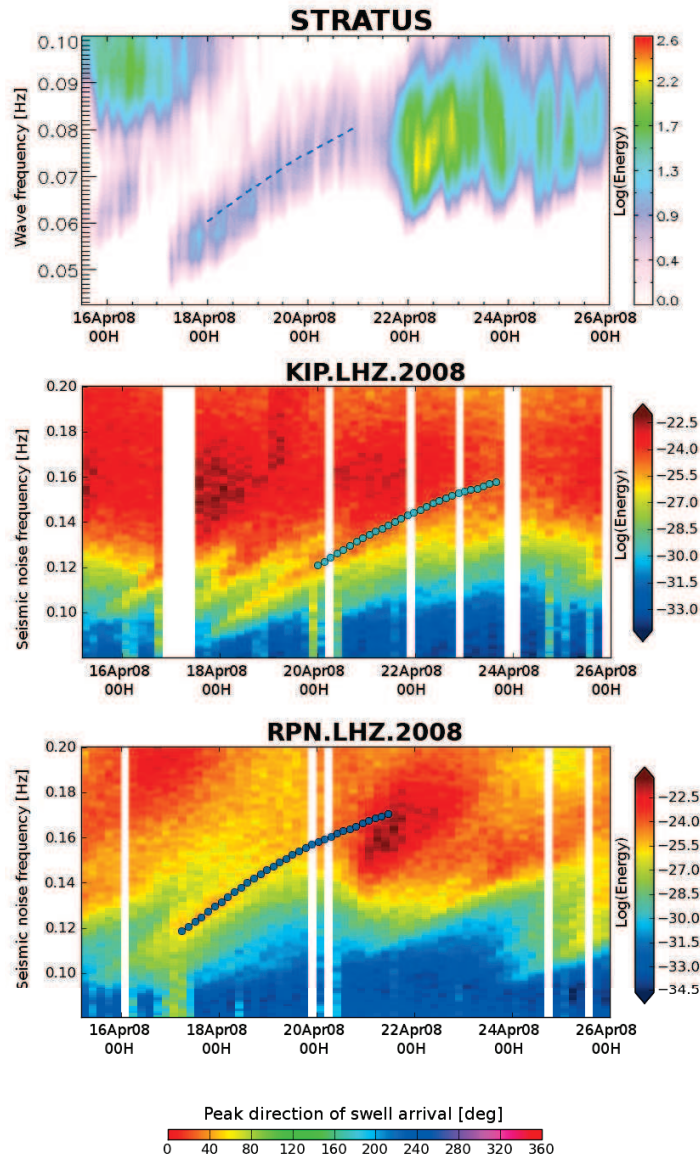


Figure 6.21: Spectra time series for buoy 'Stratus' (lon:  $-85.384^{\circ}\text{W}$ , lat:  $-19.616^{\circ}\text{N}$ ) and seismic stations KIP, RPN in mid-April 2008. SAR swell parameters estimation at secondary frequency is overlaid in colored disk indicating north-eastern propagation. Main seismic events have been filtered out.

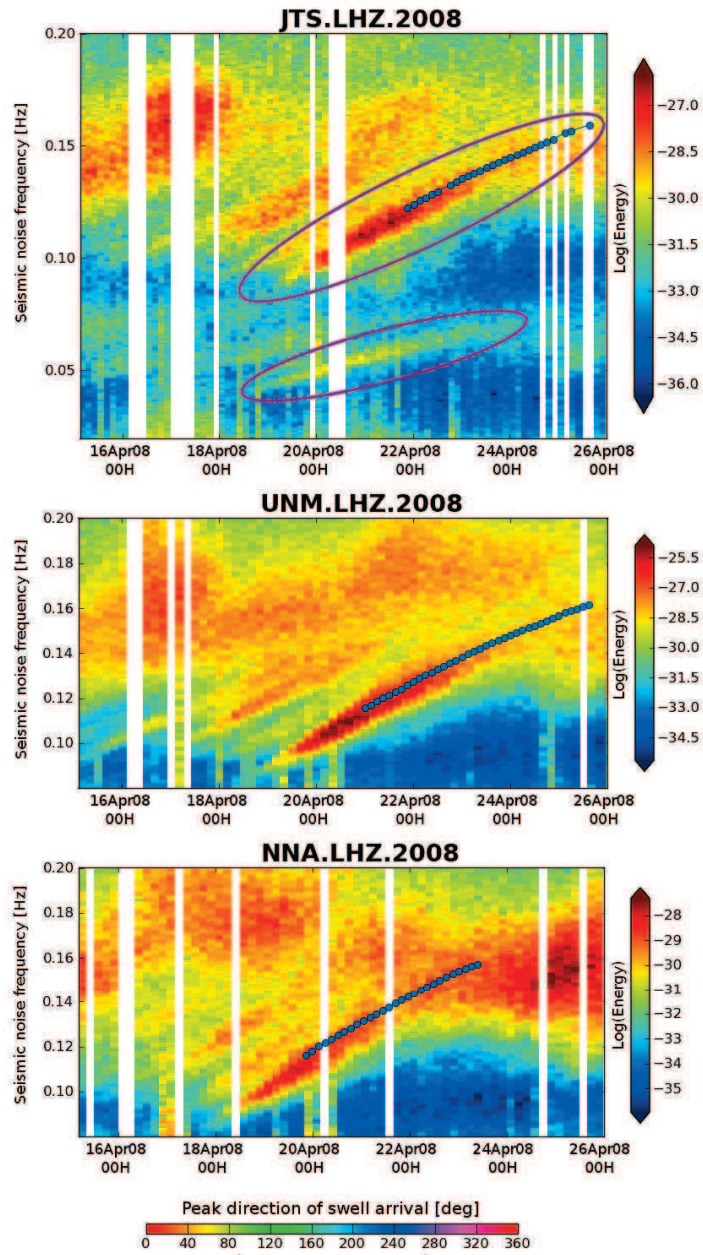


Figure 6.22: Spectra time series for seismic stations JTS, UNM and NNA in mid-April 2008. For JTS, the primary signal is shown as well and both the secondary and the primary signals are circled in dark magenta. SAR swell parameters estimation at secondary frequency is overlaid in colored disk indicating north-eastern propagation. Main seismic events have been filtered out.

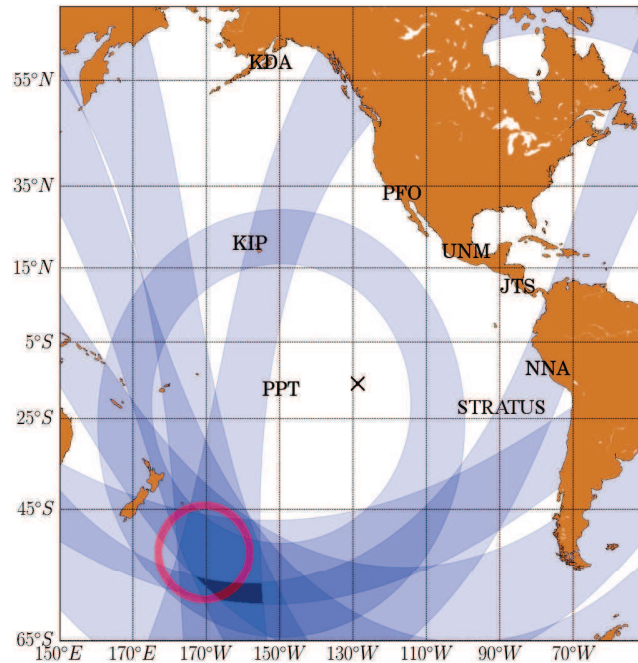


Figure 6.23: Location of the expected storm source from two independent instruments: the SAR wave mode products and seismic noise measurements. For each seismic station (UNM, PFO, KDA, PPT, JTS, NNA and KIP), a 1500 km wide blue disk is plotted, its radius being equal to the distance to the storm source estimated from the differential arrival time of the swell at the seismic station using seismic noise alone. The 1500 km width corresponds to the average accuracy of the distance estimation given by the automatic radius estimation. The storm source given by the SAR analysis is circled in red. The Stratus buoy location is also indicated and a black cross is placed at the location where the SAR observation shown in Figure 6.24 was acquired.

In the past, as no evidence of the presence of very long waves in the ocean wave spectrum could be easily and frequently provided, associated low frequency signatures were flagged in the SAR image spectra and excluded from the ocean wave spectrum inversion. Now, taking these signals into account dramatically increases the frequency range of observable swell using the SAR instrument, which is almost doubled.

Since long swell travels faster than the one presently detected by the SAR, this potential improvement would enable us forecast the swell arrival several days ahead. For operational early-warning applications, one would have to use data from seismic stations nearby the storm region or, alternatively, numerical wave models. Though, the peak period information they provide can be significantly under-estimated (*Hanson et al., 2009*) and they fail to capture the early arrival of waves at low frequencies (*Wingert, 2001*). Also, better SAR ocean swell monitoring can benefit to numerical wave models assimilating this information, thereby improving their significant swell height estimation which are largely under-estimated for long swell (*Hanson et al., 2009*). Besides, storm generation regions can be better estimated using forerunners' information since they require much stronger forcing conditions which are met over smaller ocean areas. Using the full SAR wave mode archive, starting in 1991, with seismic noise data, this information could be used for the study of storm climatology over the past two decades.

The proof of physical presence of very long swell provided by the seismic noise is a necessary information for the retrieval of the swell geophysical parameters given by the SAR. Indeed, modulation of the low frequency spectrum by phenomena unrelated to long swell like low wind area may be miscellaneously attributed. However, the previously described scheme going through the identification of a massive swell event using SAR analysis, of the corresponding ridge-like structure in the seismic noise and estimation of longest present swell can easily be automated from the moment that we have access to the seismic noise data. Extending this approach to other years, a swell with a frequency of 0.04 Hz (24.7 s) was detected using the SAR in the South Pacific Ocean in late August 2011.

Finally, even though the imaging capability of extremely long swell is limited by the ground coverage of the ASAR wave mode, barely imaging an entire wave group, the extended  $20 \times 20 \text{ km}^2$  coverage of the future Sentinel-1 SAR mission compared to the  $7 \times 10 \text{ km}^2$  of ENVISAT will easily tackle this issue.

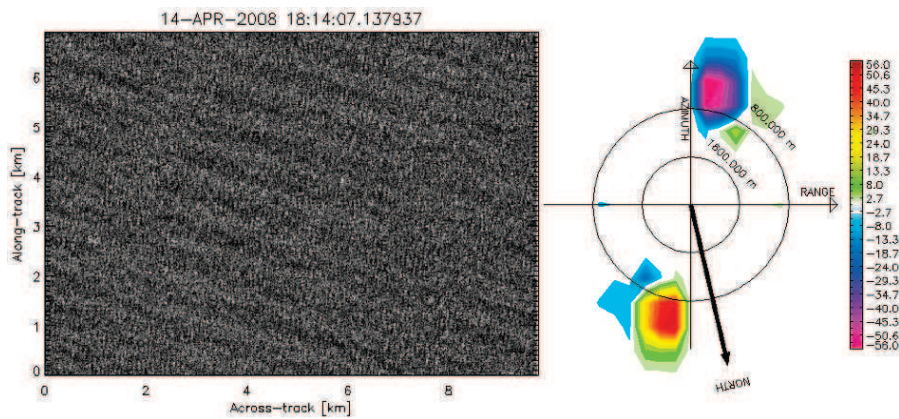


Figure 6.24: SAR ocean image exhibiting very long swell as acquired by ASAR instrument on-board ENVISAT 3 days after the storm generation (left) and associated imaginary spectrum, weighted by the energy spectrum indicating the presence of a 750 m swell propagating in North-East direction (right). The SAR measurement geographical location is indicated in Figure 6.23 by a black cross.

## Conclusion

The present study highlights ASAR wave mode capability to image very long swell whenever used together with seismic noise data from the Global Seismic Network for the observation of ocean swells. From all SAR swell observations after April 11<sup>th</sup>, 2008, a massive swell event that occurred South-East of New Zealand was reconstructed. Using the virtual buoy concept, the swell peak period and direction time series related to this event were estimated at various locations. First, they were compared to spectra given by Stratus moored buoy. In four days, the peak period slowly and linearly decreases from 17 to 12 s. Peak period and direction estimations give root mean square errors of 0.34 seconds and 23°, respectively. Similarly, the swell signal recorded in the seismic noise by coastal and island stations was simulated. Comparison to seismic noise spectra indicate very good fit within their common period range, from 14 to 17 s, demonstrating the capability of the SAR not only to provide both a global and a local view of the swell field propagation across an entire ocean basin but also its ability to reproduce its signal in seismic noise as measured by coastal stations. Thereby, ridges related to the same swell system for different seismic stations could be associated and the precise storm source of the longest swell triangulated.

By default, forerunners are not detected by the SAR but seismic noise records reveal their presence when arriving to the coast. Then, looking at

appropriate expected arrival time and location in open ocean, their signature is found in the SAR image spectra. Using this technique swell with periods up to 24.7 s were detected on SAR measurements. Their observability will even be improved by the future Sentinel-1 SAR mission extended ground coverage.

The great sensitivity of seismometers to very long waves and their high frequency resolution of these phenomena compared to moored buoys is a tremendous asset for a better calibration and validation of SAR observations of long swell. Then, the other way around, the SAR may be used to calibrate the wave-to-seismic transfer function to contribute to the development capability of a global wave monitoring network.

## Bibliography

Ardhuin, F., B. Chapron, and F. Collard (2009), Observation of swell dissipation across oceans, *Geophys. Res. Lett.*, *36*, L06,607, doi:10.1029/2008GL037030. ii, 2, 70, 71, 152, 181, 237

Ardhuin, F., E. Rogers, A. Babanin, J.-F. c. Filipot, R. Magne, A. Roland, A. v. d. Westhuysen, P. Queffelec, J.-M. Lefevre, L. Aouf, and F. Collard (2010), Semi-empirical dissipation source functions for wind-wave models: part i, definition, calibration and validation, *J. Phys. Oceanogr.*, *40*(9), 1917–1941. ii, 237, 238, 239

Ardhuin, F., J. Hanafin, Y. Quilfen, B. Chapron, P. Queffelec, M. Obrebski, J. Sienkiewicz, and D. Vandemark (2011a), calibration of the IOWAGA global wave hindcast (1991–2011) \ using ECMWF and CFSR winds, in *Proceedings, 12th Int. Workshop of Wave Hindcasting and Forecasting, Hawaii*. 239

Ardhuin, F., E. Stutzmann, M. Schimmel, and A. Mangeney (2011b), Ocean wave sources of seismic noise, *J. Geophys. Res.*, *116*, C09,004, doi:10.1029/2011JC006952. 238

Ardhuin, F., A. Balanche, E. Stutzmann, and M. Obrebski (2012), From seismic noise to ocean wave parameters: general methods and validation, *J. Geophys. Res.*, *117*, submitted. 238

Barruol, G., D. Reymond, F. R. Fontaine, O. Hyvernaud, V. Maurer, and K. Maamaatuaiahutapu (2006), Characterizing swells in the southern pacific from seismic and infrasonic noise analyses, *Geophys. J. Int.*, p. 516–542, doi:10.1111/j.1365-246X.2006.02871.x. 238

- Bernard, P. (1941), Sur certaines propriétés de la houle étudiées à l'aide des enregistrements sismographiques, *Bull. Inst. Oceanogr. Monaco*, 800, 1–19. 238
- Bromirski, P. D., R. E. Flick, and N. Graham (1999), Ocean wave height determined from inland seismometer data: Implications for investigating wave climate changes in the NE Pacific, *Journal of Geophysical Research*, 104, 20. 238
- Collard, F., F. Ardhuin, and B. Chapron (2009), Monitoring and analysis of ocean swell fields from space: New methods for routine observations, *Journal of Geophysical Research-Oceans*, 114(C7), C07,023. ii, 2, 68, 69, 70, 71, 80, 85, 111, 152, 153, 155, 219, 239
- Darbyshire, J. (1952), The generation of waves by wind, *Proceedings of the Royal Society of London. Series A, Mathematical and Physical Sciences*, p. 299–328. 2, 61, 237
- Delpey, M., F. Ardhuin, F. Collard, and B. Chapron (2010), Space-time structure of long swell systems, *J. Geophys. Res.*, 115, C12,037, doi:10.1029/2009JC005885. ii, 2, 90, 152, 180, 186, 189, 192, 241
- Edson, J., T. Crawford, J. Crescenti, T. Farrar, N. Frew, G. Gerbi, C. Helmig, T. Hristov, D. Khelif, A. Jessup, H. Jonsson, M. Li, L. Mahrt, W. Mcgillis, A. Plueddemann, L. Shen, E. Skillingstad, T. Stanton, P. Sullivan, J. Sun, J. Trowbridge, D. Vickers, S. Wang, Q. Wang, R. Weller, J. Wilkin, A. J. W. III, D. K. P. Yue, and C. Zappa (2007), The coupled boundary layers and air-sea transfer experiment in low winds, *Bull. Amer. Meteorol. Soc.*, 88(3), 341–356. 238
- Gain, L. (1918), La prédiction des houles au Maroc, *Annales Hydrographiques*, pp. 65–75. 2, 56, 61, 237
- Hanson, J. L., B. A. Tracy, H. L. Tolman, and R. D. Scott (2009), Pacific hindcast performance of three numerical wave models, *Journal of Atmospheric and Oceanic Technology*, 26(8), 1614–1633. 246
- Hasselmann, K. (1963), A statistical analysis of the generation of microseisms, *Rev. of Geophys.*, 1(2), 177–210. 238, 242
- Haubrich, R. A., W. H. Munk, and F. E. Snodgrass (1963), Comparative spectra of microseisms and swell, *Bulletin of the Seismological Society of America*, 53(1), 27. 238, 241, 242
- Heimbach, P., and K. Hasselmann (2000), Development and application of satellite retrievals of ocean wave spectra, *Elsevier Oceanography Series*, 63, 5–33. ii, 2, 239

- Holt, B., A. K. Liu, D. W. Wang, A. Gnanadesikan, and H. S. Chen (1998), Tracking storm-generated waves in the northeast pacific ocean with ERS-1 synthetic aperture radar imagery and buoys, *Journal of Geophysical Research*, 103(C4). ii, 2, 239
- Kedar, S. (2011), Source distribution of ocean microseisms and implications for time-dependent noise tomography, *Comptes Rendus Geoscience*. 238
- Kedar, S., M. Longuet-Higgins, F. Webb, N. Graham, R. Clayton, and C. Jones (2008), The origin of deep ocean microseisms in the north atlantic ocean, *Proceedings of the Royal Society A: Mathematical, Physical and Engineering Science*, 464(2091), 777–793, doi:10.1098/rspa.2007.0277. 238
- Krogstad, H. E. (1992), A simple derivation of Hasselmann’s nonlinear ocean-synthetic aperture radar transform, *J. Geophys. Res.*, 97(C2), 2421–2425. ii, 2, 34, 36, 37, 38, 45, 242
- Longuet-Higgins, M. S. (1950), A theory of the origin of microseisms, *Philosophical Transactions of the Royal Society of London. Series A, Mathematical and Physical Sciences*, 243(857), 1–35, ArticleType: research-article / Full publication date: Sep. 27, 1950 / Copyright © 1950 The Royal Society. 238
- Munk, W. H. (1947), Tracking storms by forerunners of swell., *Journal of Atmospheric Sciences*, 4, 45–57. 239
- Munk, W. H., G. R. Miller, F. E. Snodgrass, and N. F. Barber (1963), Directional recording of swell from distant storms, *Philosophical Transactions of the Royal Society of London. Series A, Mathematical and Physical Sciences*, 255(1062), 505–584. iv, 2, 56, 67, 237
- Oliver, J. (1962), A worldwide storm of microseisms with periods of about 27 seconds, *Bulletin of the Seismological Society of America*, 52(3), 507–517. 242
- Stehly, L., B. Fry, M. Campillo, N. M. Shapiro, J. Guilbert, L. Boschi, and D. Giardini (2009), Tomography of the alpine region from observations of seismic ambient noise, *Geophysical Journal International*, 178(1), 338–350, doi:10.1111/j.1365-246X.2009.04132.x. 238
- Wingert, K. M. (2001), Validation of operational global wave prediction models with spectral buoy data, *Tech. rep.* 246
- Young, I. R. (1999), Seasonal variability of the global ocean wind and wave climate, *International Journal of Climatology*, 19(9), 931–950. 237

Zopf, D. O., H. C. Creech, and W. H. Quinn (1976), The wavemeter: a land-based system for measuring nearshore ocean waves, *Mar. Tech. Soc. Journal*, 10(4), 19–25. 238



# Conclusion

Throughout this work, we have developed and validated a global observation-based deep ocean swell model using SAR derived swell 2D spectra from ENVISAT mission.

First, we presented the SAR swell imaging principle, followed by theory and observations of swell generation and propagation in deep ocean. These two first chapters enable a better understanding of the physical processes responsible for estimation errors of the SAR swell measurements proposed in Chapter 3. However, because SAR measurements are sparse, validation using *in situ* measurements from the sparse buoys moored in deep ocean provides very few co-locations and thus limited error characterization.

Yet, a refined methodology using linear propagation theory was proposed in Chapter 5 to increase swell sampling by extrapolating the SAR swell measurements in deep ocean, away from islands and in the absence of current. Besides, it has demonstrated the possibility to use SAR swell measurements to monitor swell fields' propagation over an entire ocean basin. Specifically, we showed that this methodology could be applied to complex scenarios even if long-lived and/or fast moving storms require additional filtering. Often, the spatial distribution of the propagated SAR measurements was shown to be very heterogeneous, as evidence in Chapter 4. In such cases, the estimation of swell main properties developed in the virtual buoy concept can be hazardous even though the large scale distribution of wavelength propagated measurements, for example, seems to deliver useful information.

In Chapter 6, we thus proposed a new concept, the synthetic swell field, a methodology taking advantage of the large scale distribution to detect outliers and retrieve swell information on a regular space-time grid despite the irregular distribution of the SAR propagated measurements. Estimations given by this new observation-based model could be co-located with buoy measurements more than half of the time, as opposed to the track-based SAR swell measurements offering very few co-locations. As a result, a better identification of estimation errors is possible and indicates systematic errors on peak periods and the significant swell heights. Besides, the pro-

cesses responsible for these statistical biases can be better understood when inspecting the wealth of information provided by rejected outliers. For the first time, the significant swell height error dependency on the swell direction with respect to the SAR instrument is documented. This observation-based model can provide a new validation approach for the improvement of SAR swell measurements. Inter-comparisons between the synthetic swell field and *in situ* measurements on one hand and classical numerical wave models like WW3 and the same *in situ* measurements on the other hand have shown that this observation-based model performances depended on the data density of SAR propagated observations and under identified conditions, were statistically more accurate than WW3 model. This shows that despite the large errors in individual SAR measurements, using careful filtering, they can be arranged into consistent swell fields used for the development of a global observation-based deep ocean swell model, with regular space/time sampling.

In terms of perspectives, a direct application of the present work is the use of our synthetic swell field estimations for improved parametrization and assimilation in numerical wave models. This could contribute to correct erroneous hindcasts/forecasts caused by incorrect wind forcing or swell dissipation. Reciprocally, we also expect inter-comparisons between numerical models, SAR estimations and *in situ* measurements to better identify and characterize the synthetic swell field estimation errors. Other advantages of using assimilation in numerical wave models is that they can provide the full frequency range of wave forecasts, not just swell restricted, which is available in deep as well as in shallow waters.

In addition, we showed that the major part of the systematic errors affecting the synthetic swell fields was due to systematic errors affecting the SAR observations. Therefore, inspecting the detected outliers shall lead to better estimation of SAR swell observations which, once processed, will also lead to better synthetic swell field estimates. For instance, the comparison of synthetic swell field estimated with seismic noise has highlighted the underestimation of long swell peak period and, to a larger extent, the impossibility to retrieve extremely long swell characteristics in SAR L2 wave products although the signature was present in the SAR imagette. This shows that some improvements are needed and already identified in the swell spectra inversion.

The main parameter limiting the synthetic swell model accuracy is the data density, which is determined by the orbit of the SAR instrument as explained in Chapter 4. Although, the data density could be improved using other observation sources such as moored buoys, seismometers and data from the future CFOSAT mission. Indeed, the model only requires informa-

tion on the three integral swell parameters and few additional developments are necessary to realize this extended model.

Finally, the large influence of satellite orbits on swell observation capability was shown and should certainly be taken into account for future missions targeting swell observations such as CFOSAT.

In the end, we can be very optimistic looking at the upcoming years of ocean swell observation with SAR. The future launch of the two satellites Sentinel-1A and 1B by the end of 2013 and 2014 will bring unprecedented wealth of SAR swell observations thanks to more appropriate satellite orbits, the future possibility to also retrieve swell information from SAR image mode products. Besides, these SAR observations shall be of higher quality thanks to larger SAR imageries and the frequency range of observable swell, extended to very long swell owing to the potential swell inversion improvements. All these new algorithm developments will also lead to higher quality reprocessing of the SAR wave mode archive since 1991. On top of this, if the new concept mission CFOSAT reaches its expectations, spaceborne swell observation will be even richer. Today, efforts shall be focused on the improvement of the SAR swell spectra inversion, the preparation of assimilation applications and the deployment of an operational validation scheme in order to make the most of the upcoming SAR products.



# Acronyms

ALOS	Advanced Land Observation Satellite
ALSE	Apollo Lunar Sounder Experiment
ASAR	Advanced Synthetic Aperture Radar
CDIP	Coastal Data Information Program
CERSAT	Center for Satellite Exploitation and Research
CFSR	Climate Forecast System Reanalysis
ECMWF	European Center for Medium-Range Weather Forecasts
EMH	ElectroMagnetic-Hydrodynamic
ENVISAT	ENVIronmental SATellite
ERS-1/2	European Remote-Sensing satellites
ESA	European Space Agency
GPS	Global Positioning System
GRL	Geophysical Research Letters
GSN	Global Seismic Network
JERS	Japanese Earth Resources Satellite
JPL	Jet Propulsion Laboratory
MARSEN	MARine Remote SENSing experiment
MEM	Maximum Entropy Method
MLM	Maximum Likelihood Method
MTF	Modulation Transfer Function
NCEP	National Center for Environmental Prediction
NCEP RA-2	NCEP ReAnalysis-2
NDBC	National Data Buoy Center
NODC	National Oceanographic Data Center
NRCS	Normalized Radar Cross Section
NRMSE	Normalized Root Mean Square Error
NV	Normalized Variance
OPPE	Organismo Publico Puertos del Estados (Spanish acronym for the National Harbor Organization)
PRF	Pulse Repetition Frequency
QuikSCAT	Quick Scatterometer
RAR	Real Aperture Radar
RMSE	Root Mean Square Error

SAR	Synthetic Aperture Radar
SAR L2	SAR Level-2
SAR L2P	SAR Level-2 Partition
SI	Stroboscopic Imaging
SIR-A/B/C	Shuttle Imaging Radars
UKMO	United Kingdom Meteorological Office
WAM	Wave Action Model
WAMDAS	Wave And Meteorological Data Acquisition System
WHOI	Woods Hole Oceanographic Institution
WMO	World Meteorological Organization
WW3	WAVEWATCH III <sup>®</sup>

THIS PAGE INTENTIONALLY LEFT BLANK